IMPERIAL COLLEGE

CONJUGATED PORPHYRIN DIMERS AS PROBES OF MICROVISCOSITY

MARYAM QURASHI

JULY 2015

THESIS SUBMITTED IN PARTIAL FULFILLMENT OF THE REQUIREMENTS
FOR THE DEGREE OF

DOCTOR OF PHILOSOPHY OF IMPERIAL COLLEGE LONDON

DIVISION OF CHEMICAL PHYSICS
DEPARTMENT OF CHEMISTRY
IMPERIAL COLLEGE LONDON
PRINCE CONSORT ROAD
LONDON
SW7 2AZ

Declaration of Originality

With the exception of the following, I hereby declare that all data shown and content written in this thesis; 'Conjugated porphyrin dimers as probes of microviscosity' is my own unless otherwise declared.

1. Neutron reflectrometry experiments and data analysis were performed at ISIS, Rutherford Appleton Laboratories with the assistance of Dr Arwel Hughes.
2. Ratiometric imaging, FLIM and data analysis were performed in collaboration with Aurimas Vysniauskas in the group of Dr Marina Kuimova at Imperial College London.

Maryam Qurashi

Acknowledgments

Firstly, I'd like to thank my friend and supervisor, Dr Marina Kuimova, for her advice, support, proofreading and immense patience during my PhD. Having been there from the very early days of the Kuimova research group, I feel we've seen a lot together. Marina has always heard me out, encouraged me and given sage advice during difficult times (including but not limited to, lending me emergency money when I lost my wallet in Liege).

I'd like to thank all members of the Kuimova group that came and went during my time there. In particular, Dr Neveen Hosny, who sat next to me for three years and invaded my personal space daily, often with good humour, great advice, technical assistance in all matters and immense support. I thank Dr Thanh Truc Vu, one of the most generous people I know, who is a very good friend and excellent scientist; Dr Maria Izquierdo-Arcusa, for showing me how to be calm at all times; Dr Ismael Lopez-Duarte, for ensuring my habits in the lab never got too slack; Dr Alex Thompson, for never tiring of answering my questions; Dr Rob Richardson, in particular for hours and hours of aligning the nanosecond laser and for making everything seem hugely complex; Aurimas Vysniauskas, for making everything seem simple again; Thanos Athanasiadis, for being Mediterranean in every possible way; Marketa Kubankova, for all manner of delicious baked goods; and Michael Dent, for being very good company.

I also thank the students and staff who were a daily presence: Dr Michael Cecchini, Dr Vladimir Turek, Dr Arwen Tyler, Dr Yuval Elani, Dr Sowmya Purushothaman and Youngeun Choi, who all knew exactly how it felt, in good times and bad.

I give thanks to my friends for helping more than they'll ever know, providing laughter and backbone when I was lacking both. To Meredith Wouters, for being the bravest person I know and to Joseph Kennedy, for being more important than my thesis.

Finally, I thank my family for love and support; my father, for never letting me take myself too seriously; my mother, for wishing I was more serious; my brother and long-time flatmate, for occasionally cleaning up and always being willing to talk about magnetism. My greatest motivation during my four years has been to make you all proud.

Maryam

Contents

List of Abbreviations

$^1O_2$	singlet oxygen
2-MTHF	2-methyltetrahydrofuran
BODIPY	boron-dipyrromethene
$CHCl_3$	chloroform
Chol	cholesterol
CMAM	2-cyano-3-(4-dimethylaminophenyl)acrylic acid methyl ester
Cy15/18	Cyanine15/18
DCVJ	(4-(Dicyanovinyl)Julolidine)
DiI-C_{18}	(1,1′-dioctadecyl-3,3,3′,3′-tetramethyl- indodicarbocyanine perchlorate)
DMSO	dimethylsulfoxide
DOPC	1,2-Dioleoyl-sn-glycero-3-phosphocholine
DPhPC	diphytanoyl phosphatidylcholine
DPPC	dipalmitoylphosphatidylcholine
DPPE	1,2-dihexadecanoyl-sn-glycero-3-phosphoethanolamine
D_r	rotational diffusion coefficient
DSPC	1,2-Distearoyl-sn-glycero-3-phosphocholine
D_T	translational diffusion coefficient
EMA	ethyl-methacrylate
ESR	electron spin resonance
FCS	fluorescence correlation spectroscopy
FCVJ	(2-carboxy-2-cyanovinyl)-julolidine farnesyl ester
FLIM	fluorescence lifetime imaging microscopy
FRAP	fluorescence recover after photobleaching
GM1	monosialotetrahexosylganglioside
GUV	giant unilamellar vesicles
H_2O	water
ITO	indium tin-oxide
LAURDAN	6-Dodecanoyl-2-Dimethylaminonaphthalene
L_d	liquid disordered (phase)
L	liquid ordered (phase)

LUV	little unilamellar vesicle
MCCA	7-methoxycoumarin-3-carboxylic acid
MeOH	methanol
MMA	methylmethacrylate
M_N	molecular number (polymer)
NaN_3	sodium azide
NBD-PE	1,2-diphytanoyl-*sn*-glycero-3-phosphoethanolamine-N-(7-nitro-2-1,3-benzoxadiazol-4-yl)
n-BMA	n-butyl methacrylate
NMR	nuclear magnetic resonance
PDT	photodynamic therapy
PEG_{600}	polyethylene glycol 600
POPC	1-palmitoyl-2-oleoyl-sn-glycero-3-phosphocholine
QENS	quasi-electron neutron scattering
Rho-PE	rhodamine-phosphoethanolamine
RICS	raster-imaging correlation spectroscopy
SKOV-3	ovarian cancer cell line
SLB	supported lipid bilayer
SPT	single particle tracking
T_g	gel-transition temperature
w/v %	percentage weight/ volume

Abstract

The cell membrane is a recent target for the imaging and quantification of viscosity in light of evidence which suggests that abnormal membrane behaviour is related to various disease states. We propose the use of a novel technique involving a class of compounds termed 'molecular rotors', which can image cellular viscosity with high spatial and temporal resolution. This Thesis concerns one type of molecular rotors, conjugated porphyrin dimers, which have dual functionality: as viscosity sensors and as photosensitizers for photoinduced cell death during Photodynamic Therapy of cancer (PDT).

First, we consider the photophysics of several conjugated dimers bearing various substituents and assess the effect of various parameters on dimer's intermolecular rotation. We find that the photophysical properties of most dimers are primarily sensitive to the viscosity of their environment and are minimally sensitive to temperature and solution polarity.

Secondly, using polymer solutions and melts, we establish the physical origin of the porphyrin dimer's viscosity sensitivity as detection of solvent 'free volume', which is related to both macromolecular crowding and solvent hydrodynamic pressure.

Thirdly, we establish conditions for the inclusion of a porphyrin dimer into model lipid membranes; demonstrating the detection of lipid phase as a function of temperature, sensitivity to free-volume occupancy of lipid tails according to saturation, and finally reporting viscosity values in close agreement with those from literature obtained using alternative methods.

Finally we find that under conditions of imaging using fluorescence microscopy, the porphyrin dimer has compromised fluorescence signal due to limitations of solubility during sample preparation. However, by combining the detection from a poprhyrin dimer and a well-known molecular rotor BODIPY-C_{10} we were able to detect a viscosity increase in unsaturated lipid membranes upon increased exposure to light, replicating conditions of singlet oxygen production during PDT.

I. Introduction

Many macromolecular interactions within the cell are governed by the likelihood of diffusion-controlled collisions between interacting partners. Crucial to likelihood of such collisions taking place is the viscosity of the solution in which these molecules are immersed. In light of what is known regarding the local isolation of biochemical processes, we predict that viscosity varies widely, both spatially and temporally, amongst organelles and subdomains. Multiple cellular disease states have been correlated to departures from normal cellular viscosity. Quantification of viscosity inside cells is necessary for understanding the processes that occur during these cellular dysfunctions. In addition, due to the wide spatial variety in cellular domains, imaging cellular viscosity allows a comprehensive view of these same processes in tandem.

1.1 The importance of measuring cellular viscosity

Departures from normal cellular viscosity are not yet determined as causes or consequences of cellular disease but medical research as often related abnormal cellular viscosity and impaired cellular function. In normal function, rates and mechanisms of collision-controlled biochemical processes are determined by diffusion-controlled interactions. Abnormal cellular viscosity is implicated in diseases such as arthrosclerosis[1], hypertension and hypercholesteraemia[2], diabetes[3,4], ageing[5] and during the initiation of apoptosis by the application of photodynamic therapy (PDT)[6]. Arthrosclerosis[1], and hypercholesterolemia[2] are associated with elevated cellular membrane viscosity which can alter the mechanical properties of entire tissues by alterations of the lipid components or compositions of membranes. Alternatively, high protein concentration within the cellular membrane can initiate mechanical changes to the membrane. Alzheimer's disease, for example can be diagnosed by altered character of the neuronal membrane due to the accumulation of proteinaceous plaque on the surface of neurons which exerts shear stress upon the membrane[7]. Shear stress contributes to the elevation of fluid viscosity and alters the viscoelastic and diffusive properties of the membrane[7,8]. In light of significant literature that correlates abnormal cell membrane viscoelasticity with disease states,

we aim to develop a novel technique for spatially and temporally resolved measurements of lipid bilayer viscosity to inform upon the biophysical origins of this parameter.

1.1.1 Scales of viscosity: macro and micro

The most widely used methods for measuring bulk viscosity involve mechanical deformation of fluid, e.g. in a rheometer or a flow viscometer. It is clear that such measurements are not applicable on the microscopic scale, and for measurements of hydrodynamic properties of individual organelles. The latter, here termed 'microviscosity' is intrinsically related to the organization of solvent molecules in the immediate environment of the probe used and the frictional interactions between them. For instance, Valeur et al., 2001 denotes two types of solute motion that contribute to bulk viscosity: i) Stokes-Einstein diffusion[9,10]: where translational motion of a given solute requires the displacement of solvent molecules by the kinetic energy and ii) free-volume diffusion[11], in which solutes move into 'empty' space between surrounding molecules as summarized in Figure 1.1.

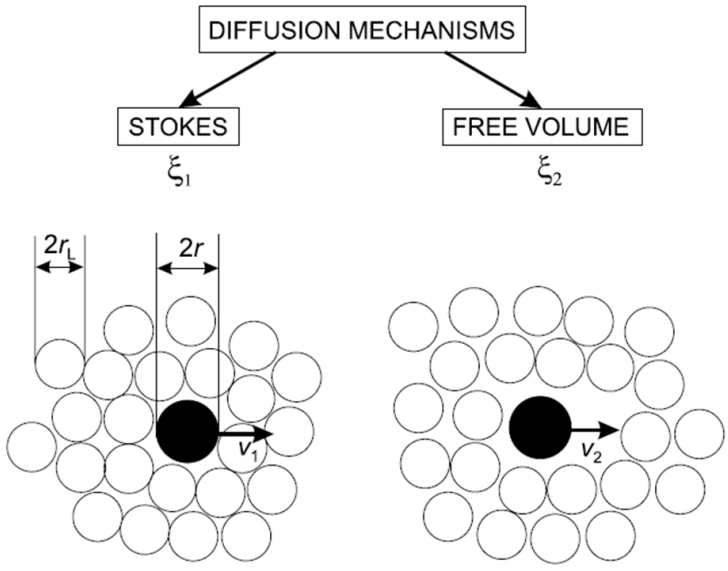

Figure 1.1: Two diffusion mechanisms of a solute (black) dissolved in solvent molecules (white); Stokes-Einstein diffusion (left) occurs by displacement of solvent molecules at velocity, v_1, with diameters $2r$ and $2r_L$ for solute and solvent, respectively, giving a friction coefficient of ξ_1.Alternatively, free volume diffusion (right) occurs by diffusion into solvent 'holes', with velocity v_2, giving a friction coefficient of ξ_2. Scheme from Valeur et al., 2001[12]

The probability of each mode of diffusion is determined, amongst physical parameters such as temperature, by the size and shape of the solute and its electrostatic interaction with the solvent[9,13]. Together, these are the physical origins of microviscosity. However, microviscosity is not equivalent to bulk viscosity that is measured by mechanical means. Microviscosity is measured as (i) translational motion of the probe in fluid and/or (ii) rotational motion of the probe, each described by a diffusion coefficient that relates to η, a measurement of bulk viscosity. Translational motion of the probe in an organized solvent is impeded by solvent friction and other dissolved solutes within the solution. Alternatively, the restriction of a probe's local rotation during rotational diffusion has been interpreted as a good means of measuring solvent viscosity as it informs upon internal friction in solution and the hindrance to an individual molecule's movement[14].

It is important to remember that while both approaches are valid, the scale of diffusion as described by both models is different: translational diffusion is measured on the scale of micrometers, while rotational diffusion is measured on the scale of the probe's diameter, often nanometers. Both models are associated with a number of assumptions regarding the nature of a probe's motion within a solvent. Previous report by our group compared both approaches for a single fluorophore and found a good agreement[15] however it is important to emphasise that such result may not be representative of all molecular rotors and/or microviscous systems. This Thesis reports microscopic viscosity measurements via the use of molecular rotors, molecules whose fluorescent behavior is intrinsically linked to solvent viscosity due to twisting and/or rotation of molecular parts. As will be seen, the use of molecular rotors poses unique advantages, namely it allow the imaging of viscosity in cells, under physiological conditions. The images provide temporal and spatial resolution, with the ability to quantification of a dynamic and complex parameter. Whenever possible, all results obtained using molecular rotors in this Thesis will be compared to the literature values obtained using translational diffusion approaches.

1.2 Microviscosity in membrane regions

Membrane fluidity is a highly relevant parameter for the maintenance of normal cellular function. The cell membrane is itself a bilayer of amphiphiles which, once assembled, create a planar layer of charged groups exposed to the external aqueous compartment which protect an inner hydrocarbon region. What at first sight seems like a two-dimensional film compared to the size and complexity of the cellular interior is, in fact, a complex three dimensional environment. Moreover, the membrane hosts many biochemical reactions that are catalyzed by proteins embedded within a largely phospholipid bilayer and must be able to diffuse laterally along the surface. Janmey et al., 2006 summarise the effects of biophysical character of the membrane on the behaviour of embedded proteins, where lateral pressure or stress can regulate integral proteins that actively alter membrane character, causing bending or stretching or can alter biochemical processes[16]. On the other hand, physical membrane properties such as lateral tension between the phospholipids, bilayer depth, asymmetry between the two layers, out-of-plane diffusion and collective undulations of the component phospholipids are all implicated in the mechanical role of the membrane; isolating subcellular locales, determining cellular volume, and the elastic properties of the cell in response to external stress. We attribute these macroscopic features of membrane behaviour to the microscopic features of individual phospholipid molecules, they undergo rotational motion, and have hydrocarbon chain and independent head group dynamics, and diffuse laterally to give the membrane its characteristic 'viscosity'[17,18]. The molecular nature of the phospholipid strongly determines its individual dynamics, two parameters we examine are acyl chain length and saturation in their effect on viscosity[19].

As such, membrane parameters such as fluidity and mechanical strength are kept in necessarily narrow ranges for cellular health[20]. The bilayer is often described as in a liquid-crystalline state, having fluid and solid properties where the component amphiphilic molecules determine the properties of the whole membrane. Marr et al., 1962, found that unicellular organisms maintain the fluidity of the cell membrane by adjusting the composition of lipids in the membrane such

that the membrane is always fluid at the temperature of growth. This exemplifies the importance of the specific fluid properties of the cell membrane as they determine protein diffusion as well as the cell's elastic properties[21]. Indeed, since then, it has been established that the liquid-crystalline state and resultant fluidity of the membrane depends strongly on the degree of saturation of its fatty acid chains [22,23].

The shape and size of the composite lipids within a bilayer determine its curvature, strength, associated proteins and their lateral diffusion. Macroviscosity of the membrane is described by the shear stress attributed to membrane-embedded or surface-associated proteins. Microviscosity in the membrane, the significant determinant of its fluidity, is defined by the order of the hydrocarbon interior of the bilayer, commonly referred to as lipid *phase*. Cogan et al., 1973, and many authors since, have modelled a considerable change in membrane fluidity upon the addition of cholesterol to liposomes or simple vesicles[20,24]. In light of this view of membrane order, the microviscosity of the hydrocarbon region is a target for viscosity-sensing in terms of quantification and viscosity.

Our approach is to measure microviscosity as a means of estimating macroscopic bulk viscosity as it translates in common bulk liquids. Where possible, we compare our measurements with those made by different techniques.

1.3 Established methodologies for viscosity measurement

Precedents for the measurement of cellular viscosity are varied and extensive. The methodologies already employed in resolution of cellular viscosity are sensitive to independent contributors (micro and macro) to cellular fluid dynamics. Consideration of these contributors and their influence upon diffusion are central in determining the suitability and relevance of a particular method for viscosity measurement.

1.3.1 Motion of 'solvent' molecules

The measurement of the motion of solvent molecules themselves is one approach to determining microscopic viscosity. Under the circumstances of the phospholipid bilayer, the

phospholipids themselves are the 'solvent' molecules. To this end, proton nucleic magnetic resonance spectroscopy (H^1NMR) has been used to determine the transverse relaxation rates of protons in a cellular environment[25,26,27]. Measurements are made relative to rates of protons in pure water, proton relaxation rates after alignment to a magnetic field reflect the random orientation of the proton dipoles and this is interpreted as a measurement of their rotational freedom in the medium. A non-invasive method for cells, H^1NMR has estimated the transverse relaxation times of cytoplasmic water dipoles to be $1/50^{th}$ of those in pure water implying that diffusion is restricted seven-fold in the cytoplasm[7,25] Another method developed to measure the motion of 'solvent' molecules is quasi-elastic neutron scattering (QENS), which measures the scattering of neutrons at high resolution inside the cell (several Angstroms). The technique gives a picosecond (10^{-12} s) time resolution of, which excludes the possibility of observing collisional interactions with solutes because they occur at longer timescales. QENS data, due to the advantageously small area of measurement inside the cell, resolves the structure of the bilayer, which can reveal the order and 'phase' of the component lipids in the bilayer. From this, viscosity is extrapolated using a range of frictional models.

QENS and H^1NMR have been performed on model membranes in order to discern the conformational dynamics of the fatty acid chains. It was shown that the number of 'kinks' in the fatty acid chain can predict certain motions within the hydrocarbon region and gel-phase dynamics can be modeled as the result of these 'kinks'[28]. However, quantification of microviscosity in the hydrocarbon region has not been attempted by QENS. In addition, methods that resolve solvent molecules such as QENS and H^1NMR, are non-ideal for cells due to harsh experimental conditions and long measurement times[7,25]. Most importantly, they are not imaging techniques and spatial resolution of microviscosity in the cell is lost.

More common than measuring proton motion or neutron scattering, is the introduction of an exogenous probe into the bilayer. Many features of this probe can be measured, for example the probe's excited electron spin relaxation or its spectroscopic behaviour depending on the

technique employed. These methods are generally more widely available and theoretical assumptions make viscosity estimation more straightforward than for methods that resolve bilayer structure. Nevertheless, any technique involving the introduction of an exogenous molecule can have the disadvantage of altering the bilayer or, in the case of biological environments, can be said to bind to a complimentary macromolecule, restricting its free motion. Below, we summarise the more common techniques employed in viscosity measurement.

1.3.2 Small 'spin' probes used to mimic solvent molecules

H^1NMR has an analogous technique that measures the spin relaxation of unpaired electrons as an indicator of their local environment. The original justification for and mechanism of using ESR in viscosity measurement is much the same as that in H^1NMR but ESR involves monitoring the motion of probe molecules rather than the random ordering of solvent molecules and so is subject to the same considerations as all methods involving the use of exogenous probes. Experimentally, ESR is performed on paramagnetic molecules, i.e. those with an unpaired electron, it informs on the highly specific localization and interactions of radicals. Electrons are separated according to their spin alignment either parallel or anti-parallel (m = ± ½) to an externally applied magnetic field, B_0, where a large proportion of the electron population is expected to be aligned parallel to B_0. A frequency of microwave radiation (typically 9-10 GHz) is applied to the magnetically aligned sample while the strength of the external magnetic field is varied. Absorption of the applied microwave radiation at a particular frequency, the resonant frequency, matches the energy difference of electrons occupying the states, m = ± ½, causing the spin alignment to collapse or 'relax'.

Structure-free ESR spectra imply an isolated atomic sample where spin alignment and relaxation are not affected by local features, and this can be observed in gas-phase ESR. Yet, in solution, spectral line widths give information about the local environment of the paramagnetic species, both in terms of intermolecular proximity to the interfering magnetic fields of closeby nuclei and external factors such as solvent viscosity. Two consequences of highly viscous

solution on spin alignment are presented by Atkins and Kivelson, 1966: 1) the angular momentum of the spinning electron is decelerated more rapidly (meaning that the rotational correlation time, the relaxation of the rotational angular momentum of the spin-probe is dependent upon the inverse of viscosity (η^{-1})) and 2) the reorientation correlation time, the frequency with which the molecule's spin coincides with B_0, is reduced[29]. Rotational correlation time is an important parameter in viscosity sensing and will be discussed in further detail in the context of fluorescence anisotropy in later sections. Mathematically, Atkins and Kivelson showed that these two phenomena are dependent upon a frictional constant (viscosity or temperature) and are represented by time-resolved parameters [29,30]. Spin-rotational coupling describes the co-dependence of these factors because as a molecule rotates, the electrons do not strictly follow the motion of the nuclei creating a temporary and tiny imbalance in charge distribution. This imperfection in the rotating molecule creates a magnetic moment that can affect the electronic spin, the very parameter measured by ESR[29,30]. So in application, the perturbation of electron spins (ESR) can measure viscosity by a probe-molecule's rotation. Cytoplasmic viscosity has been measured by ESR in several instances: Lepock et al., 1983, obtained viscosity estimates of 11 cP for Chinese hamster lung cells using the spin-probe, 2,2,6,6-tetramethyl-4-piperidone-*N*-oxide (TEMPONE)[31]. The group of Keith et al., pioneered the use of water-soluble spin probes and ESR to measure the viscosity of cytoplasm, but their measurements varied with experimental conditions. In 1977, Keith et al., explained this variation by identifying the two-fold dependence of spectral line width on concentration and on viscosity[32]. Spin-spin interactions and charge interactions are two concentration dependent factors that cause ESR line width broadening and can be confused with the effects of viscosity. He also demonstrated that different diffusion dynamics in a heterogeneous environment complicated the direct relationship between ESR line width and viscosity[32]. For this reason, measurements of viscosity are spatially compromised by averaging, similar to in H^1NMR[32].

ESR is most often applied to the investigation of membrane fluidity. Mason and Freed's 1974 simplified model relates spectral line width and rotational correlation time and has been

applied to studying the changing membrane fluidity of Chinese hamster ovary cells during the cell cycle, the importance of fluidity on regulation of certain proteins, and to the investigation of the gel-phase of egg yolk lecithin liposomes [33,34,35,36]. However, Lai et al., 1980, during their investigation of changing membrane composition through the cell cycle, found that the modeled isotropic rotation from which they extrapolated un-broadened spectral line width did not hold to anisotropic rotation in lipid bilayers and comparisons between the two did not give as clear a relation to rotational correlation time as first anticipated[34]. ESR-based viscosity sensing of lipid membranes also suffers from the same concentration-related confounding effects mentioned above that we identified by Keith et al., 1977[34]. More recently, however, membrane domains have been probed by ESR through monitoring the spin of endogenously produced oxygen radicals[37,38]. This latter approach has recently been used to image oxygen metabolism and oxygenation in live tissues, namely rabbit aorta and heart tissue[37]. Imaging by ESR is not; however, the most common approach to spatially resolving viscosity in cells due to the complex assortment of biochemical consequences of a large concentration of radicals in a membrane environment.

The techniques described above have been quickly overshadowed by those involving fluorescence spectroscopy as a means of measuring viscosity at cellular scale. These methods are sensitive to the emission of photons from molecules whose electronic configuration can be temporarily altered by absorption of light.

1.4 The phenomenon of fluorescence

A photon with sufficient energy can excite an electron between *states*, each of which is characterized by a certain spin configuration and energy of the orbitals, relative to the zero energy of unexcited *ground state* (S_0). Molecular orbitals are separated by a quantum of energy proportional to a wavelength of light as predicted by the Planck-Einstein relation (equation 1.1)

$$E = h\nu = hc/\lambda \tag{1.1}$$

Where *E* is energy (J) , h is Planck's constant (6.626 x 10^{-34} J s), and ν is frequency (s^{-1}). Equation 1.1 is often expressed in terms of wavelength, λ (m), using the proportion $\nu = c/\lambda$ where *c* is the speed of light (2.998 x10^8 m/s). Figure 1.2 depicts four (S_0, S_1, S_2 and T_1) of the most commonly accessed states in fluorescence experiments. Electronic excitation (movement of an electron to a higher energy state by absorption of light) always occurs from the highest occupied molecular orbital (HOMO, or HO as in Figure 1.2) to the lowest unoccupied molecular orbital (LUMO, LU, in Figure 1.2), regardless of the nature of the molecular orbital or occupation of lower energy orbitals. Typically, as predicted by the Pauli Exclusion Principle, both electrons occupying a ground state HOMO are spin-paired, as in S_0 (inset, Figure 1.2), where they have opposite spins, represented as↑↓. Once in separate orbitals, by excitation of one electron to the LUMO, the electrons are no longer required to be spin-paired, and can result in either a singlet excited state (S_n) or a *triplet* excited state (T_n, represented as ↑↑) where both electrons occupy the same spin state. The subscript *n* identifies the relative energy of the state to the HOMO, whereby S_1 is the first singlet excited state, T_1 the first triplet excited state and so on.

Conversion between states are characterised by various time scales and probabilities particular to each fluorescent molecule and are discussed in detail below.

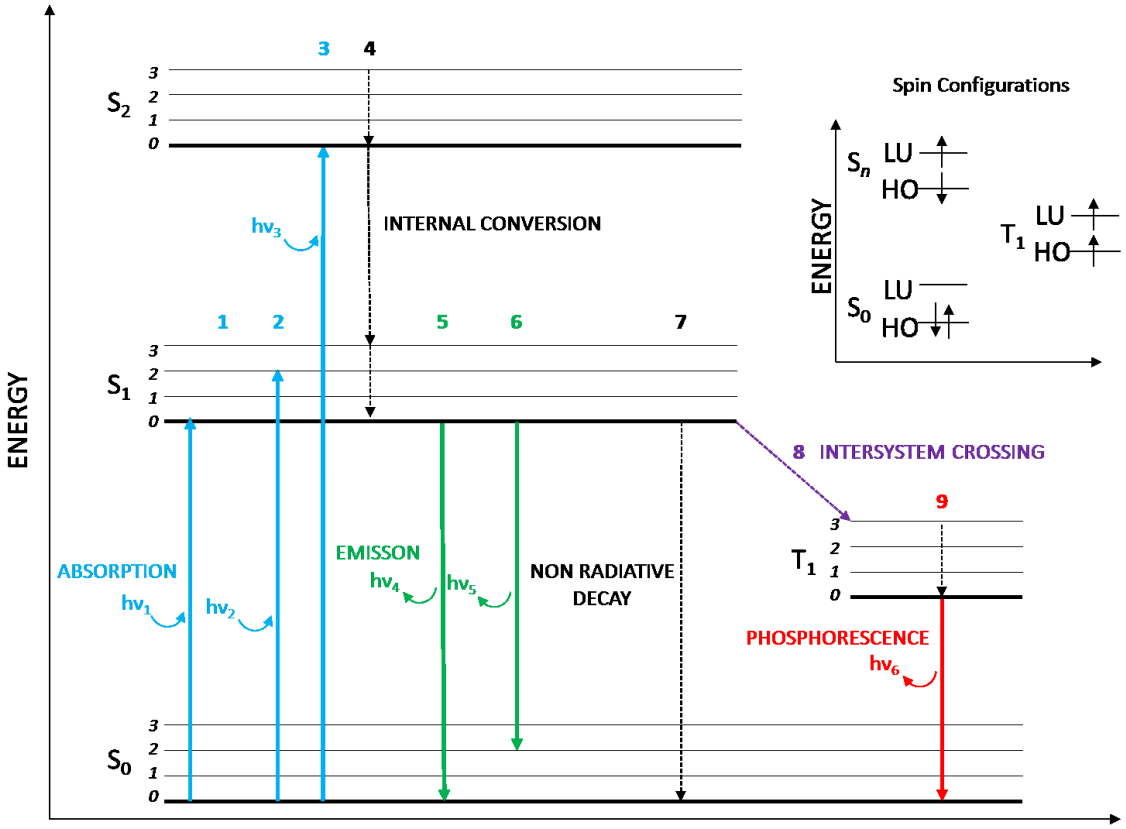

Figure 1.2: A Jablonski diagram showing instances of absorption from the singlet S_0 HOMO to the S_1 LUMO (blue solid lines, transitions 1-3), internal conversion (black dotted lines, transitions 4, 7) emission (green solid lines, transitions 5,6), intersystem crossing to the triplet T_1 state (purple dotted line, transition 8), and phosphorescence from the T_1 to the S_0 state (red lines, transition 9). Inset, showing electron spin configuration in the S_0, S_1 and T_1 states.

1.4.1 Absorption

The transition $S_0 \rightarrow S_n$ occurs by transfer of the energy of a photon to the absorbing molecule, when the energy of the photon (i.e. at appropriate λ) is matched to the energy difference between the S_0 and S_n states as shown in Figure 1.2, transition 1 where the energy of photon $h\nu_1$ is equal to the energy band gap; $\Delta E = E_{S1} - E_{S0} = h\nu_1$.

Absorbance is typically measured as 'transmittance' or the relative difference in intensity of incident light after interaction with a known concentration of the absorbing species. The decrease in transmittance is proportional to the Absorbance of the molecule at a given wavelength, which is dependent on its concentration and the path length of the light through a sample. The molar extinction coefficient ε (M^{-1} cm) is a proportionality constant that relates

Absorbance (A, in arbitrary units) to concentration (*c*, in M^{-1}) and path length (*l*, in cm^{-1}) by the Beer-Lambert Law (equation 1.2).

$$A = \varepsilon cl \tag{1.2}$$

Absorption spectra of complex organic molecules are most often observed as relatively broad bands with some structured peaks, rather than sharp lines as are observed for atomic absorption spectra. This is due to the vibrational motion of the molecule, creating multiple permutations of each electronic state. This results in multiple *substates* of varying energy associated with each state S_0, S_1 etc. In Figure 1.1, transition 2 is depicted as between the S_0 substate 0 to substate 2 of the S_2 state ($0 \rightarrow 2$) whereas transition 1 is transition from 0 of S_1 to 0 of S_2 ($0 \rightarrow 0$). The distribution of molecules into substates in the ground state is best described by the Boltzmann distribution function, reflecting its dependence on temperature. However at room temperature, the vast majority of organic molecules transition from the lowest vibrational level of the ground state.

In a stable HOMO, the geometry of the atomic nucleus is balanced against the orientation of electrons in their respective orbitals. Once absorption excites an electron, and electron density is altered, the geometry of the nucleus must reorient relative to the new magnetic dipole of the molecule. However, because absorption takes place on the order of femtoseconds ($x10^{-15}$ s), there is a brief configuration of the excited state where the nuclear configuration is unchanged, this is termed the Franck-Condon state with picosecond lifetime ($x10^{-12}$ s). The Franck-Condon principle, for which the Franck-Condon state is named, predicts that all instances of absorption are 'vertical' transitions between potential energy curves of both the ground and excited states. Under this explanation, potential energy curves of the two states only observe very small changes in shape, but are separated vertically by the energy band gap, i.e. 'vertical' transitions. Absorptive transitions to higher states are also observed in many cases, such as shown in Figure 1.2, transition 3, where the electron is excited to the S_2 state, where $h\nu_3$ represents a excitation at a shorter λ (higher ν) absorption band than seen in transitions 1 and 2.

Absorption of a photon results in formation of an excited state that can undergo several de-excitation pathways, namely: emission, internal conversion, intersystem crossing and chemical reactions leading to photochemistry.

1.4.2 Emission

In solution, at ambient temperatures, the vibrational energy of the excited state molecule in a nonzero substate (i.e. transition 2) is often dissipated by collisional interaction with the solvent. Also, higher vibrational energy can spread from one part of the molecule to others, and is often dissipated this way into the solvent. A combination of both processes is termed 'vibrational relaxation' and takes place on the order of picoseconds ($x10^{-12}$ s): prior to emission, which takes place on the order of nanoseconds ($x10^{-9}$). It is due to the difference in timescales that, as a rule, solvent-assisted vibrational relaxation always takes place faster than emission. For this reason, structure in the emission spectra that reflects the vibrational substates of the excited state is lost and emission spectra are independent of excitation λ. This phenomenon is termed Kasha's rule, and applies not only to relaxation of vibrational energy but also between higher and lower excited states. For instance, the electron that is excited to the S_2 state in Figure 1.2, transition 3, is shown to relax to the lowest vibrational substate of S_2 and subsequently relax to the S_1 state without emission of a photon. This is termed internal conversion and applies to both relaxation between states, and relaxation within their vibrational substates. Emission from excited states higher than the LU state is rare because the potential energy surfaces of excited states are commonly very close in energy, with significant overlap such that internal conversion to the lowest excited state occurs prior to emission.

The Franck-Condon principle also strongly affects the nature of emission spectra, with wavefunctions' overlap determining the substate of the ground state to which the emission of photon will be directed, i.e. transition 5 or 6 in Figure 1.2. Figure 1.2, transitions 5 and 6 show that while emission generally occurs from the lowest vibrational level of the lowest excited state, the emitted electron may drop to one of the numerous substates to the ground state. As such, emission spectra are often broad, but contain information regarding the vibrational

structure of the ground state. For the purposes of spectroscopy, most molecules are chosen that are excited in the visible range of the electromagnetic spectrum (i.e. 200-700 nm). However, absorption of longer wavelengths (700-1000 nm) of light can be used to probe an electron's movement between vibrational energy levels within a given state. Transitions 5 and 6 in Figure 1.2 are *radiative*, meaning a photon is emitted upon the decay of the excited state. Nonetheless, *non-radiative* transitions from the excited states back to the ground state are also possible and their likelihood is closely related to the environment of the fluorophore. Non radiative decay, as shown in transition 7 of Figure 1.2, can be caused by many different interactions between the fluorophore and its surroundings. For instance, upon interaction with large macromolecules, as in biological media, or by very effective dissipation of the excited state energy into vibrational or rotational movement of the molecular structure, both phenomena are sometimes referred to as q*uenching*.

Quenching by collisional interactions with neighbouring molecules occurs when the excited state fluorophore decays to the ground state following a collision, without any chemical interaction or alteration in the process. The fluorophore in the ground state can also be 'quenched' even before excitation if it should form a non-fluorescent interaction with another molecule. Thus the chemical nature of the solvent, and the presence of various solutes can strongly alter the emissive behaviour of a fluorophore.

Some interactions between excited fluorophores and heavy atoms or halogens result in *intersystem crossing*, or the formation of the triplet excited state from the singlet excited state as shown as transition 8 of Figure 1.2. Intersystem crossing occurs due to coupling between the excited electron's spin and the magnetic field created by the nucleus of the atom, causing the electron to reverse its spin. Should the potential energy surfaces of the singlet and the triplet overlap; the fluorophore can form the triplet state from the singlet, though the reverse is much more rarely observed, due to a relative position of the energy levels. The two electrons with parallel spins require less energy to repel one another, and this reduces the overall energy of

the triplet excited state relative to the singlet excited state, as shown in Figure 1.2, the triplet excited state has lower energy (but equal possibility of vibrational substates). Intersystem crossing is considered fluorescence quenching because decay from the triplet excited state back to the singlet ground state is not fluorescence, but rather *phosphorescence* as shown by transition 9 in Figure 1.2. This is a radiative transition back to the singlet ground state occurring at much longer λ than fluorescence. The triplet state has much longer lifetime than the singlet excited state, and is of interest in the framework of this Thesis due to the possibility of energy transfer with ground state molecular oxygen (O_2) which exists in a triplet ground state. Certain molecules that have triplet state energies matched well with the band gap between ground state oxygen and a singlet excited state of molecular oxygen are used for the production of the latter which has significance for therapeutic purposes. This process is the subject of one of the chapters of this Thesis and will be discussed in more detail in later sections. Other forms by which radiative decay are quenched include resonance energy transfer (RET), and electron transfer, but are not discussed in detail in this Thesis.

Fluorescence spectroscopy is concerned with the measurement of radiative decay, the quantum efficiency and the lifetime of the excited state. From these two parameters, inferences can be made about the relative rates of radiative and non-radiative decay, the energy associated with the fluorophore in various contexts which informs upon the nature of the environment surrounding the fluorophore. As will be seen in later sections of this Thesis, fluorophores can be designed in such a way that the non-radiative decay of their excited states reflects on the properties of it's environment. The dependence of the non-radiative decay in molecular rotors on the viscosity of their environment will be central to the work reported in this Thesis.

1.4.3 Parameters of measurement of radiative decay

When looking at emission spectra, the λ_{max} and intensity of emission at the λ_{max} are central to interpretation of the fluorophore's behaviour. Intensity of fluorescence can be quantified as quantum yield, a value given to the proportion of photons emitted for every photon absorbed. This may be subject to the excitation λ, solvent, and temperature surrounding the fluorophore

and so inferences about unknown environments can be made using general rules regarding emission quantum yield. However, intensity measurements are strongly affected by concentration of fluorophore and for the purposes of many experiments in heterogeneous environments such as cells, concentration is either not known or is dynamic over a given volume of measurement. For this reason, it is often beneficial to measure a fluorescence lifetime instead. The fluorescence lifetime is the average amount of time a fluorophore remains in the excited state, as mentioned before it is generally on the order of nanoseconds ($x10^{-9}$ s). Quantum yield is related to the inverse of lifetime, k_r the rate of radiative decay by equation 1.3, where Q is quantum yield and k_{nr} is the rate of non-radiative decay.

$$Q = \frac{k_r}{k_{nr} + k_r} \tag{1.3}$$

The lifetime τ, is related to k_r and k_{nr} by equation 1.4;

$$\tau = \frac{1}{k_{nr} + k_r} \tag{1.4}$$

Fluorescence lifetime is calculated by collection of single photons as they are emitted after excitation, characterised by the time difference, *t*, between excitation and emission of the photon. Because deactivation from the excited state is a variable process, a distribution of times *t*, is obtained. Fitting an exponential to the distribution allows calculation of the average lifetime τ, of that fluorophore. If the distribution can be fitted well by a single exponential decay, this signifies that 63% of the photons have been emitted prior to the time τ, while 37% will be emitted at t greater than τ.

Fluorescence lifetime is a desirable parameter to measure in fluorescence microscopy, due to its independence of fluorophore concentration. In systems involving biological trafficking of proteins and other molecules, where fluorophores can often be compartmentalised, the measurement of fluorescence lifetime allows reliable comparison of two regions with vastly different probe concentrations. Moreover, fluorophores with a long fluorescence lifetimes and high quantum yield are often used to monitor diffusion in biological environments. The longer

the fluorophore remains in the excited state, the further diffusion distances can be monitored by measurement of fluorophore intensity in a given volume; later sections discuss multiple techniques that utilize this approach.

1.4.4 Polarisation

The rotational motion allowed during the excited state lifetime of the fluorophore is a sensitive parameter for estimating a fluorophore's rotational diffusion, which can be linked to the viscosity of its environment. It is convenient to monitor such rotational motion in terms of the polarization of emitted photons. Here it is pertinent that for absorption to take place it is required that the *polarization* of incident light be aligned with the electric dipole moment of a molecule's HOMO. The electron distribution in the HOMO gives rise to a ground state dipole moment μ_A, which describes the direction of charge distribution in the fluorophore. The electric field of a light wave is described as an oscillating electric force, which must be aligned with the ground state μ_A for absorption to occur. This alignment is required to match the angular momentum of the fluorophore with that of the photon during the $S_0 \rightarrow S_n$ transition. Light that has a single direction for the electric field *vector* is plane polarized, and can be used to select molecules with matched direction of μ_A. The intensity of absorption will not be the same in all directions of polarization of incident light.

The same is true of emission. The transition $S_n \rightarrow S_0$ gives rise to an emitted photon with polarization matching the direction this time of the emission dipole moment μ_E. Thus for molecules where the dipole moments of the ground and excited states are close, the rotation of the molecule can be monitored. Generally, in these experiments, plane polarized light is used to photoselect a population of fluorophores in a sample, and the emitted light is monitored for its polarization. If the intensity of emission in the parallel direction is closely correlated with that of the polarized incident light, it shows that the fluorophore has restricted motion during its excited state lifetime. Comparison of emission intensities in two directions, parallel and perpendicular (relative to the axis of excitation) indicates the degree of correlation between the excitation direction and the emission direction, by the term anisotropy (*r*) (i.e.

$r = \frac{I_{Parallel} - I_{Perpendicular}}{I_{Parallel} + 2I_{Perpendicular}}$). Lack of correlation between the two shows a freedom of rotation, and as such this is a measure of resistance against diffusion, as discussed in section 1.5.2. This is a very useful property of fluorescence that informs upon the rotational motion of fluorophores. Furthermore, it can be used to elucidate the orientation of packing of molecules with which a fluorophore must align. Following sections expand upon spectroscopic methods that monitor the polarization of emitted light.

We have described the fundamental parameters of fluorescence that can be measured for the characterization of fluorescent molecules in various systems. It will be clear later that some of these parameters can be used for determining local microviscosity around a fluorophore. It is important to note here that fluorescent techniques are made more appealing due to their compatibility with microscopy, giving rise to spatial resolution of viscosity and other biophysical parameters. The following sections focus on the most established fluorescence-based microscopy techniques

1.5 Spectroscopic techniques for the measurement of membrane viscosity

The potential for imaging in living cells utilizes distributions in photophysical parameters such as fluorescence intensity, maximum emission wavelength, excited state lifetime, or polarization in order to create false colour maps that spatially resolve factors affecting these fluorescent properties[39]. Several techniques have been developed of late that directly link one or more of these properties to solvent viscosity.

With the use of exogenous probes, the compatibility of the probe in the cellular region being investigated must be established. Considering the large variation in pH, polarity and protein concentration amongst cytoplasmic regions and membrane regions, solubility can be a complex parameter and universally affects all methods that incorporate the use of fluorophores. In the examples cited below, probe compatibility is a vital primary step in establishing the validity of the probe and accompanying viscosity measurement technique.

1.5.1 Translational diffusion

Typically, methods that relate a probe's translational diffusion to solvent viscosity depend upon the deceleration of a probe's motion in a viscous environment as observed by fluorescence microscopy. Thus, all techniques that measure translational diffusion produce imaging data which confers spatial resolution to the viscosity measurement in a sample, however, this resolution can be limited in scale and can only give estimates of microviscosity as predicted by theory. Among these imaging methods, fluorescence recovery after photobleaching (FRAP), fluorescence correlation spectroscopy (FCS) and single particle tracking (SPT) are those most commonly used. These measurements resolve a translational diffusion coefficient (D_T) which can be related to solvent viscosity, η, by the Stokes-Einstein equation[9] (equation 1.5) where κ_B is the Boltzmann constant; T, the temperature, and V is the fluorophore's hydrodynamic volume.

$$D_T = \frac{\kappa_B T}{6\pi\eta V} \tag{1.5}$$

FRAP is a popular method in use for investigating membrane protein lateral diffusion. It involves the permanent photobleaching of a small region of the sample by an intense (up to 1 MW cm^{-2}) pulse of laser light and the subsequent detection of fluorescence in the same region by unbleached fluorophores replacing the bleached molecules by diffusion. Axelrod et al., 1976 introduced the method by demonstrating that diffusion coefficients, D (cm^2/s), could be obtained from these measurements and the data can identify diffusion, flow and a mixture of both processes[40]. FRAP was first performed on membranes, in order to observe lateral diffusion in the plane of the bilayer but diffusion coefficients have been consistently lower than those expected from Brownian diffusion[41]. To explain this phenomenon, Feder et al., 1996, supplemented FRAP data with single particle tracking (SPT) experiments which enabled them to observe the motion of a single fluorophore in the detected region and so to distinguish between Brownian motion and directed motion (termed 'anomalous diffusion' that was presumed to cause the high D values[41]. In SPT, trajectories of individual probes are analysed by algorithms that model Brownian diffusion. The data obtained by Feder et al., was explained as

'anomalous sub diffusion' within the membrane where a large proportion of fluorophores became immobile at different times in different areas of the membrane[41]. This disadvantageous phenomenon disallows accurate measurement of microviscosity. High diffusion coefficients, obtained from FRAP on cytoplasmic regions were also investigated in regard to steric hindrance. Jacobson and Wojcieszyn, 1984, demonstrated that a large degree of immobile fluorophores, even after accounting for the steric hindrance of translational diffusion by the cytoskeleton, are decelerated in their motion by macromolecular binding[42]. From this, it is apparent that assumptions about probe interactions with macromolecules are also, if not more, relevant in experimental methodologies relating translational diffusion of probes to bilayer viscosity.

Fluorescence correlation spectroscopy (FCS) brings a unique advantage to viscosity-sensing methods that measure translational diffusion, in that it can resolve the number of fluorophores in the measurement (i.e. probe concentration) and can give information about particle aggregation. In FCS, similarly to FRAP, a region of interest is probed for fluorescence from dissolved particles and fluctuations in the detection volume are monitored and attributed to Brownian diffusion. Figure 1.2a shows sample data of intensity fluctuations within the small focal volume over time[43]. The fluorescence intensity changes proportionally to the concentration of fluorophores within the detection volume. When the detection time is sufficiently long, intensity fluctuations are cross-correlated, giving an 'autocorrelation' ($G\tau$) which gives a characteristic value for the correlation time, τ of intensity fluctuations. The value of $G\tau$ is given as the product of fluorescence intensity at a given time *t, F(t)* and the intensity after a delay in time τ, $(F(t+\tau)$[14]. From this, the correlation between a fluorophores position and its position in the case of Brownian diffusion are related by the autocorrelation function as shown in Figure 1.2b. Here, we show an example of translational diffusion coefficients as they are estimated from FCS data[43]. The example shown in Figure 1.3 shows how translational diffusion is estimated from autocorrelation curves: the full width at half maximum (FWHM) of the autocorrelation function. Here, Chen et al., compared the fluorescence correlation of a

fluorophore in solution and that in a membrane environment, showing that the membrane (right hand curve) is shifted to the right: displays high values of Gτ for larger values of τ, higher correlation at longer delay times. The corresponding τ_D values of $x10^{-4}$ s to $x10^{2}$ s in the membrane environment, this yields translational diffusion coefficients of 300 to 0.01 $\mu s^2/s$, respectively. This is characteristic of translational diffusion in highly viscous environments. In the context of molecular diffusion, slower and faster diffusion can be separated. From $G\tau$, a translational diffusion coefficient D_T can be calculated which is used to estimate η, , using the Stokes-Einstein equation[9].

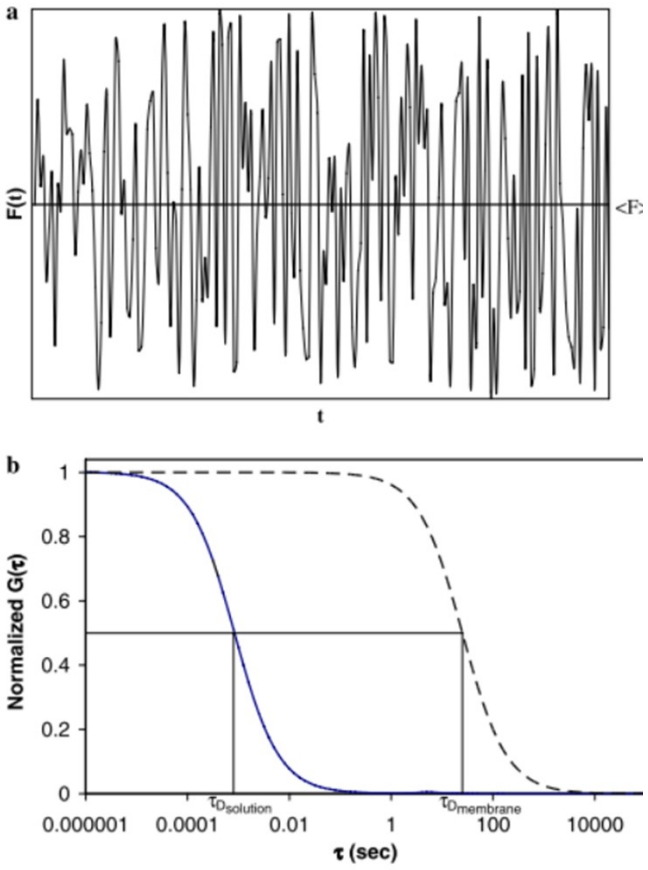

Figure 1.3: a) Sample data of fluorescence intensity fluctuations over time in confocal volume, showing the time averaged fluorescence intensity imposed upon the sample data. b) The resultant autocorrelation curve of the product of the functions F(t) and F(t+τ) as determined by the time delay τ. Two sample curves are shown, the blue curve simulates translational diffusion in free solution and in a restricted, viscous, membrane environment as the dashed line. τ_D marks the FWHM for each autocorrelation function, from which the diffusion coefficient is calculated is shown for each curve.

However, the Stokes-Einstein model [9] of translational diffusion is limited in its assumptions regarding fluorophore size and shape, which are of particular importance in the two-dimensional environment of the lipid bilayer. The nature of the probe has been shown to strongly determine the type of diffusion that can be observed, large probes undergo 'anomalous diffusion', while smaller probes undergo Brownian diffusion from which true viscosity values can be ascertained [44,45]. Instead, translational diffusion coefficients are converted to viscosity values by the use of the Saffmann-Delbrück[46] equation (equation 1.6), which itself entails assumptions about the size and shape of the fluorophore which is observed diffusing through a membrane (i.e. cylindrical shape of roughly the same volume as a single phospholipid). In equation 1.6, κ_B is the Boltzmann constant; T is temperature; μ is the kinematic viscosity of the bilayer; while μ' is that of the external aqueous solution; h is bilayer thickness; ϒ is Euler's constant; and V is the fluorophore volume.

$$D_T = \frac{\kappa_B T}{4\pi\mu h}\left(\log\frac{\mu h}{\mu' V}\right) - \Upsilon \qquad (1.6)$$

Saffmann and Delbruck et al., provided a means to reconcile the rotational and translational diffusion coefficients D_R and D_T[47]. Using FCS data, which separates intensity fluctuations by time scale assuming that translational diffusion occurs at much longer timescales than rotational diffusion, they believed they were able to distinguish between the two components. Additionally, Abney et al., describe the application of FCS to membrane regions and the advantage conferred by this method over FRAP due to the resolution of particle concentration and from that, the potential to describe macromolecular binding and/or aggregation[48]. However, Ariola et al., 2009 found that fluorophore size and shape determined the validity of both measurements and differentiation between them was compromised in large fluorophores[49]. Ultimately, they conclude that the Stokes-Einstein equation is better for predicting experimental values of D_T than the Saffmann-Delbrück equation despite assumptions of three-dimensional diffusion. Finally, another method that claims to resolve the translational diffusion in membranes is the widely used measurement of pyrene eximer fluorescence. Pyrene

is a hydrophobic fluorophore which undergoes a bathochromic shift upon excimer formation. The detection of relative intensities of the monomer and excimer emission peaks can be modelled to diffusion kinetics, from which a translational diffusion coefficient can be calculated. Chapter IV discusses some membrane viscosity measurements calculated from pyrene excimer formation.

One disadvantage associated with FCS that the fluorophore size can affect the validity and range of viscosity measurements. Also, model and cell membranes can be complex and spatially heterogeneous. This has the potential to affect local concentration gradients, skewing an autocorrelation curve. Spatial heterogeneity of membranes is a constant limitation in the three techniques described above, here focal volumes are necessarily limited in size (FRAP, FCS) or is constrained to the diffusion path of the probe itself (SPT). Recently, advances have been made in FCS, such as Raster Image Correlation Spectroscopy (RICS) that improve spatial resolution though the computational complexity of these techniques preclude them from being widely applicable. Results from these techniques on diffusion coefficients pertinent to the lipid bilayer environment studied in this Thesis are summarized in Chapter V.

1.5.2 Rotational diffusion

Steady-state and Time-resolved Anisotropy

Anisotropy, r, defines a fluorophore's orientation of transition dipole moments which can be monitored. In reference to the above section on polarization, anisotropy measurements relate the polarization of emitted light to the rotational dynamics of the probe in solution. A rotational diffusion coefficient, D_r, is related to the hydrodynamic volume of the probe and most importantly, the viscosity of the surrounding medium, hence anisotropy can measure solvent viscosity[39]. Fluorophore-emitted light is measured in two orientations, perpendicular and parallel, to the polarization vector of the excitation source, which itself is necessarily linearly polarized. Simultaneous measurement of parallel and orthogonally polarized emission has greatly increased the quality of anisotropy data collected in biological tissues by reducing artefacts from temporal changes in the sample and in the instrumentation[50]. Steady-state

anisotropy imaging makes use of the fact that most small probes have extremely high D_r values, which is inversely related to r by the Jablonski-Perrin equation (Equation 1.7) and gives most r values in non-viscous solution as nearly zero.

$$1/r = 1/r_0 (1 + 6D_r\tau_f) \quad (1.7)$$

r_0 is the initial anisotropy, a unique term determined by the orientation absorption and emission transition dipole moments of the fluorophore in that particular solution, D_r is the rotational diffusion coefficient and τ_f is the fluorescence lifetime of the probe. r_0 can give information regarding the intrinsic ordering of the fluorophore in that system. Very high or very low values of r_0 suggest that the fluorophore is non-randomly aligned in the system. As mentioned above, D_r is related to the freedom of motion of the probe in its environment. Subsequently, increases in r from restricted motion can be attributed to multiple causes, including macromolecular binding and high solution viscosity[39]. In steady-state imaging, the distribution of r values is used to create a false-colour image of the distribution of r values through a sample. Discerning between binding effects and high viscosity as the causes of distributed r values is not simple and this is the disadvantage of using steady-state anisotropy to directly map viscosity.

Alternatively, time-resolved anisotropy, r_t, describes the increasing randomisation of polarisation of the emitted light during the lifetime of the probe's excited state and provides a mechanism for distinction between macromolecular binding and high viscosity as contributors to restricted probe motion. The characteristed time scales at which anisotropy decays contains information regarding the fluorophore (i.e. size, shape and association with proteins). Additionally anisotropy decays are able to give more detailed information regarding the restriction to rotation than an averaged value as seen in steady state anisotropy. The parameter resulting from time resolution of r, anisotropy decay, is related to both lifetime and anisotropy and can inform on a number of biochemical phenomena occurring around the probe including:

complex formation, energy transfer due to molecular proximity and molecular 'tumbling'. Anisotropy decay is described by monoexponential decay by Equation 1.8:

$$r_t = (r_0 - r_\infty)^{(-t/\Theta)} + r_\infty \quad (1.8)$$

Where r_0 is the initial anisotropy, and Θ is the rotational correlation time. The non-zero value to which the probe's anisotropy decays, r_∞, is constant between long time intervals and informs on the restricted rotation of the probe. High r_∞ values can arise from restriction of rotation in one axis relative to another, whereas the time related to the rotation is given by another parameter, the rotational correlation time. During macromolecular binding, r_∞ is often used as an indicator that the probe is bound or in an anisotropic environment where rotation is not free in all axes, it is a common parameter mentioned in fluorescence polarisation studies on membrane fluidity, for example, for this reason which will be discussed further below[24]. Increasing randomness of polarization is interpreted as an indication of its rotational freedom within a solvent and demonstrates molecular tumbling. This is described by a probe's rotational correlation time, Θ, which is directly proportional to solvent viscosity as demonstrated by the Stokes-Debye-Einstein equation (Equation 1.9).

$$\Theta = \eta V/kT \quad (1.9)$$

Rotational correlation time, Θ, is directly proportional to viscosity, η and the probe's hydrodynamic volume ,V, while inversely proportional to the Boltzmann constant k and absolute temperature T. Equation 1.8 demonstrates the relationship between anisotropy decay, r_t and Θ. The term for hydrodynamic volume in this equation assumes probes to be spherical in shape and additionally, for movement of the probe to be isotropic. Time-resolved anisotropy in membranes

Microviscosity describes largely homogenous and isotropic environment. Due to the cylindrical nature of their phospholipid component parts that can be relatively rigid, membranes are inherently anisotropic environments and this property can be extrapolated to a measure of

membrane fluidity. In order to characterise the restriction of membrane fluidity by increasing cholesterol content in membranes, Veatch et al., 1977, demonstrated the increase in r_∞ of the anisotropy decay of diphenylhexatriene (DPH) inserted into liposomes as an effect of restricted probe motion[24]. Their other significant observation was biexponential anisotropy decays from liposomes with high cholesterol content. Veatch et al., 1977, determined that the rod-like shape of DPH gave anisotropic rotation amongst the lipid-chains of a phospholipid-membrane and increasing cholesterol-content decreased its rotational motion along only one axis[24]. Fluorescence anisotropy has been used on multiple occasions as an indicator of membrane fluidity, phase transitions of lipids, lipid domains in membranes, and on the dynamics of phospholipid bilayers [20,22,23]. Further, Verkman et al., also demonstrated the use of fluorescence anisotropy in membrane environments when they compared *r* values between basolateral and apical membrane regions in rabbit kidney[51]. Because of the shape of the bilayer, which is highly restricted in one axis, the probe selected for anisotropy measurements must be highly solubilised within the hydrocarbon region, where three-dimensional motion is possible for the extrapolation of viscosity measurements. Fluorescence anisotropy in membranes can be complicated by the compatibility of probe shape with membrane environment and some lipid-mediated alterations in the probe's excited state lifetime. Nevertheless, this technique is informative on the nature of solvent interactions as measured on the scale of individual probe molecules, which we believe is the origin of microviscosity.

1.6 Molecular Rotors

While fluorescence anisotropy probes the rotation of a fluorescent molecule as a whole as a function of solvent micro-friction, it is also possible to measure microviscosity by making use of rotation of a part of a molecule for the same purpose. By measuring the fluorescence quantum yield and lifetime of so called 'molecular rotors', and by correlating these parameters to classical rheology measurements of liquids, it is possible to create microscopic probes of solvent viscosity inside cells. The subject of this Thesis is the detailed investigation of the photophysical

behavior of one of one such molecular rotor and determining the limits of its applicability for viscosity measurements in lipid bilayers and other membrane model systems.

1.6.1A basis for viscosity sensitivity in molecular rotors

Fluorescent probes with photophysical properties responsive to viscosity of their environment are collectively termed *molecular rotors*. These fluorophores generally share a degree of rotational freedom that causes them to twist in solution. The perturbation of molecular orbitals in these twisted conformations alters the photophysics of the molecule and can be observed spectroscopically. Apart from viscosity, features of the local environment that affect this twisting include polarity (particularly if a charge-transfer excited state is involved), the concentration of other solutes in a solution, temperature, and pH. Any molecular rotor that is used for the measurement of viscosity in unknown samples must be well characterised for sensitivity to these other parameters in the interest of validity. Photophysical changes due to twisting can affect the fluorescence intensity, lifetime, and emission maxima of the probe. The Förster-Hoffmann equation[52] (1.10) predicts a linear relationship between log(viscosity) and the log(quantum yield) of a flexible fluorophore.

$$\log_{10} \Phi f = C + a\log_{10}\eta \qquad (1.10)$$

Quantum yield is a problematic parameter to measure in living cells due to variable uptake of a probe in different cellular regions and the impossibility of absorption measurements for determining concentration. A ratiometric approach negates the need for measuring quantum yield of a molecular rotor in order to calculate the viscosity of its surroundings. Haidekker et al., 2006, have constructed a conjugated molecular rotor which demonstrates the use of a ratiometric methodology in viscosity-sensing[53]. An electron donor moiety, 7-methoxycoumarin-3-carboxylic acid (MCCA), is conjugated to an electron acceptor moiety, 2-cyano-3-(4-dimethylaminophenyl)acrylic acid methyl ester (CMAM) by a rigid linker region that maintains a Förster distance between the two fluorophores[53]. The MCCA moiety is a reference for dye

concentration because its emission is independent of viscosity. Once the MCCA moiety is excited, energy transfer to the acceptor, CMAM, allows measurement of its viscosity-sensitive emission. The resonant energy transfer (RET) between the two moieties ensures the ratiometric legitimacy of the method because one excited molecule of MCCA yields one excited molecule of CMAM[53]. When tested in solutions of increasing glycerol content, the donor moiety fluorescence intensity has a very small linear increase that corresponds to increase in the refractive index of the solvent due to glycerol. However this increase in donor fluorescence (a = 0.09) is negligible in comparison with the highly viscosity dependent acceptor fluorescence intensity (i.e. a = 0.6)[53].

The ratiometric approach has also been demonstrated by unconjugated dyes using Ficoll 70 labelled independently with indocyanine dyes Cy3.18 and Cy5.18 [54]. Here, RET is not necessary in excitation of the viscosity sensitive moiety, as both fluorophores are simultaneously excited. The indocyanine dyes vary in the length and flexibility of a polymethine chain between two indole rings. Cy5.18 is has viscosity independent emission intensity while Cy3.18 dissipates excited state energy by non-radiative intermolecular rotation[54]. The two dyes are used concurrently as they have been demonstrated to share subcellular localisation behaviour upon entry into cells and the Cy5.18 can inform upon the concentration of Cy3.18 in a specific cellular region[54]. Thus, the ratiometric measurement of Cy3.18/Cy5.18 was used to measure the viscosity of the aqueous phase in cells and determined cytoplasmic microviscosity to be indistinguishable from that of bulk water[54].

Similarly, some molecular rotors display sensitivity of their excited state lifetimes to solvent viscosity. A *meso*-position substituted dipyrromethene boron difluoride (BODIPY) is a lipophilic probe and has been used to estimate the viscosity of cellular membranes. Due to its long excited state lifetime, BODIPY is a good candidate for viscosity sensing by anisotropy as well as fluorescence lifetime imaging microscopy (FLIM). BODIPY is capable of a ~60° twist in the ground state but adopts a planar conformation in the excited state. Rotation of a 5-phenyl group

at the meso position dissipates excited state energy by internal conversion and gives a low quantum yield (0.06) and short lifetime (500 ps) when rotation is freely allowed. Restricted rotation significantly increases its quantum yield (0.9) and increases the excited state lifetime (6 ns)[55]. Equation 1.11 summarises the direct relationship between viscosity and lifetime.

$$\tau = zk_0^{-1}\eta^a \tag{1.11}$$

Where z and a are dye-dependent constants, k_0 is the radiative decay constant. Similarly to quantum yield in equation 1.10, τ as a function of logη yields a linear calibration curve with slope a.

1.6.2 Advantages of viscosity-imaging using molecular rotors

The viscosity sensitivity of molecular rotors depends on intermolecular rotation of each individual molecule, in a manner independent of probe concentration. Examples from literature have shown that application of the ratiometric methodology or detection of fluorescence lifetimes can report viscosity in a manner independent of the probe's concentration gradient in a given sample, making the application of molecular rotors to living cells a particularly unique advantage over other viscosity imaging techniques. Indeed, molecular rotors are ideally suited to be used in conjunction with standard or confocal microscopy, and depending on the rotor, can be used for fluorescence lifetime imaging (FLIM)[56]. Equation 1.11 shows that lifetime can be used to report the viscosity of solutions, by determination of the empirical relationship between solvent viscosity and the lifetime of the molecular rotor. A calibration curve relating viscosity and lifetime is fit to the Förster-Hoffmann equation, which is used to convert values of lifetime to viscosity. During imaging, a laser scanning microscope sequentially measures the exponential decay rate of fluorescence in each pixel. The decays are fitted to values of fluorescence lifetime which are further converted to values of viscosity using the empirical relationship established by the calibration curve. FLIM experiments confers the advantage of spatial resolution of microscopic samples.

Spatial resolution allows the imaging of viscosity distribution of heterogeneous samples, in contrast with averaging techniques discussed above (NMR, ESR, QENS) and at much larger volumes than other imaging techniques (FRAP, FCS, SPT) which are limited in their detection volumes or trajectories. In addition to mapping the heterogeneity of samples, molecular rotors can give time-resolved data of the dynamic states of viscosity in heterogeneous samples, an advantage over the imaging methods mentioned previously. While anisotropy measurements also allow whole images to be obtained, this method suffers from uncertainties of fluorophore binding and low signal in a time-resolved anisotropy imaging, which to date precluded its use for cellular viscosity imaging. Table 1.1 summarises our comparison of viscosity-sensing techniques.

Table 1.1: Comparison of several techniques discussed in the introduction, suitable for the measurement of lipid bilayer viscosity

Technique	Use of exogenous probe	Imaging Technique	Spatial Resolution	Basis for viscosity sensitivity	Conversion to η
$^{1}H/^{2}H$ NMR	x	✓	x	Structural information	x
QENS	x	x	x	Structural information	x
FCS	✓	✓	Limited	Translational diffusion	SE/SD
FRAP	✓	✓	Limited	Translational diffusion	SE/SD
SPT	✓	✓	Limited	Translational diffusion	SE/SD
Anisotropy	✓	✓	✓	Rotational diffusion	Jablonski-Perrin equation
Molecular Rotors	✓	✓	✓	Free volume	Förster-Hoffmann Calibration

In this Thesis, we investigate the photophysical properties of a molecular rotor based on the structure of a conjugated porphyrin dimer, which exhibits ratiometric viscosity-sensing behaviour and displays potential for sensing viscosity changes accompanying various biophysical phenomena. We aim to characterize the viscosity sensitive fluorescent behavior of the molecular rotor, taking into account the effect of other physical characteristics of solvents such as temperature and polarity. Furthermore, we aim to investigate the nature of the viscosity measurement and its relationship to 'free volume', the volume between solvent and solute molecules. We aim to apply this interpretation of viscosity as measured by molecular rotors to lipid membranes, in order to quantify the viscosity of a model lipid membrane. We aim to give spatial resolution to this measurement, by the use of a ratiometric imaging.

1.7 References

1. Deliconstantinos, G., Villiotou, V. & Stavrides, J. C. Modulation of particulate nitric oxide synthase activity and peroxynitrite synthesis in cholesterol enriched endothelial cell membranes. Biochem. Pharmacol. 49, 1589–1600 (1995).

2. Gleason, M. M., Medow, M. S. & Tulenko, T. N. Excess membrane cholesterol alters calcium movements, cytosolic calcium levels, and membrane fluidity in arterial smooth muscle cells. Circ. Res. 69, 216–27 (1991).

3. Nadiv, O. et al. Elevated protein tyrosine phosphatase activity and increased membrane viscosity are associated with impaired activation of the insulin receptor kinase in old rats. Biochem J. 1, 443–50 (1994).

4. Osterode, W., Holler, C. & Ulberth, F. Nutritional antioxidants, red cell membrane fluidity and blood viscosity in type 1 (insulin dependent) diabetes mellitus. Diabet. Med. 13, 1044–50 (1996).

5. Maczek, C. et al. Environmental influence on age-related changes of human lymphocyte membrane viscosity using severe combined immunodeficiency mice as an in vivo model. Exp. Gerontol. 33, 485–498 (1998).

6. Kuimova, M. K. et al. Imaging intracellular viscosity of a single cell during photoinduced cell death. Nat. Chem. 1, 69–73 (2009).

7. Luby-Phelps, K. Cytoarchitecture and physical properties of cytoplasm: volume, viscosity, diffusion, intracellular surface area. Int. Rev. Cytol. 192, 189–221 (2000).

8. Luby-Phelps, K. & A. Weisiger, R. Role of cytoarchitecture in cytoplasmic transport. Comp. Biochem. Physiol. Part B Biochem. Mol. Biol. 115, 295–306 (1996).

9. Einstein, A. Über die von der molekularkinetischen Theorie der Wärme geforderte Bewegung von in ruhenden Flüssigkeiten suspendierten Teilchen. Ann. Phys. 322, 549–560 (1905).

10. Einstein, A. Eine neue Bestimmung der Moleküldimensionen. Ann. Phys. 19, 289 (1906).

11. Doolittle, A. K. Studies in Newtonian Flow. II. The Dependence of the Viscosity of Liquids on Free-Space. J. Appl. Phys. 22, 1471 (1951).

12. Valeur, B. & Berberan-Santos. Molecular Fluorescence. Methods 8, (2012).

13. Doolittle, A. K. Studies in Newtonian Flow. II. The Dependence of the Viscosity of Liquids on Free-Space. J. Appl. Phys. 22, 1471 (1951).

14. Lakowicz, J. R. Principles of fluorescence spectroscopy. Princ. Fluoresc. Spectrosc. 1–954 (2006). doi:10.1007/978-0-387-46312-4

15. Wu, Y. et al. Molecular rheometry: direct determination of viscosity in Lo and Ld lipid phases via fluorescence lifetime imaging. Phys. Chem. Chem. Phys. 15, 14986–93 (2013).

16. Janmey, P. A. & Kinnunen, P. K. J. Biophysical properties of lipids and dynamic membranes. Trends Cell Biol. 16, 538–46 (2006).

17. Sagar, G. H. & Bellare, J. R. Estimation of mechanical strength of unilamellar and multilamellar AOT/water vesicles and their rupture using micropipet aspiration. J. Phys. Chem. B 113, 13805–10 (2009).

18. Bagatolli, L. A. To see or not to see: lateral organization of biological membranes and fluorescence microscopy. Biochim. Biophys. Acta 1758, 1541–56 (2006).

19. König, S. & Sackmann, E. Molecular and collective dynamics of lipid bilayers. Curr. Opin. Colloid Interface Sci. 1, 78–82 (1996).

20. Chapman, D. Phase transitions and fluidity characteristics of lipids and cell membranes. Q. Rev. Biophys. 2, 185–235 (1975).

21. Marr, A. G. & Ingraham, J. L. Effect of temperature on the composition of fatty acids in Escherichia coli. J. Bacteriol. 84, 1260–7 (1962).

22. Klausner, R. D., Kleinfeld, A. M., Hoover, R. L. & Karnovskys, M. J. Lipid domains in membranes. Evidence derived from structural perturbations induced by free fatty acids and lifetime heterogeneity analysis. J. Biol. Chem. 255, 1286–1295 (1980).

23. Mitchell, D. C. & Litman, B. J. Molecular Order and Dynamics in Bilayers Consisting of Highly Polyunsaturated Phospholipids. Biophys. J. 74, 879–891 (1998).

24. Veatch, W. & Stryer, L. Effect of cholesterol on the rotational mobility of diphenylhexatriene in liposomes: A nanosecond fluorescence anisotropy study. J. Mol. Biol. 117, 1109–1113 (1977).

25. Clegg, J. S. Properties and metabolism of the aqueous cytoplasm and its boundaries. Am. J. Physiol. 246, R133–51 (1984).

26. Foster, K. R., Resing, H. A. & Garroway, A. N. Bounds on 'bound water': transverse nuclear magnetic resonance relaxation in barnacle muscle. Science 194, 324–6 (1976).

27. Rorschach, H. E. Protein dynamics and the NMR relaxation time T1 of water in biological systems. J. Magn. Reson. 70, 79–88 (1986).

28. König, S., Bayerl, T. M., Coddens, G., Richter, D. & Sackmann, E. Hydration dependence of chain dynamics and local diffusion in L-alpha-dipalmitoylphosphtidylcholine multilayers studied by incoherent quasi-elastic neutron scattering. Biophys. J. 68, 1871–80 (1995).

29. Atkins, P. W. & Kivelson, D. ESR Linewidths in Solution. II. Analysis of Spin—Rotational Relaxation Data. J. Chem. Phys. 44, 169 (1966).

30. Hubbard, P. Theory of Nuclear Magnetic Relaxation by Spin-Rotational Interactions in Liquids. Phys. Rev. 131, 1155–1165 (1963).

31. Lepock, J. R., Cheng, K. H., Campbell, S. D. & Kruuv, J. Rotational diffusion of TEMPONE in the cytoplasm of Chinese hamster lung cells. Biophys. J. 44, 405–12 (1983).

32. Keith, A. D., Snipes, W., Mehlhorn, R. J. & Gunter, T. Factors restricting diffusion of water-soluble spin labels. Biophys. J. 19, 205–18 (1977).

33. Mason, R. P. & Freed, J. H. Estimating microsecond rotational correlation times from lifetime broadening of nitroxide electron spin resonance spectra near the rigid limit. J. Phys. Chem. 78, 1321–1323 (1974).

34. Lai, C.-S., Hopwood, L. E. & Swartz, H. M. Electron spin resonance studies of changes in membrane fluidity of Chinese hamster ovary cells during the cell cycle. Biochim. Biophys. Acta - Biomembr. 602, 117–126 (1980).

35. Man, D., Olchawa, R. & Kubica, K. Membrane fluidity and the surface properties of the lipid bilayer: ESR experiment and computer simulation. J. Liposome Res. 20, 211–8 (2010).

36. East, J. M., Jones, O. T., Simmonds, A. C. & Lee, A. G. Membrane fluidity is not an important physiological regulator of the (Ca2+-Mg2+)-dependent ATPase of sarcoplasmic reticulum. J. Biol. Chem. 259, 8070–1 (1984).

37. Kuppusamy, P. Three-Dimensional Spectral-Spatial EPR Imaging of Free Radicals in the Heart: A Technique for Imaging Tissue Metabolism and Oxygenation. Proc. Natl. Acad. Sci. 91, 3388–3392 (1994).

38. Mojovic, M., Spasojevic, I., Vuletic, M., Vucinic, Z. & Bacic, G. An EPR spin-probe and spin-trap study of the free radicals produced by plant plasma membranes. J. Serbian Chem. Soc. 70, 177–186 (2005).

39. Levitt, J. A., Matthews, D. R., Ameer-Beg, S. M. & Suhling, K. Fluorescence lifetime and polarization-resolved imaging in cell biology. Curr. Opin. Biotechnol. 20, 28–36 (2009).

40. Axelrod, D., Koppel, D. E., Schlessinger, J., Elson, E. & Webb, W. W. Mobility measurement by analysis of fluorescence photobleaching recovery kinetics. Biophys. J. 16, 1055–69 (1976).

41. Feder, T. J., Brust-Mascher, I., Slattery, J. P., Baird, B. & Webb, W. W. Constrained diffusion or immobile fraction on cell surfaces: a new interpretation. Biophys. J. 70, 2767–73 (1996).

42. Jacobson, K. & Wojcieszyn, J. The translational mobility of substances within the cytoplasmic matrix. Proc. Natl. Acad. Sci. U. S. A. 81, 6747–51 (1984).

43. Chen, Y., Lagerholm, B. C., Yang, B. & Jacobson, K. Methods to measure the lateral diffusion of membrane lipids and proteins. Methods 39, 147–53 (2006).

44. Vaz, W. L. C., Goodsaid-Zalduondo, F. & Jacobson, K. Lateral diffusion of lipids and proteins in bilayer membranes. FEBS Lett. 174, 199–207 (1984).

45. Tocanne, J. F., Dupou-Cézanne, L., Lopez, A. & Tournier, J. F. Lipid lateral diffusion and membrane organization. FEBS Lett. 257, 10–6 (1989).

46. Petrov, E. P. & Schwille, P. Translational diffusion in lipid membranes beyond the Saffman-Delbruck approximation. Biophys. J. 94, L41–3 (2008).

47. Cherry, R. J. Rotational and lateral diffusion of membrane proteins. Biochim. Biophys. Acta - Rev. Biomembr. 559, 289–327 (1979).

48. Abney, J. R., Scalettar, B. a & Hackenbrock, C. R. On the measurement of particle number and mobility in nonideal solutions by fluorescence correlation spectroscopy. Biophys. J. 58, 261–5 (1990).

49. Ariola, F. S., Li, Z., Cornejo, C., Bittman, R. & Heikal, A. A. Membrane fluidity and lipid order in ternary giant unilamellar vesicles using a new bodipy-cholesterol derivative. Biophys. J. 96, 2696–708 (2009).

50. Siegel, J. et al. Wide-field time-resolved fluorescence anisotropy imaging (TR-FAIM): Imaging the rotational mobility of a fluorophore. Rev. Sci. Instrum. 74, 182 (2003).

51. Fushimi, K., Dix, J. a & Verkman, a S. Cell membrane fluidity in the intact kidney proximal tubule measured by orientation-independent fluorescence anisotropy imaging. Biophys. J. 57, 241–54 (1990).

52. Förster, T. & Hoffmann, G. Die Viskositatsabhängigkeit der Fluoreszenzquantenausbeuten einiger Farbstoffsysteme [Effect of viscosity on the fluorescence quantum yield of some dye systems]. Z Phys Chem 75, 63–76 (1971).

53. Haidekker, M. a, Brady, T. P., Lichlyter, D. & Theodorakis, E. a. A ratiometric fluorescent viscosity sensor. J. Am. Chem. Soc. 128, 398–9 (2006).

54. Luby-Phelps, K. et al. A novel fluorescence ratiometric method confirms the low solvent viscosity of the cytoplasm. Biophys. J. 65, 236–42 (1993).

55. Kee, H. L. et al. Structural Control of the Photodynamics of Boron-Dipyrrin Complexes. J. Phys. (main title) 109, 20433–20443 (2006).

56. Suhling, K., Levitt, J. A., Chung, P.-H., Kuimova, M. K. & Yahioglu, G. Fluorescence lifetime imaging of molecular rotors in living cells. J. Vis. Exp. e2925 (2012). doi:10.3791/2925

II. Methodology

2.1 Sample Preparation

2.1.1 Synthesis of porphyrin dimers

All variants of the porphyrin dimers were synthesized by the group of Harry L Anderson at Oxford University, by the method described in Ref [1]. Samples were aliquoted into glass vials to form 100 μl of 1mM solution and the solvent was evaporated under high vacuum for storage. The vials were stored at -20 °C and reconstituted with solvents as necessary to form 1mM solutions, Table 2.1. The chemical structures of the dimers used in this Thesis are shown in Figure 3.4, Chapter III,

Table 2.1: Stock solutions of porphyrin dimers used for preparation of samples

Stock Name	Compound	Concentration	Solvent	Source
A-DMSO	P_2NMe_3	1 mM	DMSO	Prof. Harry Anderson, University of Oxford
A-MC		1 mM	1:1 MeOH, $CHCl_3$	
B-DMSO	P_2	1 mM	DMSO	
B-MC		1 mM	1:1 MeOH, $CHCl_3$	
C-DMSO	P_2NMeI	1 mM	DMSO	
D-DMSO	P_2C_2NMeI	1 mM	DMSO	
E-DMSO	P_2Suc	1 mM	DMSO	
F-$CHCl_3$	DOPC	2 mg/ml	$CHCl_3$	Avanti Polar Lipids
G-$CHCl_3$	DPPC	2 mg/ml	$CHCl_3$	
H-$CHCl_3$	DSPC	2 mg/ml	$CHCl_3$	

2.1.2 Calibration in Methanol/Glycerol mixtures

Spectrophotometric grade methanol and glycerol (both from Sigma Aldrich) were used in mixtures. To reproducibly prepare methanol/glycerol solutions of certain %, the following method was developed: the density of glycerol[2] and methanol at various temperatures was plotted and fit with linear regression such that density could be calculated according to room temperature as measured on the day of sample preparation. Solutions of mixtures 0-100 % by volume, methanol and glycerol were prepared by weight, using the known density of each

solvent. The mixtures were sealed in vials and sonicated (PH350EL Elmasonic) for up to 5 minutes to ensure mixing. Viscosity measurements of all solutions were performed with a rotational coaxial cylinder viscometer (Stabinger 3000 SVM Anton Paar, with accuracy and precision of +/- 0.35% and 0.1% respectively[3]) at varying temperatures

Charged dimer samples were prepared by the addition of DMSO stock solution to the methanol/glycerol mixtures (P_2NMe_3, P_2NMeI P_2C_2NMeI, P_2Suc); the uncharged dimer (P_2) solutions were prepared from a 1:1 methanol: chloroform stock solution; these are summarised in Table 2.1. All dimer stocks were prepared at 1 mM concentration, and the required volume was added to yield an absorbance of 0.1 AU in each solution, the volumes varied slightly to reflect the changes in the extinction coefficients, according to the charge of the dimer or the nature of the methanol, glycerol mixture. Volumes added were roughly 1 µl each, making a final dimer concentration at 0.33 µM in methanol/glycerol solutions (containing 0.03-0.1% DMSO of the final volume). The solutions were transferred to a vial and sonicated for approx. 5 minutes in order to ensure full mixing.

2.1.3 Polymer samples

Polymer samples were prepared in the same manner as methanol/glycerol mixtures, by calculating the density of PEG600 from Refs [4,5]. Viscosities were measured on the Stabinger 3000 SVM viscometer (Anton Paar) as described above.

2.1.4 Large Unilamellar Vesicles (LUVs)

1,2-dioleoyl-*sn*-glycero-3-phosphocholine (DOPC) and dipalmitoylphosphatidylcholine (DPPC) were purchased from Avanti Polar Lipids in powder form and dissolved in chloroform to concentration of 2 mg/ml (Table 2.1). For vesicles with embedded dimer, stock solutions of dimers (A-MC, B-MC) were mixed with stock solutions of lipid (F-$CHCl_3$, G-$CHCl_3$) to a desired molar ratio. The solution was evaporated under a stream of dry N_2 for approx 1 minute and placed under vacuum for 6 hours to remove any remaining organic solvent. After dehydration the dried film was rehydrated by the addition of dH_2O (such that the final solution is 0.66 µM

dimer, 666 μM lipid in total volume) at 60 °C. The film is vortexed under dH_2O until visually dissolved. The turgid lipid solution was extruded 10 times at 85 bar pressure using a Lipex™ Thermobarrel Extruder (Northern Lipids Inc.) that had been pre-warmed to 60 °C. Inside the extruder are two polycarbonate membrane sieves (Whatman® Nucleopore™) with pore diameter 0.2 μm. LUVs without embedded dimer were made from pure lipid stock and dehydrated without the addition of dimer stock; instead, the dimer solution was added to the final volume containing fully formed lipid vesicles and allowed to incubate (for a minimum of 30 minutes). In order to perform spectroscopic measurement, stock solutions of dimer from DMSO were used, and the final samples have 0.1% volume DMSO. DMSO is fully miscible with water and we did not detect any effect from DMSO in concentrations used (between 0.1 – 0.5% by volume).

2.1.5 Neutron Reflectrometry

Experiments were performed on floating lipid bilayers (FLBs) of 1,2-Distearoyl-sn-glycero-3-phosphocholine (fully deuterated-DSPC) heated to 80 °C. Production of FLBs and collection and analysis of the data was performed by the group of Dr. Arwel Hughes, at ISIS Neuron facility at Rutherford Appleton Laboratories, using the method described in Ref [6].

2.1.6 Giant Unilamellar Vesicles (GUVs)

GUVs were produced by electroformation according to the general principles described by Angelova et al.[7] whereby a lipid film is deposited on one surface of a conductive chamber which is filled with aqueous solution. Alternating current is applied to the chamber and the lipid film swells into floating layers which combine to form enclosed vesicles of roughly 10-30 μm in size. For our experiments, a conductive chamber was composed of two square glass slides coated on one surface each with indium tin oxide (ITO glass slides, Sigma Aldrich, with surface resistivity 8-12 Ω). Aluminium foil was applied to one edge of each slide, in contact with the conductive surface in order to increase contact between the slides; crocodile clips were attached to the pulse generator. ITO-coated slides were cleaned with 2% Triton X100, chloroform, distilled

water and ethanol and dried in an oven until all solvent was removed. Stock solutions of the desired lipid (F or G-$CHCl_3$) were applied in a 0.5 µL droplet to one of the two slides and then spread to a thin layer by dragging a microscope coverslip over the solution, spreading it over the surface of the slide. The lipid layer was dried under a stream of dry N_2 gas and further dehydrated under vacuum for 30 minutes. Two slides, one with the dried lipid layer, were assembled into a chamber with the PDMS spacer and sealed with clips. The chamber was filled with a 200mM sucrose (VWR) solution, using a syringe and needle (VWR, 0.25 mm diameter), taking care to avoid bubbles, and releasing gas with a second needle. The chamber was placed on a hotplate at 60 °C, oriented such that the slide with the lipid layer was facing down. Crocodile clips were attached, to either ITO slide and the following voltage was applied: 1.6 V, 10 Hz for 3 hours, then 2.6 V, 4 Hz for 45 minutes. The chamber was then allowed to cool before disassembly. The vesicle solution was removed with a Pasteur pipette, and placed in a glass vial, where it was diluted 1:9 in a solution of 200 mM glucose (VWR). Imaging was performed using 8-chamber slides (Lab-Tek, Nunc, Thermo Scientific) holding 200 µL solution in each chamber.

2.1.7 Irradiation set up

Irradiation of samples in quartz cuvettes described in Chapter VII was performed by the use of a tuneable dye laser (Lambda Physik FL 2002), pumped by a third harmonic of a Continuum Surelite Nd:YAG nanosecond laser (Model 111-01) at 355 nm. A solution of Coumarin480 (Sigma Aldrich) was used as a laser dye medium. The setup produced nanosecond pulses at 480 nm of 5 mW at 10 Hz, the laser spot size at the cuvette was 3mm in diameter. Samples were kept at constant temperature by the use of a water-circulating cuvette holder (Ocean Optics, CUV-QPOD FLKIT), samples were stirred throughout the experiment by the use of a magnetic stirrer.

2.2 Measurements

2.2.1 Absorption

Absorption measurements were performed on an Agilent 8453 diode array spectrometer with deuterium and tungsten lamps as light sources. For all data shown the absorbance of bulk

samples (with the exception of DOPC+P_2/P_2NMe_3 LUVs) is shown after subtraction of a 'blank'. For the 'blank' measurements the sample in a quartz cuvette (Starna Scientific, Quartz Type 3 GL14) is measured prior to addition of the dimer. The spectra of all 'blank' solutions were recorded, then transferred from the cuvette into a glass vial where the stock solution of the dimer was added and the mixture was sonicated to ensure good mixing. The resulting dimer solutions were then transferred to the measurements cuvette and placed into the spectrometer for measurement. We found that using the same dimer-free solvent mixture as a 'blank' significantly improved the resulting spectral quality, probably due to high scattering by glycerol solutions. Where possible (i.e = methanol/glycerol mixtures, polymers, pure DOPC LUV suspensions) all emission measurements were performed on samples where absorbance at the specified excitation wavelength was 0.1 AU.

2.2.2 Emission, Excitation

All bulk fluorescence measurements were performed on a HORIBA Jobin Yvon Fluoromax®-4 spectrofluorometer. The general scheme for the spectrometer is shown in Figure 2.1.

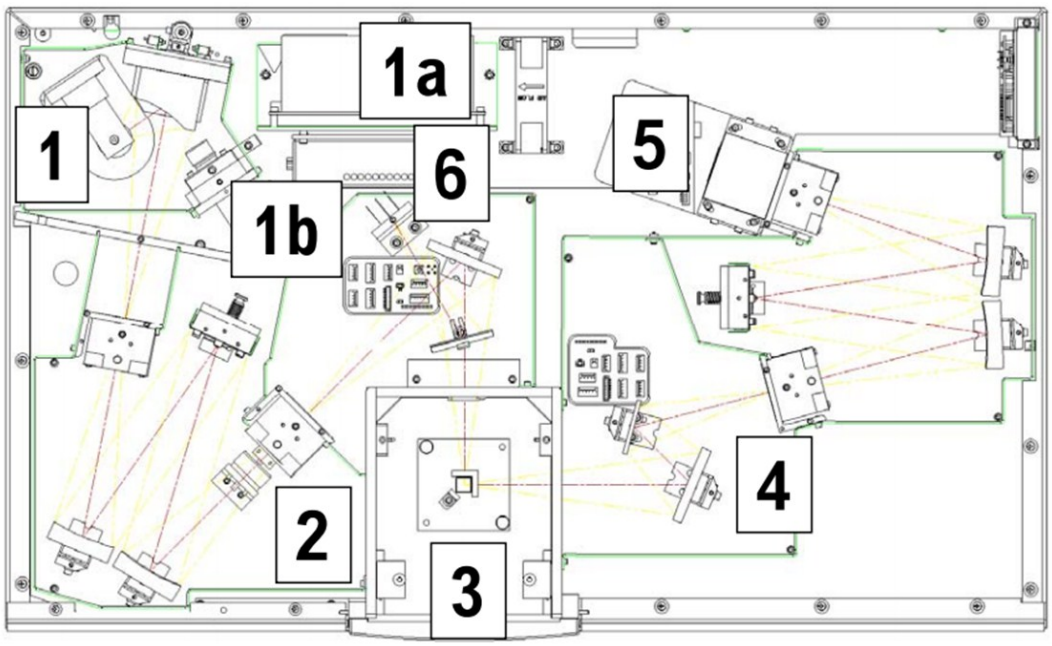

1 Xenon arc-lamp and lamp housing
1a Xenon-lamp power supply
2 Excitation monochromator
3 Sample compartment
4 Emission monochromator
5 Signal detector (photomultiplier tube and housing)
6 Reference detector (photodiode and current-acquisition module)
Host computer (not on diagram)

Figure 2.1: A schematic drawing of spectrofluorometer, taken from an operating manual for the Jobin Yvon Fluoromax-4 supplied by HORIBA Scienfitic [8]. The light beampath is shown in yellow (center in red).

Figure 2.1 is a scheme of the optical setup inside the fluorometer casing , as detailed in the specifications supplied by HORIBA[8]. Selected components of the setup are identified by number as listed in the lower panel of Figure 2.1. This numbering shall be continued below in order to expand upon the specifications of individual components.

1. *Xenon arc-lamp and lamp housing*: The 150 W Xenon (Xe) arc-lamp[8] produces continuous light with high intensities of emission throughout the visible spectrum (250-700 nm)[9]. Xe gas is ionized by exposure to a high voltage current termed the 'arc'. Recombination of free electrons with the ionized gas produces broad bands of emitted light, as opposed to solely sharp lines as expected from non-ionised spectra. An example of the emission spectrum of the Xe arc-lamp is shown below in Figure 2.2, where sharp

lines at approx. 480 nm reflect the emission from non-ionised Xe, mixed with broader emission bands. The Xe emission spectrum has steady photon output at all wavelengths relevant for excitation in these experiments. The arc lamp is made especially efficient from increasing the pressure of Xe gas in the bulb. Light from the lamp passes through a quartz window, blocking all wavelengths below 250 nm from where it is collected by an elliptical mirror and focused onto the excitation monochromator as shown in Figure 2.1.

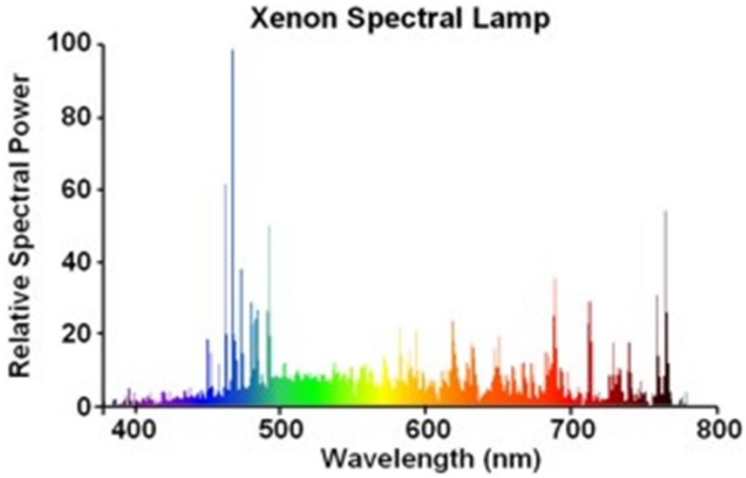

Figure 2.2: Sample Xenon arc-lamp intensity profile by wavelength. There is relatively consistent output within the visible region of the spectrum, with high peaks at approx. 480 nm, characteristic of emission from non-ionised Xe. This consistent photon intensity across the visible range makes the Xe arc-lamp a desirable light source for fluorescence experiments. Figure from [10].

2. *Excitation/emission monochromators*: the light originating from the Xe arc lamp is a mixture of the wavelengths shown in Figure 2.2. Accuracy in measuring fluorescence requires excitation from a narrow spectral range, most commonly a single wavelength. The excitation monochromator is a series of optical components which allows dispersion of the light from the Xe arc-lamp and mechanical selection of the spectral range for excitation. A similar monochromator is used to disperse the sample emission onto the fluorescence detector.

   The arrangement of the optics in a monochromator determines important features of its performance including dispersion, efficiency, wavelength resolution, and stray light level. Dispersion indicates the spatial distribution of the wavelength range by width, and

is usually given relative to the size of the slits (i.e nm/mm). It is a fixed value for reflective gratings. The width of slits thus determines the wavelength resolution of the spectrum, where higher resolution will give more structural information in spectra. This is not a crucial determinant in emission spectra, which are usually composed of broad bands. Nevertheless, the accuracy of the spectrum is strongly affected by stray light levels: light other than the selected wavelength that exits the monochromator. This can originate from either poor dispersion by the grating or leakage of light from slits. These factors together determine the efficacy of a monochromator. There are a variety of arrangements and components that can compose a monochromator, selected for advantages in the areas mentioned above.

Both the emission and excitation monochromators in the Fluoromax-4® are Czerny-Turner-type monochromators, the schematic of this type of device is shown in Figure 2.3. Czerny-Turner monochromators are characterized by the use of two mirrors with asymmetrical orientation relative to the dispersive element, in this case a reflective plane grating. The component parts are discussed in further detail below.

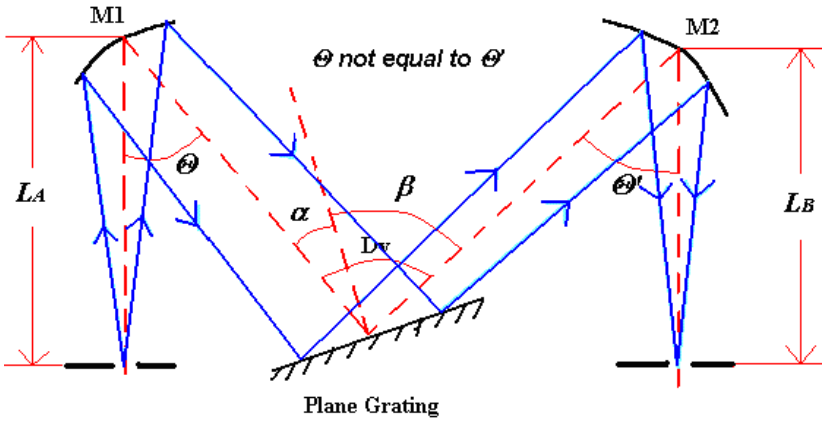

Figure 2.3: A Czerny-Turner type monochromator with two mirrors and a rotating plane grating. In this monochromator, light from the light source enters the slit at the bottom left hand of the figure, and is collimated by the first mirror (M1). The collimated light is directed into the plane grating, dispersing the light onto the second mirror (M2). The dispersed, collimated light is focused by M2 into the second slit on the bottom right hand of the figure, onto the desired component, either the sample or the detector. The Czerny-Turner configuration is asymmetrical, as the angles ɵ of reflection of the two mirrors are not equal. Figure from HORIBA Scientific [11].

a. *Mirrors:* There are two mirrors in the optical setup of each monochromator. The first mirror, M1, collimates light, while M2 is a focusing mirror (Figure 2.3).

b. *Grating:* The dispersive element of the monochromator is a plane grating as shown in Figure 2.3. Collimated light from M1 reaches the grating, which, when rotated, reflects the dispersed light onto M2. The angle of rotation determines which wavelength is focused onto the exit slit of the excitation monochromator for exposure to the sample. In the emission monochromator, sample emission is dispersed, and by systematic rotation of the grating, an emission spectrum is collected for a large range of wavelengths. The reflective grating 1200 grooves/mm and is blazed at 330 nm. Blazing concerns the angle of the grooves, which maximizes the reflective efficiency for one diffraction order – this minimizes reflection of light in directions other than M2. Blazing is optimized for one wavelength only for each grating (330 nm excitation and 500 nm emission in our setup). The grating in the Fluoromax-4® rotates to scan the emission spectrum up to 200 nm/s, with accuracy of 0.5 nm.[8] The grating's scan speed is controlled by the FluorEssence software, as *integration time*, the amount of time that the grating pauses at each wavelength for each measurement. The default integration time is set to 1s and was sufficient for most samples studied here unless otherwise stated. Integration time was decreased to 0.5 s for LUV samples in order to decrease signal to a maximum uncorrected emission intensity of $1x10^6$ counts per second (CPS).

c. *Slits:* the size of slits influences all parameters of monochromator performance. The dispersion of the monochromator is dependent on the slit size, such that an increase in slit size will increase the effective bandpass of excitation light. The above value effectively alters the dispersion when slits altered from the 1 mm value. Furthermore, slit size influences the stray light level of the monochromator and wavelength resolution of the emission spectrum. Larger

slits increase fluorescence signal by allowing a larger number of photons to reach the detector for each wavelength. However, the resolution decreases due to increased bandpass for each wavelength detected. In all experiments presented in this Thesis, slit sizes were adjusted such that the maximum uncorrected emission intensity signal was maintained at at < 1 x10^6 CPS. In all instances where relative intensities or ratios are compared (e.g. Calibration curves in Chapter III) slit sizes were kept the same between experiments from a maximum size of 5mm to 0.75mm.

The following table summarizes specifications for component parts of each monochromator:

Table 2.2: Specifications for component parts of monochromators in Fluoromax-4:

	Excitation	Emission
Dispersion (nm/mm)	4.25	4.25
Grooves (1/mm)	1200	1200
Blazed λ (nm)	330	500

3. *Sample compartment:* A toroidal mirror is used to focus light exiting the excitation monochromator onto the sample. In the beam path towards the sample, however, a beam splitter directs 8% of the incident light away towards the Reference detector, for purposes of monitoring the lamp and monochromator.

   The sample compartment itself fits a 1cm x 1cm cuvette and is temperature controlled by a Peltier plate device (F-3004 Sample Heater/Cooler Peltier Thermocouple Drive HORIBA Scientific) controlled by a thermoelectric temperature controller placed outside the fluorometer casing (Model LFI-3751 from Wavelength Electronics) Temperatures were set to vary within 0.5 °C of the set temperature. Temperature stability of the controller is 0.001 °C (10 kΩ thermistor at 25 °C) over one hour.Equilibrium times were

optimised for each type of experiment. Specifically, methanol/glycerol mixtures were equilibrated for 9 minutes, whereas LUV samples were equilibrated for 5 minutes each. Additionally, LUV samples were stirred during data collection. Experiments shown in Chapter III, Figure 3.9 were performed using a recirculating water bath in order to stabilize the temperature (Thermo Scientific, Precision)

4. *Signal detector:* Emission from the sample enters the emission monochromator (as described above) and subsequently directed onto the signal detector, a photon-counting photomultiplier tube (R928P, HORIBA Scientific). It is sensitive in the region 180-850 nm, with dark counts < 1000 CPS[8]. For photon counting, a linear relationship between number of photons and signal generation is required for accuracy. For this detector, the linear region is between 2 $x10^6$ CPS. Outside of this range, the signal/noise is reduced due to the increased volume of photons, as current generated in the PMT is no longer proportional to light intensity. For this reason, precautions were taken to keep photon counts within this range. Both this detector and the reference detector discussed below, have wavelength dependent sensitivities due to the photocathode's response (which decreases with increasing wavelength) and the transparency of windows within the instrument to particular wavelengths. Mechanisms to correct for these sources of inaccuracy are summarized below.
5. *Reference detector:* In in the interest of accuracy, particularly in the case of excitation experiments, the intensity of the lamp at different wavelengths was monitored by the reference detector. A UV-enhanced silicon photodiode with good sensitivity between 190-980 nm serves as the reference detector detecting light split directly from incident light prior to reaching the sample[8]
6. *Correction of spectra:* The main source of error in emission spectra is the wavelength dependence of sensitivity of the PMT signal detector. Other sources of error such as the transparency of the windows contribute minimal error relative to the detector. For this reason, HORIBA supply a pre-determined function for correction of raw intensity values.

This correction function multiplies the signal intensity of at each wavelength by a factor dependent on the known PMT response to that wavelength. For all data collected in this Thesis, both the uncorrected and corrected spectra were recorded, and either version of the data is used where appropriate. Where comparisons were made between data, and wherever calibration curves are used, only like-for-like data is compared (i.e. corrected with corrected and uncorrected with uncorrected).

For excitation spectra, the signal intensity is dependent on the intensity of the lamp for detection of each wavelength. Irregularities in lamp intensity contribute significantly to the noise in the spectra. For this reason, wherever excitation spectra is presented, it is divided by signal from the reference detector to correct for lamp intensity fluctuations.

2.2.3 Microscopy

All microscopy data (Chapters VI and VII) was collected on an inverted scanning confocal microscope (Leica Microsystems, TCS SP5 II). Figure 2.4 shows a scheme of selected components of the microscope interior.

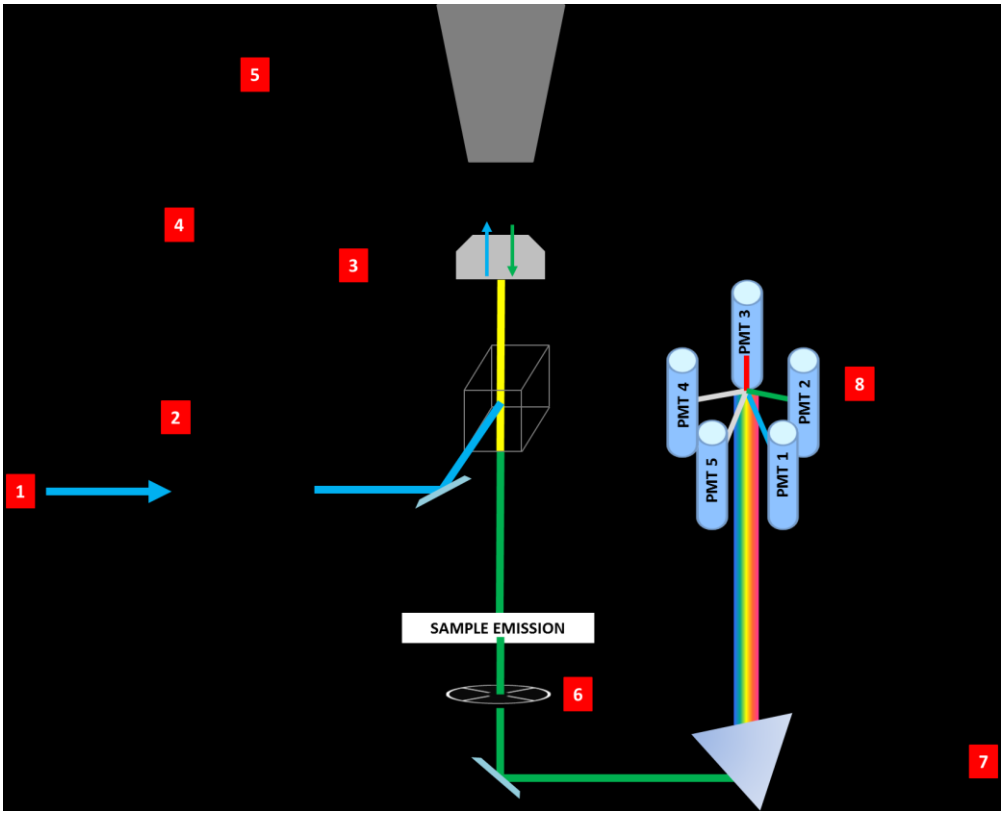

Figure 2.4: Scheme of the microscope interior of the Leica TCS SP5 II showing path of laser excitation (blue) through the acousto-optical beam splitter (AOBS, item 2) and objective (item 3) onto the sample (stage, item 4). Transmitted excitation light is used to detect a bright field image, with the use of the transmitted light detector (item 5). Sample emission (green) is transmitted through the AOBS, and confocal pinhole (item 6) and dispersed by a prism (item 7) for detection by five PMTs with varying user-defined spectral ranges).M1 and M2 are reflective mirrors and/or dichroic mirrors.

Components of the setup are identified by number which shall be continued below in order to expand upon their specifications.

1. *Laser excitation:* The excitation source used for all ratiometric and FLIM experiments was a Ti:Sapphire pulsed laser source (spot size approximately 2 mm prior to focusing), producing 140 fs pulses at 80 MHz in the range between 680-1080 nm (Chameleon Vision II, Coherent Inc.) which is coupled to the confocal microscope. Excitation light

passes through a second harmonic generating crystal (SHG, 340-540 nm at 80 MHz), resulting in frequency doubling (Harmonic, Coherent Inc.). Additional optics attenuate the power prior to entry into the microscope for sample excitation if necessary. During ratiometric imaging, as shown in Chapter VI, the porphyrin dimer was excited at λ = 453 nm (frequency doubled 906 nm output from the Ti:Sapphire source). For FLIM experiments as shown in Chapter VII, the porphyrin dimer was excited at λ = 453 nm, while BODIPY C_{10} was excited at 488 nm (frequency doubled 906 and 976 nm outputs from the Ti:Sapphire source, respectively). Laser power for all instances of excitation (and irradiation) was kept at 5 mW, this is achieved by adjustment of the power attenuation optics prior to entry into the microscope. A simplified setup of the excitation path is shown below in Figure 2.5.

Non-ratiometric images of the porphyrin dimers (Figures 5.5, 5.6, 5.9 (Chapter V) were performed with CW Argon laser fitted with the Leica SP5 with available excitation lines 458/476/488/496/514 nm. Imaging was performed by excitation at 458 nm, with maximum laser output of 200 mW, and 50 mW at the focal plane. 10-40% of the total laser output was used for imaging.

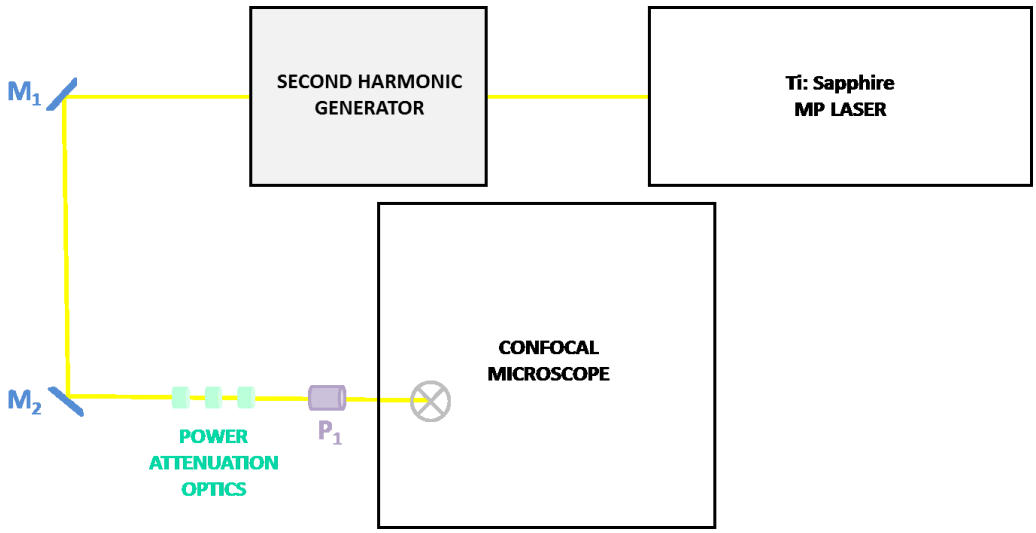

Figure 2.5: Laser excitation setup showing the path of light generated by the Ti:Sapphire multiphoton laser is frequency doubled by a second harmonic generator. Power output is attenuated prior to entry into the confocal microscope. M1 and M2 are reflective mirrors. P1 is a periscopic mirror directing the excitation beam into the microscope interior.

2. *Acousto-Optical Beam Splitter (AOBS)*: A beam splitter separates sample emission from laser excitation reflected from the surface of the sample. Traditionally, this is a dichroic mirror that transmits wavelengths longer than the excitation wavelength, though in the Leica SP5 II, this is replaced by an acousto optical device: a crystal with selective reflective and transmission characteristics depending on the frequency of acoustic waves generated by a mechanical transducer.

   Frequency can be altered from 1) transmission of laser excitation to the sample to 2) reflection of laser excitation and transmission of sample emission as fast as 10 μs. The transmission bandgap of the AOBS is 2-6 nm.

3. *Objectives:* The Leica SP5 II is fitted with four objectives, summarised below in Table 2.2. All objectives used are apochromatic, that is, corrected for chromatic aberration by bringing the light of all wavelengths (blue, greem, red) to the same focal plane. The x63 objective is a water immersion objective and has a corrective collar for refractive index-mismatch. The numerical aperture of the objective (NA) determines the resolving power and the brightness of the image. It is a measure for the width and depth of the focal spot produced by the objective. It is defined by the sine of the half aperture angle of the lens and the refractive index of the immersion medium. Thus, the larger the numerical aperture, the more narrow the focal spot and hence the higher the resolving power. According to the manufacturer's specification the point spread function width (characterizing the tightness of spot used for imaging) for all objectives used in this work except x10 is within 0.5 μm. Thus we are able to fully benefit from the diffraction limited resolution of confocal imaging.

Table 2.2: Leica Microsystems specifications for objectives used in data collection

Magnification	NA	Leica Spec.	Objective Type	Correction Collar
x10	0.30	HCX/PL/FLUOTAR	Semi Apochromatic	-
x20	0.70	HC/PL/APO	Apochromatic	-
x40	0.82	APO CS CORR	Apochromatic for Confocal Scanning	Yes
x63 (water immersion)	1.20	APO CS CORR	Apochromatic for Confocal Scanning	Yes

4. *Transmitted light detector:* brightfield measurements are made by collection of transmitted laser excitation through the sample. The optics above the sample platform allow Kohler illumination.
5. *Confocal pinhole:* confocal sectioning is enabled by the inclusion of a mechanical pinhole. Ratiometric images of dimers were not recorded in confocal mode as the signal intensity was too low for confocal sectioning. The fluorescence lifetime images using Bodipy-C10 as a marker were performed in a confocal mode.
6. *Spectrophotometer prism:* Sample emission is dispersed by a prism prior to detection.
7. *Photomultiplier Tubes (PMTs) 1-5:* Five different PMTs are used for imaging, two of which are capable of single photon counting used for FLIM. After dispersion of the sample emission light, the spectral detection range can be selected for up to three of PMTs concurrently.
    a. Ratiometric imaging is performed by two PMT channels were used to collect fluorescence signal: PMT 2 was set to detect fluorescence between 640-650 nm; PMT 3 recorded 705-715 nm. Frame averaging was differed for each image and is specified in the figure legend of all imaging data presented.

b. FLIM is enabled by the inclusion of a time-correlated single photon counting (TCSPC) card (SPC-830, Becker & Hickl). Fluorescence detection for the purposes of FLIM was performed by a FLIM PMT over the detection range 520-600 nm (PMC-100, Hamamatsu). Images were recorded at a size of 512 x 512 pixels and at a time resolution of 256 time bins. Scattering from a glass coverslip was used to record the instrument response function (IRF).

2.3 Data Analysis

2.3.1 Ratiometric image processing

Ratiometric image processing program was written using MATLAB by Aurimas Vysniauskas. Intensity from both PMTs was first summed and normalised. First, prior to ratio calculation in each pixel of the image, the user specifies a given minimum threshold value in order to improve the signal: noise ratio. Next, the user defines a value for binning pixels in the image, and subsequently adjusts the pseudo-colour scale to fit the minimum and maximum ratios in the image. The same adjustment of scale is performed for conversion of ratios to viscosity values according to the ratiometric calibration graph. For the purposes of microscopy an additional calibration curve was recorded by Aurimas Vysniauskas in solutions of methanol/glycerol measured at the microscope stage to account for detector sensitivities and optics transmission (Figure 5.3).

2.3.2 FLIM Data Analysis

Synthesis of BODIPY C_{10} was performed by Yilei Wu as described previously in Ref [12]. Calibration of BODIPY C_{10} monoexponential fluorescence lifetime (τ_f) against viscosity was performed previously Ref [13]. To summarise briefly, solutions of methanol and glycerol are mixed in increasing percentages of glycerol (w/v%), the temperature-dependent viscosity of which is measured by use of the Stabinger 3000 viscometer as mentioned previously. BODIPY C_{10} was dissolved in these solutions and the viscosity-dependent lifetime was recorded using a IBH 5000F TCSPC device (Jobin Yvon, HORIBA) and a 467 nm NanoLED excitation source (200 ps pulse duration, HORIBA). The decay in each pixel of the image was fit by a monoexponential

model using the Levenberg-Marquardt algorithm. FLIM data was analysed by Aurimas Vysniauskas using TRI2 software (Version 2.7.6.1, Gray Institute for Radiation Oncology and Biology).

2.4 References

1. Balaz, M., Collins, H. A., Dahlstedt, E. & Anderson, H. L. Synthesis of hydrophilic conjugated porphyrin dimers for one-photon and two-photon photodynamic therapy at NIR wavelengths. Org. Biomol. Chem. 7, 874–88 (2009).

2. Physical properties of glycerine and its solutions. (Glycerine Producers' Association, 1963).

3. Hosny, N. A. et al. Mapping microbubble viscosity using fluorescence lifetime imaging of molecular rotors. Proc. Natl. Acad. Sci. U. S. A. 110, 9225–30 (2013).

4. Sengwa, R., Kaur, K. & Chaudhary, R. Dielectric properties of low molecular weight poly(ethylene glycol)s. Polym. Int. 49, 599–608 (2000).

5. Trivedi, S., Bhanot, C. & Pandey, S. Densities of {poly(ethylene glycol)+water} over the temperature range (283.15 to 363.15)K. J. Chem. Thermodyn. 42, 1367–1371 (2010).

6. Hughes, A. V et al. Floating lipid bilayers deposited on chemically grafted phosphatidylcholine surfaces. Langmuir 24, 1989–99 (2008).

7. Angelova, M. I. & Dimitrov, D. S. Liposome electroformation. Faraday Discuss. Chem. Soc. 81, 303 (1986).

8. HORIBA Scientific. FluoroMax-4® & FluoroMax®-4P with USB Operation Manual Part number 810005 version B. Manual (2009).

9. Lakowicz, J. R. Principles of fluorescence spectroscopy. Princ. Fluoresc. Spectrosc. (2006). doi:10.1007/978-0-387-46312-4

10. Philips LL Spectral Xenon. at <http://www.lamptech.co.uk/Spec Sheets/Philips LL Xe.htm>

11. HORIBA. Monochromators & Spectrographs. at <http://www.horiba.com/uk/scientific/products/optics-tutorial/monochromators-spectrographs/>

12. Levitt, J. A. et al. Membrane-Bound Molecular Rotors Measure Viscosity in Live Cells via Fluorescence Lifetime Imaging †. J. Phys. Chem. C 113, 11634–11642 (2009).

13. Wu, Y. et al. Molecular rheometry: direct determination of viscosity in Lo and Ld lipid phases via fluorescence lifetime imaging. Phys. Chem. Chem. Phys. 15, 14986–93 (2013).

III. Characterisation of Porphyrin Dimers

3.1 Development of porphyrin dimers

Porphyrin dimers (Figure 3.1) were first synthesized by Anderson et al., in 1994, in an effort to make self-assembling molecular wires with unusually long π systems for electronic applications[1]. Zn^{2+} benzoporphyrins are especially efficient π-conjugated systems owing to the large area of alternating single and double bonds of the macrocycle. The overlap of p orbitals between neighbouring carbon atoms allows the delocalization of electrons across the molecule. The four orbital model proposed by Gouterman et al., 1963, identifies an 'inner' and 'outer' conjugation ring in each macrocycle[2], making the porphyrin highly stable and reducing the electron energy due to delocalization. Furthermore, the butadiyne bridge is itself a conjugated structural element, which, when bonded to the macrocycles, greatly increases the area of delocalized electrons, even, by some estimates, bridging the conjugated area over both macrocycles[3]. Overall, the porphyrin macrocycle has a high degree of planarity owing to the Zn^{2+} centre of the molecule, giving a conformational rigidity and high degree of symmetry over the dimer[1]. On the other hand, the lack of steric hindrance about the butadiyne bond allows free rotation of the two macrocycles relative to one another, making π-electron conjugation intermittent and dynamic in solution. The spectroscopic properties of the porphyrin dimer, particularly under dynamic conditions determined by solution viscosity is the subject of this Chapter.

The dimers were the monomer unit for self-assembly of the wire by aggregation. Anderson et al., noted several electronic features of the dimer that meet with criteria necessary for the production of organic semiconductor materials and attracted interest of researchers in the field. In addition, it was known that molecules with long π-systems are prized for significant non-linear optical properties which were necessary in the development for infra-red absorbing dyes.[1,4] When Anderson et al., synthesized the porphyrin dimer, it had long been known that

compounds with extended π systems had high two photon absorption cross sections and a series of porphyrin oligomers were investigated as potential two-photon absorbers.[5] Drobhizev et al., first published dimer's fluorescence spectrum and valued the two-photon cross section at 10^3 – 10^4 Goeppert-Mayer units.[5] Two-photon absorption confers two advantages during microscopic imaging, firstly it allows the use of longer, lower energy wavelengths, limiting tissue damage and secondly, it has vastly increased spatial resolution relative to single photon imaging[4].

Anderson et al., predicted that both the dimer's optical behaviour and electronic overlap would be strongly affected by intramolecular rotation about the butadiyne link, owing to the disruption of π-conjugation[1]. Indeed, this rotation has been the subject of substantial research since Anderson et al., first synthesized the porphyrin dimer.

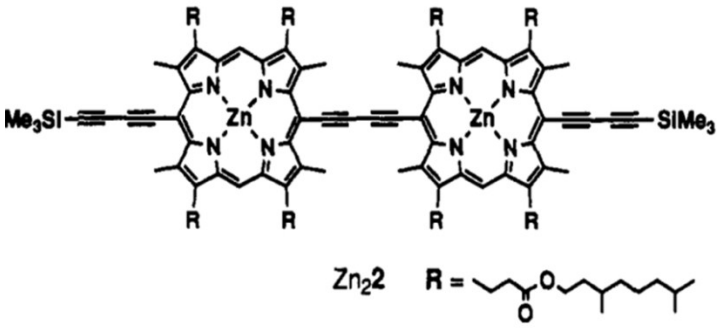

Figure 3.1: A meso-butadiyne-linked dimer of Zn^{2+} porphyrins that was synthesized and studied by Anderson et al., [1]

Under aggregating conditions, porphyrin dimers of the type in Figure 3.1 have been shown to assemble into "ladders" by the π-π interactions porphyrin macrocycles, resulting in two columns of stacked porphyrin macrocycles held together by the butadiyne links of individual dimers[1]. In this aggregated conformation, rotation about the butadiyne link is considered to be significantly restricted due to steric hindrance of the ordered aggregate[1]. The combination of enhanced optical properties and electronic properties of the self-assembling porphyrin ladder made it an intriguing target for artificial photosynthesis and solar cells[6–8]. The porphyrin dimer displayed an augmented absorption window relative to that of the butadiyne-substituated

monomer by splitting of the Soret peak and broadening of the Q bands as is shown in Figure 3.2d [1,9,3]. Anderson et al., explained the change in absorption spectra using Kasha's point-dipole exciton theory and conjectured that the absorption spectra of the dimer in solvent was a representation of a mixture of molecular conformations[1]. They described a molecular geometry where the mean planes of the porphyrin macrocycle were 'coplanar', the torsion angle about the butadiyne link was 0°, and π-conjugation was maintained over the entire long axis of the molecule. All other conformations, with porphyrin macrocycles out of alignment resulted in an interruption of electronic communication between the porphyrins[1]. This changeability of conformation and conjugation had potentially large implications upon the optical and electronic behaviour of the dimer and was further investigated by density functional theory to predict its effects[6,8,3]. Stranger et al., set out to determine the barrier to free rotation about the butadiyne axis and found that the energy of rotation changed with the torsion angle: from 0° to 60°, it was negligible but from 60° to 90° it was calculated to be as high as 14 kcal/mol[6]. This was particularly significant for the study of optically active supramolecular structures made from porphyrin dimers such as boxes and grids, which were assemblies of either the pure 'planar' confomer or the 'twisted' but not combinations of both[7–9]. Using the spectroscopic characteristics of self-assembled porphyrin-dimer boxes, Tsuda et al., confirmed the strong driving force toward planarity for the butadiyne substituated dimer[8]. The nature of the bridge between the two porphyrin macrocycles was shown to be the dominant factor in determining which conformation was energetically favourable, confirming the significance of π-conjugation in the butadiyne-linked dimer[8]. As such, rotation affects the spectroscopic properties of a range of porphyrin dimers that are conjugated by alkyne, imine, imide and alkene links alike, by splitting of the Soret band and altering the π system of these dimers [10,11].

Winters et al., conducted a detailed study of the photophysical consequences of intramolecular rotation in solution[3]. They calculated (by density functional theory) absorption spectra of the planar and twisted confomers and the absorption spectra using a Boltzmann weighted distribution of dihedral angles at room temperature (Figure 3.2a) [3]. The calculated spectrum

predicts a mixture of both twisted and planar conformations contributing to absorption spectra resulting in a heightened Soret peak and broadened Q bands. To verify the calculation, it was necessary to measure spectra from solution in which the conformation of the dimer was uniformly planar (without being aggregated). In order to achieve this Winters et al., used a planarising dipyridyl ligand (Figure 3.2c) which coordinates with the Zn^{2+} centres of both porphyrin macrocycles and forces them into a planar conformation, at 0°, relative to one another[3]. Titration of the ligand into solution with the dimer produces the spectrum of the planar confomer (Figure 3.2d). The calculated spectra are shown to coincide with the experimental spectra where a solution of the freely rotating dimer is shown to be a mixture of spectra from the twisted and planar confomers[3]. Data shown by Winters et al., contradicts the theoretical rotational energy barrier calculated by Stranger et al., as the spectrum of the dimer in solution shows a thorough mixture of both conformations, which cannot be achieved at room temperature if the barrier to rotation is 0.607 eV (14 kcal/mol). Instead, Winters et al., calculated a value of 0.03 eV (0.69 kcal/mol) as the energy barrier between butadiyne torsion angles of 0° and 90° in the ground state, and a barrier of 0.17eV (3.9 kcal/mol) in the excited state[3]. According to this estimation, free rotation is possible at room temperature (gas phase estimate of E = 0.026 eV (0.593 kcal/mol))[12]. Winters et al., calculated energies of 1.70 and 1.87 eV (39.2 and 43.1 kcal/mol) for the excited planar and twisted conformations, respectively[3] (Figure 2.2b). Though a much smaller value than what was predicted by Stranger et al., Winters et al., sustained that the excited state has an ample energetic driving force towards planarity that is not observed in the ground state, giving a uniform distribution of torsion angles [6,3].

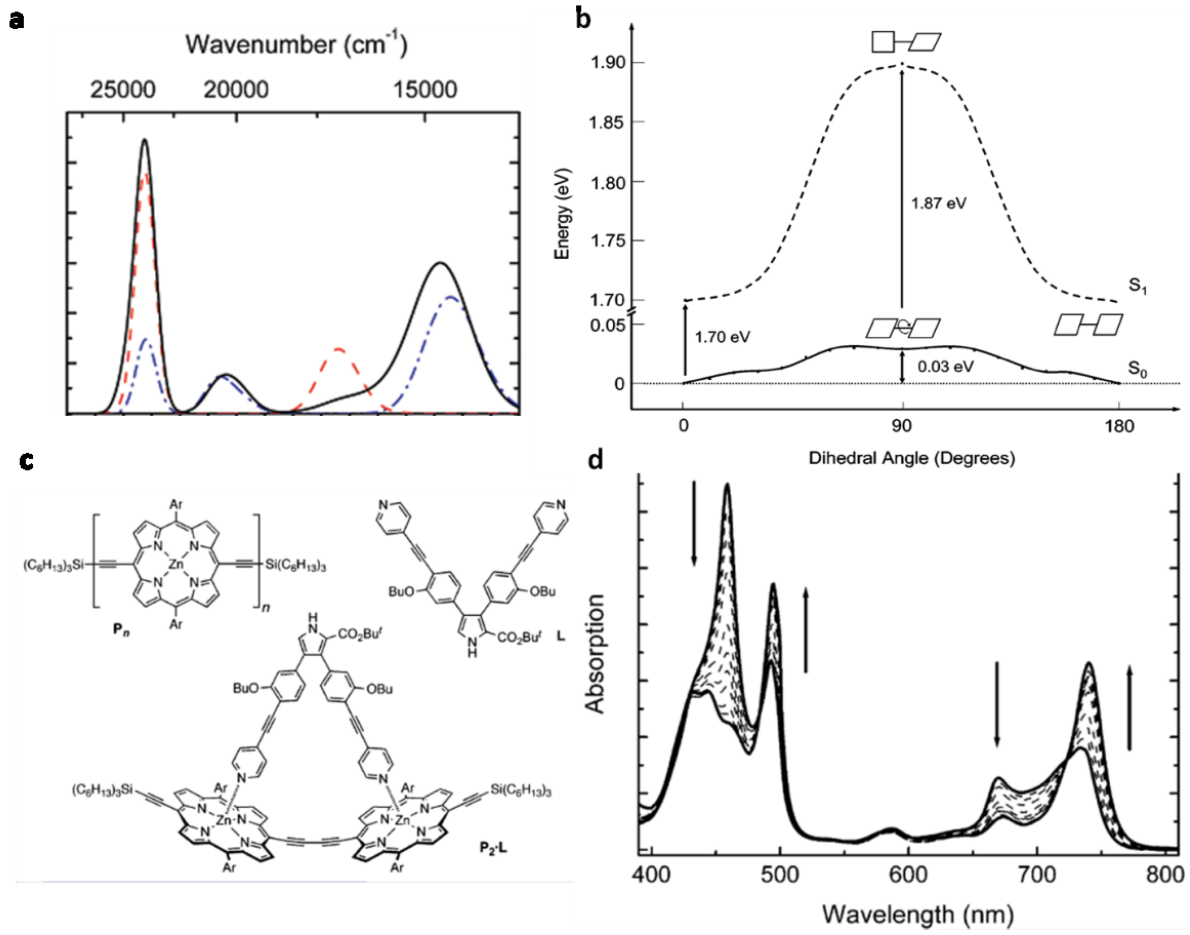

Figure 3.2: a) Calculated absorption spectra using DFT applied to: 0^0 - the planar confomer (blue dashed line); 90^0 - the twisted confomer (red dashed line) and the simulated Boltzmann-weighted distribution of torsional angles adopted by the dimer at room temperature (black solid line). b) Potential energy surfaces for the S_0 (solid) and S_1 (dashed) states. c) Structure of a dipyridyl pyrrole ligand used to form a complex with the P_2 dimer and induce planarity. d) Absorption spectra upon titration of the dimer into solution (2-MTHF) with the dipyridyl pyrrole ligand (L) in excess. All figures are adapted from Winters et al., 2007.

Winters et al., also showed for the first time that the fluorescence spectra of the dimer changed with excitation wavelength, namely in that higher energy excitation gave rise to two emission peaks when low energy excitation gave rise only to one[3]. They offered the explanation that these were emission bands corresponding to the high energy 'twisted' and low energy 'planar' peaks. Moreover, excitation of the 'twisted' confomer may reorganise its conformation and emit as the newly formed 'planar' confomer [3]. This observation went some way to explaining their finding that the relative amplitude of the two emission peaks are sensitive to the temperature of a viscous solvent, 2-methyltetrahydrofuran (2-MTHF) as shown in Figure 3.3[3]. Using Arrhenius

plots, Winters et al., asserted that the energy barrier to rotation could be appreciably changed by the viscous contribution of surrounding solvent, which, in turn, would alter intermolecular rotation, giving two conformations[3]. Due to the spectroscopic independence of the two conformations, this meant that the viscous contribution of surrounding solvent alters the emission spectrum of the dimer [3]. By this work, Winters et al., have established evidence that the porphyrin dimer could behave as a molecular rotor. Figure 3.3b shows a Jablonski diagram of the viscosity dependent conversion between the two confomers.

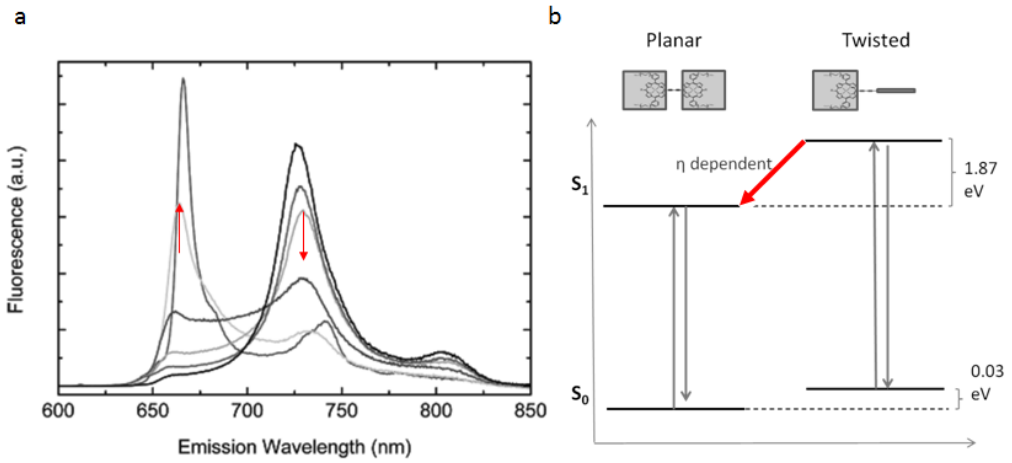

Figure 3.3: a) Temperature effects upon Twisted/Planar peak emission ratios from Winters et al., 2007 for a $P_2Si(C_6H_{13})_3$ substituated dimer[3]; b) Jablonksi scheme of the mechanism of viscosity sensitivity; unidirectional conversion from twisted to planar confomers

In 2009, Several biocompatible porphyrin dimers were synthesized by the group of Harry Anderson, with triethylene glycol moieties affixed to the β and δ positions of both macrocycles and a series of anionic and cationic charged substituents to *meso* positions of both porphyrins. Two cationic, P_2NMe_3 and P_2NMeI and two anionic, $P_2SO_3NH_4$ and P_2Suc variants are among the biologically compatible porphyrin dimers shown in Figure 3.4. Two longer dimers incorporate an ethyne link to the charged moieties, in both cationic, P_2C_2NMeI, and anionic, $P_2C_2CO_2NH_4$, variants (Figure 3.4).[13] These dimers are the subject of this work.

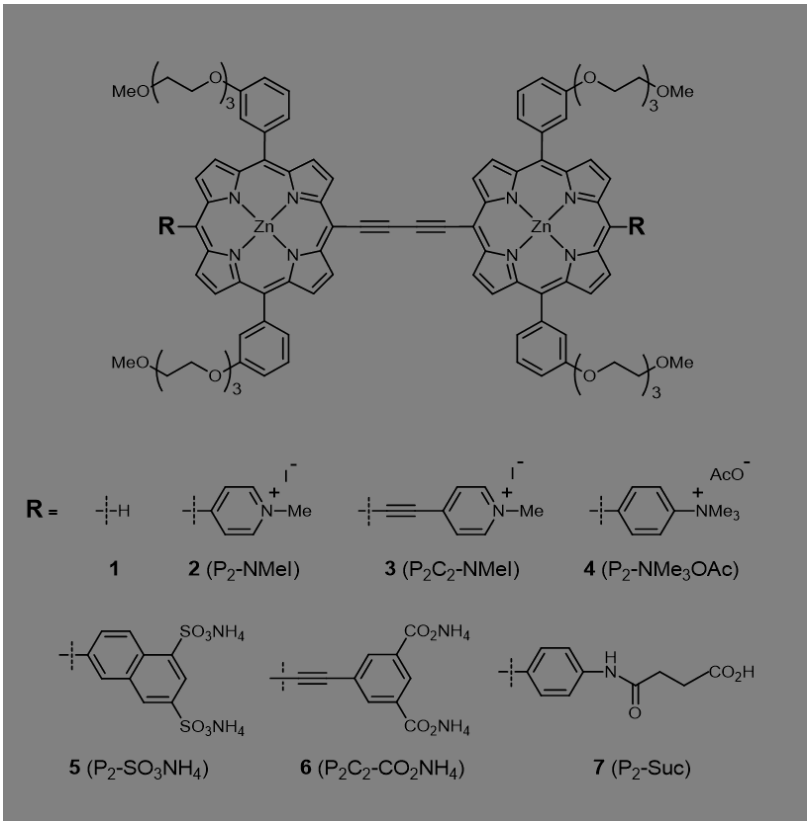

Figure 3.4: Structure of the porphyrin dimers used as molecular rotors. The butadiene link provides the rotational changes that produce viscosity sensitivity. Below, the meso conjugated charged moieties 1: P_2H, 2: P_2NMeI, 3: P_2C_2NMeI, 4: P_2NMe_3 5: $P_2SO_3NH_4$, 6: $P_2C_2CO_2NH_4$, 7: P_2Suc. (P_2: two porphyrin substituents, C_2: extended ethyne link)

Light-activated porphyrin drugs in cellular environments are known to produce singlet oxygen, often in quantities that can affect the viability of the cell. This process is known as *photosensitisation*, and can be exploited for therapeutic use against malignant and pathogen-infected cells during what is termed photodynamic therapy (PDT). The photosensitizing effect of the porphyrin dimers will be discussed in detail in subsequent chapters, though it provided an important motive for the development of the hydrophilic dimers for use within cells. The capacity of the porphyrin dimer for simultaneous viscosity sensitivity and singlet oxygen production created a unique opportunity for the visualisation of PDT in cells and its effect on cellular viscosity[14–17]. The proof of concept was published in 2009 by Kuimova et al., and this work develops on these results[18].

This chapter aims to characterise the viscosity sensing mechanism of the extended series of porphyrin dimers and to propose and investigate other physical parameters that affect its photophysical behaviour.

3.2 Spectroscopic behaviour

Here, the cationic dimer P_2NMe_3 was used as a model for the remaining variants and was subject to both absorption (Figure 3.5a) and fluorescence (Figures 3.5b, 3.5c) spectroscopy. The absorption spectrum confirms predictions from DFT that have been mentioned in literature by Winters et al., and Stranger et al., [6,3]. For this dimer, the Soret peak ($S_0 \rightarrow S_2$ transition) has multiplet character, between 400 and 500 nm, with two peaks at 453 nm and 477 nm. Q bands ($S_0 \rightarrow S_1$) are also split, and are seen between 640 and 725 nm. Since a significant overlap is observed between the Q band absorption peaks and the emission bands, all emission spectra were selectively excited at the $S_0 \rightarrow S_2$ transition.

The longer-extended dimers of the type P_2C_2 (dimers **3** and **6** in Figure 3.4) were found to have red shifted and broadened absorption bands (both Soret and Q bands are shifted) due to the increase in conjugation across the molecule. In these same dimers, it was found that the Soret bands for the two conformations are closer together and the overlap is increased, as shown in Kuimova et al., 2009 [17] (See Appendix A).

Strong absorption at red visible wavelengths in potential PDT drugs is considered a substantial advantage due to the overlap with the 'tissue optical window' as well as the corresponding red shift for two-photon excitation into the infra-red. Infra-red light is much less likely to be scattered by tissue and is much less damaging than visible light and so is ideal for photosensitization *in vivo* as the therapeutic volume can be very accurately controlled[19,20]. Structural influence upon the two-photon absorption cross section can be demonstrated by comparison between the dimer with simple *meso* substitution (P_2NMeI) and the ethyne-linked longer dimer with the same substituent (P_2C_2NMeI). Kuimova et al., 2009 found an increase in the Goeppert-Meyer number (two-photon molar extinction coefficient) from $8.7x10^3$ to $17x10^3$

GM at the relative absorption maxima.[17] Red excitation wavelengths are also beneficial for sensing applications, as in measurement of intracellular viscosity. In spite of its advantages, two-photon absorption of the dimers is not considered in this work and will be the subject of future investigations in the group.

The characteristic absorption spectrum of the porphyrin dimer has a split Soret peak (from ca. 400 – 500 nm), and two Q bands (ca. 625 -725 nm). The P_2NMe_3 dimer has an absorption maximum at 454nm (Figure 3.5a) which gives rise to the viscosity-dependent emission spectra shown in Figure 3.5b.

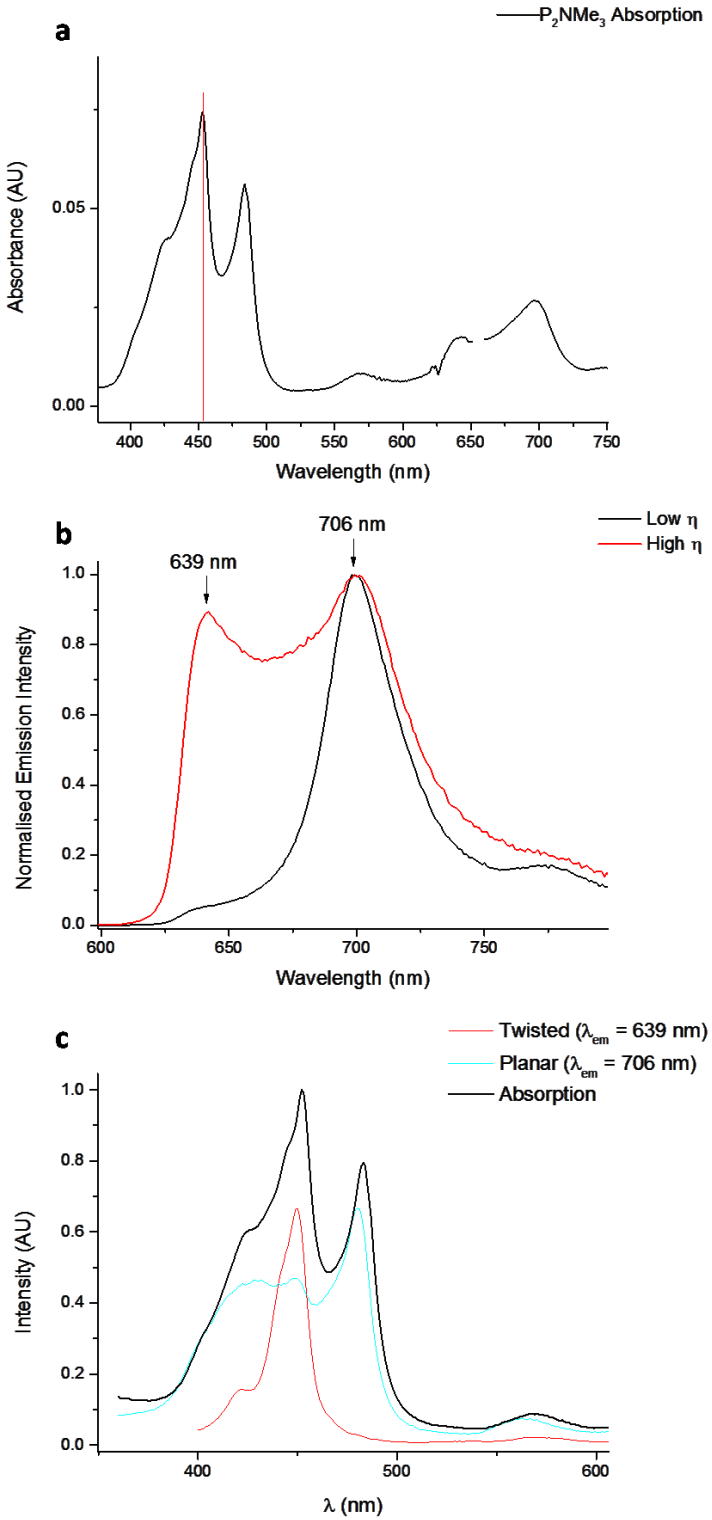

Figure 3.5: a) Absorption spectra for P_2NMe_3 (0.33 μM, 70 w/v% glycerol in methanol, 0.001 % v DMSO) b) Normalised emission spectra of P_2NMe_3 in low viscosity solution (20 w/v % glycerol in methanol) (black line) and high viscosity solution (70 % glycerol in methanol) (red line) when excited at 454 nm (red line, Fig. 5a). c) Excitation spectra of P_2NMe_3 in 70 % glycerol in methanol of emission at 639 nm (black) and 706 nm (red) showing two distinct excitation bands.

The dimer's fluorescence spectrum (at λ_{ex} = 454nm) is markedly different depending on the solvent. The two spectra shown in Figure 3.5b are collected in 20% glycerol/80% methanol (black line) and 70% glycerol/30% methanol (red line), used to simulate conditions of low and high viscosity without change in temperature. In non-viscous solution the dimer has unimodal emission as can be expected from a monomeric porphyrin, although considerably red shifted to 706 nm. In high viscosity, a second, higher energy (lower λ_{em}) band appears at 639 nm, with comparable intensity to the original 706 nm band (Figure 3.5b).

According to the assignment of Winters et al., emission from the higher energy band (639 nm), is from the 'twisted' conformation of the dimer while the constant band at 706 nm originates from the planar confomer[3]. Restriction of rotation to the planar confomer, by viscous solvent, allows emission from the twisted confomer which is not observed under conditions of low viscosity. The difference in the emission maximum suggests that the two confomers emit from excited state with different contribution of molecular orbitals – a possibility introduced by both Anderson et al., 1994[1] and Winters et al., 1997[3], when suggesting that internal rotation of the molecule interferes with the π-conjugation over the two porphyrins and the butadiyne link.

Excitation spectroscopy reveals the excitation λ that give rise to a specified emission band as shown in Figure 3.5c. In order to further investigate the conformational dependence of the emission, we recorded excitation spectra which would give the individual spectra of the absorbing species that emit at each emission maxima (639 nm and 706 nm). Figure 3.5c shows, the planar species displays its characteristic split Soret band and higher wavelength absorption (cyan line) relative to the unimodal excitation of the twisted confomer (red line). Figure 3.5c imposes the absorption spectrum on top of both excitation spectra to show that it is a combination of them, and reflects the presence of both species in the ground state, independent of solvent viscosity. It is only in the excited state that the planar confomer is strongly preferred, as shown in Figure 3.2.

Disruption of the π conjugation in the twisted confomer, causes both porphyrin macrocycles to behave as monomers, which would absorb at the same λ, as in the single peak seen in Figure 3.5c (red). On the other hand, the planar confomer behaves as expected for a conjugated dimer. A broadened Soret peak is split, with two distinct peaks: one corresponding to the dipole along the axis of the butadiyne link and one perpendicular to the link, across each macrocycle, as suggested by Anderson et al., 1994[1]. This is in agreement with spectra from Winters et al., where a planarising ligand showed that absorption by the two different confomers could be distinguished by absorption spectroscopy[3].

Thus we established that the two emission peaks correspond to the individual confomers, the twisted and the planar. The intensity of each band indicates the frequency of emission from the corresponding confomer – they are interchanging. This represents a larger relative population of the twisted versus the planar and vice versa. Figure 3.6 shows this point in detail. In this experiment, mixtures of glycerol in methanol with increasing glycerol content are used to produce a set of solutions with increasing viscosity (glycerol/methanol mixtures are w/w %, as described in Chapter II).

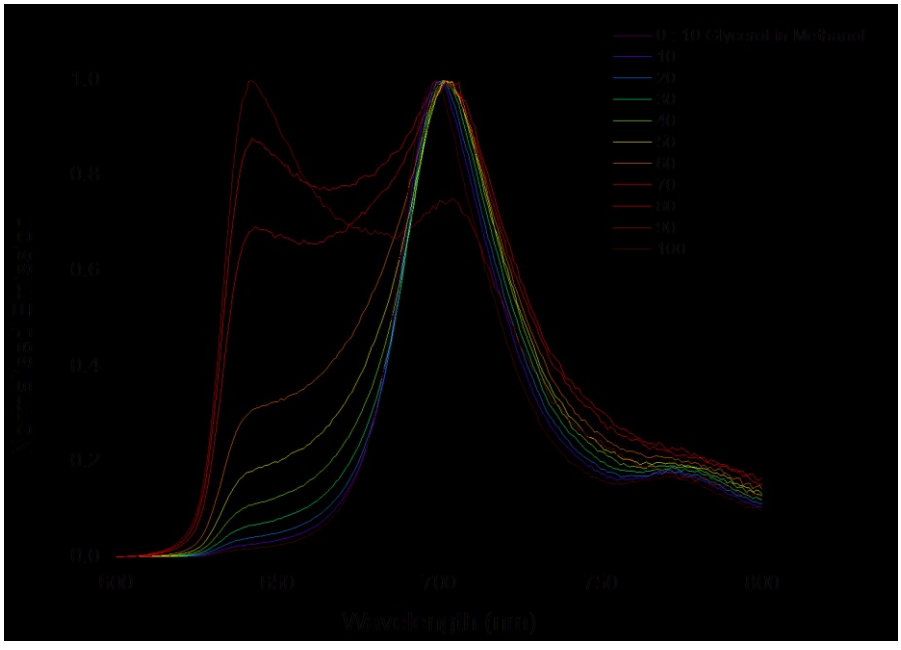

Figure 3.6: Emission spectra for P_2NMe_3 (1 μM, λ_{ex} = 453 nm) in solutions of increasing viscosity (increase in w/v % glycerol in methanol).

Systematic variation of viscosity shows a systematic rise in the 'twisted' emission (excited at 453 nm) band at 639 nm (Figure 3.6) which confirms the behaviour of the twisted confomer as a molecular rotor. Its quantum yield increases with viscosity, as predicted by Förster and Hoffmann. The intensity of emission from the planar confomer (λ_{em} = 706 nm), on the other hand decreases with increasing viscosity, as a greater quantity of dimers remain in the twisted state. In non-viscous solution, the twisted confomer is excited and rotates into the planar conformer so only emission from the planar confomer is observed. At high viscosity, rotation is restricted by friction in the solution, the twisted confomer cannot be transformed into the planar and emission from the twisted confomer can be observed. The one-way conversion of the twisted into the planar rate is viscosity dependent and thus the viscosity can be measured by the ratio of the two peaks.

3.2.1 Temperature-dependent viscosity

Another mode of manipulating the viscosity of a single solution is to change its temperature. This is in some ways a superior method of investigating a large range of viscosities due to the large number of models relating the effect of temperature on solution viscosity, making it highly predictable and the data subject to many modes of analysis. Generally, the Arrhenius equation is used to predict the effect of temperature on solution viscosity: increased kinetic energy of collisions between solvent molecules reduces the friction between them, resulting in a reduced bulk viscosity[21,22]. The activation energy of viscosity, E_η, in Arrhenius terms, is the intrinsic energy of solvent-solvent bonds or steric interactions that must be overcome for motion of the solvent molecules[23]. The equation for Stokes-Einstein diffusion (equation 1.5) also includes a coefficient for friction which is temperature dependent[24]. Furthermore, manipulation of temperature can be performed on a single sample rather than using a number of samples, as in Figure 3.6, which is subject to errors of preparation multiplied by the number of solutions required. Nonetheless, a change in solution temperature can alter the rotational behaviour of the molecular rotor independently of its contribution to solvent viscosity. As has already been noted in the literature regarding the molecular rotor BODIPY C_{10}[25], the activation energy of

rotation can be overcome at high temperatures, changing the rate of non-radiative decay. This breaks the relationship between the rate of radiative decay and solution viscosity, and the Förster-Hoffmann equation may no longer hold true. The following section explores the effect of temperature on the behaviour of the porphyrin dimer, with the aims of i) creating a calibration curve between emission ratios and solution viscosities and ii) investigating temperature as a confounding variable in the viscosity-quantum yield relationship of the porphyrin dimer.

In order to establish the classical temperature-dependent viscosity of solutions, we measured a series of methanol/glycerol mixtures using a mechanical rheometer. Viscosity measurements performed on the viscometer were compared with emission ratios of the porphyrin dimer, as shown in Figure 3.7. Crucial to our measurements is the temperature stability of all measurement equipment: the Stabinger 3000 viscometer has a Peltier plate for temperature control which has temperature accuracy of 0.005 °C[26], comparable to that of the Jobin Yvon Fluoromax 4 fluorometer, 0.002 °C[27]. Figure 3.7a shows the emission spectra of P_2NMe_3at a range of temperatures from 273 to 333 K, showing the characteristic drop in emission from the twisted band as temperature increases. The same solution was measured by mechanical rheometry to record the temperature-dependent viscosity as shown in Figure 3.7b (red data). Figure 2.7b also shows the relationship between the twisted and planar emission band ratios and temperature from the data shown in Figure 3.7a. The nature of the viscosity-temperature relationships as measured by both techniques are similar, the curves are exponential. To test the similarity between both temperature-responses we plotted them against one another on a double-log plot, and found a strong linear relationship as predicted by the Förster-Hoffmann equation as shown in Figure 3.7c. According to a least squares linear regression of the data, the slope between emission ratio and viscosity is 0.77; a higher value than predicted by Förster and Hoffmann, of 0.6 [28]. This is a highly limited viscosity range, with a small dataset, contributing to the inflated slope observed. For true comparison with the Förster-Hoffmann theory, the temperature dependence would need to be tested with greater range.

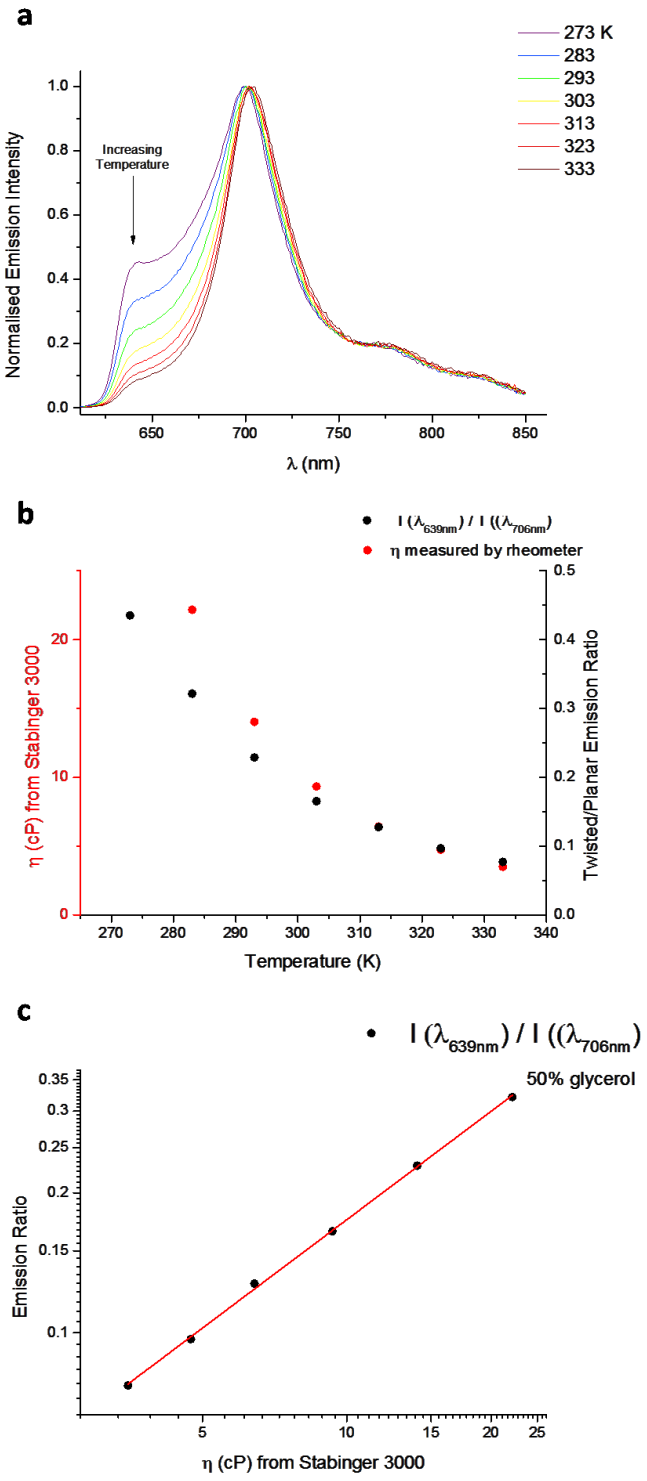

Figure 3.7: a) Emission spectra of P_2NMe_3 in 50% w/w glycerol in methanol at 273- 333K showing the characteristic decrease in the twisted confomer upon increase in solution temperature. b) Measurements performed on 50% w/w glycerol in methanol at 273- 333K by left axis: mechanical rheometry (Stabinger 3000) and right axis: the twisted/planar emission ratio, on 50% w/w glycerol in methanol at 273-33 K. c) Förster-Hoffmann double-log plot of emission ratio against mechanical rheometry measurements showing good linear agreement. Least squares linear regression yields Emission Ratio = -1.53 + 0.77η (at standard error intercept = 0.01, slope = 0.01, R^2 = 0.99).

We used the entire range of glycerol/methanol solutions shown in Figure 3.6 under temperature-controlled conditions to build a viscosity range from 1-7000 cP. Figure 3.8 shows the relationships between viscosities reported by mechanical rheometry and porphyrin dimer emission ratios as manipulated by temperature in seven more glycerol/methanol mixtures (a) 30; b) 40; c) 60; d) 70; e) 80; f) 90; g) 100 w/w % while data at 50% is shown above). Temperatures range from 273 to 373 K though at low glycerol content is restricted to 343 K due to the boiling point of methanol. All data is shown on double-log plots, in reflection of the Förster-Hoffmann equation. A strong linear relationship is observed at low viscosities, both in solutions of low glycerol content at 30, 40, 60 w/w%, and at high temperatures of solutions with high glycerol content 70-100 w/w%.

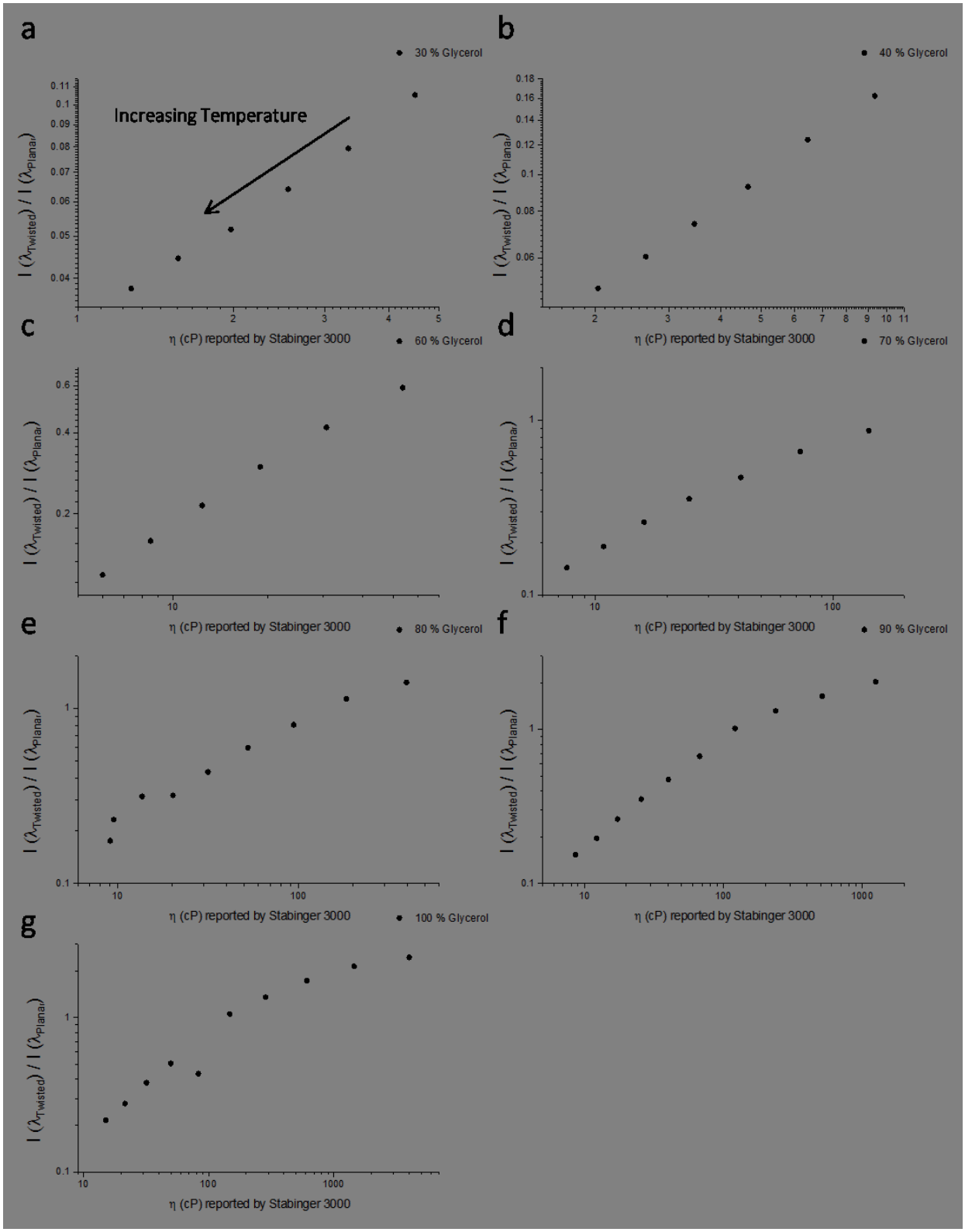

Figure 3.8: Förster-Hoffmann double-log plots of emission ratio against mechanical rheometry measurements of a)30; b)40; c) 60; d) 70; e) 80; f) 90; g) 100 w/w% glycerol in methanol. Data sets are temperature scans of ranges (a-c) 273-333 K; d) 273-343 K; (e-g) 273-373K.

At values higher than 100 cP, in all solutions, the emission ratio becomes less sensitive to changes in viscosity. The extremes of our calibration data show the breakdown of the linear relationship: at the highest measured viscosities, we observe a decrease in slope, signifying a lack of sensitivity of the dimer to temperature-related viscosity changes. This decrease in slope – or sensitivity to viscosity – in non-viscous solvents can be interpreted as the energy barrier to rotation being insufficiently affected by solvent friction to compete with planarization of the excited state of the dimer. Similarly, towards higher viscosities, decrease of the dimer's slope represents the case where the driving force towards planarity in the excited state is insufficient to overcome the viscous friction in solution.

In Table 3.1, the temperature-dependent viscosity change as measured by the porphyrin dimer's emission ratios and mechanical rheometry is fit with a least squares linear regression of the data from Figure 3.8. Parameters from the fit are shown below in Table 3.1. Only selected ranges of the curve are fit, those where the linear relationship is maintained, because, as we have discussed the porphyrin dimer loses sensitivity to changes in viscosity above approximately 100 cP. Consistently, the fitted slope is found to be <0.6 (except in the cases of 70, 80 w/w% where linear fits include the non-linear region and the data demonstrates a larger error). We propose that the high slope is indicative of a high sensitivity to the thermal expansion of the solvent. Loutfy et al., observed a similarly high slope for the sensitivity of a p-(dialkyl-amino) benzylidenemalonitrile molecular rotor to the temperature dependent viscosity of glycerol. The slope of the two viscosity measurements, quantum yield and mechanical rheometry, was found to be 0.75, a similar value to our fitted slopes. They attributed this to a combination of effects in solvent relaxation; Stokes-Einstein diffusion and the free-volume expansion of the solvent[29]. In the former, as we have explained, the Enthalpic barrier of solvent interactions is overcome by the kinetic energy of molecular collisions, reducing the steric hindrance in the path of internal rotation of the molecular rotor. The second effect involves the thermal expansion of the solvent whereby increased recoil from collisions creates excess volume around solvent molecules, this is termed free volume. The barrier against rotation is

further increased by the increase in unoccupied "free" volume, thus reducing the quantum yield of the molecular rotor. The combination of these two effects increases the temperature-dependent slope of viscosity curves further than that proposed by Förster and Hoffmann (0.6) in their theoretical paper. Loutfy et al., 1982 have proposed Doolittle's equation relating free volume and viscosity as a model for the increased sensitivity to temperature-induced viscosity change in solvents, particularly in glycerol. Here we refer to the combined activation energy of solvent diffusion as it contributes to solvent viscosity as Eη. We refer to the porphyrin dimer's barrier to rotation as E_a, the activation energy. Free volume is discussed in more detail in the next chapter[29].

Table 3.1: Least squares linear regression parameters of P_2NMe_3 in glycerol/methanol calibration curves by solution

% Glycerol	Intercept	Slope	Reduced Sum of Squares	Adjusted R^2	Range
30	-1.512	0.800	4.55E-04	0.996	1.2-4.4
40	-1.549	0.783	1.28E-04	0.999	2.0-9.3
50	-1.531	0.774	2.00E-04	0.999	2.4-22.2
60	-1.481	0.735	1.22E-03	0.996	6-53.6
70	-1.350	0.619	6.15E-03	0.985	7.6-141.7
80	-1.167	0.529	2.01E-02	0.970	20.2-395.6
90	-1.483	0.721	4.51E-04	0.998	8.9-67.3
100	-1.504	0.713	1.31E-04	0.997	15.1-50.0

*Adjusted R^2 gives the error of independent variables that are related to viscosity; that is the slope/ Adjusted R^2 is measured by the equation: Adjusted $R2 = 1 - (\frac{(1-R^2)\times(n-1)}{n-k-1})$.

We plotted the temperature-dependent viscosity curves of all the glycerol/methanol solutions on a single graph as shown below in Figure 3.9. The amalgamated curves cover a large viscosity range (1-7000 cP) with strong overlap of the curves. The overlap is good evidence that the temperature does not alter the porphyrin dimer's energy barrier to rotation outside of the

viscous effects of the solvent. As we discussed in Figure 3.8, the Forster-Hoffmann linear relationship collapses at viscosities above 100 cP. This is due to the saturation of the twisted confomer in the excited state prior to emission – the proportion of twisted confomer that emits is unchanging with viscosity.

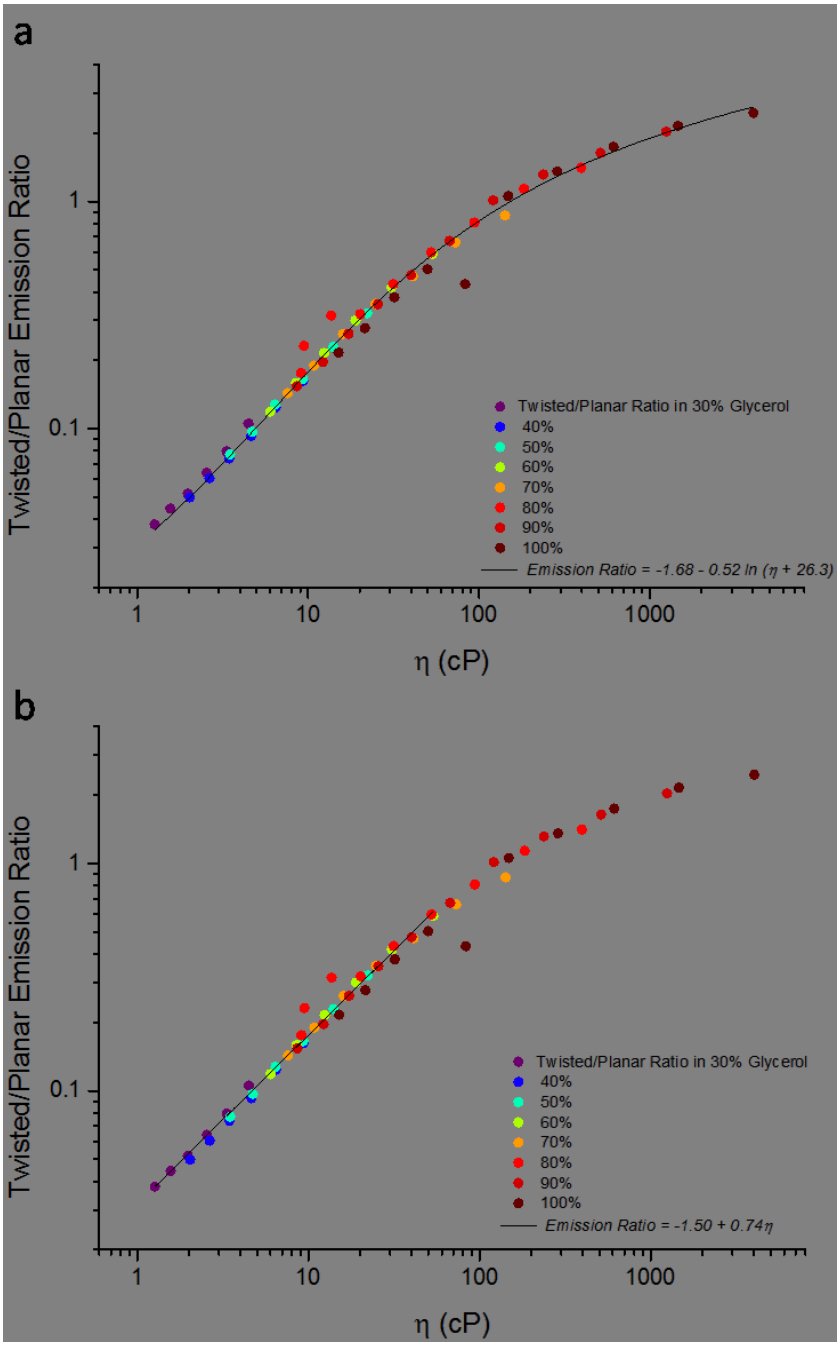

Figure 3.9: Double log plot of glycerol/methanol solution viscosity measured by mechanical rheometry a against P_2NMe_3 emission ratio. a) Fitting of data by three-parameter logarithmic function of equation Emission ratio = -1.68-0.5ln(η + 26.3) R^2 = 0.989. b) Least squares linear regression of a selected range < 100 cP fitted by Emission ratio = -1.50 + 0.74η R^2 = 0.98.

This value is intrinsically related to the size of the dimer, and its torque relative to the frictional resistance of glycerol. Nonetheless, we are able to fit the curves as one, as in Figure 3.9a, with the use of a three parameter logarithm function with the following equation:

$$log_{10}\, Emission\ Ratio = a + b(\ln \eta + c) \tag{3.1}$$

where a = -1.68, b = 0.05 and c = 26.9, with standard errors 0.095, 0.016 and 2.94, respectively, and R^2 = 0.989. This model was chosen for its goodness of fit to the empirical data in its extended range (i.e. > 100 cP) though we assert that the Forster-Hoffmann prediction of linearity is strongly maintained below this value. Figure 3.9b shows a linear fit of the same data at a reduced range with the equation:

$$log_{10}\, Emission\ Ratio = a + b\eta \tag{3.2}$$

where a = -1.50, b = 0.74 with standard error of 0.01 and 0.01, respectively and R^2 = 0.98. In light of the quality of the fit of the curve, our intention is to use this data as a calibration for unknown solvents.

Figure 3.10 shows the same calibration curve plotted against η/T to show the temperature independent relationship between the two measurements of viscosity. In Figure 3.10a we show that the relationship of emission ratios to viscosity independent of temperature is identical to the curves shown in Figure 3.9, plotted against temperature-dependent viscosity. This establishes that the dimer's rotation is only affected by the viscous barrier. From this data, we calculated the maximum twisted/planar emission ratio to be 2.83. In Figure 3.10b this value is used to calculate the viscosity-dependent ratio as a fraction of the theoretical maximum ratio, R_η/R_{Max}- R_η, and plotted against the temperature-independent viscosity. We find a very strong linear relationship between the two variables, with slope 0.75 (standard error 0.0099, R^2 = 0.99) reflecting the values estimated from the linear region of the Förster-Hoffmann calibration curve shown in Figure 3.9.

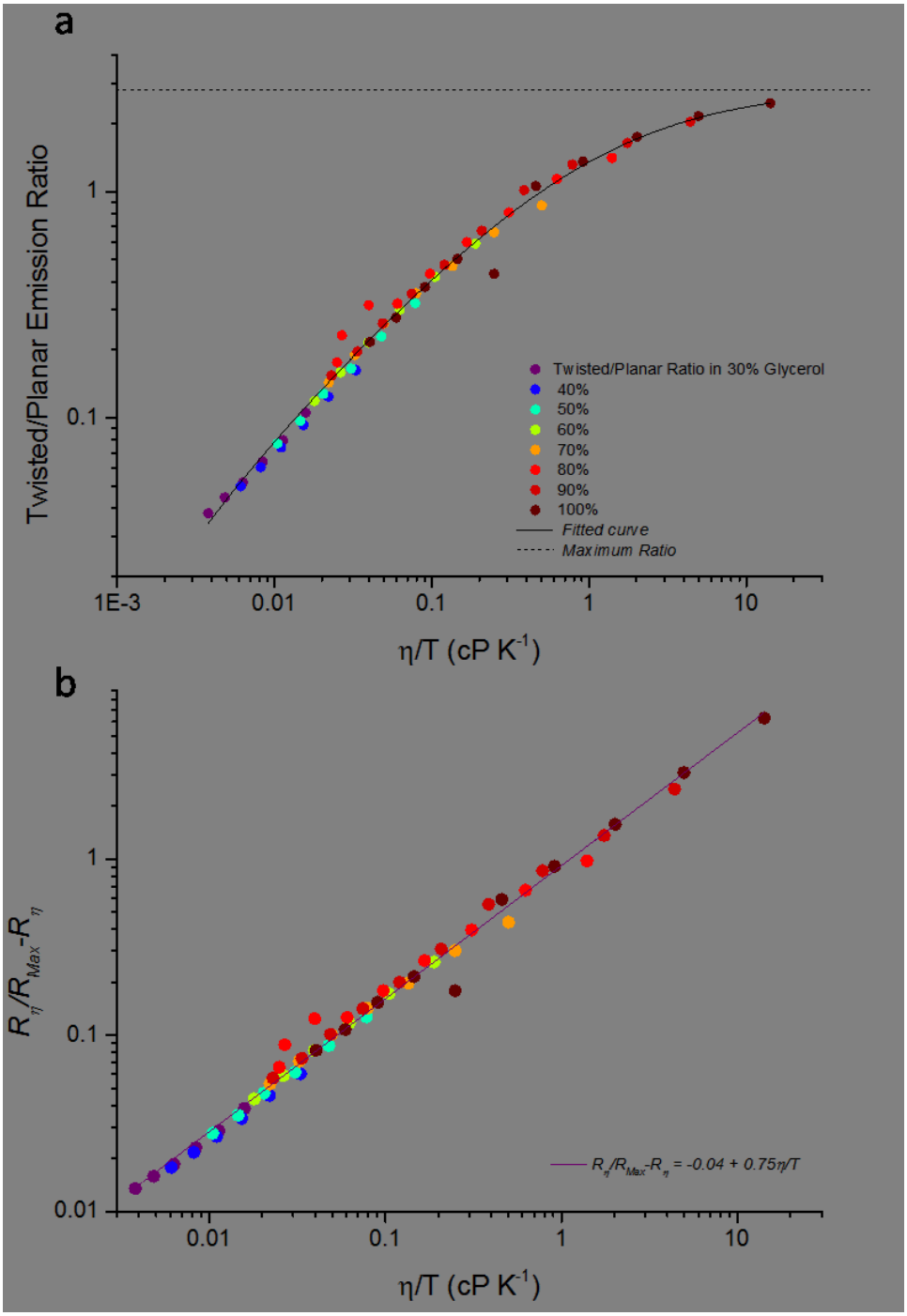

Figure 3.10: Temperature independent viscosity calibration curves of emission ratio against η/T. a) the maximum emission ratio is estimated by the fitted function Emission ratio = -0.028+(2.00-0.028) $\eta^{0.64}/(150.90^{0.64}+\eta^{0.64})$ $R^2 = 0.99$. b) Temperature independent viscosity calibration curves of the viscosity sensitive emission ratio (R_η) as a fraction of the maximum (R_{max}) such that $R_\eta/R_{ma}- R_\eta$ is plotted against η/T with good linear relationship. Least squares linear regression of the data yields the equation $R_\eta/R_{ma}- R_\eta = -0.04+0.75\eta/T$ $R^2 = 0.99$.

Our calibration curve shows good linear prediction of macroviscosity by measurement of the emission ratio of P_2NMe_3. We plan to use this calibration curve to measure viscosity in unknown solvents. However, there are a number of experimental conditions that must be met in order to

produce a reliable and applicable calibration curve. First amongst these conditions is the choice of the λ_{ex} used for ratiometric measurement.

3.2.2 Slope dependence on λ_{ex}

Table 2.1 lists the slopes and intercepts of temperature-dependent viscosity calibration curves from Figure 3.9. The significance of the slope has been discussed in some detail above; it represents the sensitivity of the emission ratio to changes in solution viscosity; the higher the slope, the higher the viscosity "resolution" of the molecular rotor. Intrinsically, as we showed above, the slope is related to quantum yield of the twisted confomer, whose emission is only observed in the absence of a significant viscous barrier (E_η). As such, we seek to maximize excitation of the twisted confomer. When the emission maximum of the twisted confomer is plainly measurable, this is the optimal λ_{ex} for generating calibration curves. Figure 3.12a and b demonstrate the effect of λ_{ex} (Figure 3.12a) on the slopes of calibration curves (Figure 3.12b). Viscosity-dependent dimer emission ratios in mixtures of glycerol and methanol are measured at four different λ_{ex}: 400, 452, 454 and 499 nm. Figure 3.12a shows the position of the λ_{ex} relative to the twisted excitation spectrum, and the absorption spectrum of P_2NMe_3. At the two extremes, 400 and 499 nm, a very small proportion of twisted confomer is excited, and the corresponding slopes of calibration curves made by excitation at these λ_{ex} is low (400 nm, black data points; 499 nm, magenta data points; Figure 3.12b). In contrast, the two calibration curves produced by excitation at λ_{ex} corresponding to the maximum of the twisted excitation peak, 452 and 454 nm, (red and cyan data points; Figure 3.12b, respectively) are significantly higher. Excitation at the peak of the twisted confomer (i.e maximised concentration of the twisted excited state) produces a greater twisted signal for ratiometric measurement of between the quantum yield of the twisted state as a function of viscosity. This is demonstrated by plotting the slopes of a large number of calibration curves according to the λ_{ex} at which they are measured, as in Figure 3.12c. The maximum value of the slope coincides with the twisted excitation peak, as predicted. For reasons summarized above, the full viscosity range measured (1-5000 cP) is not entirely linear, where the data reaches a maximum ratio at high viscosities.

This causes least squares linear estimations of slope to be lower than the true slope in the Förster-Hoffmann-predicted linear region (where $E_\eta < E_a$). Least squares linear regression of the data without the inclusion of the high viscosity region (< 1000 cP) yields a distribution of slopes that has more accurate coincidence with the twisted excitation spectrum (Figure 3.12d). Thus we have demonstrated that the slopes of calibration curves are dependent upon the λ_{ex} used to excite the twisted confomer.

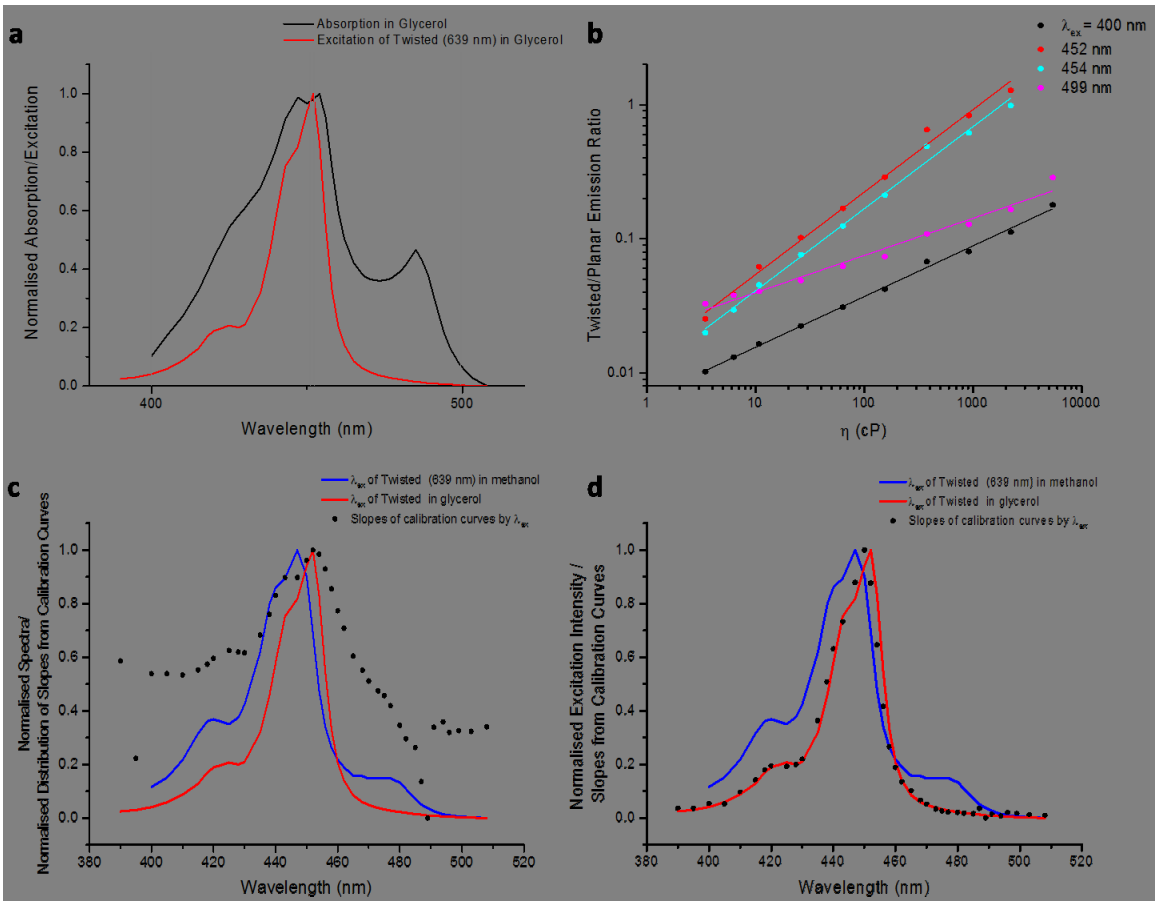

Figure 3.12: a) Calibrations of twisted/planar ratios were produced by systematically exciting solutions of increasing viscosity (w/v % glycerol in methanol) at the λ_{ex} shown in grey (400, 452, 454, 499 nm). (b) All calibration plots were plotted as twisted/planar ratios against the η of methanol/glycerol solutions and fit to linear equations. c) From a larger range of excitation wavelengths, the slopes from fitted lines were plotted against the excitation wavelength corresponding to the calibration data for that wavelength and found to coincide with excitation spectra for the twisted confomer (of emission at 639 nm). Plotting slopes of calibration data by the viscosity of solution also coincides with the increasing excitation intensity of the twisted confomer as viscosity increases. d) Removal of the 90 % w/v and 100 % w/v glycerol in methanol solutions from calibration data yields a much more accurate coincidence of the distribution of calibration slopes with the twisted confomer.

However, Figures 3.12c and d also show that the apparent maximum peak of the twisted confomer shifts depending on the solution in which it is measured. Figure 3.12d shows that the maximum slope corresponds to an λ_{ex} exactly between the two excitation peaks, from methanol and glycerol at 454 nm, in comparison to that from Figure 3.12c, which coincides only with the twisted excitation peak in glycerol. We attribute this to a small solvatochromic shift in the excitation maximum of the twisted confomer, a function of differences in solvent relaxation between the two pure solvents. The slopes in Figure 3.12d reflect the ratiometric response of mixtures of methanol and glycerol between 30 and 80 w/w %, compared with those in Figure 3.12c from mixtures between 30 and 100% glycerol. The influence of greater glycerol content is observed in Figure 3.12c, where the slopes are skewed towards the slightly red shifted twisted maximum. This observation is small evidence that the twisted confomer is subject to solvatochromism, changes in the Stokes shift determined by the magnetic dipole of solvent molecules in the solvation shell. This subject is discussed in much greater detail in subsequent sections.

Having discussed the importance of the excitation maximum on optimizing the slope of calibration curves, we propose that structural features of the porphyrin dimer that also affect the quality and shape of calibration curves. Figure 3.4 gives the structures of seven porphyrin dimers, with varying *meso* substituents that were prepared by the group of Harry Anderson for application into cellular environments. Below, we assess the structural characteristics that affect viscosity sensitivity and opportunities for applying dimers of varying structure.

3.2.3 The photophysical effects of structural differences amongst the dimers

We believe the calibration data shown in Figure 3.9 is representative of the universal mechanism for all the ionic dimers insofar as internal rotation about the butadiene link between the two porphyrin macrocycles is determined by the viscosity of the surrounding solvent. As we have shown with calibration data of P_2NMe_3 in mixtures of methanol and glycerol, the Förster-Hoffman linear region is true in a range where the viscous barrier is less than the energetic driving force towards planarity ($E_a > E_\eta$). However, the driving force towards planarity is

dependent on various features of the dimer; the degree of conjugation, its size and its shape. For instance, increased conjugation decreases the energy of the planar excited state relative to the twisted excited state. This increases E_a relative to E_η, increasing the viscosity range in which the emission ratio is sensitive to solution viscosity. Similarly, a larger dimer will have greater energy of rotation, that is, a larger volume of solvent molecules are necessarily displaced in order for internal rotation to take place. This increases the E_a of the porphyrin dimer, and makes it sensitive to higher viscosities than a smaller dimer, but alters the dynamic range. The cumulative effect of various structural features that affect the dimer's emission ratio is difficult to predict. Thus, we investigate five dimers differing in shape, degree of conjugation, charge and size of the side groups, in order to establish the dominant structural characteristics of a porphyrin dimer that optimize its viscosity-sensitive behaviour for application in biomimetic membranes.

Table 3.2: Structural features of five *meso* substituated porphyrin dimers that are calibrated for viscosity-sensitive behaviour in Figure 3.14

	Structure	H-bonding/ counterion	Charge
P_2C_2NMeI	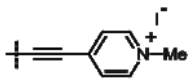	I^-	+
P_2NMeI	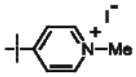	I^-	+
P_2NMe_3	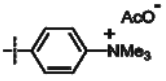	AcO^-	+
P_2Suc	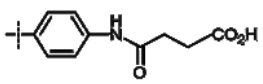	✓	-
P_2		No	None

We choose to assess a group of porphyrin dimers by a series of structure-dependent characteristics that we believe will affect the mechanism of viscosity sensitivity. These are: size, shape, conjugation, H-bonding capacity, and charge. The chemical structures and charged groups of *meso* substituents of five porphyrin dimers are shown in Table 2. Of the five dimers, three are cationic (P_2C_2NMeI, P_2NMeI, P_2NMe_3) with counterions, one is anionic (P_2Suc) and one is a simple porphyrin dimer of the internal structure lacking in charged *meso* substituent (P_2).

i. *Size and shape:* The entropic barrier to rotation from the twisted to planar confomers is dependent in part on the volume of rotation between the two conformations. The porphyrin dimer will occupy most volume during rotation, when solvent molecules are displaced. A large dimer, or one with a greater two dimensional area that rotates, causes displacement of a large number of molecules in order to achieve a change in conformation. This leads to a large value of E_a, which makes a larger dimer more sensitive to higher viscosities, with potentially less sensitivity to viscosity change. We predict that an increase in the size of a dimer will shift the Förster-Hoffmann linear region to high viscosities, and reduce its slope relative to a smaller dimer. Between the examples listed in Table 3.2, the discrepancy in size is very small and perhaps too small to engender a difference in sensitivity to viscosity. Of the five dimers listed in Table 3.2, P_2 is the smallest, P_2Suc is the largest, while all three positively charged dimers are roughly the same size, though P_2C_2NMeI is longer than its attenuated version, P_2NMeI.

ii. *Conjugation:* The energy difference between the twisted and planar states is determined in large part by the difference in entropic gain from reaching planarity prior to emission. All porphyrin dimers are ere highly π-conjugated, but addition of double bonds in the meso position can further increase conjugation. Thus, an increase in conjugation via the *meso* substituent increases the E_a of rotation. As above, we predict this increases the slope of viscosity calibration curves at higher viscosities. The long dimer P_2C_2NMeI has an extra triple bond on either side of the

porphyrin conjugated core, in the *meso* substituent, extending the length of the conjugated axis in this dimer. The effects of conjugation on calibration parameters are best demonstrated by comparison of the viscosity-sensitivity of P_2C_2NMeI with the less-conjugated version of the dimer, P_2NMeI.

iii. *H-bonding* – We have discussed that the presence of H-bonding in solvents can increase both the micro and macroviscosity, though the capacity for H-bonding with the porphyrin dimer itself can have strong consequences for determining the sensitivities to viscosity in these solvents. For instance, a cumulative effect may be observed in these dimers when the frictional barrier to rotation is increased by sterically significant H-bonds. However, we predict this effect to be minimal compared with points i and ii, listed above since the dimers under consideration in this project are not expected to participate in strong specific hydrogen bonds with the solvent..

iv. *Polarity/charge:* All charged dimers, with the exception of P_2Suc have counterions, to maintain electric neutrality. The pK_a of succinamide, at 9.62[30], is such that it is not expected to deprotonate at a neutral (or cellular) pH. All five dimers presented are highly polar, with the aim of being soluble in aqueous biological environments. For the purposes of building a viscosity calibration curve, this makes them soluble in methanol and glycerol mixtures. We have seen that the solvation shell of the dimers can exert some influence over the energies of the S_1 states in either conformation (Figure 3.12), and therefore the changing composition of solutions made to be viscous (increasing glycerol content) may affect the behaviour of these dimers. Please note, data presented in Figure 2.14, viscosity calibration curves of five porphyrin dimers, have limited viscosity ranges measured for P_2 and P_2Suc, due to the limited solubility of these dimers in methanol/glycerol mixtures. Polarity and solubility are intrinsically related, as we have described in the section above. Balaz et al., 2008 (ESI) report the high pressure liquid chromatography (HPLC) retention

times under acidic conditions (1% aqueous acetic acid, tetrahydrofuran (THF), 60:40 v/v%)[13] as a means of describing the solubility of the dimers in polar solvents. Increasing retention times are taken as a measure of decreasing polarity. The retention times of the dimers increase in the order $P_2NMeI < P_2NMe_3 < P_2C_2NMeI < P_2Suc$. P_2 was insoluble in the elution mixture.[13]

Excitation spectra measured at the peak of the twisted emission, in each dimer, reveal the excitation maximum for the twisted confomer in each of these dimers (as shown in Figure 3.13; a) λ_{ex} = 448 nm for P_2; b) 462 nm for P_2C_2NMeI; c) 458 nm for P_2Suc; d) 452 nm for P_2NMeI).

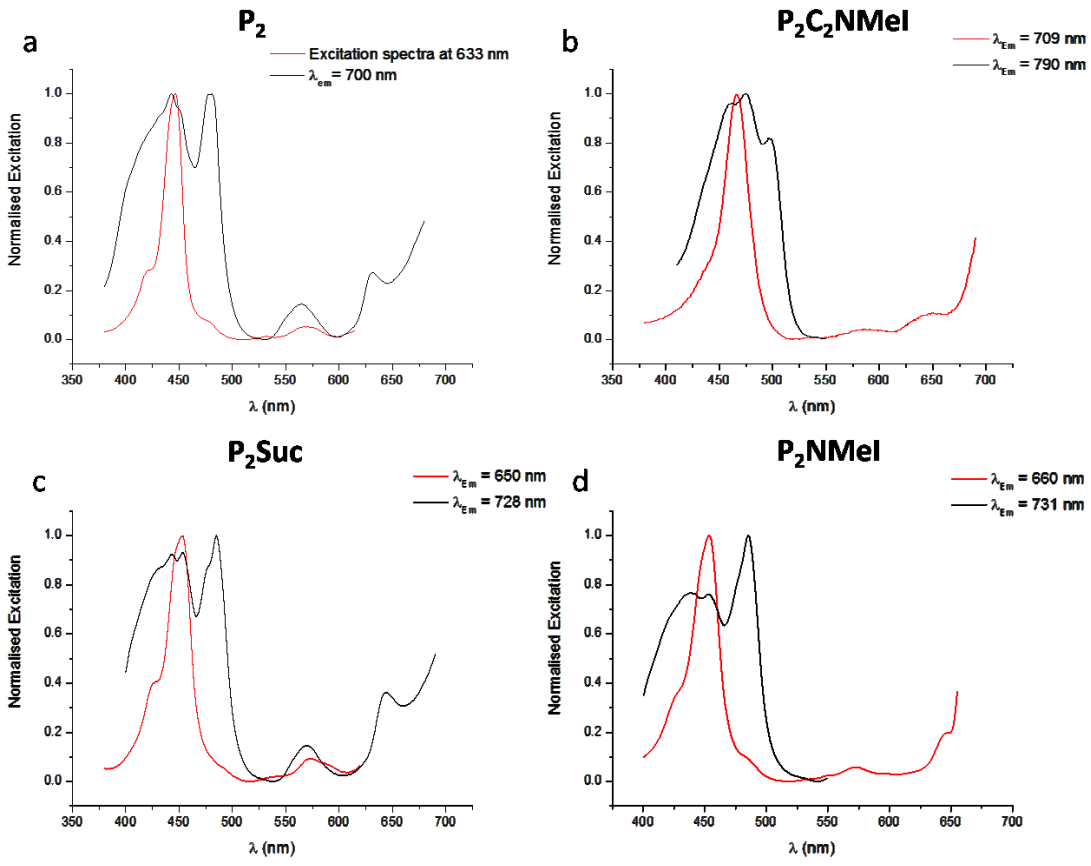

Figure 3.13: Excitation spectra of the various dimers at the twisted and planar emission peaks as indicated in the insert to each Figure. This data reveals the choice of excitation wavelength for the dimer calibration: a) λ_{ex} = 448 nm for P_2; b) 462 nm for P_2C_2NMeI; c) 458 nm for P_2Suc; d) 452 nm for P_2NMeI.

Viscosity calibrations are carried out by excitation of the dimer at these twisted conformation excitation maxima, for true comparison between emission ratios. The concentrations of all solutions were kept such that Absorbance is equal to 0.1 AU, and emission spectra are collected up to maximum intensities of $1x10^6$ CPS.

Figure 3.14 compares viscosity and ratiometric measurement calibrations between the series of dimers in mixtures of glycerol and methanol; good evidence that emission ratio between the twisted and planar peaks increase with increasing macroviscosity (Figure 3.14). These experiments are carried out in solutions of increasing glycerol content in methanol (10-100 w/w%) without alteration of temperature. Thus all experiments are measuring temperature-independent viscosity change.

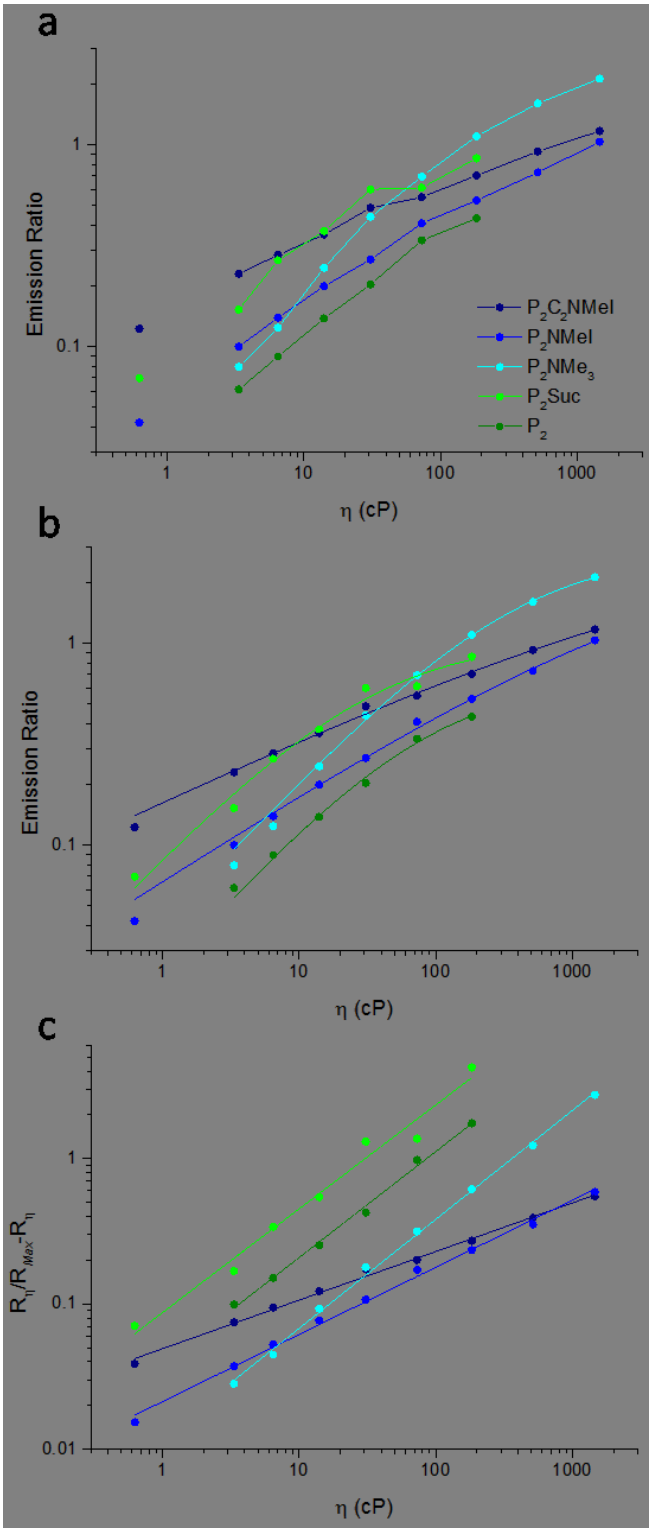

Figure 3.14: a) Trend in dimer emission ratio against viscosity of methanol and glycerol mixtures (10-100 w/w %) at 293 K; for the dimers P_2C_2NMeI (dark blue), P_2NMeI (blue), P_2NMe_3 (cyan), P_2Suc (light green), P_2 (green) b) Calibration plots of dimer emission ratio against viscosity fitted to Hill functions (as in equation 3.3). Fitted parameters for P_2C_2NMeI emission ratio: V_{Max} = 3.30, k = 9422.64, n = 0.32 with R^2 = 0.99; P_2NMeI: V_{Max} = 2.80, k = 5087.30, n = 0.44 with R^2 = 0.99; P_2NMe_3: V_{Max} = 2.90, k = 368.76, n = 0.72 with R^2 = 1.00; P_2Suc: V_{Max} = 1.06, k = 31.00, n = 0.72 with R^2 = 0.96; P_2 = V_{Max} = 0.68, k = 83.41, n = 0.75 with R^2 = 0.9. c) Saturation-adjusted twisted/ planar emission ratios vs. viscosity using the excitation wavelengths chosen in Figure 3.13.

The Förster-Hoffmann linear regions appear to be present in all dimers, extending to approximately 100cP, as predicted by initial experiments with P_2NMe_3. In Figure 3.14b, the data is fit with a Hill function, in order to predict the maximum ratio achievable by the dimer. The Hill function has following equation:

$$log_{10}Emission\ Ratio = V_{Max}\frac{\eta^n}{k^n+\eta^n} \quad (3.3)$$

Fitted parameters are summarized in the legend of Figure 3.14. Hill functions fit to this data have predicted the maximum achievable ratios for each dimer. This is intrinsically related to the viscosity sensitivity, a function of the E_a of rotation, for each dimer. For all dimers, the linear relationship between log_{10} emission ratio vs. log_{10} viscosity curves is limited as we first noted in Figure 3.9 (Figure 3.14). However slopes of the linear region can be estimated by least-squares regression and are summarised in Table 3.3, along with the fitted parameter for the maximum emission ratio, (V_{Max}, in the above equation). The important parameters that affect viscosity sensitivity are (i) the dynamic range i.e. the maximum vs. the minimum emission ratio and (ii) the slope. The former determines the accuracy in the measurements (the larger the dynamic range the smaller changes in viscosity can be resolved) and the latter determines the sensitivity of the dimer to viscosity (unit of ratio per unit change in cP).

From this, we determine that P_2C_2NMeI and P_2NMeI have the smallest slope, i.e. the lowest sensitivity to viscosity change. This should be compared with our predictions above that a highly conjugated dimer would have a strong entropic gain from planarity (i.e. lower sensitivity to viscosity). In practice, it appears that higher conjugation or a larger size of P_2C_2NMeI relative to P_2NMeI does not play a role, or at least the two effects negate one another, resulting in similar slopes for the two, which are much smaller than the slopes for other dimers.

A possible factor that may contribute to the spectra is aggregation. We believe that aggregates of the porphyrin dimer are still fluorescent, but aggregation induces a planarising effect, such that the relative proportion of the planar confomer is increased, reducing the overall emission ratio.

The spectral effects of aggregation are discussed in further detail in subsequent sections. HPLC retention times of the two smaller cationic dimers are roughly similar (6.2 and 6.8 minutes for P_2NMeI and P_2NMe_3, respectively[13]) from which we conclude that they are both similarly polar and soluble in methanol/glycerol mixtures. A comparison of slopes between them shows that P_2NMe_3 has a much higher slope in methanol/glycerol mixtures in this range of viscosity. Considering the similarity in size, and polarity, we suggest that P_2NMeI has a smaller slope than P_2NMe_3 due to the different overlap of twisted and planar excited state level due to structural differences. Such differences cannot be currently predicted within our model of porphyrin dimer behaviour, however, are very important in determining the spectroscopic behaviour.

As we mentioned before, these experiments were carried out in solutions of methanol and glycerol at a uniform controlled temperature. Thus in Figure 3.14 the ratios are plotted against η rather than η/T. Figure 3.14c shows the ratio plot adjusted for the saturation of emission at higher viscosity and appears linear as shown before, Figure 3.10. This plot shows that P_2Suc and P_2 both show an impressive sensitivity to viscosity of methanol and glycerol at a limited range, though the data has a larger source of error. The slopes of these dimers are similar to that observed in the most sensitive dimer, P_2NMe_3. However, experiments have shown that spectral quality of P_2 emission is compromised by aggregation at high glycerol content (i.e. high viscosity). The anionic dimer appears to have a maximum ratio of 1.06, much less than that of similarly sized cationic dimers in methanol/glycerol solutions. Balaz et al., 2009 observed the anionic dimer to be less hydrophilic than the cationic variants, even more so than the long conjugated dimer, P_2C_2NMeI [13]. The poor quality of the linear regression is likely due to a loss of signal quality in solutions of increasing glycerol content, where aggregates may be less fluorescent than planar aggregates of the P_2C_2NMeI dimer.

Table 3.3: Hill function fitting parameters from least squares regression analysis of emission ratios from five *meso* substituated porphyrin dimers

	Max Ratio (V_{Max})	Slope	Intercept	Dynamic Range (Max – Min Emission Ratio)
P_2C_2NMeI	3.30	0.33	-0.131	1.04
P_2NMeI	2.79	0.46	-1.67	0.99
P_2NMe_3	2.90	0.75	-1.92	2.08
P_2Suc	1.06	0.71	-1.06	0.79
P_2	0.68	0.73	-1.41	0.40

From this data, we conclude that the cationic dimers are the best for viscosity measurement in hydrophilic environments. Effects of solubility are more fundamental to maintenance of the ratiometric viscosity calibration than increases in conjugation, as is demonstrated by the calibration curve of the P_2C_2NMeI dimer. P_2NMe_3 has proven to be the superior probe for viscosity and has demonstrated good solubility under our chosen calibration conditions. We keep these observations in mind upon application of the porphyrin dimer to biomimetic lipid membranes. The cationic dimers have a higher likelihood of associating with the phosphate groups of phospholipids, ruling out the efficacy of the anionic dimer P_2Suc. Chapter V provides a comparison of the electrostatic interactions between the three cationic dimers and the phospholipid membrane.

Solubility is one physical parameter that precludes easy interpretation of the data and comparison between substituated porphyrin dimers. As can be seen from Figure 3.14, for all dimers, a good linear calibration is observed between 5-100 cP excluding that for the unsubstituated dimer P_2 which has extremely low emission ratios and a non-linear relationship at higher viscosities. Due to its insolubility in solutions of methanol and glycerol, we dissolved

the neutral dimer, P_2 in a hydrophobic solvent that can provide a significant viscosity range by altering temperature. We chose to use Castor oil, a high viscosity solvent with strong temperature-dependent viscous behaviour that has solvent molecules that mimic our target environment, the lipid bilayer. The data for P_2 in this hydrophobic and viscous environment complements the set of data obtained for charged dimers in solutions of glycerol and methanol.

3.3 Viscosity of hydrophobic environments

3.3.1 P_2 viscosity-sensitive emission in Castor oil

Castor oil is a mixture of multiple unsaturated fatty acids (87-91% ricinoleic acid, 4-5 % oleic acid, 4-5% linoleic acid and others)[31] all with chain lengths of 18-carbons. Castor oil dissolves the neutrally charged dimer, P_2, which we showed previously does not dissolve completely in solutions with high glycerol content. This is reflected in the complete loss of colour of viscous solutions of P_2, visible precipitation of P_2 and the complete loss of fluorescence intensity beyond 200 cP (Figure 3.14). Mechanical rheometry reveals that stepwise variation in the temperature of a solution of Castor oil yields a temperature-dependent viscosity curve similar in shape to that for methanol/glycerol mixtures. Thus we predict that the measurement of the P_2 porphyrin dimer emission in Castor oil will reveal similar temperature-dependent microviscosity as we observed in methanol/glycerol solutions for the soluble charged dimers.

Nevertheless, there are important discrepancies between the conditions of these two experiments, the uncharged dimer in a non-polar solvent and the charged dimer in a mixture of polar solvents. Firstly, it is likely that the internal order of the solvent will be different, as Castor oil does not participate in hydrogen bonding, which is a major contributor of solvent friction, contributing to the Stokes-Einstein hydrodynamic friction coefficient, which affects rotational diffusion of probes. On the other hand, the average size of the fatty acid components of Castor oil relative to that of the porphyrin dimer is much larger than that of methanol and glycerol molecules. Contrary to expectation, theory suggests that large volume solvent molecules exert less steric hindrance against rotational diffusion. The increase solvent molecular volume similarly increases the free volume surrounding them during collisional motion – as in a

uniform population of large molecules; none are small enough to fill gaps between them. This is reflected in Gierer and Wirtz' 1953 model of microscopic viscosity where one of two frictional components is inversely dependent upon the ratio of solvent/solute volume[32]. However, the long chain nature of the component fatty acid chains in Castor oil can induce a high degree of entanglement, creating a steric boundary to diffusion. This is most likely the dominant physical cause of high macroviscosity in Castor oil, and so serves as a good model for the hydrocarbon region of lipid bilayers. P_2 emission in Castor oil under a range of temperatures thus serves as the best possible calibration curve for interpretation of microviscosity of this same dimer dissolved in the hydrocarbon region of lipid bilayers.

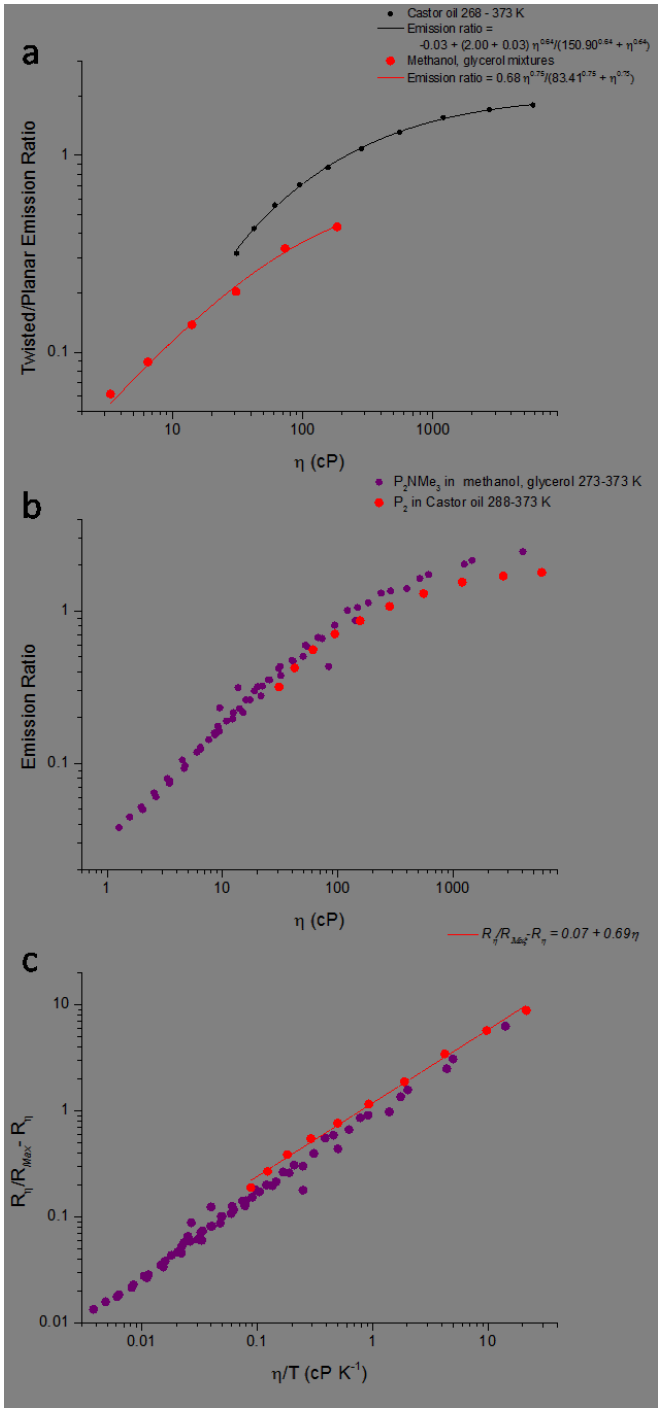

Figure 3.15: a) P_2 emission ratios ($I(\lambda_{629})/ I(\lambda_{689})$) versus mechanical viscosity measurements in Castor oil (black) at from 268-373 K and methanol, glycerol mixtures (red) at 273-373 K . Data is fit by a Hill function with equation $Emission\,ratio = -0.03 + (2.00 + 0.03)\frac{\eta^{0.64}}{150.90^{0.64}+\eta^{0.64}}$ *and* $Emission\,ratio = 0.68\,\frac{\eta^{0.75}}{83.41^{0.75}+\eta^{0.75}}$ *respectively (standard errors listed in text). b) Emission ratios of P_2NMe_3 in glycerol and methanol solutions between 273- 373 K (purple) and P_2 in Castor oil from between 273-373 K (red) against mechanical rheometry measurements. c) Temperature independent viscosity calibration curves of the viscosity sensitive emission ratio (R_η) as a fraction of the maximum (R_{max}) such that R_η/R_{ma}- R_η is plotted against η/T for P_2 in Castor oil, with P_2NMe_3 in glycerol/methanol solutions overlayed. Castor oil data is fit with the equation R_η/R_{Max}-R_η = 0.07 + 0.69η.*

A calibration curve of the P_2 emission ratio and a mechanical viscosity measurement is shown in Figure 2.15a. As we mentioned previously, the Förster-Hoffmann linear relationship is limited to a viscosity range where the E_η of solvent diffusion is less than the E_a of rotation from the twisted to the planar confomer. Nonetheless, we observe a predictable relationship between emission ratio and solution viscosity up to the value 5850 cP, as shown in Figure 3.15a. The temperature-scan of Castor oil between 373 and 273 K is yields a range of viscosities from 31 to 5850 cP, higher than that probed by temperature scans of glycerol/methanol solutions from 1 to 1450 cP, though the calibration curve shows good agreement with data collected in Castor oil at the higher viscosity range. We observe a non-linear relationship between the ratio and viscosity in Castor oil, familiar in shape from the high-viscosity region of the methanol/glycerol viscosity calibration curve shown in Figure 3.14. As expected, emission ratios in methanol, glycerol and in Castor oil are not perfectly aligned in slope, we attribute this to partial aggregation of P_2 in methanol/glycerol, increasing the error in emission ratios at high viscosities in methanol/glycerol data. We fit the data with a Hill function of the following equation:

$$Emission\ Ratio = a + (b - a)\frac{\eta^n}{k^n + \eta^n} \tag{3.4}$$

Where in Castor oil: a =-0.03; b=2.00; k=150.90; n=0.64 with standard errors 0.16, 0.06, 27.26, and 0.07 respectively, and R^2 = 0.99, in methanol, glycerol mixtures are fit by a Hill function with equation 3.3 where V_{Max} =0.68; k=83.41; n=0.75 with standard errors 0, 44.97, and 0.10 respectively, and R^2 = 0.99. The justification for the use of the Hill equation was recently reported by our group[33].

Absorption spectra of the dimers P_2NMe_3 and P_2 show a very close overlap[17] , meaning that the proportion of twisted and planar confomers being excited are roughly equivalent. Thus, we have compared the viscosity sensitivity of the P_2NMe_3 dimer in glycerol, methanol mixtures and the P_2 dimer in Castor oil, Figure 3.15b. When plotted according to the Förster-Hoffmann variables on a double log plot, the curves appear to coincide well. That is, a high degree of overlap is observed between emission ratios of the two dimers (P_2NMe_3 and P_2) at the same viscosities, as

measured by mechanical apparatus. Nevertheless, we observe the same decrease in sensitivity to temperature-induced viscosity increase as observed using the P_2NMe_3 dimer in glycerol/methanol mixtures, that is, above approx 100 cP the emission ratio reaches a maximum value. This data is good evidence that various porphyrin dimers with varying size and charge have highly compatible behaviour in predicting mechanical viscosity measurements by conformational emission ratio. There is a small vertical shift downward in emission ratio relative to mechanical viscosity for the uncharged P_2 dimer compared with P_2NMe_3. The overlap between the two curves coincides best at lower viscosities in the range measured (i.e. 30 – 100 cP) compared with the higher viscosity range (280 – 5850 cP) where they appear to "saturate" at different maximum values. We attribute this to a decreased E_a of rotation in the P_2 dimer relative to P_2NMe_3, due to a decrease in conjugation by the lack of *meso* substituents. In this case, E_a (P_2NMe_3) > E_a (P_2), such that rotation of P_2NMe_3 remains sensitive to E_η of the solvent at higher viscosities than rotation of P_2.

Furthermore, from the comparison of data in these two solvents, we infer that the porphyrin dimer can reflect temperature-dependent viscosity changes in solutions with greatly varying internal structure. Hydrogen bonding of the polar solvents and the large solvent size of Castor oil do not significantly alter the relationship between the observed microviscosity in relation to measured macroviscosity of the solvents. Again, we observe the likely mixture of both effects of Stokes diffusion (which is temperature dependent) and free-volume diffusion, as proposed by Gierer and Witrz, 1953[34], though it is impossible to determine the relative contribution of either the effects from this data.

Normalization of the emission ratios (R_0/R_{Max}-R_0), as in Figure 3.15c shows that the relationship with temperature-independent viscosity in Castor oil is linear as predicted by the Förster-Hoffmann theory. Normalization of the emission ratios allows us to compare the behaviour of the two dimers, each with their own maximum emission ratio. We fit the linear relationship between the normalized ratio and temperature independent viscosity with the equation

R_0/R_{Max}-R_0 = 0.07 + 0.69η, with standard errors 0.011 and 0.015, respectively and R^2 = 0.996 (Figure 3.15a).

Thus we have shown that two porphyrin dimers, with entirely different electrostatic properties, and varying degrees of conjugation, are both sensitive to temperature-dependent and independent viscosity in the manner predicted by Förster and Hoffmann. Furthermore, we have established that the porphyrin dimer is well suited to relating the micro and macroviscosity of non-polar solvents, as well as those composed of large macromolecules, such as the hydrocarbon region of the lipid bilayer. The P_2 dimer is a good candidate for measurement of the hydrocarbon tails in biomimetic lipid membranes, and we explore this application further in Chapter V.

3.4 Sources of Error in Calibration curves

Given we are planning to use the calibration curves such as Figure 3.9 for quantification of viscosity in unknown media it is important to discuss the errors associated with these measurements. Also, we have fit viscosity calibration data with three different empirical relationships. The application of these diverse functions and their relevance to the mechanism of viscosity sensitivity are discussed in this section. Errors in viscosity calibration will fall in two categories: (i) instrumental errors and (ii) sample errors. We will discuss each in turn.

3.4.1 Instrumental Errors

Our ratiometric methodology is dependent upon the relative intensities of spectra at different wavelengths. Thus, the quality of the signal and the sensitivity to a change in relative ratio are both crucial aspects of the validity of our measurement. As measured by the steady state fluorometer, accuracy is optimal when emission intensity gives a linear response to detection, i.e. has an uncorrected emission intensity of less than 10^6 CPS. At this value, errors are less than 1%, as stated by the manufacturer's recommendation (HORIBA) [35]. Likewise, the instrumental errors of mechanical viscosity measurements are defined by the rheometer manufacturer to be 0.1% (Anton Paaar) [26]. Furthermore, the wavelength dependence of sensitivity in detection has been offset by the inclusion of a correction function. The nature of the correction function is

specified in Chapter II, Methodology, and is further discussed in Chapter V. Nonetheless, because the ratiometric method is relative, calibration curves produced with consistent application or consistent exclusion of the correction function are comparable for the purposes of building of a calibration curve. As could be seen, these low instrumental errors cannot account for the experimental spread of data observed in this work, e.g. Figure 3.9. Errors of detector sensitivity are most likely limited to increasing the noise in calibration curves.

3.4.2 Sample errors

Due to the nature of viscosity measurements, we must have strict control of the physical variables used to create solutions of varying viscosity. Such errors will occur due to two reasons: (i) imperfect sample preparation and (ii) imperfect temperature control. Mistakes in either of these items will result in large variations of solution viscosity and hence imperfect calibration curve. We have therefore performed the following steps in order to minimize the user errors and thus reduce the uncertainty in the calibration data.

(i) Sample preparation

It is first important to note that the concentration of the dimer in the sample is not expected to affect the readout value, due to the ratiometric nature of the measurements, which is concentration independent. As mentioned previously, dimer concentrations are kept purposefully low (Absorbance = 0.1 AU, Emission ≤ 10^6 CPS) at between 0.4 and 0.3 μM depending on the molar absorption coefficient, ε, of the dimer. Thus, small variations in dye concentration between samples are not considered a source of error affecting calibration curves.

However, the precise compositions of mixtures of glycerol and methanol are of crucial importance in determining the viscosity of these solutions. We minimized this possible error by producing large batches of methanol, glycerol mixtures and using the same solutions for mechanical rheometry as were used in fluorometry. Thus, any unavoidable errors of compositional accuracy are consistent over two measurements. Nonetheless, we developed a

protocol (detailed in the Chapter II, Methodology) in order to control compositional accuracy based on weight/weight measurements of both solvents rather than the volume (which is more challenging to measure accurately for viscous glycerol). The variable density of glycerol creates inconsistencies in volumetric measurements, so that we used the temperature-independent mass of both glycerol and methanol to compose solutions. Furthermore, glycerol can be difficult to mix, particularly at room temperature in large volumes, so all mixtures were sonicated prior to and subsequent to the addition of the dye, removing any striations of glycerol and homogenizing the solution. For this reason, we can be confident that differences between solubility of the dimer in glycerol are not due to differences in mixing between samples. Furthermore, all solutions were stored at 4 °C (377 K) to prevent evaporation of methanol.

(ii) Temperature control

We noticed early on that small variations in the laboratory temperature (e.g. 1-2 °C due to the warming up of the fluorometer) can significantly alter the readout of the ratiometric measurement, due to the strong dependence of viscosity on temperature. Therefore for all experiments reported here we have utilized a Peltier device for temperature control within the fluorometer, and a compatible one installed inside the rheometer. Temperature is controlled within a range of ± 0.5 °C on the fluorometer, though the manufacturers estimating temperature stability as 0.001 °C over the course of one hour[27]. Equilibrium times were tested prior to experiments being carried out, and determined to be approx. 9 minutes for pure glycerol, which was then used for all methanol/glycerol mixtures.

Temperature control within the Stabinger 3000 rheometer is equally crucial to reproducing the same temperature-dependent viscosity within both instruments. Anton Paar have estimated the temperature stability of the sample chamber to be 0.005 °C [26].

Thus, the magnitude of errors in temperature control and stability are estimated to be minimal in comparison to the ratiometric viscosity dependence we have observed in our experiments. Ultimately, we propose that the major source of experimental errors originates from sample

preparation. With this in mind, we have determined the aforementioned protocol for minimization of errors in solution preparation and have taken precaution to use the same solution for both measurements, eliminating differences between them.

3.4.3 Empirical models used to fit calibration data

We have used three different models to fit viscosity calibration data shown in this Chapter (equations 3.1, 3.3, 3.4). Fits were found by the iterative least squares Levenberg-Marquardt algorithm. Equation 3.1, a three-parameter log function, is fit to the behaviour of P_2NMe_3 in methanol/glycerol solutions at different temperatures, with good agreement (R^2 = 0.99). The log function is a good predictor of Forster-Hoffmann predicted linearity at low viscosities and can also model the 'saturation' of viscosity sensitivity at larger viscosity values.

The calibration curves of five distinct dimers are all fit by Hill functions, again found by the Levenberg-Marquardt algorithm for reduction of the sum of squares. The use of this model was previously rationalized by our group[33] and predicts the data with a high degree of accuracy (R^2 = 0.99-0.96) The Hill function allows the particularly useful measurement of V_{Max}, a value we took to represent the maximum twisted/planar ratio, where we see 'saturation' of the conformational change. The value of V_{Max} is used to calculate normalized linear regressions by plotting the observed emission ratio as a fraction of its maximum, and is used as a good means of comparing different calibration curves, of different ranges.

3.5 Confounding variables

The previous sections focused on production of a calibration curve that establishes the effect of viscosity on torsional relaxation of the porphyrin dimer about its butadiyne bond. The energy difference between the two conformations is shown to be independent of temperature, outside of its effects on solvent viscosity. We have briefly summarized the features of a solvent that contribute towards friction during flow, i.e. towards the viscosity of the solvent. In light of what we know to be true about the dependence of the calibration slope upon the λ_{ex}, we are concerned with any variables that affect the shape of spectra or have the ability to shift spectra, such as a generalized polarity effect, known to affect polar chromophores. A polarity effect, or

solvent effect is the subject of the following section as part of a discussion of variables that can affect the relationship between solvent viscosity and porphyrin dimer rotation.

3.5.1 Specific solvent effect

Previously, we have mentioned the specific chemical interactions that engender viscosity change in solvents, for instance, hydrogen bonding may contribute towards the barrier against solvent motion. However, we have not found any evidence of a specific solvent effect impacting the photophysical behaviour of the dimer by any other means, such as, for instance, losing the chelation of the Zn^{2+} metal centre of the porphyrin macrocycle.

Here we investigate the effect of solvent polarity on the spectra of the dimers. Figure 3.16 shows the absorption (3.16a) and emission (3.16b) spectra of the most polar dimer, P_2NMeI in a range of different solvents. Absorption spectra show spectral changes, namely in the shape of the absorption peak suggesting that aggregation can also play a strong role in the photophysical characteristics of the dimer in solution. We also observe a shift in emission maximum in apparent correlation with increasing polarity of solvent. This is subject to systematic investigation in the next section. Furthermore, there are clear signs of aggregation in some non-polar solvents such as trichloroethane (TCE) and toluene, as well as in water. –

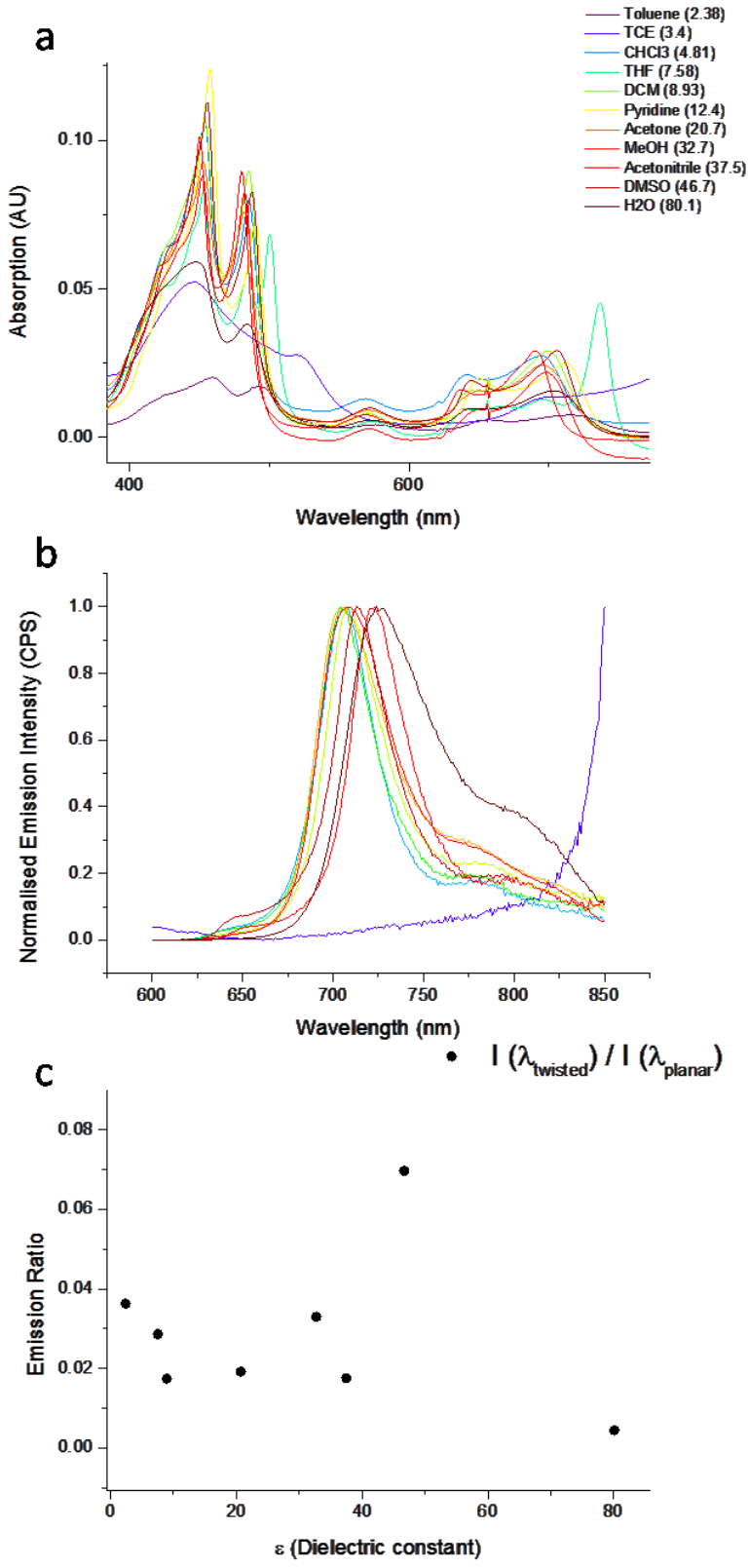

Figure 3.16: a) Absorption and b) Emission spectra of P_2NMeI (0.33 uM from DMSO stock, 0.001%) recorded in solvents of varying polarity (ε on graph). Emission spectra are excited at the maximum of the high energy twisted excitation band for each dimer, Figure 3.13.

We carried out a preliminary investigation of the effects of these solvents on the measured emission ratio as the pure solvents have a very small range of viscosities (0.6 – 2 cP). We found no correlation between the observed emission ratio (at the corresponding emission wavelengths, adjusted for shift) and the dielectric constant of the solvents. One outlying data point with a higher emission ratio than the others represents dimethylsulfoxide (DMSO), which has a higher viscosity than the other solvents, at 2 cP, thus confirming our observation that the emission ratio is sensitive to viscosity above any specific solvent effect. However, analysis of this data requires flexibility in defining λ_{em} maxima for either confomer. In order to rationalize this solvatochromic effect, we investigated the general solvent effect as described below.

3.5.2 Polarity sensitivity

We have recorded the absorption and emission spectra of the dimers as a function of solvent polarity to ascertain the presence of this affect on porphyrin dimers' properties (Figure 3.16). We note that in some solvents (toluene, trichloroacetic acid, tetrahydrofuran) it is difficult to isolate twisted and planar excitation bands. However, we find that we cannot distinguish between spectral effects being the signs of aggregation or those due to solvatochromism. For this reason, systematic change of solvent dielectric constant was generated by preparing stepwise mixtures of methanol and chloroform which have similar viscosities at room temperature (0.60-0.59 cP, respectively) yet vastly different dielectric constants (ε = 32.7, 4.8 respectively) though both are good solvents for the P_2NMeI dimer with no evidence for aggregation. Figure 3.17 summarises the results.

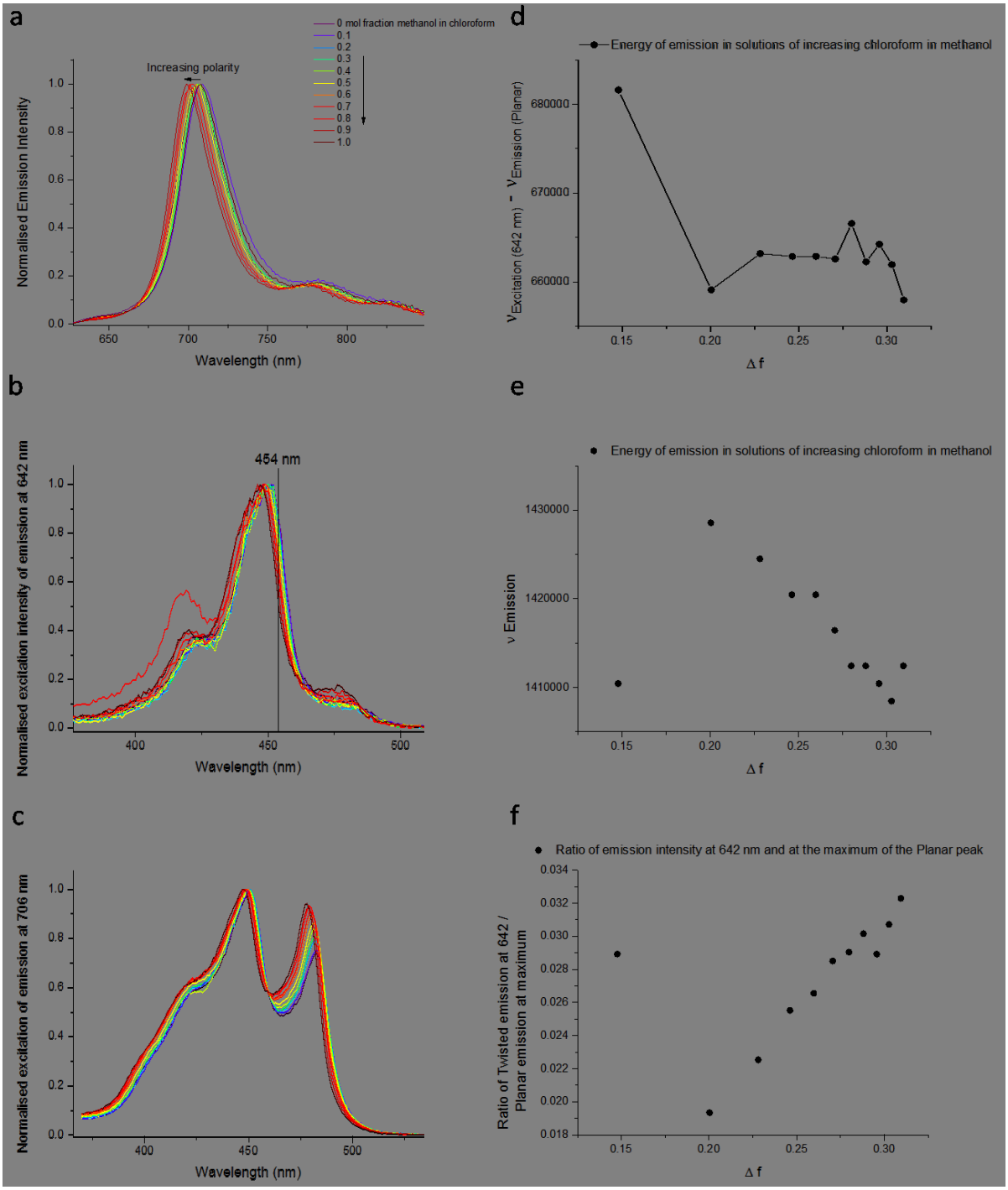

Figure 3.17: P_2NMe_3 in solutions of increasing combinations of v/v % methanol and chloroform. a) Emission spectra λ_{ex} = 452 nm; b) 'twisted' (variable between 695 and 710 nm) Excitation spectra monitoring emission at 639 nm; c) 'planar' excitation spectra monitoring emission at 710 nm; d) Lippert plot of the data from a-c; e) emission energy vs Δf; f) twisted: planar emission ratio vs Δf

Emission spectra are shown in Figure 3.17a that confirm the solvatochromic shift observed in Figure 3.16 where decreasing polarity was associated with blue-shifted spectra. Excitation

spectra of both the twisted (Figure 3.17b) and planar (3.17c) conformations are shown, both of which appear to shift slightly to the blue with increasing solvent dielectric constant.

The solvent polarity can affect the spectra of fluorescent molecules, primarily those with charge- transfer states, by stabilising the polar excited state and causing shifts in emission and absorption spectra. This behavior is termed solvatochromism. The dipole moment of any solute exerts an ordering effect upon the group of solvent molecules in close proximity, termed its 'solvent shell'. Dipole moments of the solvent molecules in the shell become aligned with those of solutes in order to minimize the energy of solvation. We summarized in Chapter I that the Franck-Condon state is the short lived ($x10^{-12}$) excited state, where a new magnetic dipole is produced by the localized displacement of a single electron. Redistribution of the electron density in the chromophore causes solvent molecules to rotate such that their dipole moments are in alignment with the new dipole of the excited chromophore. The reorganization of solvent molecules lowers the overall energy of the excited state, and so the $S_0 \rightarrow S_1$ bandgap. As such, spectral emission maxima undergo shifts according to the degree of stabilization provided by the solvent shell. In bulk, this is the solvent polarity and sensitivity to it is observed as changes in the Stokes shift ($\nu_{ex} - \nu_{em,}$ in frequency units). In general, this refers to the effect of positive solvatochromism, an increase in the Stokes shift with increasing solvents polarity. The opposite, negative solvatochromism, is associated with an increase in excited state energy during solvation.

The process of solvent shell reorientation is termed 'solvent relaxation', occurs at a timescale of roughly 10^{-10} s in non-viscous solvents. Viscous solvents can take longer for full solvent relaxation to be observed, due to the frictional barrier against rotation, such that the rate of solvent orientation is close to the lifetime of the excited state ($x10^{-9}$ s)[36]. In this case, time resolved measurements can show the effects of these competing processes[36], however our steady state experiments are not able to resolve whether solvent reorientation is time-

dependent or not in viscous solvents, another advantage of using a combination of methanol and chloroform, both at low viscosity.

Figures 3.17d-e summarize the data by plotting the emission gap, the emission maxima, and the emission band ratio against Δf, the orientation polarizability of the solvents to generate a Lippert plot. The orientation polarizability is a value that describes the capacity of a solvent to reorient around a magnetic dipole, it is composed of two terms: a high and a low frequency component of polarization. The high frequency component is a function of the refractive index of the solvent, *n*, describing the reorganization of electrons in solvent molecules that compose the solvent shell, this is instantaneous. The low frequency component is dependent on the dielectric constant, ε, of the solvent, representing the rotational orientation of the solvent into alignment with the magnetic dipole of the chromophore, this process occurs at longer timescales, (10^{-10} s). The difference between them is the value Δf, the orientation polarizability and is correlated with the Stokes shift in the case of solvatochromism.

$$\Delta f = \frac{\varepsilon - 1}{2\varepsilon + 1} - \frac{n^2 - 1}{2n^2 + 1} \tag{3.5}$$

This plot, Figure 3.17d, for the cationic dimer P_2NMe_3, shows no trend between Δf and Stokes shift, with the exception of the Stokes shift in pure methanol. We investigated the dependence of excited state conformational ratio upon Δf and found that though there was an apparent increase in twisted: planar ratio with increasing Δf, or decreasing polarity, this change was relatively small when compared with the magnitude of absolute ratio changes that we have observed in a large range of viscosities of methanol/glycerol mixtures, e.g. Figure 3.9. The magnitude of the trend relating Δf against η suggests that it could be due to a small shift in excitation maximum of the twisted confomer, which we have shown can affect emission ratios, the systematic nature of the change in solution polarity would reflect this change. Figure 3.17b shows evidence of a slight shift in the twisted emission spectrum. In conclusion, solvent polarity seems to have an effect on the emissive behaviour of the dimer which cannot be fully

rationalized, however in most cases the effect is minor. We can also confirm that the twisted/planar ratio is independent of polarity at least at low viscosity. One outlying data point shows the collapse of the relationship, at an extremely low value of Δf, giving an extremely low emission ratio and significantly high Stokes shift (Figure 3.17d,f). This outlier is an exception to the observed trend of negative solvatochromism. The biggest variable appears to be the excitation ratio of twisted versus planar confomer that is excited by the chosen excitation wavelength and the resulting uncertainty in calibration is caused by band shifts in solvent.

We conclude the cationic porphyrin dimers P_2NMeI and P_2NMe_3, display negative solvatochromism in solutions of methanol and chloroform. However, this effect need not alter the viscosity sensitivity of the porphyrin dimer nor the quality of spectra. Calibration curves can be applied as long as the twisted dimer is excited near its maximum, such that emission ratios are comparable amongst each other. Further research is needed to illuminate the solvatochromic effect as a function of solution viscosity, whether or not the reorientation of solvent dipoles is viscosity dependent will affect the emission maxima of both confomers.

Throughout this chapter, we have noted instances of low solubility of the dimers and the effects of solubility upon the quality of calibration data and the effect on the viscosity sensitivity. Below we summarize some of the spectral signs of aggregation.

3.5.3 Aggregation and Aging

Aggregation has been described above as a major practical component that affects the validity of spectroscopic measurements. For example, the presence of aggregation is often revealed as spectral broadening, and low fluorescence intensity which complicates the measurement of emission band ratio, as is observed in Figure 3.16 for the P2NMeI dimer in solutions of TCE (blue, Figure 3.16a,b). Moreover, aggregation is a time dependent phenomena which introduces the variable of sample age as a factor that affects viscosity measurements. For example, aggregates are presumed to be forced into the planar conformation, which alters the distribution of angles in the ground state. Furthermore, fluorescence intensity decreases

markedly even if absorption spectra is relatively sharp. Figure 3.18b shows the emission spectra of P_2Suc in DMSO (red, disaggregated) and water (black, aggregated) immediately after mixing in solution.

The aggregation behaviour of an anionic dimer P_2Suc in water is summarised in Figure 3.18a. The effective extinction coefficient of the dimer decreases rapidly in the first three hours of solution preparation in water, and slowly up to 28 hours manifested by the observed broadened spectra with low intensity. Incubation at 333 K prevents aggregation over the course of the first 30 minutes in water but is irreversible once aggregation has begun.

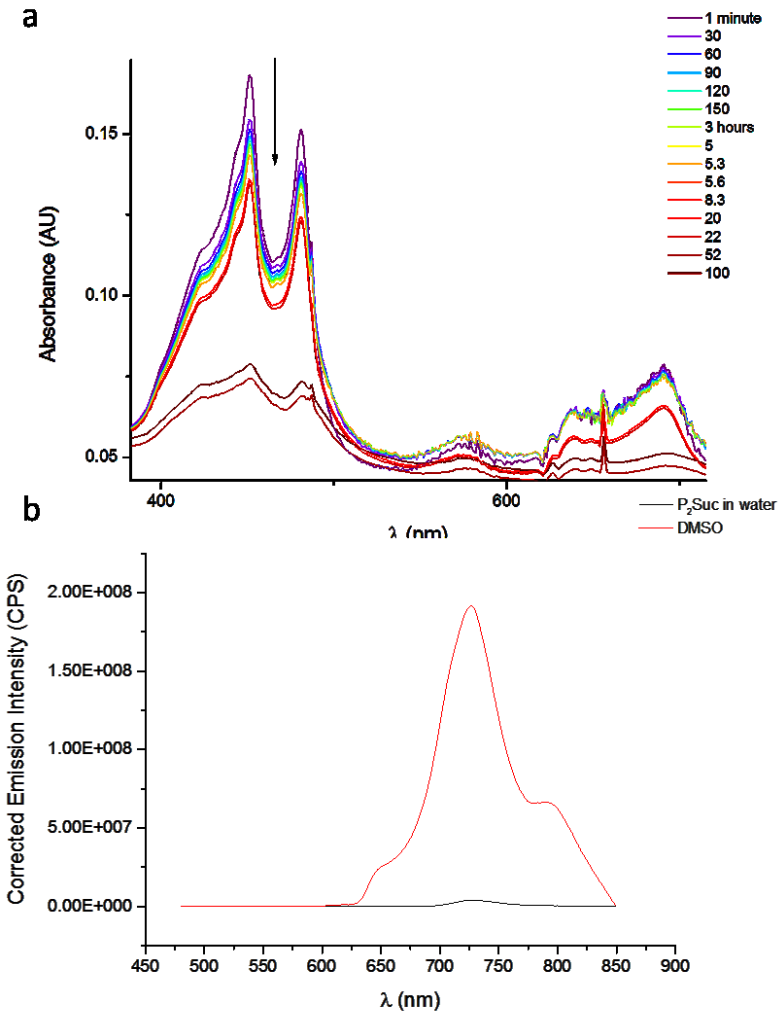

Figure 3.18: a) Absorption spectra recorded for P_2Suc in water (1 μM from DMSO stock) over time up to 100 hours incubation. b) Fluorescence spectra for P_2Suc in water (black) and DMSO (red) with λ_{ex} = 453 nm.

The important consequence of aggregation is unreliability of spectroscopic data obtained from the solution containing aggregates. This can arise due to (i) low emission intensity from aggregated solutions and (ii) forced planarization of the dimer upon aggregation leading to the exaggerated presence of a planar conformer. Thus we have established the necessity for carrying our calibration experiments in a "good" solvent for each substituated dimer.

3.6 Conclusions

Here we have investigated the series of biocompatible charged conjugated porphyrin dimers, potentially suitable for use as 'molecular rotors', fluorophores sensitive to the viscosity of their environment. We have shown that the emission from these porphyrin dimers in solution is sensitive to viscosity in the manner predicted by Förster and Hoffmann. Two conformations, a 'twisted' and 'planar' conformation have distinct spectroscopic identities. During intermolecular rotation, π conjugation between the two porphyrin macrocycles gives a strong driving force towards planarity which is in competition with solvent friction. This friction results in a restriction to rotation from 'twisted' to 'planar' conformation in viscous solvent, and the degree of restriction can be observed by the ratio of the two emission bands representing these conformations.

We have investigated the effects of variables such as temperature, solvent polarity and sample aggregation to describe the variation in sensitivities and dynamic ranges of the substituated porphyrin dimers. This shows the necessity of tailoring the use of each dimer to a specific application by the relevance and influence of these factors. For the positively charged dimers studied here it was established that they can be reliably calibrated in methanol/glycerol solutions of moderate-to-high polarity. The solution polarity itself was found to have a minor effect on the ratiometric measurement of viscosity. The positively charged dimers were classified in order of their sensitivity to viscosity, with P_2NMe_3 being the most sensitive, while P_2NMeI and P_2C_2NMeI displaying less sensitivity to a unit change in viscosity.

The uncharged dimer P_2 was shown to be poorly soluble in polar methanol/glycerol mixtures, which precluded its full calibration in this media. However, P_2 was successfully calibrated in nonpolar environment of a castor oil and was shown to have high viscosity sensitivity comparable to the sensitivity of P_2NMe_3. As a result, P_2 and P_2NMe_3represent best choice of molecular viscometers that might be useful for viscosity measurements in polar (P_2NMe_3) and non-polar (P_2) compartments of cells and model biological systems. We will test the applicability of these two dimers for viscosity measurements in model lipid membranes in Chapter V.

It is worth noting that the series of substituted porphyrin dimers described above offers a huge advantage for the purposes of cell and tissue imaging, namely in that the ratiometric method of viscosity sensing is concentration independent. Therefore, upon application of the dimer in living cells and ultimately in living tissues, the heterogeneous and highly variable uptake of dimers in cells will not influence the validity of a viscosity measurement. We have been able to show that the viscosity measurement is consistent and reliable for the large viscosity range between 1-10000 cP and for a large range of temperatures, which enables us to measure viscosity in many environments. The red shifted absorption spectra of the dimers compared to monomeric porphyrins also give the advantage of being able to be used for deep tissue penetration of light. Likewise, the application of photodynamic therapy for the production of $^1O_2$ is an important feature of these new probes, it is discussed in further detail in Chapter VI.

3.7 References

1. Anderson, H. L. Conjugated Porphyrin Ladders. Society 972–981 (1994).

2. Gouterman, M., Wagniere, G. & Snyder, L. Spectra of porphyrins Part II. Four orbital model. J. Mol. Spectrosc. 11, 108–127 (1963).

3. Winters, M. U. et al. Photophysics of a Butadiyne-Linked Porphyrin Dimer: Influence of Conformational Flexibility in the Ground and First Singlet Excited State. J. Phys. Chem. C 111, 7192–7199 (2007).

4. Anderson, H. L., Martin, S. J. & Bradley, D. D. C. Synthesis and Third-Order Nonlinear Optical Properties of a Conjugated Porphyrin Polymer. Angew. Chemie Int. Ed. English 33, 655–657 (1994).

5. Drobizhev, M. et al. Understanding strong two-photon absorption in pi-conjugated porphyrin dimers via double-resonance enhancement in a three-level model. J. Am. Chem. Soc. 126, 15352–15353 (2004).

6. Stranger, R., McGrady, J. E., Arnold, D. P., Lane, I. & Heath, G. a. Communication between Porphyrin Rings in the Butadiyne-Bridged Dimer Ni(OEP)(μ-C 4)Ni(OEP): A Density Functional Study. Inorg. Chem. 35, 7791–7797 (1996).

7. Tsuda, A., Hu, H., Watanabe, R. & Aida, T. ethynylene-bridged zinc porphyrin dimer. J. Porphyr. Phthalocyanines 388–393 (2003).

8. Tsuda, A., Hu, H., Tanaka, R. & Aida, T. Planar or Perpendicular? Conformational Preferences of π-Conjugated Metalloporphyrin Dimers and Trimers in Supramolecular Tubular Arrays. Angew. Chemie 117, 4962–4966 (2005).

9. Drobizhev, M. Photon energy upconversion in porphyrins: one-photon hot-band absorption versus two-photon absorption. Chem. Phys. Lett. 370, 690–699 (2003).

10. Screen, T. E. O. et al. Making conjugated connections to porphyrins: a comparison of alkyne, alkene, imine and azo links. J. Chem. Soc. Perkin Trans. 1 320–329 (2002). doi:10.1039/b109915a

11. Frampton, M. J. et al. Synthesis, crystal structure, and nonlinear optical behavior of beta-unsubstituted meso-meso E-vinylene-linked porphyrin dimers. Org. Lett. 7, 5365–8 (2005).

12. Atkins, P. & Paula, J. de. Atkins' Physical Chemistry. (OUP Oxford, 2010). at <https://books.google.co.uk/books/about/Atkins_Physical_Chemistry.html?id=BV6cAQAAQBAJ&pgis=1>

13. Balaz, M., Collins, H. a, Dahlstedt, E. & Anderson, H. L. Synthesis of hydrophilic conjugated porphyrin dimers for one-photon and two-photon photodynamic therapy at NIR wavelengths. Org. Biomol. Chem. 7, 874–88 (2009).

14. Dahlstedt, E. et al. One- and two-photon activated phototoxicity of conjugated porphyrin dimers with high two-photon absorption cross sections. Org. Biomol. Chem. 7, 897–904 (2009).

15. Kuimova, M. K. et al. Determination of the triplet state energies of a series of conjugated porphyrin oligomers. Photochem. Photobiol. Sci. 6, 675–82 (2007).

16. Kuimova, M. K., Yahioglu, G., Levitt, J. A. & Suhling, K. Molecular rotor measures viscosity of live cells via fluorescence lifetime imaging. J. Am. Chem. Soc. 130, 6672–3 (2008).

17. Kuimova, M. K. et al. Photophysical properties and intracellular imaging of water-soluble porphyrin dimers for two-photon excited photodynamic therapy. Org. Biomol. Chem. 7, 889–96 (2009).

18. Kuimova, M. K. et al. Imaging intracellular viscosity of a single cell during photoinduced cell death. Nat. Chem. 1, 69–73 (2009).

19. Denk, W. et al. Anatomical and functional imaging of neurons using 2-photon laser scanning microscopy. J. Neurosci. Methods 54, 151–162 (1994).

20. Denk, W. & Svoboda, K. Photon upmanship: why multiphoton imaging is more than a gimmick. Neuron 18, 351–7 (1997).

21. Arrhenius, S. Über die Dissociationswärme und den Einflusß der Temperatur auf den Dissociationsgrad der Elektrolyte. Z Phys. Chem. 4, 96–116 (1889).

22. Arrhenius, S. Über die Reaktionsgeschwindigkeit bei der Inversion von Rohrzucker durch Säuren. Z Phys. Chem. 4, 229–248 (1889).

23. Shutilin, Y. F. Use of the Williams-Landel-Ferry and Arrhenius equations in describing the relaxational properties of polymers and polymer homologues. Polym. Sci. U.S.S.R. 33, 119–127 (1991).

24. Einstein, A. Über die von der molekularkinetischen Theorie der Wärme geforderte Bewegung von in ruhenden Flüssigkeiten suspendierten Teilchen. Ann. Phys. 322, 549–560 (1905).

25. Wu, Y. et al. Molecular rheometry: direct determination of viscosity in Lo and Ld lipid phases via fluorescence lifetime imaging. Phys. Chem. Chem. Phys. 15, 14986–93 (2013).

26. Anton Paar. SVM 3000 Stabinger Viscometer - Manual. (2015). at <http://www.anton-paar.com/?eID=documentsDownload&document=1039&L=8>

27. Electronics, W. LFI-3751 with Autotune PID Thermoelectric Temperature Controller - Datasheet. (2014).

28. Förster, T. & Hoffmann, G. Die Viskositatsabhängigkeit der Fluoreszenzquantenausbeuten einiger Farbstoffsysteme [Effect of viscosity on the fluorescence quantum yield of some dye systems]. Z Phys Chem 75, 63–76 (1971).

29. Loutfy, R. O. & Arnold, B. A. Effect of viscosity and temperature on torsional relaxation of molecular rotors. J. Phys. Chem. 86, 4205–4211 (1982).

30. Haynes, W. M. & Lide, D. R. CRC Handbook of Chemistry and Physics. (CRC Press, 2015).

31. Ullmann's Encyclopedia of Industrial Chemistry. (Wiley-VCH Verlag GmbH & Co. KGaA, 2000).

32. Gierer, A. & Wirtz, K. Molekulare Theorie der Mikroreibung. Zeitschrift für Naturforsch. A 8, 532–538 (1953).

33. Vyšniauskas, A., Balaz, M., Anderson, H. L. & Kuimova, M. K. Dual mode quantitative imaging of microscopic viscosity using a conjugated porphyrin dimer. Phys. Chem. Chem. Phys. 17, 7548–54 (2015).

34. Gierer, A. & Wirtz, K. Molekulare Theorie der Mikroreibung. Zeitschrift für Naturforsch. A 8, 532–538 (1953).

35. HORIBA Scientific. FluoroMax-4® & FluoroMax®-4P with USB Operation Manual Part number 810005 version B. Manual (2009).

36. Lakowicz, J. R. Principles of fluorescence spectroscopy. Princ. Fluoresc. Spectrosc. 1–954 (2006). doi:10.1007/978-0-387-46312-4

IV. Intrinsic Viscosity and Free Volume of Polymer Solutions

In the previous chapter, we showed that the porphyrin dimer can measure the temperature-dependent solution viscosity of pure and binary mixtures of organic solvents. For Newtonian liquids, shear stress is related to shear rate by the proportionality factor η, or viscosity. In these liquids, viscosity can be modelled as a function of molecular collisions, and as such is described by the Arrhenius equation in its relationship to temperature. However, ultimately, we are interested in the dynamics of biological environments. These are far more likely to behave like crowded colloidal suspensions due to the involvement of globular proteins and complex macromolecular architecture within the cell. These large solutes can contribute towards viscous effects in two distinct ways: firstly, large solutes cause organisation and ordering of solvent at short distances altering the viscous properties of the solvent itself. Secondly, depending on concentration, large solutes can cause molecular crowding and limit free-volume which will alter the way a solvent molecule diffuses, giving an effect similar to high viscosity. In this Chapter, we used polymers in solution to simulate the effects of large biological solutes. We compare our results to functional models that predict the behaviour of polymers as well as the viscosity of polymer solutions, as functions of concentration, molecular weight, temperature and solvent-polymer interaction.

4.1 Polymer structure and solution viscosity

The degree of overlap and/or entanglement between polymer chains is a major source contributing to solution viscosity in polymer suspensions, and is an effect dependent upon polymer concentration: thus models for polymer viscosity are separated into i) dilute and ii) concentrated solutions. Higher the concentration, the larger the degree of overlap between polymer chains, the higher the likelihood of entanglement and thus the higher the frictional resistance to deformation in the fluid - this is observed in ‘concentrated’ solutions. However, in dilute solutions, polymers have been shown to have complex solute-solvent interactions which

exert a 'structuring' effect upon their solvation shell. In dilute solutions where the likelihood of chain overlap is not observed, this is the major contributor towards concentration-dependent viscous behaviour. Thus the segregation of models viscous behaviour into dilute and concentrated regimes are based on polymer shape and size[1] though, a functional definition of either regime is give by the rule that concentrations less than 1 w/v % are considered dilute, and those greater than 1 w/v % are considered concentrated[2]. However, more recent literature has shown that this definition is variable [1,3].

First, we consider how measurement of viscosity in polymer solutions can be used to estimate the size and shape of the solvated polymer. The structure-dependent viscosity of suspensions is based on the hydrodynamic behaviour of polymers at dilute concentrations[4] due to some of the effects we summarised previously in Chapter III: increased frictional interactions between molecules (e.g. electrostatic) and increased steric obstruction to Brownian motion[4]. This is exemplified by the Staudinger rule, for colloidal polymers, which states that with knowledge of the shape of the solute, and having means to characterise its interaction with the solvent, we can estimate its size (in terms of mass, or molecular weight)[5]. Staudinger's rule has been formalised a number of times including by Simha et al., 1940[6] and by Debye et al.,1946[7], who each proposed the physical origins of increased solution viscosity upon solvation of a polymer, even expanding the theory to non-colloidal polymers. Both theories, amongst others, used a parameter known as *intrinsic viscosity* to describe the effects of a semi-flexible solute upon the hydrodynamic behaviour of the bulk solution[1,6,8,9]. The application of the theory has been highly successful, ultimately even being used to measure the molecular weight of globular proteins by intrinsic viscosity measurements[10,11].

Our second area of investigation is by dissolving the porphyrin dimer in concentrated polymer solutions, or rather, pure 'polymer melts' which display extremely complex viscous behaviour. In these systems, theory predicts that limitations on diffusion are due to polymer chain entanglement and physical obstruction of solute diffusion by highly crowded molecular

environments[1,2,4,9,12]. Under this assumption, the unoccupied 'holes' or 'free-volume' determines diffusion of molecules and viscous behaviour, in a manner similar to that described by Doolittle's equation for solvent diffusion in the previous chapter[4,9,13,14]. We hypothesise that the intermolecular rotation of the porphyrin dimer is strongly sensitive to the magnitude of free-volume in solution, as the limitation of free volume will prevent changes in molecular volume by internal rotation about the dimer's butadiyne bond. We have shown that intermolecular rotation of the dimer is a measurable quantity with strong calibration to bulk solution viscosity, and we seek to relate this measurement to free-volume in crowded suspensions.

Ultimately, we aim to use the porphyrin dimer's as a viscosity probe in an hydrocarbon environment of lipid chains and the previous chapter showed that the temperature-dependent viscosity of Castor oil, a solution composed mainly of lipid chains, was well predicted by the fluorescent response of the porphyrin dimer. However, Castor oil is composed of a large number of molecules with different molecular weight, and with very complex entanglement behaviour. In order to simplify the application of Staudinger's rule and free-volume estimations, we used a simple and well documented linear polyethylene glycol with molecular weight of 600 Da (PEG_{600}). The use of PEG_{600} confers a number of advantages: its solvent-dependent behaviour is well reported[15], it is soluble in a wide range of solvents, it does not interact chemically with the porphyrin dimer, and finally its size and shape are highly comparable with those of the lipid chains we intend to investigate in biomimetic lipid membranes. Namely, PEG_{600} has 13 repeating units, giving an average polymer length on a very similar scale to that of the most biologically common phospholipids (3-5 nm).

The length of the PEG_{600} is also comparable with that of the length of the porphyrin dimer itself, according to our estimations of dimer-length (approx 3 nm; Appendix B). Particularly in the case that the PEG chain adopts a random-walk motion, with flexibility of the chain, the porphyrin dimer is ideally suited to measuring both the dilute and concentrated regimes we previously described. That the PEG molecule and the porphyrin dimer are roughly the same size

gives a high probability of a good match between the enthalpy of motion, which we hypothesize, would make the dimer's motion highly sensitive to the polymer-volume related contribution towards the viscosity of the bulk solution. Thus, we used the porphyrin dimer in dilute and concentrated solutions in order to better understand the mechanism of viscosity-sensitivity and to predict its behaviour in biological solutions.

We hypothesise that the porphyrin dimer will be sensitive to the intrinsic viscosity of dilute polymer solutions. The following section tests our hypothesis by application of Staudinger's rule to estimate the molecular weight of PEG_{600} dissolved in different solvents. Using our knowledge of the dimer's solubility in each solvent,, we draw conclusions regarding its interaction with the polymer molecule.

4.2 Intrinsic viscosity and polymer molecular weight

The most commonly used and simplest equation for diffusion within a solvent – Stokes-Einstein[16] diffusion (equation 4.1) includes a term, ζ, for solvent friction of solvent molecules as they displace one another during diffusion as it impacts the rate of diffusion, signified by the diffusion coefficient, D. Below in equation 4.1, κ is the Boltzmann constant and T is temperature.

$$D = \frac{kT}{\zeta} \tag{4.1}$$

The Stokes-Einstein equation[16] is normally used to describe diffusion of solvent molecules amongst each other, in a homogenous solution, where diffusing molecules are of identical size[17]. It was known that dilute solutions of colloidal particles displace solvent and increase frictional interactions between the solute and solvent in a manner proportional to the hydrodynamic volume of the solute[4,5]. However, the measurement of Einstein's diffusion coefficient fails to adequately relate the friction coefficient ζ, to a quantity of macroscopic viscosity, η[18]. Assumptions of size and shape of the solute and solvent molecules which are relevant in terms of local diffusion (measured as D, the diffusion coefficient) are not easily extrapolated to the scale of the bulk property, viscosity (This is discussed in detail in Chapter VI). Moreover, it has been observed that very low concentrations of large dissolved solutes can alter the bulk

viscoelastic properties of the solution, and has been observed in the case of colloids, globular proteins and polymers[1,4–6,10]. To address this, in 1906, Einstein defined the term which is now known as *specific viscosity,* η_{sp}, (equation 4.2) [16,19], which expresses the volume fraction of a solution that is occupied by a solute, assuming the volume of the solute can be well described by a sphere, as in equation 4.2, where κ is the Boltzmann constant, V is the solution volume, and V_η is the volume of the solute that contributes to solution viscosity[17].

$$\eta_{sp} = 2.5 \times \frac{\kappa V_\eta}{V} \tag{4.2}$$

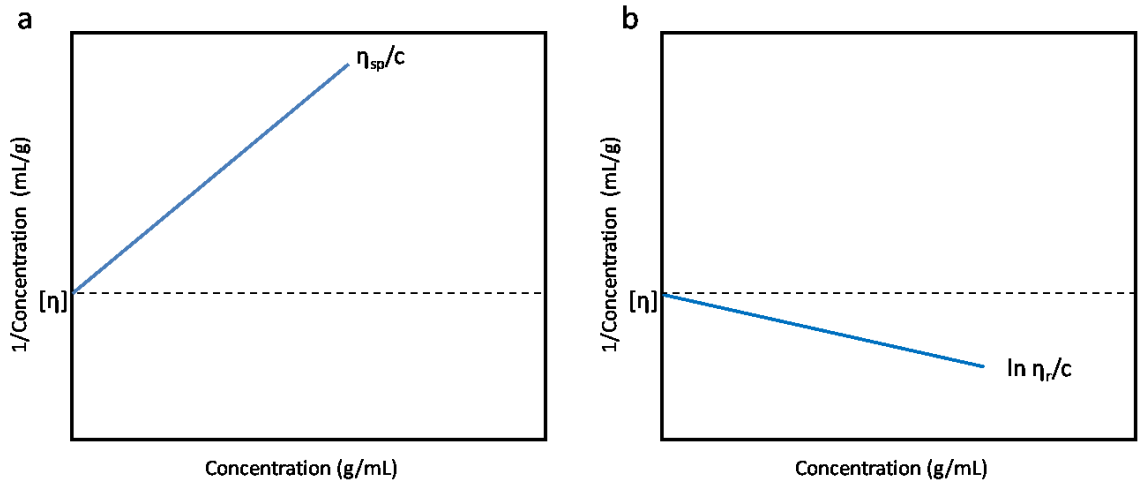

Figure 4.1: a) η_{sp}/c and b) ln η_r/c are linear with polymer concentration. Both parameters have the units of 1/Concentration (mL/g). Theory predicts that the intercept of both parameters against concentration is the intrinsic viscosity, [η].

In estimating the fraction of solution volume that is occupied by solute, it is possible to extrapolate the viscous contribution of that same solute to bulk viscosity by estimating friction generated by interaction with the solvent, creating, as Weissberg et al., 1951, describe, a solvent 'cage'[4] that disrupts the normal hydrodynamics of the solvent and increases the activation energy of diffusion in a manner dependent on its size and shape.

As an experimentally measured value, specific viscosity is defined as in equation 4.3, where η_0 is solvent viscosity or the viscosity of solution prior to addition of the solute or polymer.

$$\eta_{sp} = \frac{\eta - \eta_0}{\eta_0} \tag{4.3}$$

It is measured alongside the quantity *relative viscosity*, η_r as in equation 4.4.

$$\eta_r = \frac{\eta}{\eta_0} \tag{4.4}$$

The quantities specific and relative viscosity can be normalised to concentration, giving the incremental viscosity change per unit concentration of a large solute (polymer) in a solution (Figure 4.1). Extrapolation to zero concentration of both parameters gives a value known as *intrinsic viscosity*, [η] which describes a concentration-independent value for internal friction of the polymer chain in relation with itself. Theoretical specific and relative viscosities, normalised for concentration of a polymer solution intercept the zero-concentration y-axis at the same point, the intrinsic viscosity.

The value of the intrinsic viscosity relates to polymer molecular weight, asserted by the Mark-Houwink[20,21] equation (4.5)

$$[\eta] = KM^a \tag{4.5}$$

Here, K is a proportionality-constant specific to the polymer species, regarding its shape, which makes the intrinsic viscosity value applicable to non-linear polymers or flexible linear polymers with a collapsed or semi-collapsed configuration. a, is a constant relating to the combination of polymer and solvent, which describes the nature of polymer conformation in that particular solvent[20]. Values for a are measured in what are known as theta-solvents for the polymer in question, in which it is optimally solvated, such that polymer chains assume random walk coil dimensions (neither completely collapsed nor tensed coil conformations)[20]. These 'shape' factors, K and a, give an approximation of the shape of the polymer, and the nature of its interaction with the solvent, which directly inform the theoretical hydrodynamic shell of the polymer, which is the origin of increased bulk viscosity of in solution[20]. Thus, M, in equation 4.5, is the molecular weight. Typical values for both K and a are widely available from sources such as the Polymer Handbook[15].

Measurement of intrinsic viscosity is an established method for fast and reliable measurement of polymer molecular weight and is increasingly applied to biological systems to measure protein molecular weight[11,22]. We first aim to measure intrinsic viscosity in a system with known polymer molecular weight using the porphyrin dimer in order to test the molecular rotor mechanism in polymer suspensions where it will be used to measure the molecular weight of dissolved solutes in a rapid and accurate way. Determination of the values of *K,* M and *a,* as measured by the porphyrin dimer will confirm our hypothesis that the local microviscosity measurement is related to solvent friction and solute shape.

4.3 Ratiometric viscosity measurements of dilute solutions of PEG_{600}

We prepared solutions of PEG_{600} in solutions of water, chloroform, dimethylsulfoxide (DMSO) and methanol, as model systems for the measurement of intrinsic viscosity. We systematically increased the concentration of PEG_{600} in the four solvents mentioned above, and measured their viscosities by both mechanical rheometry and fluorescence, to determine the emission ratio. We measured the viscosity-sensitivity of fluorescence spectra of the molecular rotor P_2NMe_3, characterised in the previous chapter, upon increase in PEG_{600} concentration (Figure 4.2).

In all four solvents, upon addition of PEG_{600}, we observe the appearance of a high energy, short wavelength emission band (the peak of the 'twisted' confomer), characteristic of P_2NMe_3 emission in high viscosity solutions. This is consistent with our hypothesis that solution viscosity increases when the polymer concentration is increased. However, in Figure 4.2a, we also observe a dramatic blue shift in the low energy, planar emission maximum upon addition of PEG_{600} in water. This shift can be associated with disaggregation as seen in the previous Chapter, which we interpret as a sign of increasing solubility of the dimer in solutions of increasing $PEG_{600.}$ Previously, P_2NMe_3 has been shown to be largely insoluble in water[23], and displays, in our experiments, the characteristic signs of aggregation: red-shifted emission, decreased emission intensity, and loss of viscosity-sensitivity. Aggregation was confirmed by recording the absorption spectra of the same solutions, as in Figure 4.2b, where solutions of very low concentrations of PEG_{600} are shown to have decreased absorption intensity in both the

Q bands and the Soret peaks, which appear broadened. Loss of viscosity sensitivity is attributed to the conformational inflexibility of aggregates, making the planar confomer dominant in the ground state, such that excitation at the maximum of the twisted confomer excites a large proportion of the planar confomer as well. Thus the ratio of twisted to planar is low in the ground state of the aggregated porphyrin dimer, P_2NMe_3, and this collapses the ratiometric calibration of viscosity in the excited state. However, addition of greater quantities of the less polar PEG_{600} into solution appears to reverse spectral signs of aggregation, shifting the planar peak, and restoring the appearance of the twisted peak in response to increased polymer concentration, as predicted by Staudinger's rule that the presence of the polymer increases bulk viscosity. We attribute this to preferential solvation of P_2NMe_3 in PEG_{600}, in close proximity to the polymer chains rather than fully solvated by water. This ensures that the dimer remains disaggregated and therefore sensitive to the viscosity of its locale. We observe a combination of two spectral effects, a blue shift indicative of increased solubility of the dimer (in PEG_{600}) and the appearance of the twisted confomer indicative of increased bulk viscosity. This combination of effects makes the correlation between increased concentration of PEG and increased emission ratio more difficult to interpret as the rise of the twisted peak is suppressed by aggregation conditions in combination with the effects of low viscosity.

To test the validity of our data in water, we made a comparison with two solvents where both the polymer and P_2NMe_3 are completely soluble. We prepared solutions of PEG_{600} in DMSO (Figure 4.2c, d) and in methanol (Figure 4.2 g, h) where the rise in intensity of the 'twisted' emission peak is seen without any change in peak maxima. P_2NMe_3 is highly soluble in both DMSO and in methanol, as can be seen in the absorption spectra in these solutions shown in Figure 4.2d and h – all spectra show sharp Soret absorption peaks. Due to good solubility of the dimer in these solvents, there is no preferential solvation by PEG_{600}, such that emission arises equally from dimers solvated by the solvent and those in close proximity to PEG_{600} chains. Thus the presence of PEG_{600} chains at ever increasing concentrations creates solvent 'cages', as per the theory of Weissberg et al., 1951[4].

Indeed, from this comparison, we infer that the consistently low emission ratios observed in water are due to poor dimer solubility and not to any specific interaction with the polymer that negates the ratiometric viscosity sensitivity. Furthermore, we tested the behaviour of P_2NMe_3 in a non-polar solvent with increasing concentrations of PEG_{600} to test whether viscosity-sensitivity is still maintained or whether effects of insolubility are observed. We sought to repeat the experiment with non-polar solvents as a mimic for the conditions of the hydrocarbon interior of the lipid membrane; that is, we sought to test the sensitivity of the charged dimer to large solutes in a non-polar environment (Figure 4.2e,f). Absorption spectra of P_2NMe_3 in solutions of PEG_{600} in chloroform indicate that the dimer is relatively well dissolved, with signs of minor aggregation at very low concentrations of PEG_{600}, as expected for the positively charged P_2NMe_3 (Figure 4.2f). We observe a good relationship between the increasing concentration of PEG_{600} and the rise of the twisted peak in emission spectra, in a manner consistent with that observed in DMSO and methanol solutions. From this, we infer that the dimer is moderately solvated in chloroform but does show an increase in twisted emission upon addition of PEG_{600} without significant aggregation or solvatochromic spectral effects to the extent observed in water.

Thus, we established that the quality of absorption and fluorescence spectra (shown in Figure 4.2) reflects the solubility of the porphyrin dimer in both the solvent and in the polymer and is of primary importance in the analysis. Ultimately, we conclude that viscosity measurements by the porphyrin dimer in aqueous solution must be limited to samples in which the absorption peak maximum is close to the value expected in a disaggregated state. According to our data this includes concentrations of PEG_{600} of > 0.4 g/mL. This is due to the nature of the microviscosity measurement performed by the molecular rotor, in that, it is only sensitive to its immediate solvation shell. Imperfect solubility in mixtures of solvents or structured solvents with large solutes can thus strongly affect the interpretation of 'bulk' viscosity from the dimer's ratiometric measurements. With this in mind, here we discuss how the porphyrin dimer's viscosity

measurements of polymer solutions compare with theory and whether the dimer's solubility is an obstacle against viscosity-sensing in these solutions.

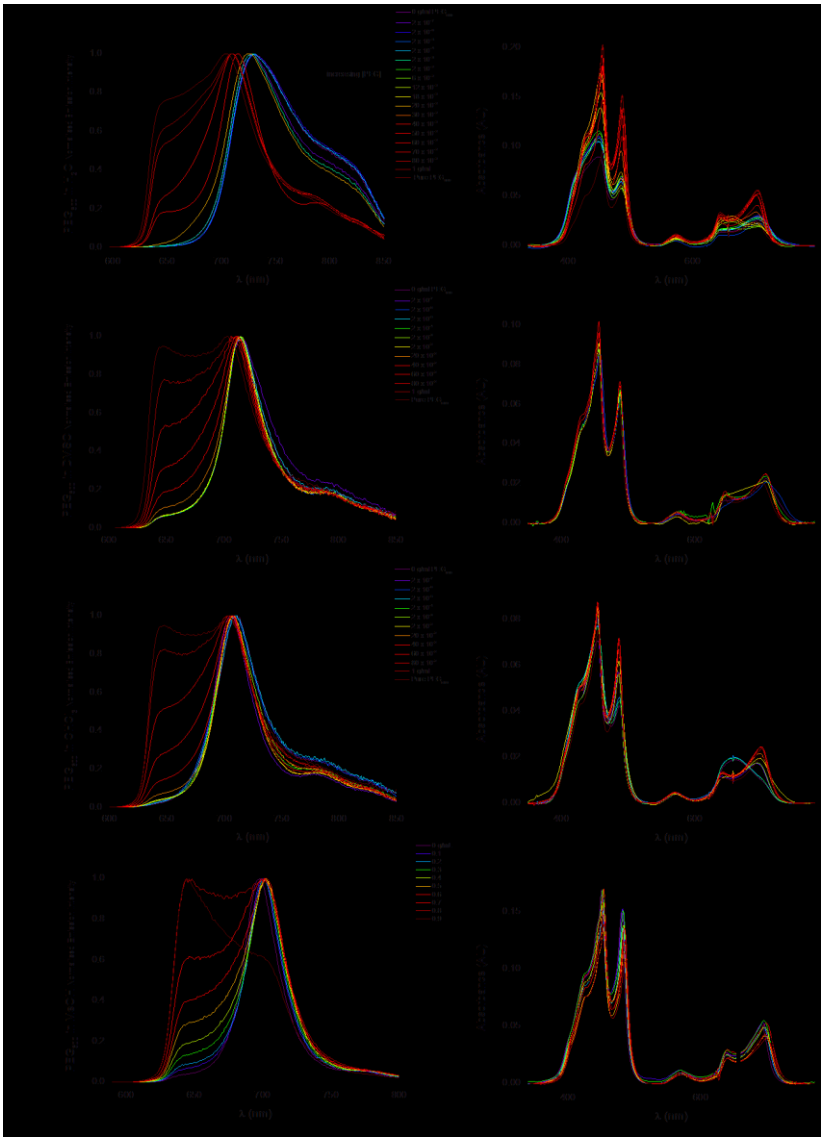

Figure 4.2: Ratiometric viscosity sensitivity of P_2NMe_3 to polymer concentration in solutions of a,b) water; c,d) chloroform; e,f) DMSO; g,h) methanol containing PEG_{600}. Emission spectra (λ_{ex} = 453 nm): left column; absorption spectra: right column: Concentrations of PEG_{600} range from 2 x 10^{-7} to 1 g/mL. Concentration of P_2NMe_3 is 0.33 μM, giving an absorption intensity of 0.1 AU at 453 nm. The exception is the case of H_2O + PEG_{600} where the molar absorption coefficient of P_2NMe_3 increases significantly in the presence of PEG_{600}.

In Chapter III, we showed that the dimer's emission ratios in solutions of methanol and glycerol are well-correlated to the mechanical measurements of viscosity, as predicted by the Förster-Hoffmann equation. Here, we seek to investigate whether this linear relationship (on a double log plot) is upheld in PEG_{600} solutions in varying solvents. For these plots, emission ratios in

methanol and glycerol solutions are compared with the kinematic viscosity (ν, mm^2/s) as measured by mechanical rheometry of the same solutions. Kinematic viscosity is the dynamic viscosity independent of density (ρ, g/cm^3) as (equation 4.6):

$$\nu = \frac{\eta}{\rho} \tag{4.6}$$

In Chapter III, we compared emission ratios against the dynamic viscosity (η, cP) as predicted by the Förster-Hoffmann equation. However, Staudinger's rule and constants for the Mark-Houwink equation are all given in proportion to kinematic viscosity rather than dynamic viscosity. As such, all viscosity data of polymer solutions is presented in terms of kinematic viscosity, ν (mm^2/s).

Though the Förster-Hoffmann equation applies to pure solution viscosity, where the solvent molecules are of roughly equal size, and much smaller relative to the dimer, we expect to see the viscosity-dependent spectroscopic changes in structured solutions of PEG_{600}. However, we also hypothesise that the exact trend will vary according to the solvent in which the polymer is dissolved. To this end, we show calibration curves, comparing the dimer's emission ratio and the viscosity as measured by mechanical rheometry in solutions of PEG_{600} in Figure 4.3a.

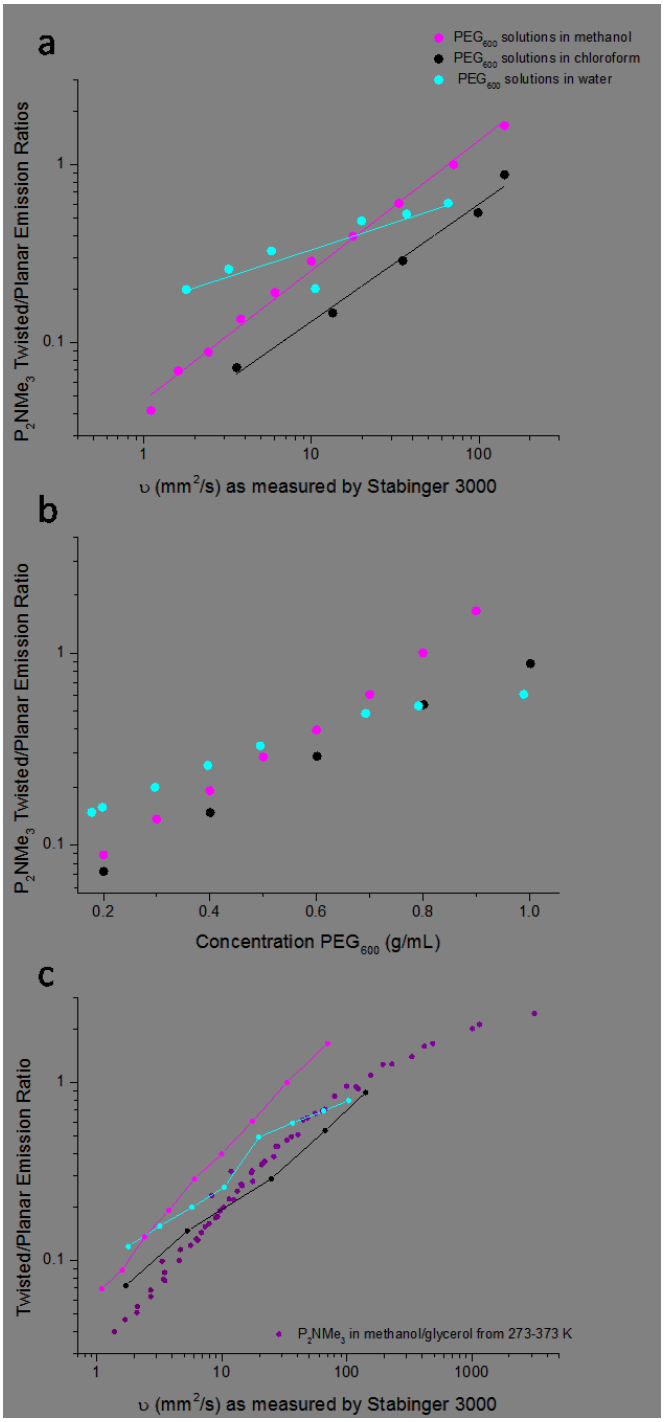

Figure 4.3: a) P_2NMe_3 emission ratios from solutions of PEG_{600} in methanol (pink) chloroform (black) and water (cyan) plotted against the kinematic viscosity measurements of the same solutions by mechanical rheometry using the Stabinger 3000 viscometer. Least squares linear regression of the data gives Emission ratio = 0.72ν – 1.30 with R^2 = 0.97 (methanol); Emission ratio = 0.65ν – 1.56 with R^2 = 0.99 (chloroform); Emission ratio = 0.31ν – 0.78 with R^2 = 0.69 (water). b) P_2NMe_3 emission ratios against PEG_{600} concentration (g/mL). c) Combined graph showing P_2NMe_3 emission ratios from solutions of PEG_{600} as well as in mixtures of methanol and glycerol, reproduced from Chapter III.

Figure 4.3 shows that P_2NMe_3 emission ratios increase with increasing concentration of PEG_{600} and thus with increasing solution viscosity, as measured by mechanical rheometry. This is true

in solutions of methanol and chloroform (pink, black data respectively), where both the polymer and the dimer are highly soluble. In these two solutions we observed strong linear relationships (in a double log plot) with approximately equivalent slopes (0.73, 0.66, respectively). However, linear regression of the data in chloroform shows that the curve is shifted slightly to the right relative to that for methanol: that is, the emission ratios in chloroform are lower than those observed in methanol for the same viscosity values. By contrast, data collected in solutions of PEG_{600} in aqueous solutions has a reduced slope (0.31) and increased emission ratio at low viscosities. We propose that this is a reflection of the dimer's location in close proximity to (or immediate contact with) PEG_{600} chains to the exclusion of water molecules. The small slope is an indicator that the dimer's emission intensity is changes only slightly upon increasing concentration of PEG_{600} as it is not as sensitive to the presence of the polymer in the bulk solvent, i.e. the hydrodynamic effects upon the order of water molecules. Instead, we can hypothesise that the dimer's viscosity-sensing mechanism of rotation is mainly affected by the motion of the PEG_{600} chains local to the dimer, and their increasing entanglement as that local concentration increases. Thus, a positive correlation between emission ratio and solution viscosity is observed, but does not reflect both contributing effects of the polymer upon solvent viscosity, simply the steric barriers of PEG_{600} in close proximity to the dimer (Figure 4.3b). This is further demonstrated by the increased error of the linear regression to the data, signifying a large degree of noise from data with low emission intensity, which we take as a sign of aggregation. If we attempt to discern the two concentration-dependent components of bulk viscosity concentration of polymer: i) hydrodynamic effects and ii) chain entanglement, we propose that both effects are observed in solutions of PEG_{600} in methanol and chloroform, while only the second effect, chain entanglement is observed in aqueous solutions.

In order to compare sensitivity to viscosity of P_2NMe_3 in bulk homogeneous solutions and in PEG_{600} solutions, we also plotted the data discussed above together with the data from methanol and glycerol solutions at various temperatures, discussed in Chapter III, Figure 4.3c. We plotted the kinematic viscosity of solutions of methanol and glycerol with those of the polymer

solutions as measured by mechanical rheometry against corresponding emission ratios (Förster-Hoffmann plot of dimer emission and kinematic viscosity is discussed in the next section). A direct comparison between solvents i.e. in methanol, glycerol mixtures (purple, Figure 4.3c) and PEG_{600} in methanol, (pink, Figure 4.3c) shows that we observe a similar slope with increasing viscosity, but emission ratios are vertically translated such that emission ratios in PEG_{600} solutions are higher than observed in methanol glycerol mixtures. We interpret these differences to be due to the relative size and shape of the polymer chain in comparison with glycerol molecules. Evidently, interaction between the PEG_{600} chain and the porphyrin dimer results in a higher emission ratio than observed in methanol/glycerol mixtures. We attribute this difference to the conformational organisation of the PEG_{600} chain in methanol as compared to the complete mixture of glycerol molecules 'dissolved' in methanol. Thus, the calibration of the dimer appears to be non-universal and shows small effects depending on the exact nature of the solvent molecules. In case of the larger polymer molecule dissolved, a possible effect of polymer chain conformations also has to be taken into account.

4.3.1 Mark-Houwink parameters and polymer chain conformation

Mark-Houwink parameters (K and a, Equation 4.5) describe the expansion of the polymer chain in solution, and the relationship between polymer shape and the effects on solvent organisation. The parameter 'a' is a descriptor of the potential of mixing between the polymer and the solvent. At what is known as 'theta' conditions, the chemical potential of mixing between polymer and solvent is zero. Under these conditions, a is always 0.5 and the polymer adopts a 'random walk' coil dimension, defined as a relaxed polymer chain where each monomer adopts random walk dynamics, as shown in Figure 4.4, in chloroform. On the other hand, solvents with values of 'a' greater than 0.5 are termed 'good' solvents, where the polymer expands to adopt a conformation that enables greater mixing with the solvent.

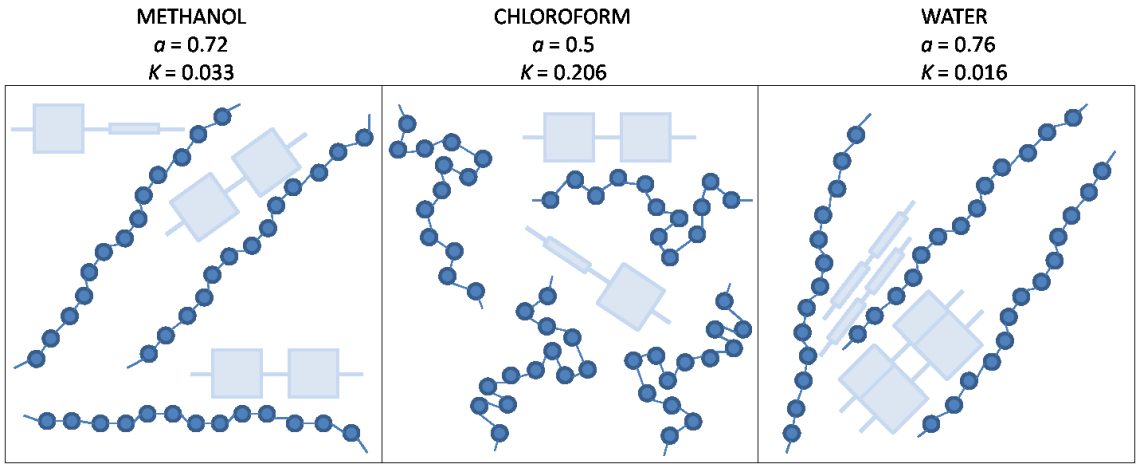

Figure 4.4: Predicted conformation of PEG_{600} chains in solutions of methanol (left), chloroform (middle) and water (right) according to the Mark-Houwink parameters for PEG_{600} in these solvents, detailed in the Polymer Data Handbook[24]. Hypothesized interaction of P_2NMe_3 with the PEG_{600} based on the relative solubility of the dimer with the solvent.

Here, polymer chains are more likely to be linear, with large bond angles between the polymer main chain and the side groups, as shown in Figure 4.4 in methanol and water. Polymers in good solvents have greater molecular volume than when they are dissolved in theta solvents. At a > 0.5, the Mark-Houwink equation adheres best to experimental data. Figure 4.4 also depicts a hypothetical scheme for the interaction of the dimer with the polymer chain depending on the dimer's solubility in the solvent. For instance, in methanol, PEG_{600} adopts an expanded conformation, and the dimer is well solvated, able to detect the solvent shell of the dimer. Alternatively, in water, the dimer is preferentially solvated near the polymer chains, where they are in contact with one another as opposed to freely dissolved in the solvent. In chloroform, the polymer is relaxed, adopting a smaller molecular volume, on average, while the dimer is slightly preferentially solvated near the polymer chain. This is reflected in the calibration curves shown in Figure 4.3, where the incremental change in ratio (slope) with concentration of PEG_{600} is lower in water, due to aggregation, and in chloroform due to the reduced molecular volume compared to methanol. The ratios in PEG_{600} in methanol compared with glycerol are higher at all concentrations due to the structured nature of the polymer chain, and its hydrodynamic shell that occupies larger volume. The parameter 'K' is related to similar volume effects. In theta solvents, K is largely unchanging in different solvents, reflecting the relaxed conformation of the

polymer chain under theta conditions. Both parameters are sensitive to temperature and change depending on a given molecular number $M_{N.}$

Thus, in our experiments, for true comparison between solvents, all experiments were performed at 293 K and using the same batch of PEG_{600}. We predict that the molecular weight estimation performed using the porphyrin dimer is likely to reflect the differences in polymer conformation in different solvents. The next section discusses the application of the Mark-Houwink equation to data collected for the porphyrin dimer from PEG_{600} solutions in methanol, chloroform and water.

4.4 Intrinsic viscosity and molecular weight

In the introduction to this chapter, we summarised Staudinger's rule, stating that the viscosity of a solution of polymer is dependent upon the molecular volume of the polymer, a function of its molecular weight. The Mark-Houwink equation formalises this relationship by relation of polymer molecular weight to the parameter, 'intrinsic viscosity', a concentration-independent parameter unique to the interaction between the polymer and the solvent, which is reflected by bulk viscosity. In this section, we seek to apply the Mark-Houwink equation to the porphyrin dimer's ratiometric measurements of polymer viscosity in the PEG_{600} solutions shown in Figure 4.2 and 4.3 by the following steps:

1. First we sought to convert ratiometric viscosity measurements to units of kinematic viscosity. We did this by application of the calibration curve for P_2NMe_3 in methanol and glycerol solutions at varying temperature, Figure 4.5. We intend this data to be the definitive correlation between twisted/planar emission ratio and viscosity, as it is independent of the effects of temperature, aggregation and solvatochromism as summarised in Chapter III. Above, we discussed the source of disagreement between calibration curves in PEG_{600} and in mixtures of methanol and glycerol suggesting that interaction between the dimer and long PEG_{600} chains are the cause. However, the intended application of the Mark-Houwink Sakurada equation is as a predictor of

polymer size purely from the hydrodynamic effect of the polymer on its solvation shell. Thus, the methanol/glycerol data should be a good model for application of the equation and use of the parameters from literature. We plotted the P_2NMe_3 emission ratio against kinematic viscosity, ν, as below in Figure 4.5.

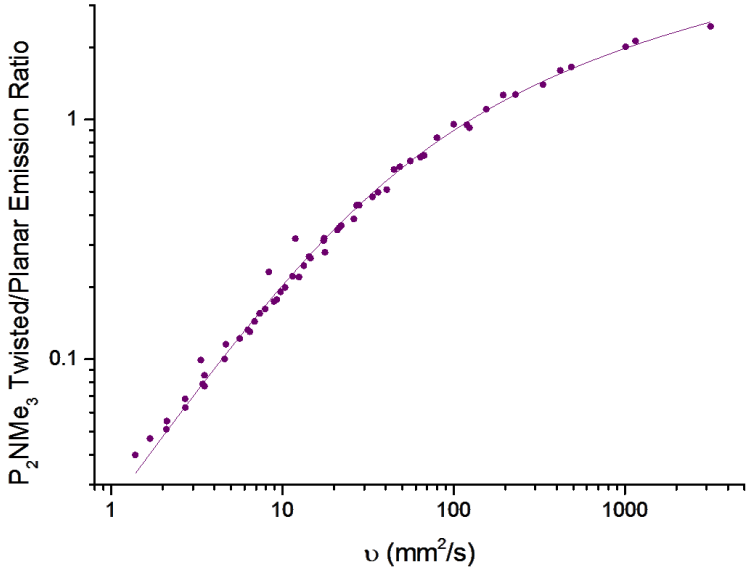

Figure 4.5: The calibration curve for P_2NMe_3 vs. kinematic viscosity recorded in methanol/glycerol solutions. The data was fit by least squares regression (Levenberg-Marquardt algorithm) to the following equation: Emission ratio $= a - bln(\nu + c)$ Where a = -1.51, b =-0.50 and c = 20.15.

2. Next, we calculated specific and relative viscosities, η_{sp} and η_r to be plotted against the polymer concentration. By convention, the character η is used to denote these parameters, though they are calculated using values of kinematic viscosity (ν) in accordance with theory and existing literature. The values η_{sp}/c and $\ln \eta_r/c$ are expected to change linearly with the concentration of PEG_{600}, and their common intercept is termed [η], the intrinsic viscosity. Figure 4.6 summarises these plots for solutions of PEG_{600} in methanol (Figure 4.6a); PEG_{600} in chloroform (Figure 4.6b); and PEG_{600} in water (Figure 4.6c).

Plots of η_{sp}/c and ln η_r/c against concentration are expected to change linearly with PEG_{600} concentration. However, we find that in Figures 4.6a and b, in the solvents methanol and chloroform, η_{sp}/c clearly shows exponential dependence on concentration. We hypothesise that deviations from linearity can arise due to artefacts: namely the concentration at which we made these measurements might exceed that at which the dilute-solution conditions are met, and polymer-polymer entanglement is a major component of observed viscosity.

Furthermore, $\eta_{sp/c}$ becomes smaller as it approaches 0 concentration, at [η], and here is where the linear region is expected to occur, however, we were limited in the minimum concentration at which we could make measurements due to the insensitivity of the porphyrin dimer's emission ratio at viscosities less than 1 mm^2/s. However, ln η_r/c is shown to be linear with concentration, even at the high concentrations we tested in this experiment, due to the compound nature of the hydrodynamic and entanglement components of viscosity. Data obtained in aqueous solution displays a roughly linear relationship between both η_{sp}/c and ln η_r/c against concentration, though with very shallow slope. The relative insensitivity of ratiometric viscosity measurements against the large change in concentration leaves estimates of [η] highly unreliable, and as can be seen, the two curves for η_{sp}/c and ln η_r/c do not appear to share a common intercept.

From these plots, we calculated the respective [η] expected for each solution and compared it with values from literature. Our intention is to use the Mark-Houwink equation to predict the molecular weight of PEG_{600} as a means of confirming the accuracy of ratiometric viscosity measurements by P_2NMe_3. Mark-Houwink parameters are provided in the Polymer Data Handbook[24] and are used to calculate the molecular weight as predicted by ratiometric viscosity measurements in solutions of PEG_{600} in methanol, chloroform and water. Further, using the ratiometric measurement of [η], and the known molecular weight (600 Da) we calculated the Mark-Houwink parameters as predicted by the porphyrin dimer for comparison with those from literature. Parameters of the fit are summarised below in Table 4.1.

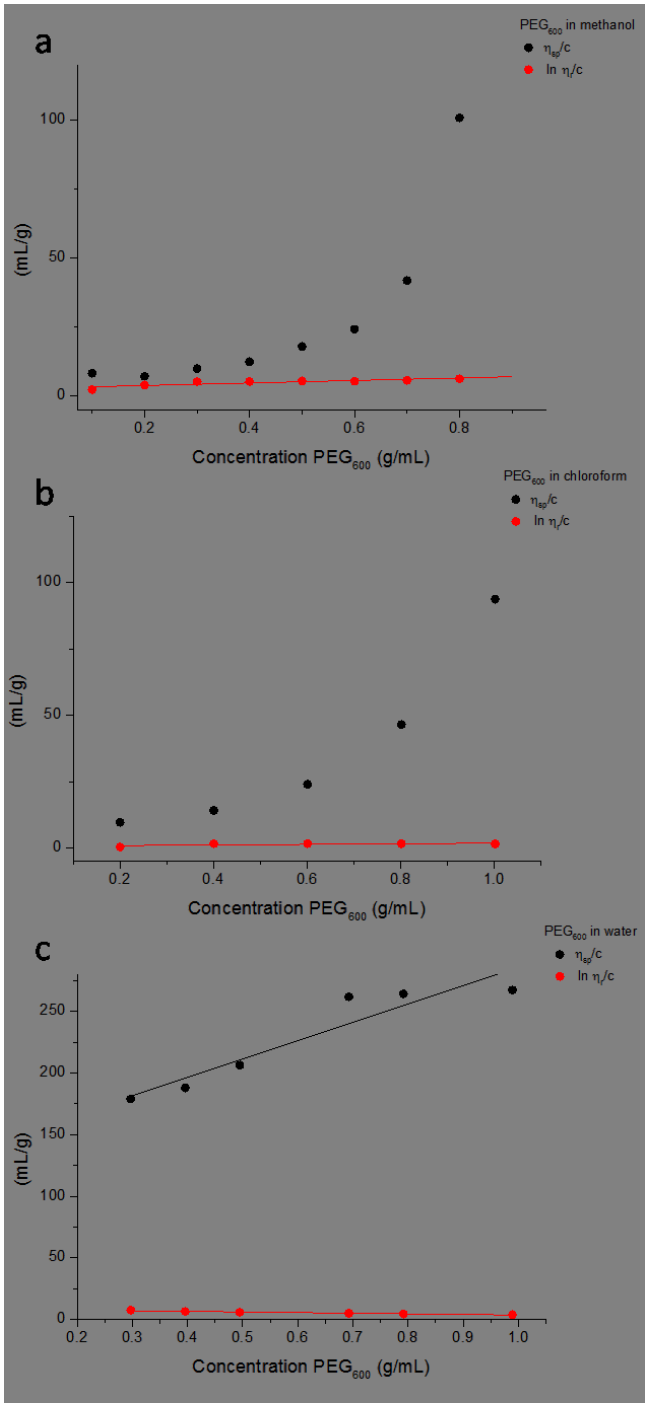

Figure 4.6: Mark-Houwink plots made by conversion of P_2NMe_3 emission ratios to kinematic viscosity by application of calibration curve from Figure 4.3. η_{sp}/c and ln η_r/c for a) PEG_{600} in methanol b) chloroform and c) water at concentrations from 0.2-3 – 1.0 g/mL. Least squares linear regression of the ln η_r/c against concentration gives mL/g = 4.55C +2.68 with R^2 = 0.99 in methanol, and mL/g = 1.14C + 0.67 with R^2 = 0.99 in chloroform. η_{sp}/c against concentration gives mL/g = -9.4C + 11.79 R^2 = 0.77 and ln η_r/c against concentration gives mL/g =80.9C + 186.4 R^2 = 0.42; both in water.

Table 4.1: Mark-Houwink analysis of PEG_{600} in water, methanol and chloroform

		Literature	η_{sp}/c	$\ln \eta_r/c$
Methanol	**[η]**	3.30	Non-linear	2.68
	a	0.72		0.69
	K	0.033		0.027
	MW	600		448.63
Chloroform	**[η]**	5.04	Non-linear	5.32
	a	0.5		0.51
	K	0.206		0.22
	MW	600		664.62
Water	**[η]**	2.07	137.0	8.60
	a	0.76	1.00	1.00
	K	0.157	0.093	0.35
	MW	600	149442	3913.2

The data summarised in Table 4.1 shows that we had limited success in predicting the molecular weight of PEG_{600} from application of the Mark-Houwink equation to ratiometric measurements of intrinsic viscosity. Ratiometric intrinsic viscosity measurements of PEG_{600} in methanol and chloroform reported a molecular weight estimate of 449 and 664 Da, respectively. Experiments performed on PEG_{600} in aqueous solution returned an extremely high estimate of molecular weight, in keeping with our interpretation that the P_2NMe_3 dimer is localised to tangled PEG_{600} chains and insensitive to the bulk viscosity of the whole solution. Thus it reports an exaggerated measurement of solutions viscosity, as rotation of the dimer is only affected by steric hindrance of the PEG_{600} and not the solvent shell.

However, we find that the calculated shape parameters, *K* and *a* are well matched to those from literature, suggesting that the porphyrin dimer is sensitive to the conformation of PEG_{600} dissolved in chloroform and must be well solubilised in proximity to the polymer chain and its solvent shell. Additionally, the molecular weight estimate at 665 Da (in chloroform) is well within the margin of error of these experiments. Thus we are satisfied that the application of the Mark-Houwink equation to ratiometric measurements of viscosity in chloroform is successful. The molecular weight estimate of PEG_{600} in methanol is less than expected, as are the shape parameters *K* and *a*, suggesting that the emission ratio of the dimer is not reporting true conformation of the PEG_{600} chain. This is the same phenomenon we observed in the mismatch between the two calibration curves as shown in Figure 4.3c. We maintain that the dimer solubility is not a limiting factor in methanol, but rather, errors in molecular weight estimation in methanol solutions arise due to two factors: i) the concentrations used are higher than those recommended for application of the Mark-Houwink equation and ii) at these concentrations, entanglement of PEG_{600} with the dimer is a viscous mode that affects emission ratios but is not detected in mechanical rheometry measurements.

4.5 Viscosity measurements in pure polymer 'melts' and concentrated solutions

In the previous section, we determined the applicability of the dimer to 'measure' the molecular weight of a dissolved polymer, by its affect on the ordering of solvent molecules. Although the molecular weight measurements in chloroform were successful, the measurements in water and methanol were marred by errors. We attributed these errors to a different conformation of polymer chains in solution, as well as the problem of aggregation of the P_2NMe_3 dimer in water. Due to a very complex mixture of environments that might be found in a biologically relevant situation, we thus conclude that the ratiometric measurements of dimers are unlikely to provide a reliable measure of the molecular weight os a surrounding polymers and/or macromolecules at present. Nonetheless, we still believe that the dimer be used to measure viscosity in highly concentrated polymer melts where entanglement is the major mode of viscous friction. While

not a biological sample, this situation is close to the setting that may be found in tightly packed lipid membranes, or concentrated macromolecular solutions in certain cell compartments, such as the synaptic cleft or a cellular cytoskeleton.

There is an existing precedent for the use of molecular rotors, or other volume-dependent methods to describe the viscoelastic behaviour of concentrated polymer solutions or pure polymer melts. Loutfy et al., used a series of three p-(N,N-dialkylamino) benzylidene malononitrile dyes which were shown to behave as molecular rotors in solutions of various polymers[14]. Figure 4.7 shows that the fluorescence quantum yield of the relevant molecular rotor increased with time in polymerisation reactions, confirming the assertion that molecular rotors could report the increase in viscosity of polymer solution[14].

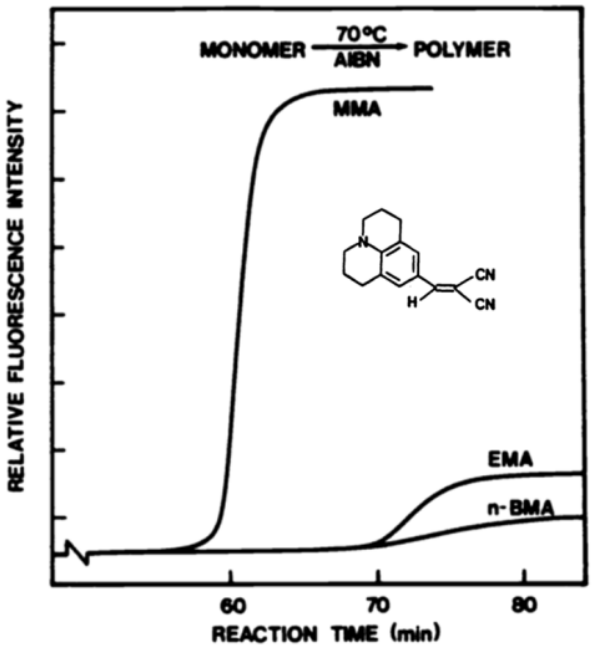

Figure 4.7: A fluorescence intensity measurements of molecular rotor, [p-(N,N, dialkylamino)-benzylidene] malonitrile (structure shown in the inset) is sensitive to the polymerisation of methyl methacrylate (MMA), ethyl methacrylate (EMA) and n-butyl methacrylate (n-BMA). Figure from Loutfy et al., 1986, Ref [14].

To further develop the connection between solute molecular weight and microviscosity as measured by molecular rotors, Loutfy et al., demonstrated that the dye's quantum yield was related to free volume in the polymer solution[14]. Beuche et al., showed that free volume in

polymer solutions is related to macroscopic viscosity of the solution and the specific glass-transition temperature T_g, for a particular polymer but independent of its molecular weight [25]. Approaching the glass-transition temperature of the polymer solution decreases the available free volume for the dye's rotation, increasing its quantum yield. Victor et al., 1987, among others, have expanded upon Loutfy's work using photoisomerisation of stilbene dyes to demonstrate the reduction of free-volume in polymer solutions approaching the glass transition.[26,27]

4.5.1 Viscosity of pure polyethylene glycol 'polymer melts'

As discussed in the introduction to this chapter, the viscosity of pure polymer melts or concentrated polymer solutions is a function of free volume which is related to the motion of polymer chains, as determined by, amongst other parameters, temperature. We measured the viscosity of different molecular weight PEGs (400, 600, 900 Da) as a function of temperature, by measuring ratiometric response of P_2NMe_3. The resulting data is shown in Figure 4.8. We found that emission ratios are roughly equal between PEGs of different molecular weights between 273 and 340 K, with the exception of PEG_{400} which can boil at temperatures above 340 K. We know that entanglement of polymers is the main source of viscous friction in polymer melts. The nature of branching and polymer main chain bonding are strong determinants of this entanglement. The coincidence of P_2NMe_3 emission ratios in these polymer melts are good evidence that the viscous contribution from chain entanglement, and its restriction of free volume, is independent of molecular weight. We discussed in the previous section that intrinsic viscosity measurements used to estimate polymer molecular weight failed at high concentrations due to the restriction of free volume, and that we presumed the porphyrin dimer to be sensitive to this effect. Here we show good evidence that the porphyrin dimer is sensitive to viscosity changes by temperature-induced free volume change, and that this is independent of the molecular weight of the chosen polymer.

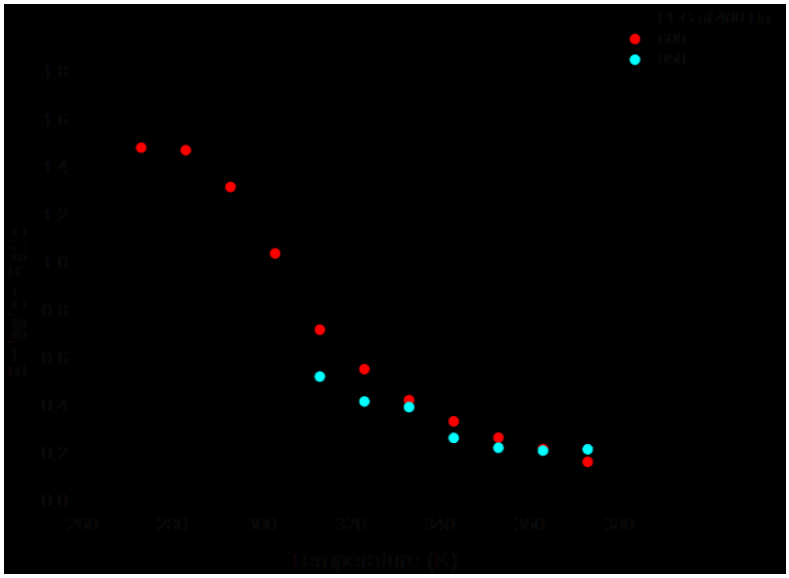

Figure 4.8: Emission ratios of P_2NMe_3 in PEG melts of varying molecular weight; 400 (black), 600 (red), 900 Da (cyan), measured by fluorescence under temperature change from 273-373 K

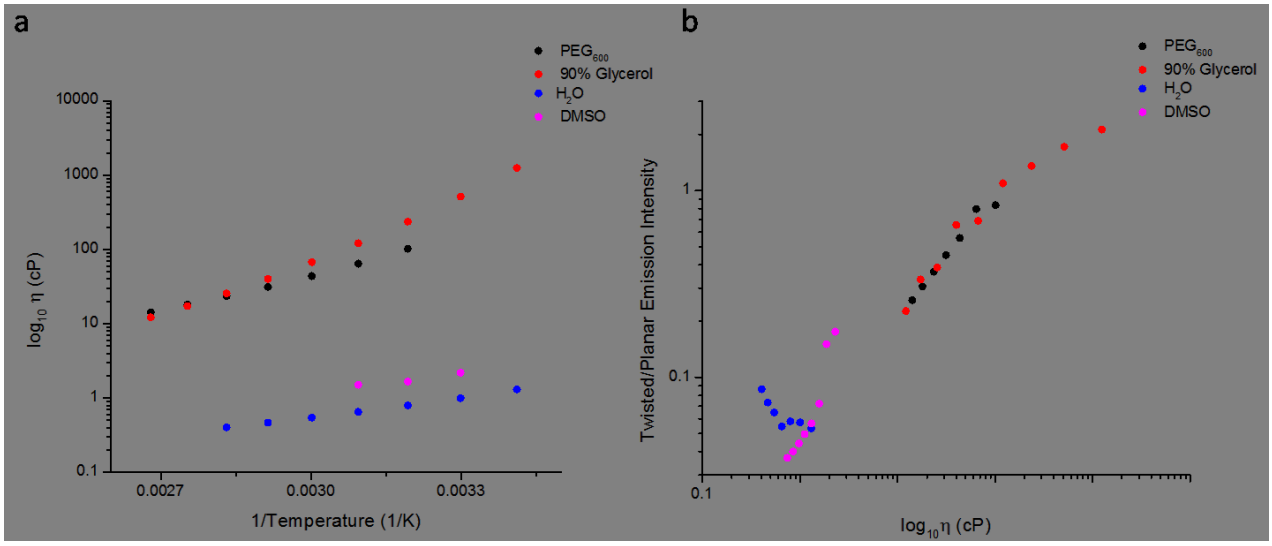

Figure 4.9: a) Viscosities of various solutions as measured by ratiometric detection from P_2NMe_3: PEG_{600} melt (black), 90% glycerol/10% methanol (red), H_2O (blue), DMSO (magenta) recorded at varying temperature, shown a) in Arrhenius coordinates and b) vs mechanically measured viscosity.

Figure 4.9 shows ratiometric viscosity measurements obtained using P_2NMe_3 of various solutions against temperature (Figure 4.9a) and viscosity (Figure 4.9b). As can be seen from Figure 4.9a, there is no clear correlation of the ratiometric viscosity measurement with temperature, which is consistent with temperature-independent behaviour of P_2NMe_3. A much clearer correlation is observed between the measured twisted: planar ratio and mechanically measured bulk viscosity of these solutions, Figure 4.9b. As shown in Chapter III, we expect the

Förster-Hoffmann correlation between the emission peak ratio and viscosity; from the data in Figure 4.9b, this correlation is indeed observed for DMSO, 90% glycerol, and PEG_{600} solutions with the particularly close correlation between PEG_{600} and 90% glycerol. Since in the glycerol mixture, a Newtonian solvent, we are confident that emission band ratios for P_2NMe_3 accurately reflect the temperature-dependent change in viscosity, we can now conclude that the same is true for the polymer melt, PEG_{600}.This leads us to the possibility that in polymer melts, the temperature-dependent viscosity change is independent of molecular weight. Indeed, this is reflected in the Williams-Landel-Ferry and Beuche models for free volume as a function of temperature[25,28]. An aqueous solution is a noteworthy exception, since here the rotor P_2NMe_3 seems unable to accurately measure solution viscosity. However, this is perhaps not surprising given the low solubility of P_2NMe_3 in water and its strong propensity to aggregate, as shown earlier in this Chapter.

4.6 Conclusions

In conclusion, in this Chapter we have investigated the response of a molecular rotor to viscosity, modulated by an addition of high molecular weight polymer to simple organic solvents such as methanol, chloroform, water and DMSO. We have tested the applicability of the dimer to provide the molecular weight of polymers dissolved in these simple solvent, when measured in highly diluted solutions. Where the dimer is preferentially solvated near the polymer chain, we were able to use conformational behaviour to predict the polymer molecular weight. Our proof-of-principle preliminary study indicates that in dilute polymer solutions, the porphyrin dimer can accurately measure intrinsic viscosity, which can be used to report the molecular weight of dissolved polymers. However, the precise quantitative parameters needed for this measurement are not clear at present.

Although the molecular weight measurements in chloroform were successful, the measurements in water and methanol were marred by errors. We attributed these errors to a different conformation of polymer chains in solution, as well as the problem of aggregation of the P_2NMe_3 dimer in water. Overall, we conclude that the ratiometric measurements of P_2NMe_3

are not suitable for molecular weight determination of dissolved polymers. Firstly, the cellular environment is expected to be significantoly crowded, and as such the dilute solution conditions will never be satisfied. Secondly, our investigation revealed a very large dependence of results on the nature of the solvent and, consequently, the shape of the polymer chains in this particular solvent. Due to a very complex mixture of environments that might be found in a biologically relevant situation, we thus conclude that the ratiometric measurements of dimers are unlikely to provide a reliable measure of the molecular weight of a surrounding polymers and/or macromolecules.

We have next investigated the applicability of the dimer ratiometric fluorescence to determine viscosity in highly concentrated polymer melts. We judge this situation to be close to the setting that may be found in tightly packed cellular domains, such as lipid membranes, or concentrated macromolecular solutions in certain cell compartments, such as synaptic cleft or a cellular cytoskeleton.

Thus we have shown that we are able to measure the temperature-dependent viscosity behaviour of concentrated polymer melts and the viscosity predicted by the dimer matches the values measured experimentally by mechanical methods, as well as matches viscosity determined by ratiometric measurements in methanol/glycerol mixtures, and DMSO. Based on this promising data, we were able to confirm that in the case of polymer melts, the relationship between polymer melts the relationship between viscosity and temperature is independent of polymer molecular weight, but rather determined by the 'free volume' of the polymer's conformation.

4.7 References

1. Onogi, S., Masuda, T., Miyanaga, N. & Kimura, Y. Dependence of viscosity of concentrated polymer solutions upon molecular weight and concentration. J. Polym. Sci. Part A-2 Polym. Phys. 5, 899–913 (1967).

2. Rao, M. V. S. Viscosity of dilute to moderately concentrated polymer solutions. Polymer (Guildf). 34, 592–596 (1993).

3. Kumar, N. G. Viscosity–molecular weight–temperature–shear rate relationships of polymer melts: A literature review. J. Polym. Sci. Macromol. Rev. 15, 255–325 (1980).

4. Weissberg, S. G., Simha, R. & Rothman, S. Viscosity of dilute and moderately concentrated polymer solutions. J. Res. Natl. Bur. Stand. (1934). 47, 298 (1951).

5. Staudinger, H. Ueber hochpolymere Verbindungen. Kolloid-Zeitschrift 51, 71–89 (1930).

6. Simha, R. The Influence of Brownian Movement on the Viscosity of Solutions. J. Phys. Chem. 44, 25–34 (1940).

7. Debye, P. The Intrinsic Viscosity of Polymer Solutions. J. Chem. Phys. 14, 636 (1946).

8. Debye, P. & Bueche, A. M. Intrinsic Viscosity, Diffusion, and Sedimentation Rate of Polymers in Solution. J. Chem. Phys. 16, 573 (1948).

9. Fedors, R. F. An equation suitable for describing the viscosity of dilute to moderately concentrated polymer solutions. Polymer (Guildf). 20, 225–228 (1979).

10. Mehl, J. W., Oncley, J. L. & Simha, R. Viscosity and the shape of protein molecules. Science 92, 132–3 (1940).

11. Harding, S. E. The intrinsic viscosity of biological macromolecules. Progress in measurement, interpretation and application to structure in dilute solution. Prog. Biophys. Mol. Biol. 68, 207–62 (1997).

12. Fujita, H. & Kishimoto, A. Interpretation of Viscosity Data for Concentrated Polymer Solutions. J. Chem. Phys. 34, 393 (1961).

13. Doolittle, A. K. Studies in Newtonian Flow. II. The Dependence of the Viscosity of Liquids on Free-Space. J. Appl. Phys. 22, 1471 (1951).

14. Loutfy, R. O. Fluorescence probes for polymer free-volume. Pure Appl. Chem. 58, 1239–1248 (1986).

15. Mark, J. E. Physical Properties of Polymers Handbook. (AIP Press, 2007). doi:10.1007/978-0-387-69002-5

16. Einstein, A. Eine neue Bestimmung der Moleküldimensionen. Ann. Phys. 19, 289 (1906).

17. Einstein, A. Über die von der molekularkinetischen Theorie der Wärme geforderte Bewegung von in ruhenden Flüssigkeiten suspendierten Teilchen. Ann. Phys. 322, 549–560 (1905).

18. Valeur, B. & Berberan-Santos. Molecular Fluorescence. Methods 8, (2012).

19. Einstein, A. Zur Theorie der Brownschen Bewegung. Ann. Phys. 19, 371 (1906).

20. Flory, P. J. Principles of Polymer Chemistry. (Cornell University Press, 1953). at <http://www.cornellpress.cornell.edu/book/?GCOI=80140100145700>

21. Tanford, C. Physical Chemistry of Macromolecules. (John Wiley & Sons Inc, 1961). at <http://www.amazon.com/Physical-Chemistry-Macromolecules-Charles-Tanford/dp/0471844470>

22. HESS, E. L. & COBURE, A. The intrinsic viscosity of mixed protein systems, including studies of plasma and serum. J. Gen. Physiol. 33, 511–23 (1950).

23. Balaz, M., Collins, H. a, Dahlstedt, E. & Anderson, H. L. Synthesis of hydrophilic conjugated porphyrin dimers for one-photon and two-photon photodynamic therapy at NIR wavelengths. Org. Biomol. Chem. 7, 874–88 (2009).

24. Mark, J. E. Polymer Data Handbook. (Oxford University Press Inc., 1999).

25. Bueche, F. Segmental Mobility of Polymers Near Their Glass Temperature. J. Chem. Phys. 21, 1850 (1953).

26. Law, K. Y. Fluorescence probe for microenvironments: anomalous viscosity dependence of the fluorescence quantum yield of p-N,N-dialkylaminobenzylidenemalononitrile in 1-alkanols. Chem. Phys. Lett. 75, 545–549 (1980).

27. Victor, J. G. & Torkelson, J. M. On measuring the distribution of local free volume in glassy polymers by photochromic and fluorescence techniques. Macromolecules 20, 2241–2250 (1987).

28. Williams, M. L., Landel, R. F. & Ferry, J. D. The Temperature Dependence of Relaxation Mechanisms in Amorphous Polymers and Other Glass-forming Liquids. J. Am. Chem. Soc. 77, 3701–3707 (1955).

V. Viscosity measurements in biomimetic lipid membranes

Having established the capacity of the porphyrin dimer to measure the viscosity of both isotropic liquids (Chapter III) and polymer suspensions (Chapter VI), we sought to measure the viscosity of lipid membranes. We hypothesize that the fluidity of the membrane bilayer is related to the *free volume* between phospholipid tails. This chapter discusses membrane viscosity, measured by fluorescence spectroscopy, in order to establish grounds and conditions for imaging it in larger lipid structures. Our interest in lipid membrane fluidity stems from the fact that the fluidity of membrane bilayers is thought to be important for its impact on the biochemical function of the cell membrane and the mechanical aspects of the membrane's function.

5.1 Currently existing non-imaging methodologies for the measurement of bilayer viscosity

5.1.1 Bilayer fluidity, friction and viscosity

In Chapter I, we define membrane viscosity by listing the physical origins of friction in the hydrocarbon region. Among them: the length and degree of saturation of lipid chains, as well as composition of lipid bilayers that determine thermodynamic behaviour. We also establish that our definition of bilayer viscosity is a three-dimensional measurement describing the hydrophobic, hydrocarbon region of the membrane. Given this definition, here we aim to compare our definition of membrane viscosity against existing parameters in literature such as membrane fluidity, bending rigidity and monolayer density. These parameters are widely used to describe the mechanical properties of a bilayer under strain, as such they are directly related to the two dimensional surface viscosity of membranes as well as the three-dimensional viscosity of the hydrocarbon region of membranes. However, bending rigidity, elasticity and compressibility are generally measured under conditions of applied stress, as in membrane

aspiration or during membrane motion, as in fluctuation analysis, both of which require the measurement of macroscopic membrane deformation rather than a microscopic measurement of probe behaviour or motion[1]. The following section briefly summarises the most common biophysical methods that investigate the viscoelastic behaviour of membranes by monitoring membrane motion.

5.1.2 Mechanical methods

Of the most common mechanical methods that measure membrane viscosity, micropipette aspiration is the best established. Several of these studies have already been performed on living cells, including, that by Hochmuth et al., 2000, and Henricksen et al., 2003[2,3]. However, membrane aspiration is more commonly applied to model membranes[4,5], whereby negative pressure is applied to the surface of a giant unilamellar vesicle by a micrometric pipette under a microscope. The surface of the vesicle is deformed into the micropipette in degrees proportional to the negative pressure applied[4]. The magnitude of deformation is calculated from changes in vesicle radius (of the remaining circular portion) giving the change in vesicular area. Resistance to deformation is determined by a variety of bilayer properties, on both macro and microscopic scales. For instance, the rate of deformation of the vesicle can be related to curvature and osmotic pressure: macroscopic properties, as well as individual phospholipid area and membrane density: microscopic properties. In aspiration experiments, separation of these effects can be difficult. The same is true for fluctuation analysis, a technique that measures thermodynamic membrane deformation without the application of external stress: a bilayer's natural undulations within the membrane reveal viscoelastic properties. However, the extrapolation of a value for membrane viscosity can be complicated: Seifert et al., 1993 observe that relaxation of membrane undulations are determined by two independent viscous modes, which are separated by their characteristic rate constants[6]. At slow time scales, i.e. membrane fluctuations at 0.003 MHz[6], both monolayers have 'relaxed densities' and lipids can reorient, making intermonolayer friction the primary source of dissipation (often measured as 'area

compressibility'. At fast timescales, (0.3 MHz and above)[6] however, where both monolayers are static and lipids cannot move independently, the apparent bending rigidity increases. Thus the speed of undulations can also be taken as a signifier of the area of the measurement on the bilayer surface. For instance, viscous modes of dissipation at fast timescales for undulations dominate on the microscopic scale of measurement (nm) such as the surrounding media whereas the frictional component of translational reorientation of lipids is observed at slow timescales for undulations. We suggest that the former component, the slow reorientation of lipids is closely related to the viscosity measurement performed by molecular rotors. However Seifert et al., 1993 show that these two effects are coupled; and the combination requires a complicated derivation to separate them[6]. The measurement of lipid lateral reorientation within the bilayer is the subject of multiple imaging techniques that measure the translational diffusion coefficient D_T. These techniques, D_T and its relationship with three-dimensional membrane viscosity are the subject of Chapter VI. This chapter discusses the physical origins of membrane viscosity as it is measured by the porphyrin dimer, which is different from the parameters commonly used in the existing literature on the subject and we believe can supplement a biophysical interpretation of the viscoelasticity of lipid bilayers.

5.1.3 Spectroscopic measurements of membrane viscosity

Prior to the increase in availability of microscopy for spatial resolution in membrane systems, membrane viscosity was measured by spectroscopy in bulk solutions of suspended lipid vesicles; fluid-filled sacs enclosed by lipid bilayers. Lipid vesicles are formed with fluorescent dyes embedded within the bilayer, creating opportunities for spectroscopic study. For the measurement of bilayer viscosity in bulk systems, well established techniques include measurement of pyrene eximer formation[7,8], and fluorescence depolarisation or molecular 'tumbling' [9,10]. The fluorophore pyrene forms emissive excimers, at a rate proportional to the viscosity of the surrounding medium; this property can be used to measure diffusion, and extrapolate viscosity. Alternatively, in measuring the changing angles of polarised light from

selected fluorophores, the tumbling of a molecule can be monitored, and has been shown to be proportional to the surrounding viscosity. Chapter I describes the theoretical basis of judging viscosity by anisotropy measurements of fluorescence depolarisation. Recently, imaging of rotational correlation times (θ, in nanoseconds), the characteristic parameter defining molecular tumbling, has been used to provide spatial resolution of viscosity in cells. However, it is commonly a technique performed on homogenous samples of large volume (i.e. bulk solution) [11]. Table 5.2, at the end of this chapter, summarises some instances of fluorescence depolarisation used to measure viscosity in pure lipid systems. We use this data for comparison against viscosity measurements performed by molecular rotors, with the hypothesis that the measurements will be roughly equivalent due to the nature of the measurement, involving a single fluorophore, that can either internally rotate (molecular rotor approach) or tumble (anisotropy approach).

We propose the use of our molecular rotor, the porphyrin dimer in order to directly and easily measure the viscosity of model membranes. In the literature there exists a wealth of evidence that suggests membrane fluidity is a crucial determinant of cellular health and biochemical functionality[12–14]. For this reason, we sought to quantify and image the dynamics of membrane viscosity using our chosen molecular rotor, the porphyrin dimer. The nature of the viscosity measurement is described in detail in Chapters III and IV. This methodology is applied to a range of biomimetic lipid bilayers that we use as a model for the intact cellular membrane.

5.2 Variables affecting membrane viscosity

During our investigation of membrane viscosity, we determined that there are four basic requirements that must be met in order for our viscosity measurements to be comparable with literature values and legitimately related to membrane fluidity as it influences cellular function.

1. *Incorporation:* The dimer must be able to incorporate into a bilayer from aqueous solution in a disaggregated state. This requirement is specific to the measurement of

vesicles or cells suspended in bulk solution as uniform localisation of the dye is assumed within the membrane. Figure 5.1a demonstrates the hypothetical insertion of the dye into the membrane from aqueous solution. Here, the dye is disaggregated in the external aqueous phase (Figure 5.1a (1)) such that electrostatic interactions can take place between exposed *meso* substituents (Figure 5.1a (2)) and the phosphate head groups of phospholipids. After this initial interaction, we expect that the hydrophobic core of the porphyrin macrocycles will have sufficient energetic driving force to pull the dimer into the hydrocarbon region ((Figure 5.1a (3)) such that both macrocycles are embedded and the dimer is anchored vertically by its *meso* substituents (Figure 5.1a (4)). Data in Figure 5.1b shows the increase in emission peak ratio over time after a solution of the charged porphyrin dimer is added to a suspension of lipid vesicles. This data reflects the gradual attachment, and potentially, embedding of the dimer into the hydrocarbon region of the bilayer. Likewise, the emission intensity of the dimer increases drastically upon association with the vesicles , as shown in Figure 5.1d.

2. *Localisation:* The orientation and depth of the dimer within the membrane is dependent upon various features of the dimer including the charge of its substituent, size, and rate of aggregation in water. Interactions between the dye and the membrane are likely to be complex such that a proportion of dimer molecules may be partially embedded (Figure 5.1c (1)), or only surface attached (Figure 5.1c (2)). Fluorescence from dimer molecules in these positions may contribute to the bulk signal from a bulk sample. We must be confident that a significant majority of dimer molecules are solubilised within the hydrocarbon region such that we can be sure the conformational dynamics of the dimer are truly reflecting viscosity (Figure 5.1c (3)) rather than other types of interactions with the membrane.
3. *Lipid: Dimer Ratio:* We have described the localisation of the dimer into the lipid membrane as a dynamic process, which competes with another major dynamic process in aqueous solution, aggregation. If added to lipid vesicle suspensions in excess, it is

reasonable to assume that a large proportion of dimer molecules will aggregate prior to entering the bilayer. They may also cause aggregates to form on the surface of vesicles, perturbing the curvature and preventing the entry of monomeric dimer molecules. During these processes, the porphyrin dimer continues to contribute fluorescence signal to the bulk measurement, potentially occluding signal from membrane-embedded dimer molecules. Data in Figure 5.1d shows the increase in intensity and blue shift of its emission maximum once the dimer solution is allowed to interact with lipid vesicles. This can disrupt the ratiometric method, as bulk measurements will show a combination of emission from planar, viscosity-insensitive aggregates and real viscosity-sensitive monomers. For this reason, we seek to reduce the relative amount of dimer to lipid upon formation of the bilayer.

4. *Bilayer integrity*: In bulk measurements, we must ensure that the bilayers we measure are consistent in phase and composition as these factors will have a vast impact upon the measured viscosity of the membrane. This does not apply to microscopy, where we would have spatial resolution of the sample. This is one of the potential strengths of our technique and is discussed in further detail in Chapter VI.

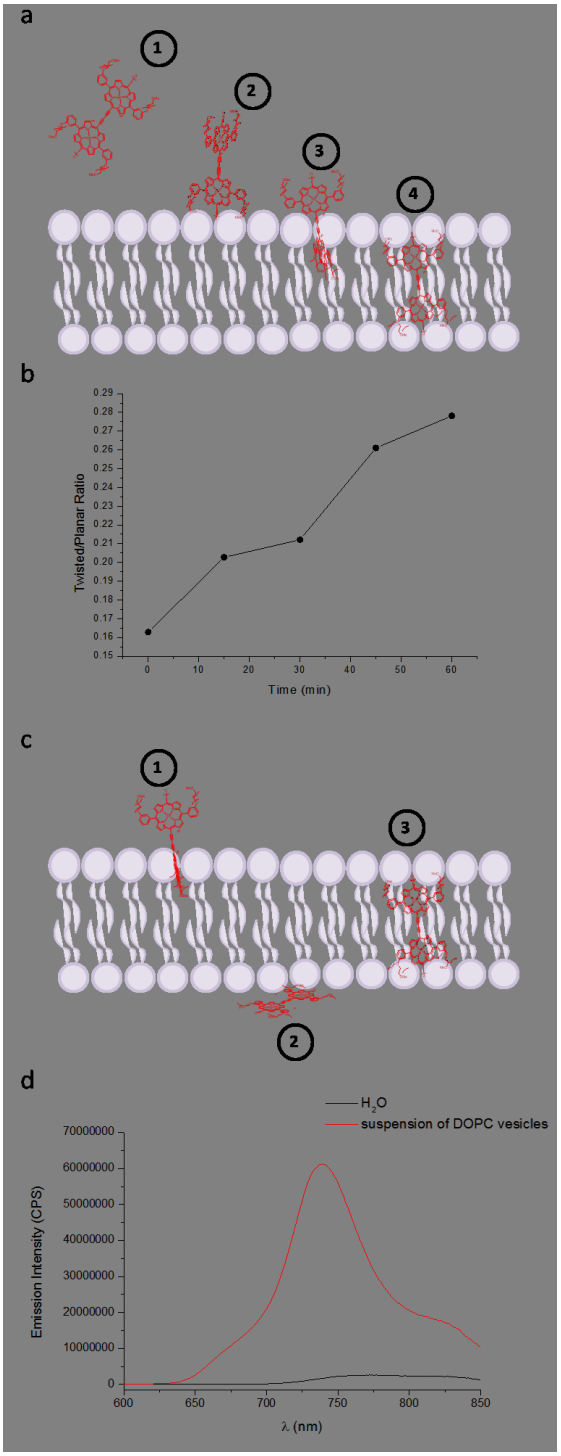

Figure 5.1: a) Hypothesized mechanism for dimer penetration into the bilayer (1) dimer soluble in aqueous solution; (2) meso-position association with phosphate head groups; (3) hydrophobic macrocycles penetrate the hydrocarbon region; (4) dimer embedded in the bilayer, aligned vertically. b) P_2NMe_3 (0.33 μM) emission ratio peaks increase over time in DOPC Large Unilamellar Vesicles (LUVs) suspensions (23.1 μM), indicating the dimer's interaction with the bilayer is time-dependent. c) Possible interactions between the dimer and bilayer (1) partial penetration into the bilayer; (2) surface association; (3) full penetration of the bilayer with vertical alignment. d) P_2NMe_3 (0.33 μM) emission spectra recorded in water (black) and suspension of DOPC LUVs (23.1 μM) (red).

5.2.1 Insertion into the membrane

Amphiphilic phosphate groups isolate the hydrocarbon region of the membrane from the aqueous compartment. The dimer must penetrate this phosphate layer in order to incorporate into the hydrocarbon region of the bilayer. Insertion into the membrane by this route requires that the hydrophobic driving force of the macrocycles be strong enough to overcome the attractive tension between phosphate head groups and remain completely disaggregated as only the monomer is likely to be small enough for penetration of the bilayer. An aggregate would likely significantly disrupt the bilayer. As such, the dimer's solubility in the hydrocarbon phase is crucial to successful incorporation into the membrane. The size and charge of the dimers will strongly affect their capacity for disaggregated insertion into the bilayer.

We tested four dimers - two cationic (P_2C_2NMeI, P_2NMeI) one anionic (P_2Suc) and one neutral (P_2) - in their capacity for incorporation into the membrane bilayer. To do this, we made large unilamellar vesicles (~180 nm) by extrusion in two different ways (the full description of methodology is available in Chapter II, Section 2.1.4):

- *Pure lipid stock vesicles*: here, a known quantity of stock solution of lipid in chloroform is placed under vacuum to remove the organic solvent. Once dehydrated, water is added to the lipid solution and allowed to dissolve. The mixture is repeatedly passed through a small diameter porous membrane (200 nm) at high pressure (~ 80 psi), resulting in a highly homogenous solution of unilamellar vesicles at approximately the same diameter as the membrane pores. The dimer solution is then added to the suspension of vesicles and allowed to incubate for a minimum of 30 minutes.
- *Lipid and dimer mix vesicles*: the extrusion process is identical to that for the pure lipid stock vesicles. However, the pure lipid stock in chloroform is mixed with a solution of porphyrin dimer in a 1:1 methanol, chloroform solution. The molar ratio of lipid to dimer is known and held constant. In order to maximise solubility of the dimer in solution, the extrusion process is carried out at 60 °C.

Using a suspension of the resulting vesicles, we compared viscosity measurements from the two preparations. In the samples of pure lipid, dimer solution was added after preparation of the vesicles and we expected to see the dimer penetrate the bilayer and incorporate itself into the hydrocarbon region of the membrane. We compared this with what we considered a control measurement of vesicles made from a mixture of the dimer with pure lipid stock in which interactions with aqueous solution do not influence the dimer's partitioning in the membrane For instance, the dimer will display a significantly higher emission ratio after penetration into the membrane, and this is a time-dependent process. Figure 5.1b shows data that supports our initial hypothesis of a time-dependent uptake. This process is also strongly affected by the concentration ratio of dimer to lipid, as we have previously mentioned. In Figure 5.1b, at a dimer: lipid ratio of 1:70, the emission ratio increases for 60 minutes during incubation. Subsequent experiments are carried out at a ratio of 1:1000, where the dimer's emission ratio stabilizes after approximately 30 minutes due to the increased surface area of lipid vesicles for penetration. The comparison between these two preparation methods elucidates membrane penetration and localisation by the dimer and will be a major component of making the porphyrin dimer suitable for use in living cells.

In order to gather putative evidence of the dimer's location within the membrane, we used various spectroscopic features (emission maximum, peak ratio etc.) that we had characterised earlier. Chapter III summarises the effect of solvent polarity on the λ_{max} of emission for the charged dimers where emission from polar solvents is red shifted relative to that of non-polar solvents. Using this property, we used the λ_{max} as a first indicator of whether or not the majority of the signal originates from polar, aqueous solution outside or non-polar hydrocarbon region within the membrane. Similarly, we used the viscosity-sensitive ratio of the bimodal emission peaks to confirm the position of the dimer within the membrane as we know from literature that the room temperature fluidity of a DOPC membrane is much higher than that of water[15–17]. This method of assigning the dimer's sub-membrane locale is not without shortcomings, particularly considering that the measurement is performed on bulk solution where spatial

resolution is lost. Emission signal could be originating from a range of sub-membrane locales from dimer molecules in varying states of membrane penetration, surface attachment to the vesicle, or states of aggregation. We have seen that aggregation forces planarization of the dimer and, along with low signal intensity and the red-shifted, broadened emission spectrum, gives a very low emission ratio (e.g. Figure 5.1 d, aqueous environment). Similarly, we hypothesize that surface attachment to the vesicle will give an artificially low ratio due to the planarization of the dimer as it associates with the lateral surface. However, we used this early spectroscopic data to investigate whether incorporation of the dimer into the membrane was at all possible. We used our findings to optimise experimental conditions for subsequent measurements.

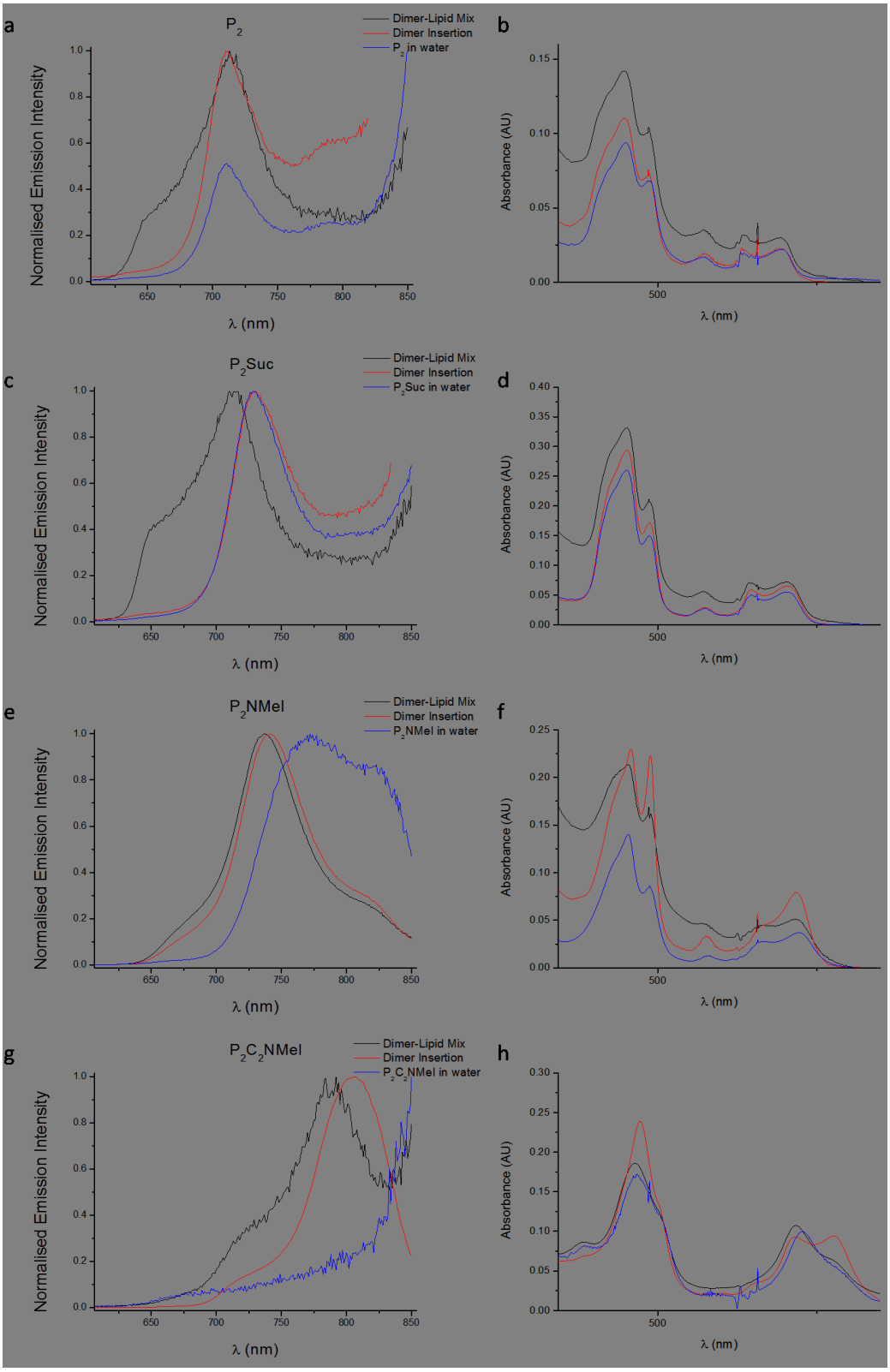

Figure 5.2: Normalised emission spectra (left column) and Absorption spectra (right column) recorded for dimers in water (blue) or incorporated in DOPC LUVs: either added to LUV solution post pure lipid vesicle preparation (black), or preformed from a dehydrated mixture of DOPC and dimer to ensure a full dimer insertion into the bilayer (red). Dimer concentrations are kept at 1μM, and lipid concentrations at 70μM. a,b) P_2, λ_{ex} at 440nm; c,d) P_2Suc, λ_{ex} at 458nm; e,f) P_2NMeI, λ_{ex} at 447nm; g,h) P_2C_2NMeI, λ_{ex} at 463nm.

Figure 5.2 shows absorption and emission data obtained from DOPC vesicle suspensions of four different dimers (emission spectra were obtained by excitation at the corresponding absorption λ_{max} of the high energy 'twisted' confomer). Black lined spectra represent emission spectra of vesicles that are preformed from a mixture of DOPC and dimer, used as a control for membrane localisation; we term this preparation method 'dimer-lipid mix'. Red lined spectra, alternatively, represent the emission spectra recorded from DOPC vesicles prepared from pure lipid and then incubated with dimer solution for 30 min; termed 'dimer insertion'. Blue lined spectra show emission and absorption of the dimers in water, at the same concentration of the dimer. For these experiments, the concentration of all dimers was kept equal, at 1μM, such that the dimer: lipid ratio and thus lipid concentration (70 μM) can be kept equal in order to avoid errors due to concentration effects of either component. Due to differences in the molar extinction coefficient, ε, in water, of all dimers, the Absorbance at the λ_{ex} varies. Furthermore, absorption spectra shown in Figure 5.2 is strongly affected by scattering of incident light by the suspension of LUVs, giving a scattering curve that decreases in intensity with wavelength (this is discussed in further detail later in this Chapter).

Note, all emission spectra shown in Figure 5.2 were corrected for the decreasing sensitivity of the emission detector with increasing wavelength. In regions of particularly low intensity this led to artefacts, i.e. a perceived increase in intensity at long wavelengths, which was due to the correction function, rather than to the actual emission from the sample.

Comparison of λ_{max} of both emission and absorption measurements allows us to speculate on the interaction of the dimer with LUVs in free solution. We expected to observe a number of possible interactions, possibly in combination with one another:

i) Aggregation of the dimer in aqueous solution, and no interaction with LUVs, which would be signified by red shifted emission, broad absorption peaks and low emission ratio observed;

ii) Surface association of the dimer with the LUV, which would keep it disaggregated (and resulting in no shift or broadening in spectra). This mode of interaction, however will likely report no increase in twisted/planar emission ratio signifying preferential face to face binding to a bilayer surface.

iii) Partial or total penetration of the dimer into the vesiclular bilayer, in which case we expect to observe no spectral shift and the appearance of a twisted emission band, signifying high viscosity.

We speculate that the charge and size of the dimer will dictate the likelihood of these interactions and we will be able to interpret emission and absorption spectra for indications of the above interactions.

Figures 5.2a and b show that the neutrally charged dimer, P_2 has extremely low emission in water and broadened absorption peaks (blue spectra, Figure 5.2 a,b respectively), consistent with our expectation that it aggregates in aqueous environment. When P_2 is allowed to incubate with DOPC LUVs, we observe a small increase in emission intensity and the same broadened absorption peaks (red spectrum, Figure 5.2 a, b). In contrast, when DOPC LUVs are formed from a mixture of lipid and dimer, we observe stronger emission and the appearance of the twisted band (black spectrum, Figure 5.2a, b). From this data, we conclude that P_2 cannot penetrate the LUVs from solution, consistent with the low emission and low emission peak ratio observed in the 'dimer-insertion' samples. Instead, the emission spectrum is more similar to that observed in water, a unimodal peak but with slightly augmented emission, indicative of some degree of surface-association with LUVs.

Similarly, P_2Suc, the anionic dimer, displays a strong coincidence between the emission and absorption spectra in water (blue, Figure 5.2 c, d) and when incubated in solution with DOPC LUVs (red, Figure 5.2c, d). Emission from preformed DOPC containing P_2Suc LUVs (black, 5.2c) displays a higher emission ratio and a blue shifted emission maximum, signifying good

incorporation into the membrane bilayer. From this, we conclude that, similar to P_2, P_2Suc is unable to penetrate LUVs from external aqueous solution. Instead, it appears that P_2Suc remains solvated in the aqueous fraction, possibly due to extensive aggregation.

The cationic dimers, P_2NMeI and P_2C_2NMeI (Figure 5.2 d-h) behave markedly differently than the neutrally charged, P_2 and anionic P_2Suc discussed above. Emission from P_2NMeI after incubation with DOPC LUVs (red, Figure 5.2e), in particular, shows good coincidence with emission from P_2NMeI 'dimer-lipid mix' LUVs (black, Figure 5.2f). Indeed, absorption spectra of these samples show a strong increase in absorption and a sharpening of the absorption maxima, signifying a well-solvated disaggregated state of the dimer. Furthermore, the emission ratio (Figure 5.2 e) between the pre-incorporated and subsequently mixed samples is roughly equal and the emission maximum is approximately the same. We believe this is good evidence that the cationic dimers can (at least partially) penetrate the lipid bilayer for access to the viscous hydrocarbon region of the bilayer.

The longer cationic dimer, P_2C_2NMeI also displays good coincidence between the 'dimer-insertion' and 'dimer-lipid mix' samples (Figure 5.2g). However, in this case, the control experiment, 'dimer-lipid mix' which shows emission from LUVs with the dimer embedded in the bilayer is extremely weak. We take this as evidence that the long cationic dimer, P_2C_2NMeI does not fit well within the DOPC bilayer, perhaps due to the increased length and thus increased distance of the positive *meso* substituents from the phosphate groups. Indeed, absorption spectra of P_2C_2NMeI (Figure 5.2h) show that the 'dimer-lipid mix' spectrum coincides with that in water, showing broad absorption peaks and reduced absorption intensity. From this, we speculate that P_2C_2NMeI is aggregated under aqueous conditions, and disaggregates upon incubation with LUVs due to surface association, planarising the dimer. This is supported by the low emission ratio observed in emission (red, Figure 5.2g). However, P_2C_2NMeI does not incorporate well into lipid bilayers, with possible partial penetration (increased twisted peak emission, Figure 5.2g) but overall predominant evidence of aggregation.

Overall, the data shown in Figure 5.2 gives good evidence that cationic dimers (in particular P_2NMeI) are the most likely to successfully incorporate into lipid bilayers from aqueous solution. The length of the dimer is a possible variable determining the extent of penetration into bilayer, with the shorter dimer, P_2NMeI displaying better evidence of incorporation and viscosity-sensitivity than the longer dimer P_2C_2NMeI.

5.2.2 Localisation of the dye within the lipid bilayer

Once a bilayer is assembled, the hydrocarbon and phosphocholine regions are expected to display fundamentally different viscous behaviours. Literature predicts that in its liquid phase, the hydrocarbon region acts as an isotropic liquid with Newtonian properties[18]. The phosphocholine region, on the other hand, consists of tightly packed charged molecules with large ionic volumes that form the interface between the hydrocarbon region and the excluded aqueous solution[18]. Thus, from fluorescence spectroscopy, we expect to observe a combination of viscous effects within the membrane in different micro-domains; the hydrocarbon region, the phosphocholine layer and the interface between them. Considering this, the partitioning of the porphyrin dimer into the membrane must be such that rotation about the butadiyne bond is free of interactions with and steric hindrance from the phosphate head groups.

We have calculated the length of the dimer along the butadiyne axis to be approximately 30.09 Å (See Appendix B), which is compatible with the depth of the DOPC bilayer at 38 Å, as reported in the literature by studies from molecular dynamics[19] and ^{2}H NMR[20]. We approximated the volume of the dimer to be 54.12 nm^3 (Appendix B), as a cylinder, to account for the freedom of rotation in the butadiyne bond. From this, we hypothesize that the hydrophobic core of the dimer will be able to fit in the hydrocarbon region of the membrane. If both macrocycles are solvated by the hydrocarbon region, the charged *meso* substituents will be exposed to the aqueous solution, acting as anchors holding the dimer vertically across the width of the membrane. With this orientation, viscosity-dependent rotation of the macrocycles will be affected only by the hydrocarbon region. We assumed that the negative charge of the phosphate

head group would interact with positively charged *meso* substituents. However, we were also aware that there could be interaction between the phosphate head group and the Zn^{2+} at the centre of the porphyrin macrocycle. This would raise the relative position of the dimer within the bilayer and interfere with free rotation within the hydrocarbon region as shown in Figure 5.1c.

To settle these concerns we turned to neutron reflectrometry. We characterised the structure of a floating deuterated 1,2-distearoyl-*sn*-glycero-3-phosphocholine (DSPC) membrane bilayer in the liquid disordered phase at 50 °C prior to and after incubation with an aqueous solution of the positively charged dimer P_2C_2NMeI for 12 hours. These experiments are carried out in collaboration with Dr Arwel Hughes at ISIS neutron facility at Rutherford Apple Laboratories in Didcot, Oxford. Preparation of a floating lipid bilayer suitable for neutron reflectrometry experiments has been described previously in Hughes et al., 2008 [21]

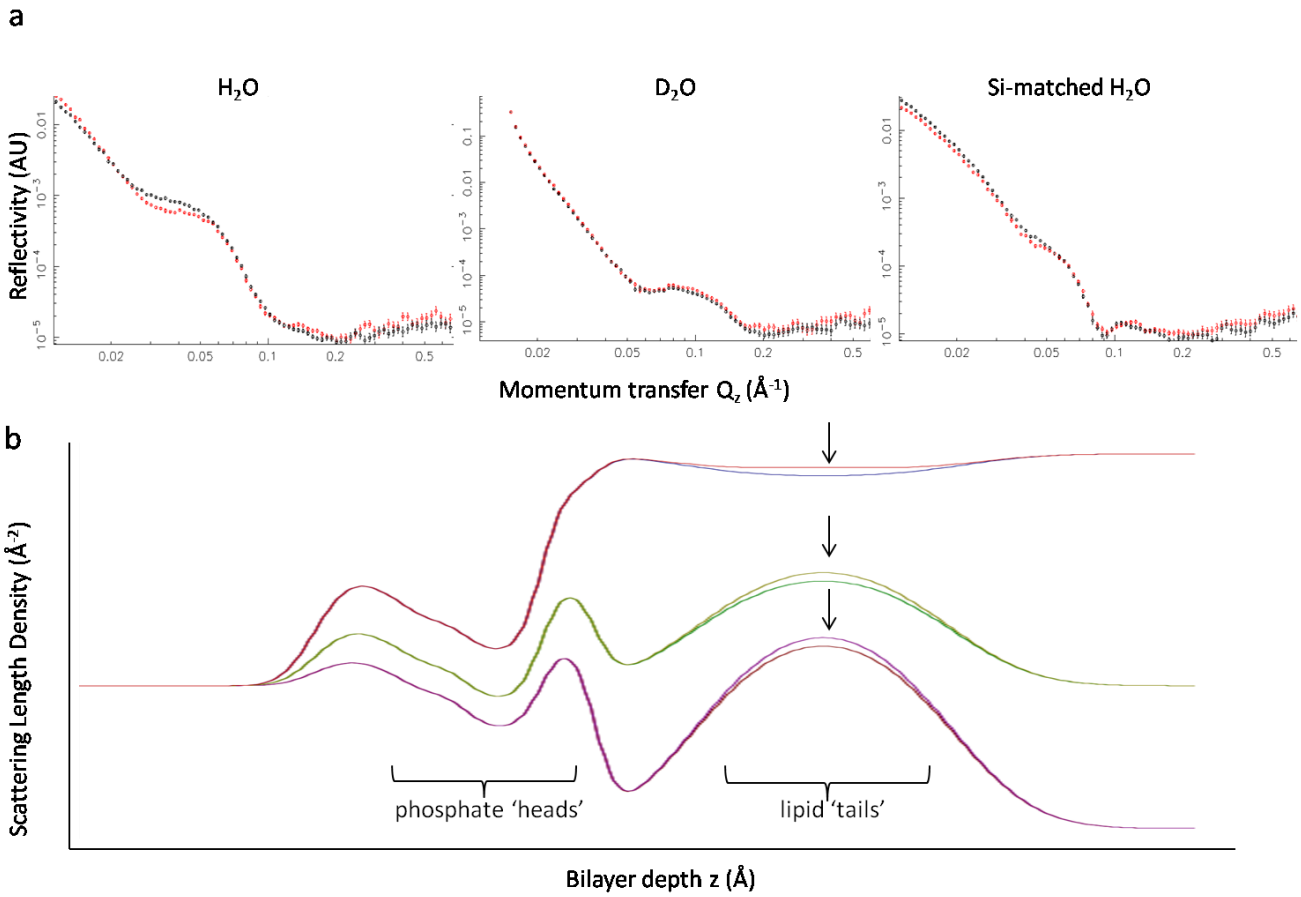

Figure 5.3: a) Neutron reflectrometry data for the floating self-assembled bilayer[21] composed of d[70]-DSPC: P_2C_2NMeI, at 70:1, recorded at 50 °C; momentum transfer Q (Å) against Reflectivity (AU) for three solvents exchanged over the bilayer prior to (black) and after incubation with the dimer for 12 hours (red). b) Structural information is extracted from neutron reflectivity data when plotted in scattering length density, showing a change in the lipid tail region of the bilayer.

Neutron reflectrometry is a non-destructive specular reflection technique often used to characterise lipid membranes at wavelengths that are approximately equal to lipid mono and bi-layer thickness, giving high resolution of structure. Figure 5.3 shows the results of a neutron reflectrometry experiment on a floating d[70]-DSPC (an 18 carbon lipid chain, fully saturated but with hydrogenated choline group) the bilayer at 50 °C, where the intensity of reflected neutrons is plotted against the momentum transfer vector q_z, a function of the neutron angle of incidence, θ, as shown in equation (5.1).

$$q_z = \frac{4\pi}{\lambda} \sin\theta \qquad (5.1)$$

As θ is varied, neutrons penetrate into the depth of the membrane, along the *z*-axis. Momentum transfer, increases with increasing θ (equation 5.1). Structural components are associated with depth into the membrane, intensity profiles of phosphate 'head' groups and hydrocarbon lipid 'tails' can be separated and identified, as shown in Figure 5.3.

In the sample chamber, contrast in neutron scatter between the bilayer and its solvent must be maximised to achieve the highest possible resolution for the experiment. In NR, this contrast is determined by differences in the 'scattering length density' (SLD) between atomic nuclei. For example, the SLDs of hydrogenated water and of deuterated water are -0.56 $Å^{-2}$ and 6.35 $Å^{-2}$, respectively (the SL of hydrogen is negative due to a 180° phase shift of the neutron radiation after interaction). Relative to the SLDs of other atomic nuclei that are major components of biological molecules (e.g. oxygen, phosphorus, nitrogen etc.), the difference in scatter between hydrogen and deuterium is extremely large, making them a good pair for the creation of contrast in neutron reflectrometry. In the experiment shown in Figure 5.3, the bilayer is composed of phospholipids with hydrogenated phosphocholine head groups and deuterated lipid tails while the assembled bilayer is supported on a silicon block, under a large volume of solvent. Due to the difference in scattering intensity, the deuterated lipid region of the bilayer has most contrast when it is suspended in H_2O. However, the three elements of the bilayer sample can be identified using a method of varying the solvent while the bilayer remains in the sample chamber: in H_2O, both the silicon support and the lipid region contrast against the solvent, in D_2O, the silicon support and the phosphocholine groups are contrasted. In order to contrast the whole bilayer alone, a mixture of D_2O and H_2O is produced that matches the scattering of the Silicon block, which then disappears into the solvent 'background'. These three solvent conditions (H_2O, D_2O and Si-matched H_2O) are shown in Figure 5.3a, where reflectivity is plotted against the momentum transfer vector Q. The bilayer is measured in these three solvents prior to (black, Figure 5.3a) and after (red, Figure 5.3a) incubation with the dimer. As expected, the panel showing the deuterated bilayer under H_2O shows the highest reflectivity at low values of Q. Each floating lipid bilayer has a slightly different intensity profile though

characteristic curves in both the shallow 'heads' and deep 'tails' regions. For this reason, we needed to characterise the bilayer before incorporation of the (hydrogenated) dimer in order to be able to compare intensity profiles reliably. The bilayer without dimer is shown as black in Figure 5.3a, and after incubation with the dimer is shown in red. Figure 5.3b shows the inverse of 5.3a: scattering length density against the bilayer depth with data from all three solvents represented. In all three curves, the changes observed upon incubation of the dimer-solution with the membrane, are observed at greater depths within the membrane, towards the hydrophobic tail region. This confirms our hypothesis and preliminary data that positively charged dimers can penetrate a pure lipid bilayer. We were constrained by the limited ISIS beam time to test the positioning of only one dimer within the bilayer. However, as shown in our fluorescence study (Figure 5.2) we have evidence that cationic dimers behave similarly upon interaction with the phospholipid bilayer, and we used this reasoning to extrapolate that the remaining cationic dimers would also penetrate the bilayer and localize in the hydrocarbon region.

We determined that the scattering length density of the bilayer with the dimer included is composed of both the bilayer and the dimer:

$$SLD_{total} = \chi_1 SLD_1 + \chi_2 SLD_2$$

Where χ_1 and χ_2 are mole fractions;

$$SLD_{total} = \chi_{dimer} SLD_{dimer} + (1 - \chi_{dimer}) SLD_{lipid}$$

Here X_{dimer} is the mole fraction of the dimer within the bilayer. Having measured the bilayer alone, prior to incubation with the dimer, we made the assumption that the SLD of this sample reflects scattering from pure phospholipid components of the bilayer and can be calculated

from fitting of the data shown in Figure 5.3a. In order to calculate the contribution of the SLD_{dimer} to the SLD_{total}, we calculated the scattering length density of the porphyrin dimer using:

$$SLD_{dimer} = \frac{\sum_i n_i b_i}{V}$$

Where we sum the scattering length, *b*, of *n* atoms of the molecule of the component atoms of the dimer (*i*) and the molecular volume of the dimer is *V*. SLD_{dimer} is found to be:

$$SLD_{dimer} = \frac{5.7604 \times 10^{-3}\ \mathring{A}}{5412.41\ \text{Å}^3} = 1.04 \times 10^{-6}$$

Using the value $SLD_{lipid} = 6.01\text{x}10^{6}$ Å^{-2}, we found the change in SLD after incubation with the dye. The SLD_{total} is found to be less than the SLD_{lipid} because the deuterated lipid component of the bilayer occupies less volume in the presence of the dimer, which is hydrogenated and so does not contribute significantly to the scatter from the bilayer. As such, SLD_{lipid} - $SLD_{total} = 3.655\text{x}10^{-7}$ Å^{-2}. Using this value, in order to determine the χ_{dimer}, we calculated:

$$(6.01 \times 10^{-6} - 3.655 \times 10^{-7}) = \chi_{dimer} 1.04 \times 10^{-6} + (1 - \chi_{dimer}) 6.01 \times 10^{-6}$$

$$(5.6445 \times 10^{-6}) = \chi_{dimer} 1.04 \times 10^{-6} + (1 - \chi_{dimer}) 6.01 \times 10^{-6}$$

$$(5.6445 \times 10^{-6}) = (\chi_{dimer} 1.04 \times 10^{-6}) + (6.01 \times 10^{-6}) - (6.01 \times 10^{-6} \chi_{dimer})$$

$$(-3.655 \times 10^{-7}) = \chi_{dimer} (-4.97 \times 10^{-6})$$

$$0.0735 = \chi_{dimer}$$

Thus we can calculate that the bilayer is composed of 7% P_2C_2NMeI after incubation under these experimental conditions. 7% is a sufficiently small proportion of dimer within the bilayer that we observe no changes in the structurally-dependent scattering curves, we are confident we have not perturbed bilayer structure. While promising, this data is collected at a very high concentration of dimer in solution, (lipid: dimer is approximately = 13:1). Furthermore, our

data proves less clear regarding the surface of the bilayer than it does about the lipid region of the bilayer, we are limited in observing the outside of the bilayer where dimer molecules may aggregate. On the other hand, we have highly resolved data that proves the dimer is able to penetrate the bilayer and incorporate into the hydrocarbon region. However, the conditions of the experiment are highly significant in that higher concentrations of dimer, the length of the hydrocarbon chain, the saturation state of the hydrocarbon region, and temperature of incubation may alter the nature of incorporation into the bilayer. We sought to characterise these conditions, particularly that of the concentration of the dimer, relative to the bilayer, which we term dimer to lipid ratio.

5.2.3 Treating emission data obtained in highly scattered LUVs solutions

Fidelity of our measurements in the lipid bilayer system required that we use as low amount of dimer as possible within the bilayer. However, in order to carry out spectroscopic measurements, we had to ensure that the dimer signal can be observed in highly scattering vesicular suspensions. Imaging on the microscope is less sensitive to the effects of scattering but our initial investigations, presented here, are bulk measurements. For this reason, we carried out studies to find the lowest possible lipid: dimer ratio that was suitable for spectroscopic measurements. The nature of the measurement requires that we keep the dye concentration the same over all samples, and so the lipid concentration was changed in each sample. However, single measurements would not fully describe the viscosity-sensitivity of the dye within these environments. The lipid viscosity of a bilayer is sensitive to temperature variation, which is ideal for bulk spectroscopy, having shown in Chapter II that the dimer's ratiometric viscosity sensitivity is temperature independent. We sought to test whether dye penetration, disaggregation and viscosity sensitivity were affected by experimental conditions while we manipulate lipid viscosity. We explored how the relationship between the dimer's emission and viscosity of the lipid bilayer were dependent upon the ratio between dimer and lipid concentration between 2 % and 0.02 % (50:1 to 5000:1 lipid: dimer ratios).

However, our ratiometric analysis was hindered by intense scattering from the vesicle suspensions. Figure 5.4 shows the nature of scattering from colloidal suspensions of the vesicles' size and its interference with analysing the dimer's emission spectrum for ratiometric analysis. Emission spectra of lipid: dimer vesicle suspensions have an asymmetric baseline with relatively high intensity (Figure 5.4).

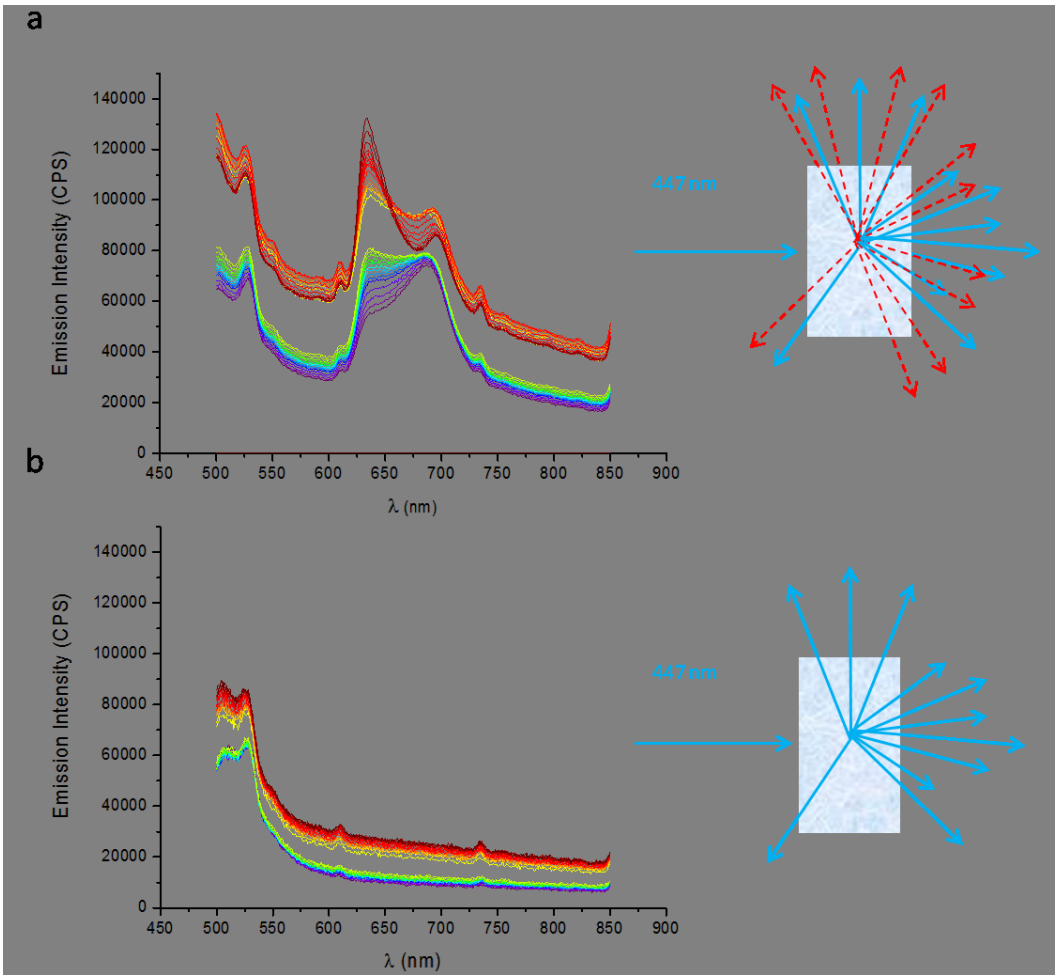

Figure 5.4: a) Fluorescence spectra of P_2 (0.33 μM; λ_{ex} = 447 nm; 1000:1 lipid: dimer ratio) from pre-formed DPPC LUVs. The emission from the dimer is seen on top of the asymmetrical baseline tentatively assigned to the incident light scattering by concentrated solutions of LUVs (right) scheme of emission from P_2 and scattering of excitation light b) emission spectra recorded following 447 nm excitation of pure DPPC LUVs. This signal is assigned to pure scattering from LUVs. c) Scheme of showing simultaneous scattering and emission of light by the solution of P_2 in DPPC LUVs.(left) scattering of excitation light by LUVs, as inferred from scattering curve in spectra.

The baseline created by scattering decreases in intensity with increasing wavelength, and has evidence of structure at roughly 540 nm. Upon measuring the emission spectra of lipid vesicles

lacking any fluorescent dye, excited at 447 nm, we observe the same asymmetric baseline, skewed towards smaller wavelengths. We attribute this curving baseline to scattering of incident light by the lipid vesicle suspension. Excitation light at 447 nm is strongly scattered in all directions by the vesicle suspension and becomes mixed with fluorescent light collected from the sample (Figure 5.4).

Small colloidal suspensions, such as those of lipid vesicles, are known to scatter light in a manner dependent upon size of the particle and wavelength of light, the relationship between them is described by the following:(equation 5.2)

$$x = \frac{2\pi r}{\lambda} \tag{5.2}$$

Where r is the radius of the spherical particle in suspension and λ is the wavelength of incident light. Values of x can describe the likely nature of scattering: when $x < 1$, such that $r < 1/10$ of λ, the sample is effectively transparent for the wavelength, λ. The reverse is also true, such that short wavelengths have a large value of x, and are highly scattered. This is due to the relative curvature of the interacting particle: if an incident light wave interacts with a particle of the same or larger radius, the curved surface of the particle is sufficiently large to refract the incident light, sending it in a different direction. Longer wavelengths will have a much lower likelihood of interaction with the surface of the particle and will continue in the same direction. For lipid vesicles with diameter 180 nm, excited at 447 nm, x = 2.52. In these cases, where $x < 1$, excitation light is strongly scattered in all directions including towards the direction of the fluorometer's detector and is mixed with the dimer's emitted light which is dispersed by the emission monochromator, Figure 5.4c.

To enable data interpretation for samples with significant scattering observed we developed a correction method, as shown in Figure 5.5. Scattering decreases with wavelength, as predicted by equation 5.2, and some structure is clearly visible at 525 cm, with smaller peaks at 615 and 730 nm (Figure 5.6a) which we have identified as possible Raman peaks, with chemical shifts of

3300, 6000 and 8700/cm, respectively. Literature values for Raman shifts of phospholipid bilayers have reported a peak for DPPC at 2881/cm[22], and/or a broad Raman band from 2800-3080/cm[23], while Suga et al., have assigned a Raman shift for choline at 3040 cm/cm[24]. It appears that the thickness of the bilayer, the curvature of lipid vesicles and the number of lamellae in the vesicle can strongly affect the observed Raman shift[22–24]. Coupled with scattering of excitation light as we showed above, this is one possible explanation for the structure observed in Figure 5.5a for plain DPPC LUVs excited at 447 nm.

Irrespecive of the nature of the features in the spectra, we have assumed that in the region between 615 and 728 nm, the signal of pure LUV sample can be modeled by a straight line. Figure 5.5b shows a superimposition of the original scattered spectra and the modeled linear baseline which was created using a geometrical tool in Origin 8.5 which uses existing points in the spectrum to estimate a linear baseline between two points. Consequently, this calculated baseline was subtracted from each spectrum. Our efforts to fit the baseline, or to use the temperature-dependent scattering curve as collected from plain LUVs (Figure 5.5a) proved to introduce a large amount of noise to the spectra, which complicate the accuracy of our measurements of emission ratio.

Figure 5.5c shows the resulting of spectra after subtraction of the linear baseline in the region 615-728 nm. This method was found to show good agreement between the hypothesized spectra of the dimer in lipid vesicles and the manually determined baseline subtracted spectra. Figure 5.5d shows twisted/planar emission peak ratios plotted against temperature in bulk solutions of lipid vesicles of mixtures of DPPC and the neutral dimer P_2. For this system, we clearly observe a strong relationship between the emission peak ratio and temperature which was expected from this particular lipid systems and is discussed in more detail in the next section.

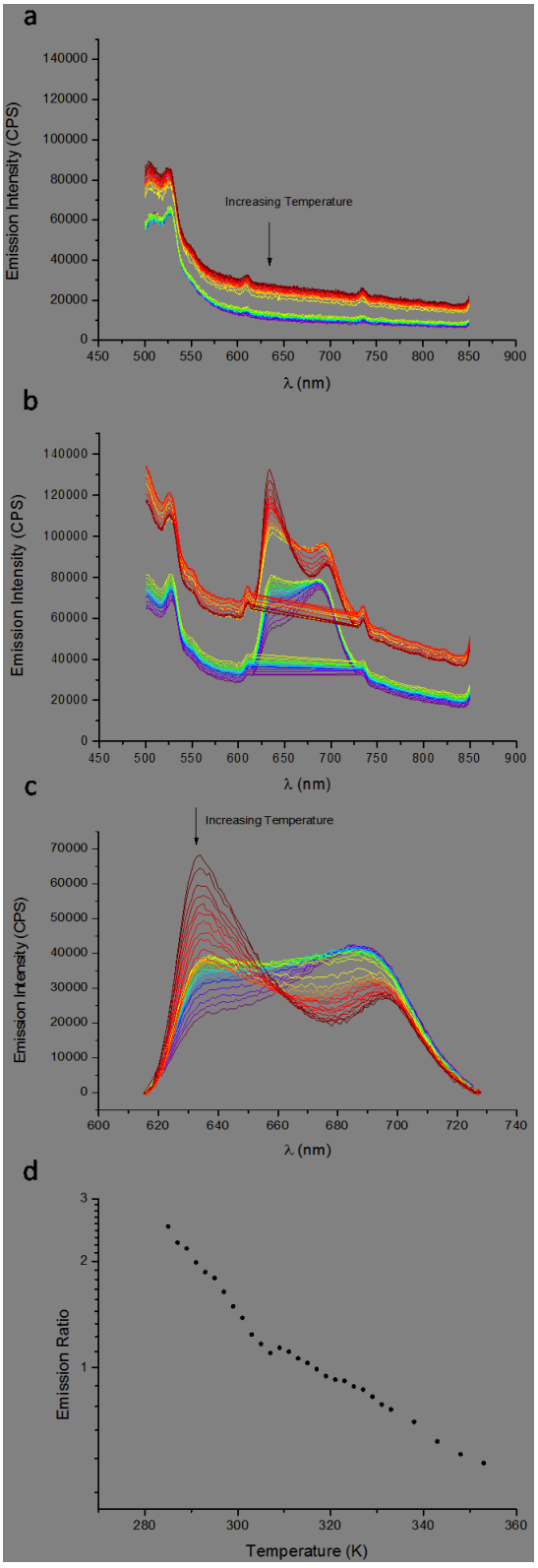

Figure 5.5: a) Scattering curve of λ_{ex} = 447 nm in DPPC LUVs at varying temperature (273-353 K; red to blue); b) P_2 emission in DPPC LUVs (1000:1 lipid: dimer ratio) interpreted as a mixture of fluorescence and scattering, the spectra are corrected manually using a linear approximation of the scattering between 600 and 730 nm; c) emission spectra after subtraction of the linear region from the baseline, d) P_2 dimer emission ratios in DPPC LUVs at varying temperature.

5.2.5 Dimer to lipid ratio

Having established the way to treat the data recorded at high concentration of lipid, we have moved on to study the temperature dependence of the twisted/planar ratio, in LUVs prepared at various dimer/lipid ratios.

The hydrocarbon region of lipid membranes is known to adopt physical phases determined by temperature. Below a given temperature, the hydrocarbon chains of phospholipids adopt 'gel' like behaviour. Above the gel transition temperature (T_g), however, the 'liquid' phase is observed in two discrete regimes: liquid ordered (L_o) and liquid disordered (L_d). The L_d and L_O phases both have a predictable, Arrhenius-like relationship with temperature similarly to isotropic liquid phases. However, the nature of the relationship, the slope of the temperature-dependent viscosity curve is different and can be observed.

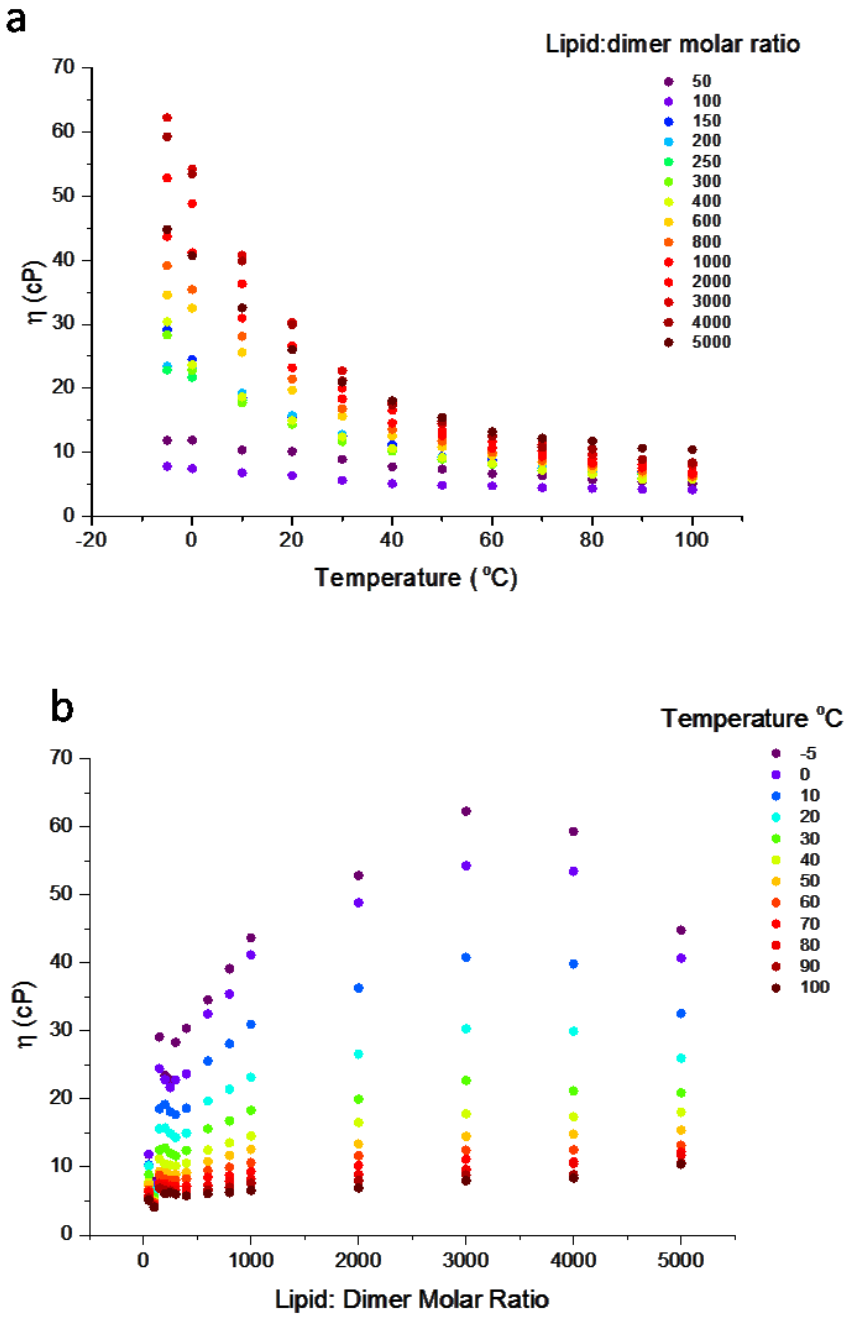

Figure 5.6: a) P_2NMe_3 ratiometric viscosity measurement of DOPC LUVs at varying temperature change with lipid: dimer ratio b) P_2NMe_3 ratiometric viscosity measurement of DOPC LUVs have varying temperature-dependent viscosity at different ratios (λ_{ex} = 454 nm).

Figure 5.6 shows viscosity measurements from suspensions of doped LUVs made from 1,2-dioleoyl-*sn*-glycero-3-phosphocholine (DOPC), which has an 18 carbon lipid chain with a single double bond at C_9. We extruded LUVs made from mixtures of DOPC and the cationic dimer P_2NMe_3 (as shown in Chapter I). Due to the same charge and similar size, we expect that the

partitioning behaviour of this dimer will be similar to that shown in Figure 5.1c of the other positively charged dimer, P_2NMeI in membranes at the beginning of this chapter. Figure 5.6 displays temperature scans over the range 268 – 373 K of samples varying in dimer: lipid ratio. For DOPC membranes, as observed in LUVs in suspension, the gel transition temperature is at 253 K, outside of the temperature range that we tested. We expected to see an increase in the measured viscosity (ratio of the dimer's two emission peaks) commensurate with decreasing temperature of the sample, an Arrhenius-type relationship between temperature and viscosity. All temperature curves show an increase in viscosity with decreasing temperature. However, the absolute emission band ratio increase measured over the same temperature range increases with the lipid: dye ratio, as is demonstrated in Figure 5.6b. The lowest lipid: dimer ratio, 50:1, demonstrates a temperature dependent increase from 5 cP to 11 cP, whereas the ratio 3000:1 increases from 8 cP to 63 cP over the same range. Moreover, the viscosity measured at 373 K increases gradually with lipid: dye ratio. This effect is related to the intermediate solubility of dimer molecules which are separated into two fractions, those that are dissolved in water and those that are associated with the vesicle surface. The dimer's emission signal will be a combination of the membrane-embedded fraction *and* the aqueous fraction due to a dynamic equilibrium between membrane penetration or surface attachment. The aqueous fraction displays low viscosity and is unable to access the hydrocarbon region which displays the strong temperature dependence upon viscosity. The combination of these signals reduces the apparent viscosity of the LUV because the low viscosity signal from the aqueous solution is present. Moreover, the relative quantity of dimer in the aqueous solution will determine by how much the apparent viscosity of the suspension is reduced. Therefore as lipid: dimer ratio increases, (reducing the probability of free dimer in the aqueous phase) the magnitude of temperature induced viscosity change as measured by the emission spectrum of the sample also increases, signified by a steeper curve on Figure 5.6a. However, the composition of the sample only dictates the temperature-dependent curve up to roughly 1000:1 lipid: dimer molar ratio. At 1000:1 ratio, the vast majority of the signal originates from the membrane-embedded fraction.

In order to maximise the dimer's signal from solution by avoiding scattering, we used the lowest possible lipid: dimer ratio with the steepest temperature-dependent curve, at 1000:1 lipid: dimer molar ratio. All subsequent experiments are performed at this ratio. The temperature-dependent viscosity curve at lipid: dimer ratio 5000:1 drops below that of the lower ratios. This can be explained as an artefact from increased scattering at such high lipid concentrations, and demonstrates the necessity for low lipid concentrations for the accuracy of the experiment.

5.3 Detection of Lipid Phase in Saturated and Unsaturated Lipids

The degree of saturation of the hydrocarbon tail of a phospholipid is crucial in determining phase transition temperatures, fluidity and temperature-dependent viscosity. Saturated hydrocarbon tails occupy more volume within the membrane and are generally more rigid than unsaturated carbon chains, which we believe can be reflected by an increase in viscosity as measured by molecular rotors. The length of the carbon chain also affects the apparent changes in phase behaviour though the effect is much smaller than that of saturation. We compare the temperature-dependent viscous behaviour of DOPC, a monounsaturated lipid of 18 carbons, and dipalmitoylphosphatidylcholine (DPPC), a saturated lipid of 16 carbons as shown in Figure 5.7.

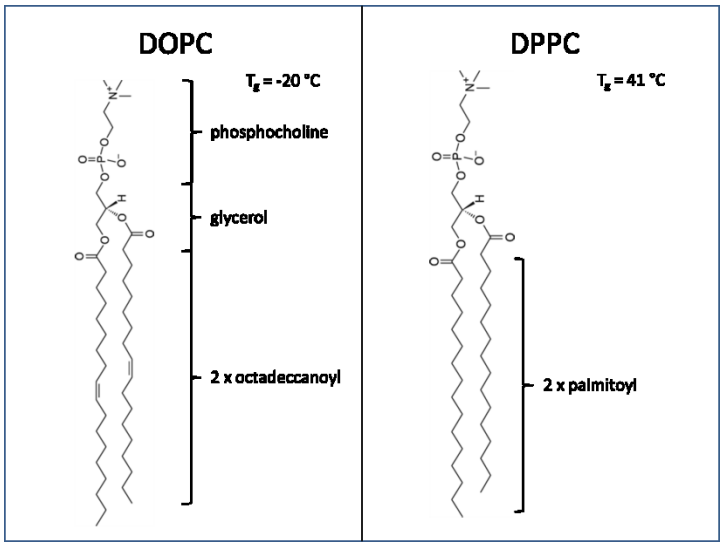

Figure 5.7: Structures of DOPC (C_{18}:1) and DPPC (C_{16}:0) lipids. Figures adapted from Avanti Polar Lipids Inc.

We tested the temperature-dependent viscous behaviour of pure-lipid LUV suspensions of either of these lipids using the cationic dimer P_2NMe_3.

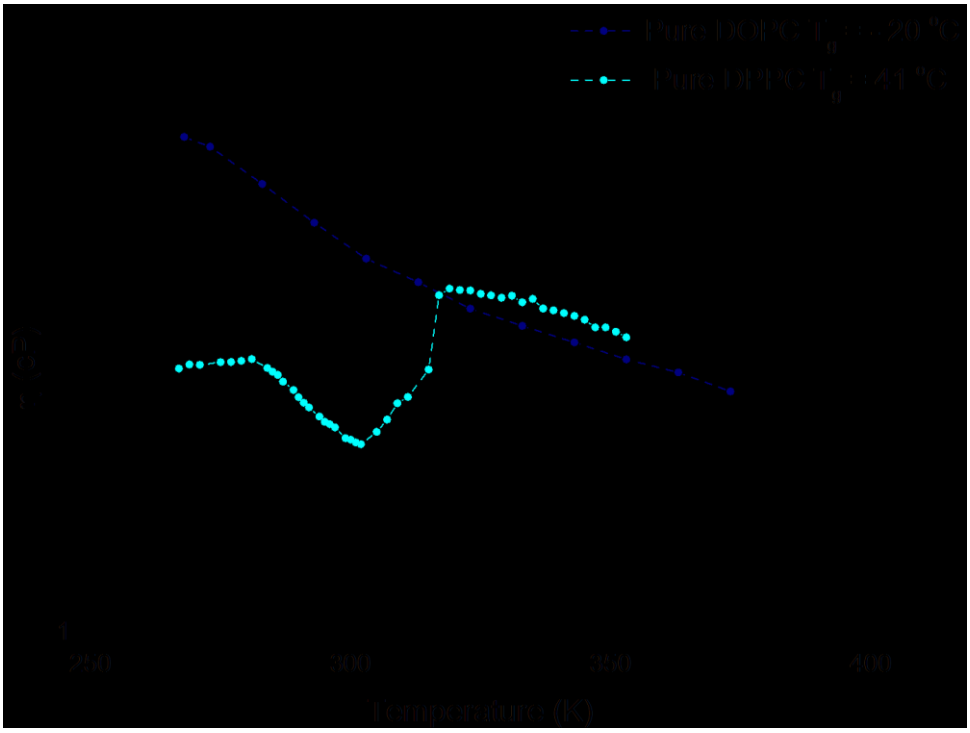

Figure 5.8: P_2NMe_3 in LUV suspensions at varying temperature (273-373 K), where temperature-dependent viscosity in DOPC (dark blue) is shown to change approximately linearly; whereas data recorded in DPPC (cyan) shows irregular change with temperature .(λ_{ex} = 454 nm; lipid: dimer ratio is 1000:1)

Figure 5.8 shows the temperature-dependent viscosity curves of these two lipids in a bilayer. In contrast to the regular viscosity increase at low temperatures observed in DOPC vesicles, samples of DPPC vesicles exhibit much more complex behaviour with respect to temperature; an initial increase in viscosity up to the transition temperature of DPPC, a sharp drop from 314 to 308 K and a subsequent increase in viscosity from 303 to 283 K. This is unexpected behaviour, literature suggests a gradual increase in DPPC bilayer viscosity upon lowering temperature[15,25]. We note that a predictable and linear viscosity-temperature relationship collapses at 314 K, the gel transition temperature for DPPC. One explanation for the apparent drop in viscosity at low temperatures is that the dimer is ejected from its embedded position within the membrane at the transition between L_d and gel phases. We know from Wu et al., 2013, and Dent et al., 2015 that the molecular rotor BODIPY-C_{10} partitions to the hydrophobic

region of the lipid bilayer in its L_d phase [25,26]. After performing similar experiments varying the temperature of DPPC vesicles Wu et al., showed that a hydrophobic molecular rotor, boron-dipyrromethene conjugated to a C_{10} chain (BODIPY-C_{10}) is similarly ejected from the hydrocarbon region of the membrane after a transition into the L_o phase. Given this combined data, it follows that the charged dimer is most likely ejected from the bilayer below transitional temperature. We conclude that the positively charged dimer is not suitable for the accurate measurement of the viscosity of membrane viscosity during the phase transition from liquid to gel.

We sought to test this explanation, and to confirm whether or not the charged *meso* substituents are primarily responsible for ejection of the P_2NMe_3 from the membrane. We performed the same experiment with the neutrally charged dimer P_2, which, due to its hydrophobicity, has a higher likelihood of remaining within the DPPC membrane after its transition to L_o phase. Chapter III (Figure 3.9) shows our viscosity calibration of the emission peak ratio of P_2 in Castor oil, in varying temperature which was used to calculate viscosity values of vesicles measured with P_2. Figure 5.9 shows the temperature-dependent viscosity measurement of DPPC membranes as measured by the P_2 dimer.

The data shown in Figure 5.10 (red) shows a change in the slope of the temperature-viscosity behaviour at roughly 309 K, just below the T_g of DPPC at 315 K. We observe an increase in the gradient of the curve relating temperature and viscosity after 309 K, as is predicted in the gel phase of phospholipid membranes. The transition we observe at 309 K rather than at 315 K is most likely indicative of a pre-transition, as described by Lichtenberg et al., 1984[27–29]. Riske et al., 2009 predict that this is due to the coexistence of L_o and L_d phases prior to the emergence of a homogenous phase[29]. Also, Lichtenberg et al., 1984 and Heimberg et al., 2000 predict that pre transition behaviour in vesicles depends on the size and distribution of vesicles[27,28]. Our experimental chosen experimental conditions including vesicle size, direction of temperature gradient, and equilibrium time can be used to explain the observation of the pre transition in

DPPC phase, but nevertheless, this is indicative of a complete transition between the L_d and L_o phases, which we have successfully observed.

The data in Figure 5.9 is shown in terms of emission ratio rather than viscosity, to be able to better compare the behaviour of the two dimers as they have different relationships between ratio and viscosity. The increase in ratio suggests a higher viscosity at low temperature, which is in agreement with our hypothesis regarding the hydrocarbon region of lipid membranes.

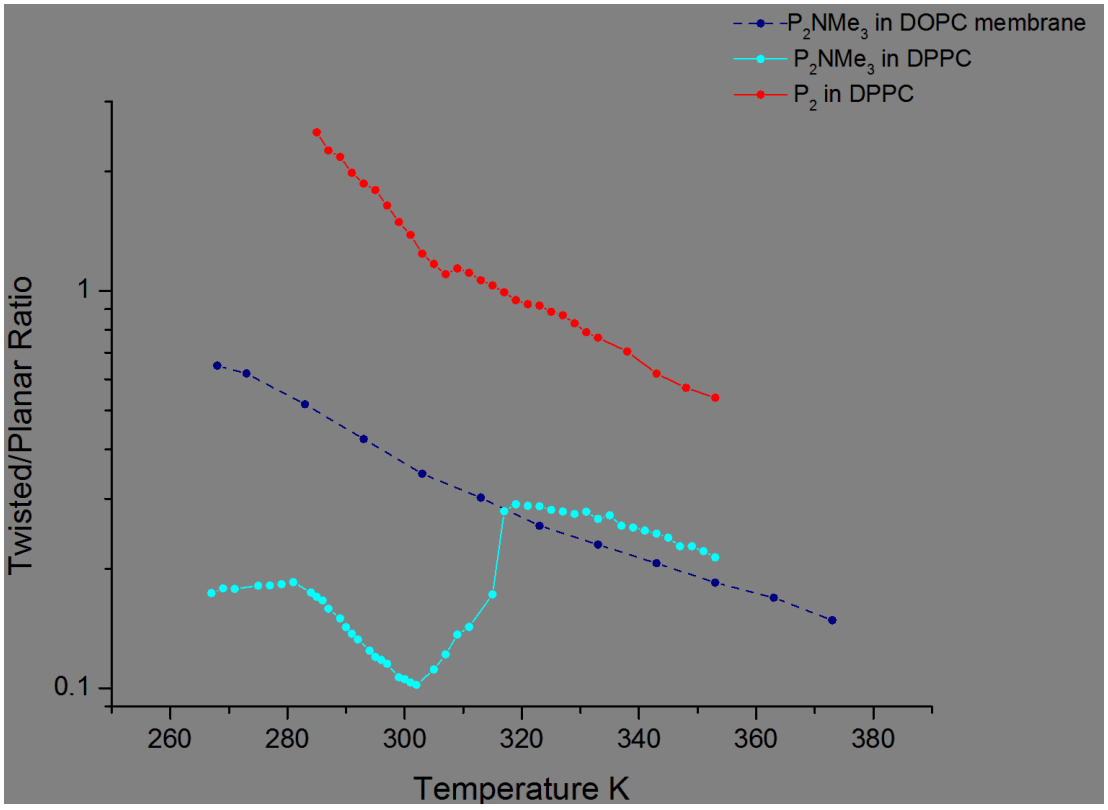

Figure 5.9: P_2 dimer emission in DPPC LUV suspension (λex = 447 nm) ratios are plotted against temperature (red) in comparison with P_2NMe_3 emission from LUV suspensions at varying temperature, DOPC (dark blue) and DPPC (cyan) λ_{ex} = 454 nm; (lipid: dimer ratio is 1000:1 for all samples)

We have evidence to suggest that the cationic charge in the *meso*-positions of the dimer prohibits its full solubility within the membrane. Alternatively, we have identified the neutrally charged dimer, P_2 as a suitably accurate and sensitive molecular rotor that can be embedded within the hydrocarbon region of the bilayer. We explain the disparity between measurements at high temperatures to the differences in membrane position of the two dimer species, based

on our understanding of the behaviour of the cationic dimer. The temperature-dependent viscosity of DPPC membranes taken with the P_2 dimer is considered the more accurate of the two data sets.

Thus we have shown the sensitivity of membrane viscosity measurements to a myriad of physical variables as well as to variables in sample preparation. We have shown that the accuracy of the measurement depends upon the method of dimer incorporation into the membrane, whether the vesicles are formed from lipid and dimer mixtures, or the dimer is inserted from aqueous solution. The ratio also strongly affects the validity of the bulk signal in minimising artefacts from dimer located in solution. Ultimately, the nature of the dimer species determines its location within the membrane and its accuracy for relating hydrocarbon viscosity, namely its size, charge, and concentration. In order to investigate these variables, we used temperature and the lipid species as modes of manifesting bilayer conditions such as phase. The following table summarises results from experiments relative to these variables. Table 5.1 summarises data from both the charged and neutral dimers, P_2NMe_3 and P_2 in LUV suspensions of the lipids DOPC and DPPC. Our data reveals that P_2NMe_3 consistently reports lower viscosities under the same conditions as P_2. We attribute this to weak attachment within the membrane, most likely with significant protrusion into the aqueous solution. Consequently, P_2NMe_3 is not probing the most viscous hydrocarbon region of the membrane.

Table 5.1: Summary of ratiometric viscosity measurements from dimers in LUV suspensions

Dimer	Lipid	Lipid: Dimer Ratio	Preparation Method	Temperature (K)	Measured viscosity (cP)
P_2NMe_3	DOPC	1000:1	From lipid: dimer mixtures	293	31.5
				310	27.8
			Insertion from aqueous solution	293	0.05
	DPPC	1000:1	Lipid: dimer mixtures	293	5.6
				310	6.39
P_2	DOPC	1000:1	Lipid: dimer mixtures	293	171
				313	132
	DPPC	1000:1	Lipid: dimer mixtures	293	207-214
				313	191
BODIPY C_{10} from [25]	DOPC	600:1	Lipid: dimer mixtures	293	177
				313	121
	DPPC	600:1	Lipid: dimer mixtures	293	-
				315	ca 170

In comparison, the dimer P_2 gives viscosity values reflecting the truly hydrocarbon environment of the bilayer. We have compared the results from the P_2 dimer with those from another hydrophobic molecular rotor, BODIPY-C_{10}, which were recently published by our group [25]. Due to the much smaller size of this rotor and lipid tail, it has been observed that BODIPY-C_{10} partitions to the hydrocarbon region of the membrane very successfully.[26] We found good agreement between the viscosity measurements for both DOPC and DPPC membranes between BODIPY-C_{10} and P_2, particularly for DOPC which was measured by P_2 to be between 170-177 cP at 293 K and by BODIPY to be between 122-132 cP at 313 K [25].

Table 5.2: Literature values of viscosity in plain bilayers using bulk methods measuring rotational diffusion or depolarisation

Technique	Ref	System	Fluorophore	Φ (ns)*	Temp (K)	η (cP)	
Fluorescence Depolarisation	15	DOPC/DOPC LUVs	DHA			DOPC	DPPC
					333.2	0	0
					322.5	25	50
					312.4	37.5	100
					302.9	60	1000
					294	100	1700
					277.6	240	3200
Fluorescence Depolarisation	30	DPC LUVs	DHA	6 (0.01) 50 (0.27)			
		DPC + 20% Cholesterol LUVs		6 (0.04) 50 (0.24)			
		DPC + 30% Cholesterol LUVs		6 (0.11) 50 (0.16)			
Fluorescence Depolarisation	31	Egg Lecithin micelles	Egg Lecithin-2-methylanthracene	3.4	293	140	
		Egg Lecithin micelles	Egg Lecithin-perylene	5.3		90	
		Egg Lecithin micelles	Egg Lecithin-9-vinylanthracene	11.1		180	
Fluorescence Depolarisation	32	lymphocyte lipid extract	DPH		298	175	
		lymphoma lipid extract	DPH			135	
Molecular rotor	33	DPPC vesicles LUVs	DCVJ		333	70	
					RT	120	
Molecular rotor	17	DLPC	FCVJ		RT	61	
Eximer formation	7	DPPC	Pyrene		RT	127	

* Depolarisation Φ was fit with two components, amplitude (contribution) from either component is shown in parentheses.

Table 5.2 summarises viscosity measurements from a range of viscosity-sensing techniques previously used in the literature. It is noteworthy that none of these techniques are currently able to provide the 'gold standard' for viscosity measurements. While the pyrene eximer formation is measuring the diffusion-controlled rate of a photochemical reaction, the measurement of fluorescence depolarisation (anisotropy) and molecular rotors method both provide the measure of rotational diffusion, connected to the free volume available for the fluorophore. The literature viscosity values summarised in Table 5.2 are in good agreement

with our measurements of pure lipid unilamellar bilayers. In Table 5.2, Lentz et al., 1976 report two correlation times. The contribution of either φ alters with increasing cholesterol in the membrane, making it more rigid. The authors, Veatch and Keller et al., attribute this to the ejection of the fluorophore with increasing rigidity of the membrane, this is in agreement with what we observed with the charged porphyrin dimer at the DPPC phase transition. We attribute the small changes in reported viscosity to the size and shape of molecular rotors, which have varying sensitivities to and dynamics ranges of viscosity, as was previosuly described in Chapter III.

5.4 Conclusions

We have examined the mode of interaction of a series of conjugated porpyrin dimers of various charge and size with lipid bilayers and established protocols for inclusion of a maximum proportion of sensor molecules in the bilayers, to enable measurements of viscosity with good signal/noise ratios. Using our knowledge of the dimer's spectroscopic sensitivity to its environment, we judged the localisation of the dimer in the lipid membrane. Localisation was observed to vary with the size and charge of the dimer, as judged by spectroscopy. We have consequently discovered that negatively charged dimers do not fully interact with lipid bilayers, while the positively charged dimers can incorporate efficiently, even from the aqueous solution. The neutral dimer P_2 was shown to aggregate in water and as such was not able to incorporate efficiently into the pre-formed lipid vesicles. However, when pre-incorporated in the lipid bilayer via formation of dry lipid:dimer films, shown very good incorporation and allowed viscosity measurements of the hydrocarbon region of the bilayer.

We have investigated in detail the effect of lipid: dimer ratio and lipid composition upon the viscosity measurements performed. Firstly we have established that the lipid:dimer ratios of at least 1000:1 are required to perform reliable measurements of viscosity, the high ratio necessary to prevent the interaction between reporter molecules. We have also shown that the charged dimer $\mathbf{P_2NMe_3}$ is suitable for measuring viscosity in liquid disordered phase of the

bilayers, however, the resulting viscosity values are low compared to the literature. We have interpreted this data to demonstrate that the low viscosity values reflect the positioning of **P_2NMe_3** in the membrane close to lipid heads (where viscosity is known to be lower) rather than deep in the viscous hydrocarbon tail region. We have also demonstrated that upon liquid-to-gel transition **P_2NMe_3** is expelled from the bilayer, resulting in irregular viscosity vs Temperature curve. As such **P_2NMe_3** is not deemed suitable to measure the liquid-to-gel transitions in bilayers or, indeed, the viscosity of the gel phase.

We have also shown that using the neutral uncharged porphyrin dimer P_2, we were able to measure the true viscosity of a hydrocarbon region of a phospholipid bilayer, in both the liquid ordered and the gel phases, as well as accurately determine the phase transition temperature.

Finally, we have compared the viscosity values obtained in our experiments with those available in the literature and consequently find a good match. Thus, comparison of this data with existing studies in literature confirms that the porphyrin dimer is indeed a molecular rotor, which measures three-dimensional viscosity which informs on rotational diffusion and free volume. However, care needs to be exercised when choosing an appropriate dimer for a certain measurement, as these experiments are extremely sensitive to the dimer localization and uptake by the bilayer.

5.5 References

1. Dimova, R. Recent developments in the field of bending rigidity measurements on membranes. Adv. Colloid Interface Sci. 208, 225–34 (2014).

2. Henriksen, J. R. & Ipsen, J. H. Measurement of membrane elasticity by micro-pipette aspiration. Eur. Phys. J. E. Soft Matter 14, 149–67 (2004).

3. Hochmuth, R. M. Micropipette aspiration of living cells. J Biomech. 33, 15–22 (2000).

4. Evans, E. A. & Hochmuth, R. M. Membrane viscoelasticity. Biophys. J. 16, 1–11 (1976).

5. Evans, E. A. New membrane concept applied to the analysis of fluid shear- and micropipette-deformed red blood cells. Biophys. J. 13, 941–54 (1973).

6. Seifert, U. & Langer, S. A. Viscous Modes of Fluid Bilayer Membranes. Europhys. Lett. 23, 71–76 (1993).

7. Kyu Han, S., Kim, J.-S., Lee, Y.-S. & Kim, M. Effect of Drug substances on the microviscosity of lipid bilayer of liposomal membrane. Arch. Pharm. Res. 13, 192–197 (1990).

8. Soutar, A. K., Pownall, H. J., Hu, A. S. & Smith, L. C. Phase transitions in bilamellar vesicles. Measurements by pyrene excimer fluorescence and effect on transacylation by lecithin-cholesterol acyltransferase. Biochemistry 13, 2828–2836 (1974).

9. Klausner, R. D., Kleinfeld, A. M., Hoover, R. L. & Karnovskys, M. J. Lipid domains in membranes. Evidence derived from structural perturbations induced by free fatty acids and lifetime heterogeneity analysis. J. Biol. Chem. 255, 1286–1295 (1980).

10. Hungerford, G. et al. Monitoring sol-to-gel transitions via fluorescence lifetime determination using viscosity sensitive fluorescent probes. J. Phys. Chem. B 113, 12067–74 (2009).

11. Levitt, J. A., Matthews, D. R., Ameer-Beg, S. M. & Suhling, K. Fluorescence lifetime and polarization-resolved imaging in cell biology. Curr. Opin. Biotechnol. 20, 28–36 (2009).

12. Zubenko, G. S., Wusylko, M., Cohen, B. M., Boller, F. & Teply, I. Family study of platelet membrane fluidity in Alzheimer's disease. Science 238, 539–42 (1987).

13. Ben-bassat, H., Polliak, A., Rosenbaum, S. M., Naparstek, E. & Shouval, D. Fluidity of Membrane Lipids and Lateral Mobility of Concanavalin A Receptors in the Cell Surface of Normal Lymphocytes and Lymphocytes from Patients with Malignant Lymphomas and Leukemias Fluidity of Membrane Lipids and Lateral Mobility of Normal Lymphocy. Cancer Res. (1977).

14. East, J. M., Jones, O. T., Simmonds, A. C. & Lee, A. G. Membrane fluidity is not an important physiological regulator of the (Ca2+-Mg2+)-dependent ATPase of sarcoplasmic reticulum. J. Biol. Chem. 259, 8070–1 (1984).

15. Lentz, B. R., Barenholz, Y. & Thompson, T. E. Fluorescence depolarization studies of phase transitions and fluidity in phospholipid bilayers. 2. Two-component phosphatidylcholine liposomes. Biochemistry 15, 4529–4537 (1976).

16. Lentz, B. R. Use of fluorescent probes to monitor molecular order and motions within liposome bilayers. Chem. Phys. Lipids 64, 99–116 (1993).

17. Nipper, M. E., Dakanali, M., Theodorakis, E. & Haidekker, M. A. Detection of liposome membrane viscosity perturbations with ratiometric molecular rotors. Biochimie 93, 988–94 (2011).

18. Marsh, D. General features of phospholipid phase transitions. Chem. Phys. Lipids 57, 109–120 (1991).

19. Reddy, A. S., Warshaviak, D. T. & Chachisvilis, M. Effect of membrane tension on the physical properties of DOPC lipid bilayer membrane. Biochim. Biophys. Acta 1818, 2271–81 (2012).

20. Filippov, A., Orädd, G. & Lindblom, G. Influence of Cholesterol and Water Content on Phospholipid Lateral Diffusion in Bilayers †. Langmuir 19, 6397–6400 (2003).

21. Hughes, A. V et al. Floating lipid bilayers deposited on chemically grafted phosphatidylcholine surfaces. Langmuir 24, 1989–99 (2008).

22. Nakata, A., Nomoto, T., Toyota, T. & Fujinami, M. Tip-enhanced Raman spectroscopy of lipid bilayers in water with an alumina- and silver-coated tungsten tip. Anal. Sci. 29, 865–9 (2013).

23. Lee, C. & Bain, C. D. Raman spectra of planar supported lipid bilayers. Biochim. Biophys. Acta 1711, 59–71 (2005).

24. Suga, K. et al. Membrane surface-enhanced Raman spectroscopy for sensitive detection of molecular behavior of lipid assemblies. Anal. Chem. 87, 4772–80 (2015).

25. Wu, Y. et al. Molecular rheometry: direct determination of viscosity in Lo and Ld lipid phases via fluorescence lifetime imaging. Phys. Chem. Chem. Phys. 15, 14986–93 (2013).

26. Dent, M. R. et al. Imaging Phase Separation in Model Lipid Membranes Through the use of BODIPY Based Molecular Rotors. Phys. Chem. Chem. Phys. 17, 18393–18402 (2015).

27. Lichtenberg, D., Menashe, M., Donaldson, S. & Biltonen, R. L. Thermodynamic characterization of the pretrasition of unilamellar dipalmitoyl-phosphatidylcholine vesicles. Lipids 19, 395–400 (1984).

28. Heimburg, T. A model for the lipid pretransition: coupling of ripple formation with the chain-melting transition. Biophys. J. 78, 1154–65 (2000).

29. Riske, K. A. et al. Lipid bilayer pre-transition as the beginning of the melting process. Biochim. Biophys. Acta 1788, 954–63 (2009).

30. Veatch, W. & Stryer, L. Effect of cholesterol on the rotational mobility of diphenylhexatriene in liposomes: A nanosecond fluorescence anisotropy study. J. Mol. Biol. 117, 1109–1113 (1977).

31. Cogan, U., Shinitzky, M., Weber, G. & Nishida, T. Microviscosity and order in the hydrocarbon region of phospholipid and phospholipid-cholesterol dispersions determined with fluorescent probes. Biochemistry 12, 521–8 (1973).

32. Shinitzky, M. & Inbar, M. Difference in microviscosity induced by different cholesterol levels in the surface membrane lipid layer of normal lymphocytes and malignant lymphoma cells. J. Mol. Biol. 85, 603–15 (1974).

33. Kung, C. E. & Reed, J. K. Microviscosity measurements of phospholipid bilayers using fluorescent dyes that undergo torsional relaxation. Biochemistry 25, 6114–6121 (1986).

VI. Imaging viscosity of biomimetic lipid membranes

Chapter V introduced some complexities of the viscous behaviour of lipid bilayers, particularly in relation to the quantification of viscosity by porphyrin dimers. We described what is commonly referred to in the literature as 'membrane fluidity'; as originating from the viscous behaviour of the hydrocarbon region. This led us to hypothesize that the hydrophobic phase of the membrane determines the diffusive movement of membrane proteins and the structural integrity of cellular membranes and organelles. We modelled the non-polar region as an oily liquid which obeys Arrhenius-type temperature-dependent viscosity change due to spatial arrangement of the hydrocarbon chains of phospholipids. Our experiments in Chapter V isolated some components of viscous behaviour on the sub-molecular scale: the shape, length, and charge of lipid hydrocarbon chains determine the volume filled by each molecule, and so the resistance to free diffusion or molecular rotation within it, which is equivalent to our measurement of viscosity. In experiments comparing bilayers formed of saturated or unsaturated lipid we found a significant difference in temperature-dependent viscosity between the two. Moreover we found that the nature of dimer interaction with the membrane was largely determined by its charge, which can limit solubility within the hydrocarbon region. We used spectral analysis of solvatochromism and ratiometric analysis to determine the location, solubility, and state of aggregation of the dimers within their membrane environment.

These insights refined our approach to the measurement of phospholipid membranes and we were able to successfully quantify the viscosity of the bilayers that we tested. We are confident that our detailed spectral analysis has characterised the dimer's interaction with the membrane, and has confirmed that the viscosity-sensing mechanism is valid in small (< 200 nm) vesicles. We did this by producing a solution of vesicles in suspension that can be measured and manipulated in the same manner as viscous organic solvents, which we had used previously in calibrating the dimer's emission to solvent viscosity. However, this approach to lipid

membranes is far from complete in depicting the complex macroscopic determinants of viscosity. In fact, literature on membrane biophysics continues to identify factors such as size, concentration of lipid, osmotic tension, and curvature as strongly influencing what we would describe as hydrocarbon viscosity (or its inverse definition 'membrane fluidity) in bilayers. Due to lack of spatial resolution, bulk experiments of the type we performed in Chapter IV were unable to explore these effects. For this reason we turned to microscopy to provide an imaging perspective on membrane bilayer viscosity.

6.1 Existing techniques in microscopic imaging for the measurement of bilayer viscosity

So far, methods comparing diffusive behaviour in lipid bilayers have measured either translational or rotational diffusion. Translational diffusion is measured by the displacement of fluorescent molecules over time in a given area of the lipid membrane. On the other hand, rotational diffusion measures the rate of change in orientation of a fluorophore during its motion. Both types of diffusion can be related to viscosity though the viscous contribution towards translational and rotational diffusion differs radically; this is reflected in the difference in scale of the measurements and the interpretation of data.

6.1.1 Imaging methodologies measuring translational diffusion

The following are all techniques that exploit microscopy and fluorophores to measure diffusive movement over time. In live cells, translational diffusion compares differences in Brownian motion between biologically relevant locales that have been used to quantify the frictional contribution of phospholipids to membrane diffusion as well as the cytoskeleton, protein structures and other components. Typically, imaging techniques to ascertain membrane viscosity are measuring translational diffusion, among them are: fluorescence correlation spectroscopy (FCS), fluorescence recovery after photobleaching (FRAP), single particle tracking (SPT). In Chapter I, we discussed in detail the technical aspects of these methodologies and the accompanying analysis that yield estimations of viscosity. To summarise, the former two techniques rely on the illumination of a single point within the cell in order to analyse the

fluctuations in fluorescent intensity, indicating molecular size, concentration and motion within a solvent (FCS) or the rate of recovery of fluorescence intensity within a previously photo bleached area (FRAP), which indicates the diffusive dynamics of particles entering the observed area. All three methods measure D_T, the translational diffusion coefficient which, in its most simple estimation, can be related to viscosity by the aforementioned Saffmann-Delbrück equation[1,2] (Chapter I).

In addition to the analytical assumptions about data from these techniques, we suggest that a major shortcoming of these techniques is the lack of spatial resolution relative to that of molecular rotors. FCS and FRAP in particular, are limited to a given observation area or volume that is monitored from which overall parameters such as viscosity must be extrapolated. This is particularly true of membranes with complex dynamics such as those with varying lipid domains that give rise to intrinsic heterogeneity. SPT has been used more often, particularly by Veatch and Keller, 2003to explore varied domains within GUVs that can arise from the spontaneous ordering effects of cholesterol, for instance[3]. SPT provides spatial resolution on the scale of the trajectory of the given fluorophore over the time of the measurement, and can, in this way, probe greater areas than a single laser sport. However, we suggest that SPT measurements lack the time resolution offered by molecular rotors.

Below is a summary of D_T values from literature data from the three major techniques described above from systems comparable to those that were used in our experiments involving the porphyrin dimer. In some instances, the authors have calculated η from D_T and those values are shown here, in Table 6.1. Further discussion on the details of FCS, FRAP and SPT in comparison with molecular rotors can be found in Chapter I.

Table 6.1: Literature values of D_T from imaging techniques in model membranes

Technique	Reference	System	Fluorophore	D ($\mu m^2/s$)	SD	η (cP)
FRAP	[4]	POPC GUVs	DiI-C18 lipid analogue	**7.5**	1.2	
RICS	[4]	POPC GUVs	DiI-C18 lipid analogue	**7**	3	
FRAP	[5]	DLPC GUVs	FCVJ	**1.7 times less than MR**		
FRAP	[6]	POPC SLB	NBD-PE	**1.8**	0.2	
FRAP	[6]	POPC GUVs upper	NBD-PE	**3.3**	1.8	
FRAP	[7]	POPC GUVs	TMR-POPE	**0.77**	0.13	
FCS beam expander	[4]	POPC GUVs	DiI-C18 lipid analogue	**8.02**	0.01	
FCS	[8]	DOPC GUVs	DiI-C18/ DiO-C18	**7**	1.2	
FCS	[8]	DOPC GUVs	ctxB-488 GM1	**3.6**	1.4	
FCS/Tracking	[9]	Ld 1:1/1:2 DOPC/DPPC 30% Cholesterol	Texas Red DPPE	**0.4-0.07**		$1x10^{-7}$
FCS	[10]	DOPC	DiI-C18 lipid analogue	**6.25**		
FCS	[6]	POPC SLB	Rho-PE	**2.8**	0.2	
FCS	[6]	POPC GUVs lower	Rho-PE	**6.1**	1.1	
z FCS	[6]	POPC SLB	Rho-PE	**4.8**	1.1	
z FCS	[11]	DOPC GUVs	BODIPY C8	**7.8**	0.8	
FCS	[11]	DOPC SLB buffer	BODIPY C8	**2.7**	0.3	
FCS	[11]	DOPC SLB glucose	BODIPY C8	**3.1**	0.3	
FCS ITIR	[6]	POPC SLBs	Rho-PE	**4.9-15.0**		
FCS	[12]	DOPC GUVs	BODIPY-Chol	**7.4**	0.3	
Tracking	[13]	Lo 1:1/1:2 DOPC/DPPC 30% Cholesterol	Texas Red DPPE	**$3x10^{-3}$ - 1.5**		3000-150000
SPT	[14]	Ld POPC Cholesterol	NBD/DPPE or LAURDAN GM1	**1.1**		
SPT	[15]	POPC SLB	TRITC-DHPE	**4.4 0.07**		
SPT	[7]	POPC GUVs	TMR-POPE	**1.42**	0.23	
SPT	[6]	POPC GUVs	Rho-PE	**4.1**	3.9	
SPT	[16]	POPC GUVs	Rho-PC	**3.5**		

* MR = molecular rotors

Table 6.1 shows that measurements of translational diffusion in model membranes vary somewhat amongst one another according to the probe and technique. We know from the Stokes-Einstein and Saffmann Delbruck equations that D_T is inversely proportional to

viscosity[1,17]. Cicuta et al.,2007 convert D_T to a three dimensional measurement of viscosity[13], estimating it to be between 3 and 150 Pa S (3000 – 150000 cP)[13]. Petrov et al.,2008 [9] calculated viscosity of the L_d phase of a ternary mixture of 1:1/1:2 DOPC/DPPC at 30% cholesterol to be much lower at $1x10^{-9}$ Pa S ($1x10^{-6}$ cP)[9]. These values are vastly different from one another and from what we have observed in the L_d phase of DOPC GUVs, a viscosity of approximately 180 cP. The conversion from D_T, a rate constant in two dimensions, to viscosity, a three-dimensional parameter can be difficult to justify in experimental terms as well as theoretically. Indeed, the influence of the external fluid viscosity, as it affects dissipation of bilayer tension, is a subject that has been discussed in depth by Hughes et al., 1982, who determined that the Saffman-Delbruck approximation is based on the assumption that the fluid viscosity external to the membrane the is significantly lower than the lipid bilayer viscosity, making lateral diffusion a source for determining the three-dimensional parameter viscosity in two-dimensions, as D_T implies[18]. They propose that measurement of rotational diffusion, a three dimensional process may be able to supplement data for the estimation of bilayer viscosity.

6.1.2 Imaging methodologies measuring rotational diffusion

In Chapter V we discuss the measurement of rotational diffusion, and extrapolation of bulk viscosity from the application of the Jablonksi-Perrin equation. Comparison between our measurement of lipid bilayer viscosity and published values obtained from D_r, have shown good agreement. Measurement of fluorescence depolarisation, or 'anisotropy', is by far the most common means of estimating rotational diffusion, in its ability to estimate the rate of individual molecular tumbling. More recently, techniques measuring anisotropy have been developed to supply spatial and temporal resolution by the use of confocal microscopy. Here, we summarise recent estimations of rotational diffusion from anisotropy imaging that can be directly compared to our measurements presented in this Chapter.

Table 6.2: Literature values of D_R from imaging techniques in model membranes

Reference	System	Fluorophore	D_R	SD	η (cP)	Units of D_R
[19]	rabbit kidney proximal tubule	TMA-DPH	2.4 - 2.8	0.01		NA
[16]	POPC	Rho-PC	$0.7x10^{-7}$			rad^2/s
[16]	DPPC	Rho-PC	1.2			rad^2/s
[20]	SKOV-3 cell membrane	BODIPY			140-260	NA
[12]	DOPC GUV	BODIPY-Chol	2.0-0.4		47-225	1/s

The viscosity values as calculated from rotational diffusion coefficients are much closer to those that we reported in Chapter V than the corresponding values extracted from translational diffusion coefficient measurements. Ariola et al., 2009 have explored the relationship between D_T and D_R, by measuring the same system by FCS and by anisotropy imaging. They report D_T on the order of 7.8 $\mu m^2/s$, typical of D_T values reported in Table 6.1, and D_R on the order of 2.0 - 0.4 s^{-1}, which are representative of D_R values reported in Table 6.2 [12]. They used D_R to calculate viscosity of DOPC GUVs to be 47-225 cP, which is in agreement with our measurements. This study shows that direct viscosity calculations from D_R are much more comparable with those measured with molecular rotors.

Recently in our group simultaneous measurements of viscosity in model membranes[21] (LUVs and GUVs) were performed using three complementary methods applied to the same molecular rotor fluorophore, namely:

(i) measuring the lifetime of boron dipyrromethene (BODIPY) molecular rotors that can be converted to viscosity using the calibration curves, as described in this Thesis;

(ii) measuring the FCS diffusion coefficients of BODIPY molecular rotors that can be converted to viscosity using the Saffman-Delbruck equation

(iii) calculating the diffusion coefficients of BODIPY molecular rotors using molecular dynamics simulations that can be converted to viscosity using the Saffman Delbruck equation

Consequently a very satisfactory agreement was found between the three methods, even when the measurements were performed at different temperature. Even though the viscosity estimated from the lifetime of molecular rotor was up to two times different from that estimated from FCS, given the uncertainties in parameters of Saffman Delbruck equation used for conversion, it was concluded, that when different methods are applied to the same molecule, the values are essentially interconvertible. Likewise, earlier studies on Bodipy molecular rotors using combined lifetime and time-resolved anisotropy approaches shown essentially the same resulting viscosity[22,23]. As such we can conclude that

(i) The literature values of both diffusion coefficients and viscosities in membrane show a large spread that can be partly due to the lack of reproducibility between the measurements from different groups and partly due to different molecules used as probes that can affect their membrane localisation (Table 6.1).

(ii) Measurements using different techniques are performed on the same fluorophore, give comparable values of viscosities.

Having the assurance that the molecular rotor measurements produce values in bulk membrane solutions of LUVs that are comparable with the literature, in this Chapter, we extend the ratiometric methodology reported in Chapter V to imaging.

6.1.3 Large unilamellar vesicles (LUVs) to giant unilamellar vesicles (GUVs)

The advantages of measuring bilayer viscosity using a suspension of vesicles include ease of sample preparation and homogeneity of the vesicles produced, which made them ideal for the bulk measurements performed in Chapter V. These vesicles are suspended in aqueous solution with diameter of 180 nm and are highly homogenous due to the extrusion process. However, our aim for microscopy was to gain spatial resolution of the lipid macrostructure in which the dimer is embedded. We faced an obstacle to imaging LUVs of the type described in the previous Chapter due to their size and the diffraction limit of our imaging system at the optimal excitation wavelength of the dimer: at λ_{ex} = 453 nm, using the highest magnification available on

our microscope (x63 in water; NA = 1.20). Our solution to the limit on imaging LUVs was to make much larger fluorescent lipid vesicles. These vesicles would have to be unilamellar, and at osmotic equilibrium in order to be comparable with bulk measurements on LUV suspensions. In order to produce these, we used *electroformation*, a method pioneered by Angelova et al., in 1986 and described in detail in the section: Methodology[24]. Vesicle electroformation has become standard practice in the field of membrane biophysics for the production of unilamellar vesicles of roughly 10-30 μm[24]. The method has a much lower yield of unilamellar relative to multilamellar vesicles than mechanical extrusion or spontaneous formation in aqueous solution (termed the 'gentle hydration' method, used for production of large vesicles)[25]. It is less likely to be compatible with charged molecules because electroformation depends upon the generation of an oscillating electric field between two solid electrodes. In our case, the electrodes used are glass slides coated on one side with indium tin oxide (ITO; a solid mixture of w/w%: 90% In_2O_3 and 10% SnO_2) which is transparent in thin films and conductive. Layers of dried lipid swell in response to the field and, under specific values of current, amplitude and frequency, can form giant unilamellar vesicles.

The exact mechanism of liposome formation is as yet, not completely understood but has been proposed as following one of three schemes shown in Figure 6.1[24,26]. Angelova et al., 1986 have suggested that bilayers are hydrated from dried films, and separate from one another due to the uptake of water between the layers[24]. Once separation is sufficiently far such that van der Waals attractive forces are overcome, the bilayers bend from line tension[24]. Indeed, Taylor et al., 2003 showed that the formation of defects within the bilayer which exposes the hydrophobic interior to the aqueous solution increases line tension between phospholipids, increasing the likelihood of swelling to protect the hydrophobic interior.[27] Figure 6.1 shows three alternative modes of liposome formation as a result of bending: in the first instance (Figure 6.1b), osmotic forces cause swelling of bilayers and induce bending[24]. Alternatively, (Figure 6.1c), solutes or other particles can enter unclosed liposomes in order to increase osmotic pressure. Lastly, Angelova et al., 1986 (Figure 6.1d) propose that the hydrophobic regions of bilayers cause line tension,

causing planar bilayers to bend towards the ends of other bilayers, once these close, liposomes form[24]. The central parameters that have been identified that determine the size and shape of liposomes are the number of bilayers in the dried film, as attractive forces from the electrode will affect bilayers depending on their distance from the electrode[25,26]. Also, Angelova et al., 1986 applied the external electric field as a means of manipulating counterion concentrations between bilayers as this manipulates separation between bilayers, making liposome formation more likely with large inter-bilayer distances[24,26]. The same principal governs the likelihood of formation of unilamellar and multilamellar vesicles.[24–28]

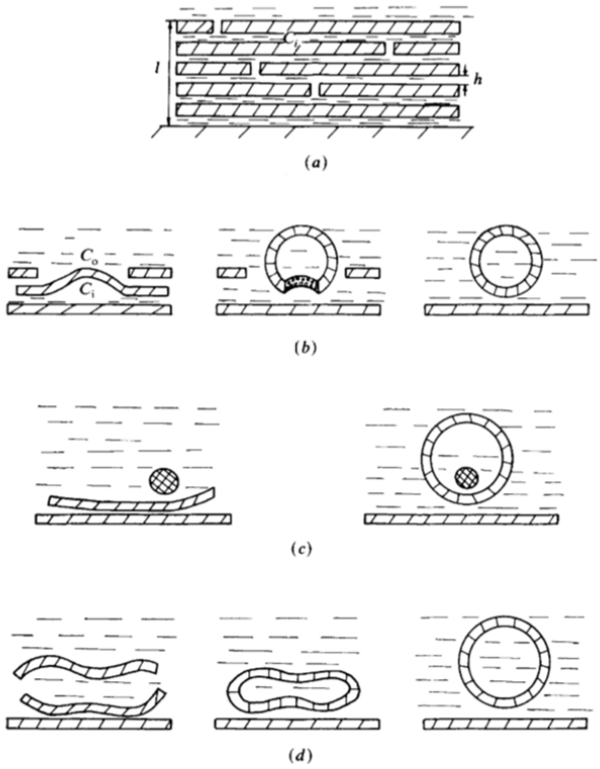

Figure 6.1: Lipid GUV electroformation mechanism as hypothesized by Angelova et al.,a) thin lipid film is deposited in bilayers; b) swelling of the lipid layers in aqueous solution, which part due to electrostatic interactions; c) alternatively, debris in solution causes bilayers to assemble around it, forming vesicles; d) alternatively lipid tension causes tension and bending in the bilayers, the ends of which associate to enclose the internal aqueous solution, forming vesicles. Figure from Angelova et al., 1976 [24]

We used electroformation to produce the same conditions of the experiments as in Chapter V, whereby as previously we compared two scenarios (Please note, that the methodology described here is purely qualitative, please see Chapter II, Methodology, for exact details)

- *Pure lipid stock GUVs*: pure lipid stock (9:1 chloroform: methanol) at a concentration of 1mg/ml is applied in a thin film directly onto the ITO-coated surface and dried under vacuum for 30 minutes. Once dehydrated the lipid-coated ITO slide is placed opposite a second clean ITO-coated slide and the two are separated by a thick ring of polydimethylsiloxane (PDMS) to create a chamber between the two surfaces. The chamber is sealed by clips and filled with a 500 mM sucrose solution. Once assembled, crocodile leads are attached to the exposed edges of both ITO slides, in contact with the coating, to a function generator in order to create a circuit. An AC voltage (square pulse) of 1.6 V was applied at 10 Hz for 3 hours, followed by 2.6 V at 4 Hz for 45 minutes. Afterwards, the solution is a highly concentrated suspension of unilamellar and multilamellar vesicles (of diameter 10-30 μm[24]). These are diluted in a solution of 500 mM glucose solution to an appropriate density of vesicles for microscopy. We add a volume of P_2NMe_3 or P_2 (1mM in DMSO) to a final concentration of 10 μM. We observe the degree of dimer penetration into GUV membranes and the resulting viscosity measurements.
- *Lipid and dimer mix GUVs*: exactly as in Chapter V, we compared the plain lipid vesicles to those electroformed from a thin film of a lipid and dimer mixture in a solution of 9: 1 chloroform: methanol. Lipid to dimer ratios are kept at 1000:1 as in the LUV bulk experiments. Similarly to extrusion, all electroformation steps are carried out at 60 °C to maximise the solubility of the dimer in aqueous solution.

Comparison between these two regimes is necessary because we observed that vesicles produced from the lipid: dimer mix, of the charged dimer; P_2NMe_3, were considered to have compromised partitioning due to interaction of the charge with the electrodes during sample production. This will be further discussed in the Results section of this Chapter.

6.2 Ratiometry on the Leica SPII confocal microscope

For ratiometric imaging on the microscope, we lose spectral resolution in exchange for spatial resolution, of a heterogeneous sample. Each pixel of the image emits a mixture of fluorescence from the two confomers, just as we had seen in fluorometry data in Chapter V of bulk samples. Typically for fluorometry, we visually assigned λ_{max} of 'twisted' and 'planar' emission peaks and took intensity ratios accordingly. However, a full emission spectrum for each pixel is not easily accessible for ratiometric *imaging*.

In the microscopy experiment, the sample's fluorescent light is collected onto one of the three available PMT detectors. Fluorescence is spectrally dispersed using a prism (one for each of the detectors). Once dispersed, complementary spectral wavelength ranges of light can be isolated by the use of slits. Figure 6.2a shows the process of assigning the relevant spectral ranges which correspond to what we observed to be the 'twisted' at 635-645 nm and 'planar' at 690-700 nm emission peaks for P_2NMe_3. We assigned these regions after collecting full spectra of the dimer's emission in relevant solutions (methanol/glycerol solutions and DOPC vesicles). This data is shown in the section 6.2.1, below. Either detector integrates intensity data over its assigned wavelength range for each pixel in the image, Figure 6.2b. This creates two images of the same sample: of the intensities of the 'twisted' and 'planar' emitting species, which, once divided, produce a single 'ratiometric' image resolving the differences in emission ratio by pixel of the image, (Figure 6.2c).

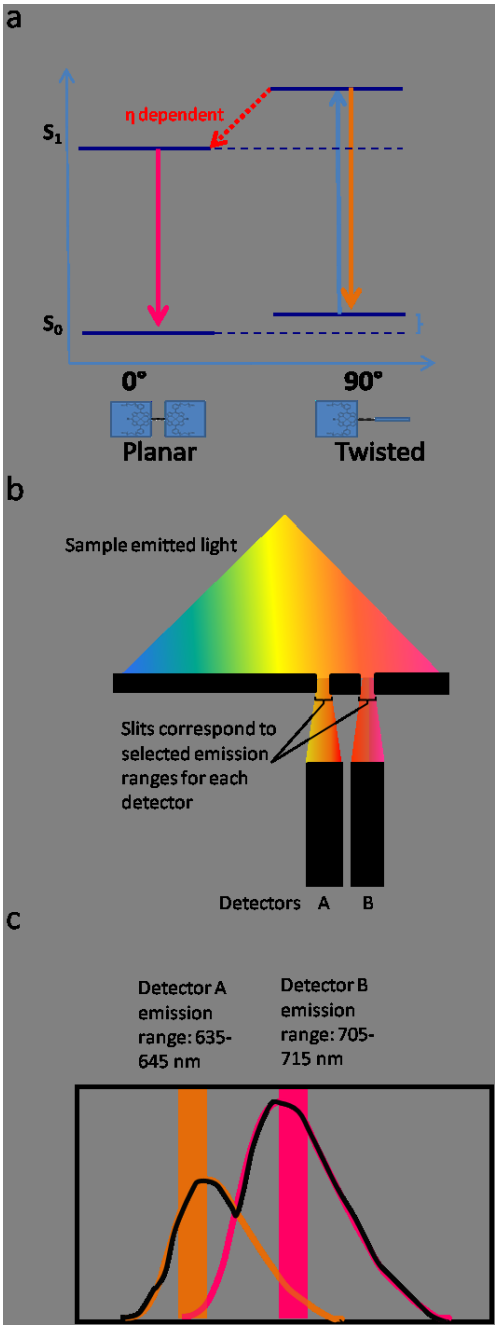

Figure 6.2: a) Spectral ranges are selected according to the emission peak of either twisted (635-645 nm) and planar (705-715 nm) confomers; b) upon sample emission from the microscope stage, light is dispersed and spectral ranges can collect light based on conformational source; c) intensity in each pixel from detector A (twisted emission) is divided against intensity in each pixel from detector B (planar), giving a ratiometric image.

6.2.1 Ratiometric viscosity calibration

Differences in detector sensitivity are fundamental to the validity of viscosity measurements. For instance, detector sensitivity at a certain wavelength and a slit size amongst other features of the spectrometer used can alter the quality of spectra, and thus emission ratios for

interpretation of viscosity. As we explained above, microscope images are made ratiometric by the use of two separate detectors where intensity is the integrated signal over a fixed wavelength range and not, as in fluorometry by the use of a single detector with wavelength resolution. The fluorescence signal from bulk solution as in Chapter V is collected by a PMT fitted inside the fluorometer. PMTs amplify fluorescence signal by use of the photoelectric effect and subsequent secondary emission steps using a series of electrodes. The kinetic energy of emitted electrons is inversely proportional to the wavelength of light that reaches the electrode, meaning that PMTs have reduced sensitivity at long wavelengths (e.g. $\lambda > 650$ nm for our experiments). The sensitivity of the detector is greatly affected by the metals used for the photocathode as well as the composition of transparent windows within the instrument. However, all photocathodes display a wavelength dependent sensitivity that is compromised at longer wavelengths. Given this property, the emission signal collected by the fluorometer comes with an option for multiplying emission signal by a wavelength-dependent function in order to correct towards the red ends of collected spectra. Figure 6.3a shows an example of this 'correction function' that is available on the FluorEssence software of the Horiba Fluoromax 4 fluorometer (Fig 6.3a, black trace) in comparison with the uncorrected spectra (Figure 6.3a red dotted trace). Figures 6.3b shows data for P_2NMe_3 (in pure glycerol at room temperature) without correction (Figure 6.3b, black trace) and with correction (Figure 6.3b, red trace) showing the amplified intensity of the dimer's fluorescence after correction. When normalised, the difference between the shape of the corrected and uncorrected spectra become obvious (Figure 6.3c, black and red traces, respectively). There is a considerable change in relative intensities of the twisted and planar peaks upon application of the correction function. The uncorrected and corrected calibration curves however, will have a consistent relationship, if all spectra are corrected or all are uncorrected. This is demonstrated in Chapter III, for instance, where calibration data in methanol/glycerol mixtures were calculated from the emission ratios of corrected spectra and data in Castor oil is uncorrected (Figures 3.9 and 3.10, respectively). Both types of calibration curves can be used, however, it is imperative that a calibration curve

must only be applied to spectra of the same type, whether corrected or uncorrected, in order to stay true to the calibration.

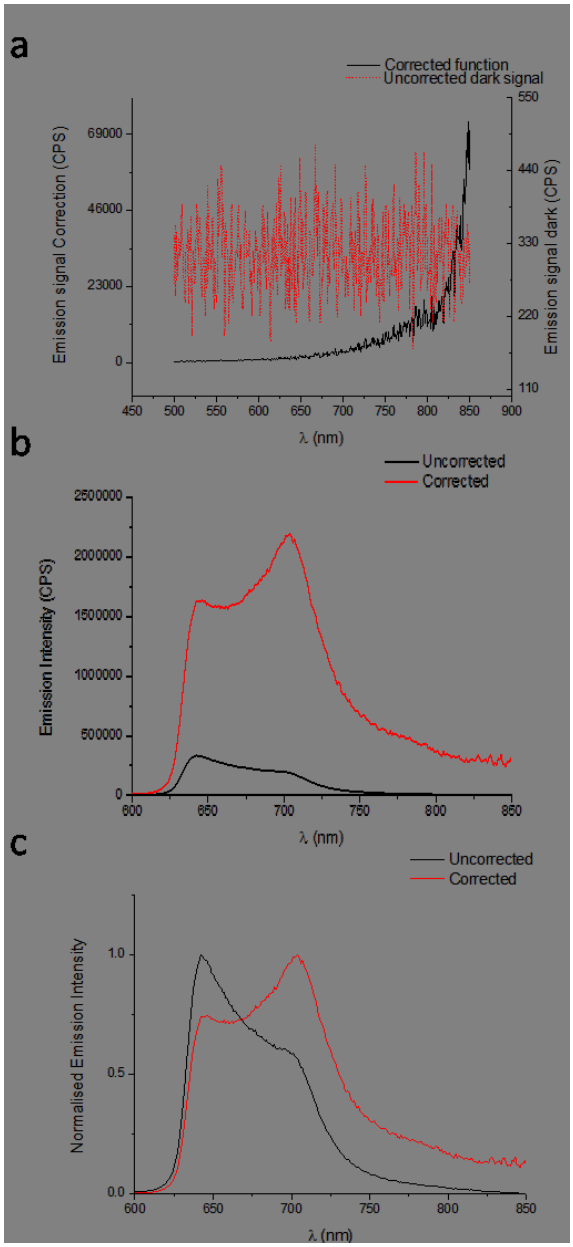

Figure 6.3: a) The Fluoromax 4 (Jobin Yvon, Horiba) PMT signal (red) does not reflect the decreased sensitivity of the detector in the red. Software to analyse the signal is supplemented by multiplication to a correction function (black) which can be used to augment the uncorrected signal to the correct intensities; b) P_2NMe_3 emission (0.33μM; in glycerol at 323 K; λ_{ex} = 453 nm) corrected (red) and uncorrected (black) demonstrating differences in sensitivity such that the corrected spectra shows higher signal and; c) normalised spectra shown in (b) clearly showing an altered ratio from the uncorrected spectrum – demonstrating that the two cannot be compared for viscosity estimation.

Thus, only ratiometric data collected on the same equipment, with the same optics and detector(s) can be used for calibration purposes. For this reason, the calibrations performed on the fluorometer cannot be automatically transferred to a microscope detection.

Figure 6.4 demonstrates the difference between the shape of spectra obtained on the Jobin Yvon Fluoromax 4 fluorometer (corrected spectra, Figure 6.4, black) and the Leica SPII Microscope (red, Figure 6.4). The first difference between the two is the signal/noise ratio, where the microscope-spectra has greater levels of noise than that collected on the fluorometer due to the significantly reduced number of counts collected to build up the spectra. Due to the difference in excitation volume between the two instruments, the time of image acquisition is a significant factor that affects the quality of microscope spectra. However, when imaging GUVs, we are significantly limited in the maximum image acquisition time (to approx. 100s) due to diffusion of the vesicles into/out of the field of view and bleaching of the dimer (these effects are discussed in further detail in later sections of this Chapter). Due to the constraints of measuring vesicles, we have limited image acquisition time available for each image, which reduces the signal/noise ratio. Also, the spectral resolution on the microscope data is much lower than the fluorometer, as the minimum slit width that can be used on the Leica SPII is 5nm, rather than the 1 nm slit size used to collect fluorometer data shown in Figure 6.4. This further reduced the signal/noise ratio. It is possible that this lower resolution also contributes to the alteration in shape of the spectra, where it appears to be shifted slightly to the red, particularly in the planar emission maximum, around 730 nm on microscope spectra, but 710 nm on the fluorometer.

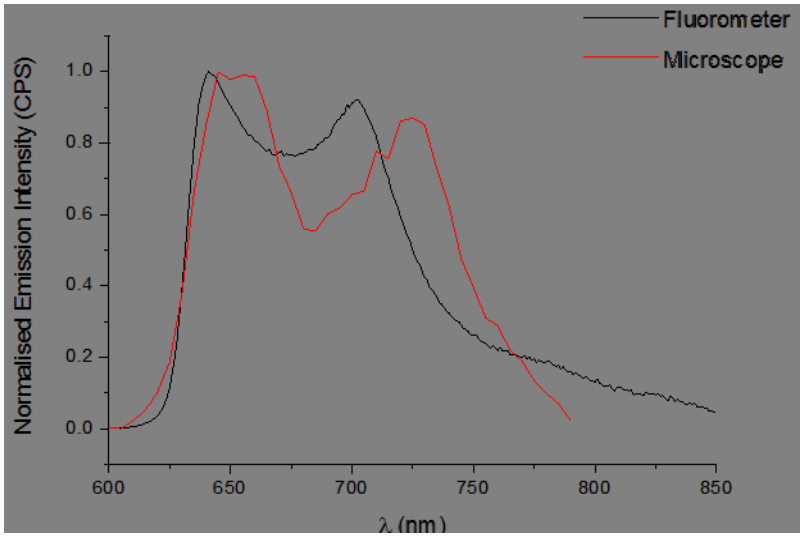

Figure 6.4: Normalised P_2NMe_3 emission spectra (0.33μM; in 80 w/w % glycerol at 293 K; λ_{ex} = 454 nm) as collected by the fluorometer (black) and microscope PMT (red) showing the difference in signal/noise ratio as well as spectral shifts recorded by these instruments.

Considering these differences in spectral quality, it is apparent that we could not apply the calibration curves from Chapter III, collected on the fluorometer, to data obtained during imaging on the Leica SP5. Due to the unique technical conditions of the optics available within the confocal microscope, it was necessary to create a new ratiometric viscosity calibration that would serve as a standard for reference.

Thus we have produced a calibration curve from methanol/glycerol solutions of the dimer using the microscopy setup. To reduce the signal/noise instead of recording a full spectrum at each concentration we have recorded single point ratios of the two peaks as described in Figure 6.2.

The curve can be fitted with equation 6.1 where parameters a = 11.32, x = -0.77 and c = 0.59:

$$Emission\ Ratio = \frac{1}{a+\eta^{x}+c} \qquad (6.1)$$

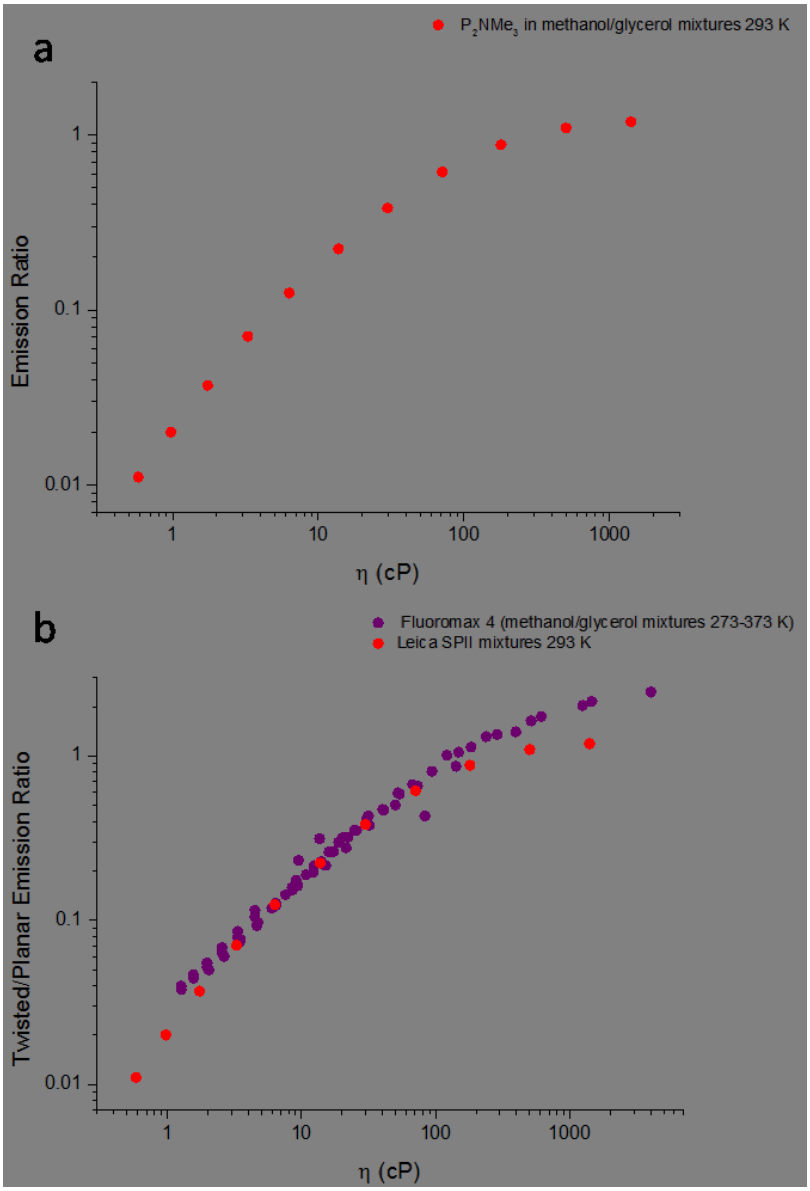

Figure 6.5: (a) Calibration of P_2NMe_3 emission peak ratios against solution viscosity for w/v % methanol/glycerol mixtures as performed on the Leica SP5 II confocal microscope under temperature controlled environment. Calibration was performed according to the method described in Figure 6.2. (b) overlay between the microscope and the fluorimeter setup calibrations.

The most significant difference between the calibration curve shown in Figure 6.5 and that from Chapter III (Figure 3.9, also shown in Figure 6.5 b) is the method of ratiometry: single point recording or the whole spectra recording. Figure 6.5 shows the two calibration curves in relation to one another. They have good agreement within the range 2- 100 cP, but values greater than this show a significant decrease in sensitivity to increasing viscosity.

6.2.2 Spectral imaging on the Leica SPII

We used the ratiometric method described above as the primary way of measuring vesicle viscosity on the microscope. However, the Leica SPII is equipped with a spectral-detection mode enabling us to gain spectral information on images. This is achieved by step-wise integration of a user-defined wavelength window (generally 5-10 nm) across a large spectral range, i.e. 500-800 nm. This method is not a preferred mode of ratiometric viscosity imaging. Firstly, the volume of raw data generated, would have to be analysed pixel-by-pixel in order to achieve ratiometric values for an image. Also, the time required to collect a full spectral range per image is considerable depending on the size of the selected wavelength window. For high resolution spectra, i.e. 5 nm, there can be a 20-30 second delay between intensity values collected at 650 nm and those at 710 nm. This can compromise the accuracy of fluorescence spectra – at high magnification, vesicles may diffuse into/out of the field of view, artificially altering the intensities at longer wavelengths. Also, even if the vesicle is sufficiently immobilised within the field of view, long periods of imaging are likely to bleach the dimer's emission, which can reduce the amount of light collected at longer wavelengths relative to shorter ones, compromising the ratiometric relationship of the emission peaks to viscosity. Though we did not use spectral detection for ratiometric purposes, we continuously collected spectrally resolved microscopic images in order to confirm the presence of two peaks in the dimer's fluorescence and to look for solvatochromic shifts in emission peak wavelength. Some of the data presented below will be spectral data as collected on the microscope.

6.3 Membrane viscosity as measured by the porphyrin dimer

In order to assess the suitability of electroformation as a method of producing GUVs, first we looked at the morphology of vesicles produced under a range of conditions.

6.3.1 P_2NMe_3 in GUVs

Figure 6.6 shows differential interference contrast (DIC) images taken of vesicles electroformed from dehydrated films of lipid and the charged porphyrin dimer (Figures 6.6a and c) and those incubated in solutions with dissolved porphyrin dimer (Figures 6.6b and d). As in Chapter V,

where the lipid and dimer are mixed prior to electroformation, molar ratios are kept at 1000:1, lipid: dimer. Where the vesicles are mixed with solutions of porphyrin dimer, the concentration is kept at 10 μM.

There is significant vesicle production when GUVs are electroformed from a mixture of DOPC and P_2NMe_3, they appear to have a wide size distribution and are evenly suspended throughout the solution as expected from successful electroformation (Figure 6.6a). At higher magnification (Figure 6.6b), smaller vesicles are visible in which dimer fluorescence is more intense possibly due to multiple smaller vesicles, micelles or aggregates trapped within larger ones, though this is not an unusual by product of electroformation. Upon incubation with the dimer, the sample shows a large degree of spatial heterogeneity. True aggregates can be seen in Figure 6.6b, where after addition to aqueous solution minute solids begin to appear in an otherwise transparent solution. At high magnification, and after sufficient incubation time, large lipid aggregates are observed as in Figure 6.6d. These are most likely to be islands of lipid aggregate that have formed spontaneously upon incubation in the presence of the dimer and could be the result of exposure of lipid vesicles to a high concentration of the porphyrin dimer. These bright field images show that addition of the charged dimer to a solution containing GUVs is not appropriate for incorporation of the charged porphyrin dimer.

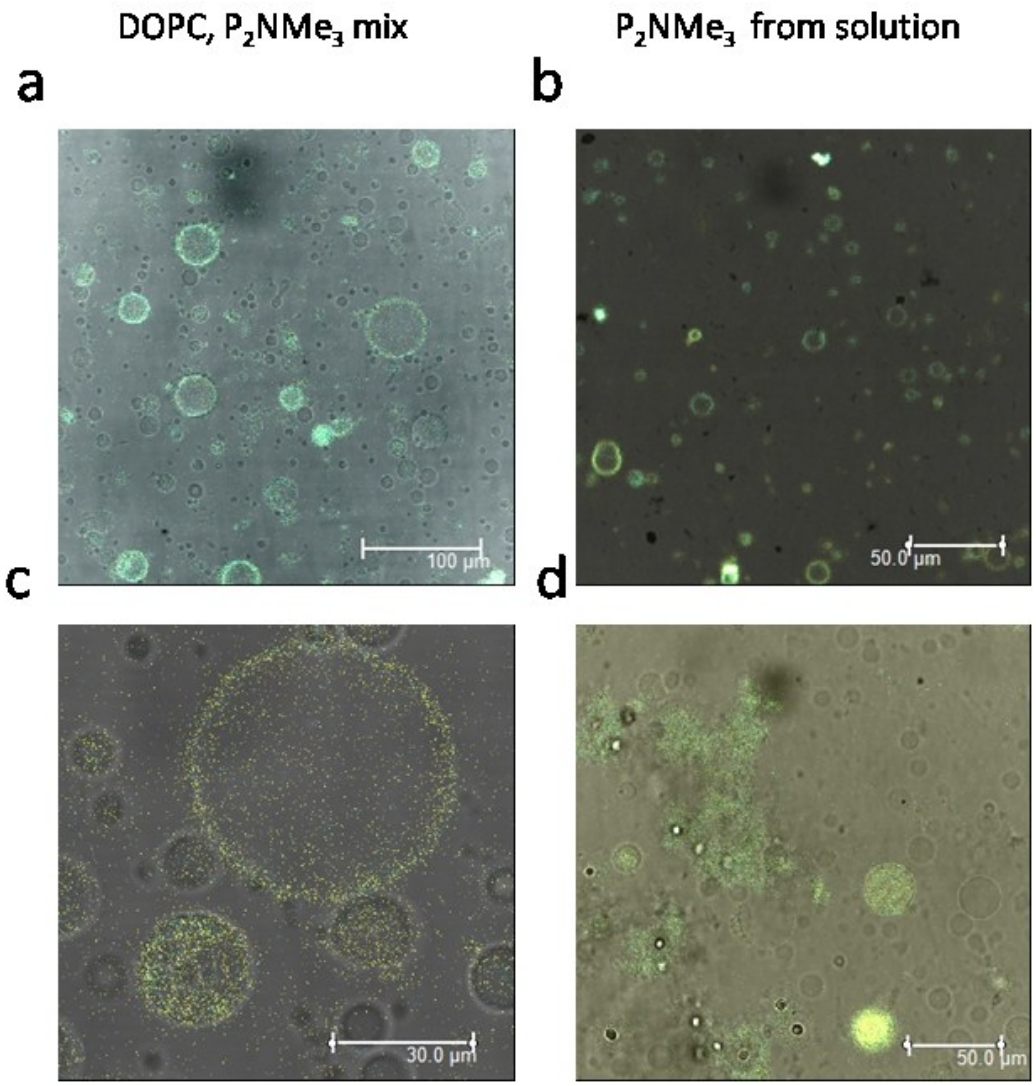

Figure 6.6: Overlayed brightfield and fluorescence images of a, c) DOPC-dimer mix GUVs, where the dimer is embedded (DOPC: P_2NMe_3 1000: 1; λ_{ex} = 454 nm; detection range = 500-800 nm). Images are 512 x 512 pixels with a) x20 magnification; 135884 counts and c) x60; 28224. b,d) DOPC GUVs left to incubate with P_2NMe_3 from solution (10 µM dimer in 200mM sucrose for 3 hours; λ_{ex} = 454 nm; Detection range 500-800 nm) both at x20 magnification, 512 x 512 pixels with b) 35070 and c) 84733 counts.

In light of what we observed from Chapter V, we tested the compatibility of the neutral dimer, P_2 into GUVs. Figure 6.7 shows morphology of vesicles electroformed in the presence of P_2, (Figures 6.7a, b), and pure DOPC vesicles incubated with aqueous solutions of P_2 (Figures 6.7c, d). Figures 6.7and b show two bright field images of GUVs electroformed in the presence of P_2 which are well distributed in size and suspended evenly in solution with minimal evidence of visible aggregates but with almost no fluorescence originating from vesicles themselves. P_2 added to a suspension of GUVs shows signs of strong aggregation at the given concentration, consistent with our knowledge that P_2 is insoluble in water (Figure 6.7b). However, these

aggregates are different from those observed for the charged dimer, P_2NMe_3, shown above in Figure 6.7 in that the GUVs have not become fixed to one another in a lipid mass, but instead stay intact with visible plaque-like aggregate forming on the surface of the bilayers.

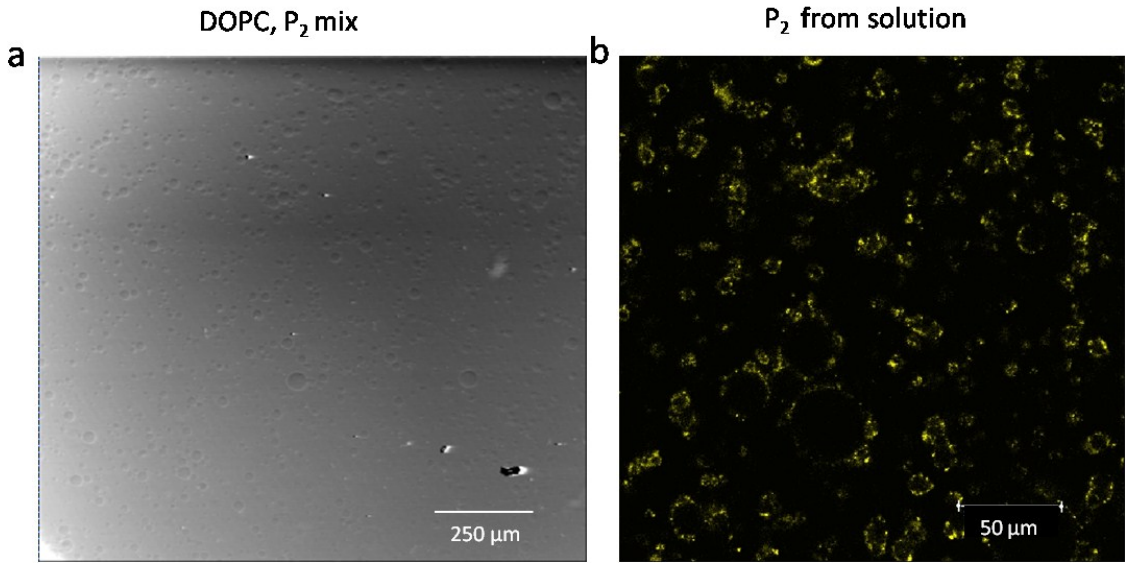

Figure 6.7: a) Bright field DIC image of GUVs electroformed from a dehydrated lipid: dimer mixture (DOPC: P_2; 1000:1) No fluorescence is detected in the sample; b) DOPC GUVs incubated with P_2 in solution (10 µM, in 200 mM glucose). λ_{ex} = 448 nm for all samples; 512 x 512 pixels; detection range = 600-800 nm, 6646 counts.

Vesicles are seen to be evenly suspended in solution after formation, indicating that even if the dimer aggregates, the electroformation process is largely unperturbed. We do not know whether this is because electroformation occurs over a long time scale during which the dimer has aggregated and cannot interfere with electroformation of vesicles or because the dimer does not interact with unstructured lipids. Bright field images of P_2 in aqueous solution incubated with GUVs, show the effect of high concentrations of the dimer in a lipid suspension, causing large scale aggregation of lipid solids. We observed aggregation at extremely fast timescales (approx 10 min at 293 K) apparently adherent to the surfaces of vesicles, which may cause the vesicles to adhere to one another. Spectral imaging of P_2 in DOPC GUVs confirmed our interpretation, as we observed unimodal emission, with low intensity, indicative of the aggregated dimer. This is discussed in further detail later in this Chapter, in Figure 6.10.

Studying the morphology of vesicles according to the electroformation and dimer penetration conditions will allow us to contextualise localisation of the dimer within the membrane. We establish here that electroformation of vesicles from mixtures of DOPC and the P_2NMe_3, can be successful though they have weak fluorescence, but those made from the uncharged dimer P_2 are not fluorescent.

We sought to optimise imaging conditions to increase fluorescence intensity from weakly emitting signals. Fluorescence signal from Figures 6.6 and 6.7 are optimised by opening the confocal pinhole to its maximum section (600 μm), collection of fluorescence over a large wavelength range (500-800 nm, Figure 6.6; 600-800, 6.7) by maximising the dwell time of the laser at each pixel to increase the number of counts, and increasing the number of frame averages for each image to increase accuracy. We had moderate success with observing fluorescent signal from P_2NMe_3 (Figure 6.6). However, despite taking measures to maximise fluorescence signal, it is seen to be relatively weak in both Figure 6.6b and d. Figures 6.6c and d show a high magnification image of a single GUV in focus, here the extent of background noise can be compared with signal from the GUV membrane. Nonetheless, in order to perform ratiometric imaging, we find that we will have to separate this weak emission signal into two distinct channels. The next section explores the effect of signal intensity on ratiometric measurement.

6.4 GUVs with embedded dye

6.4.1 Ratiometric imaging with the charged porphyrin dimer, P_2NMe_3

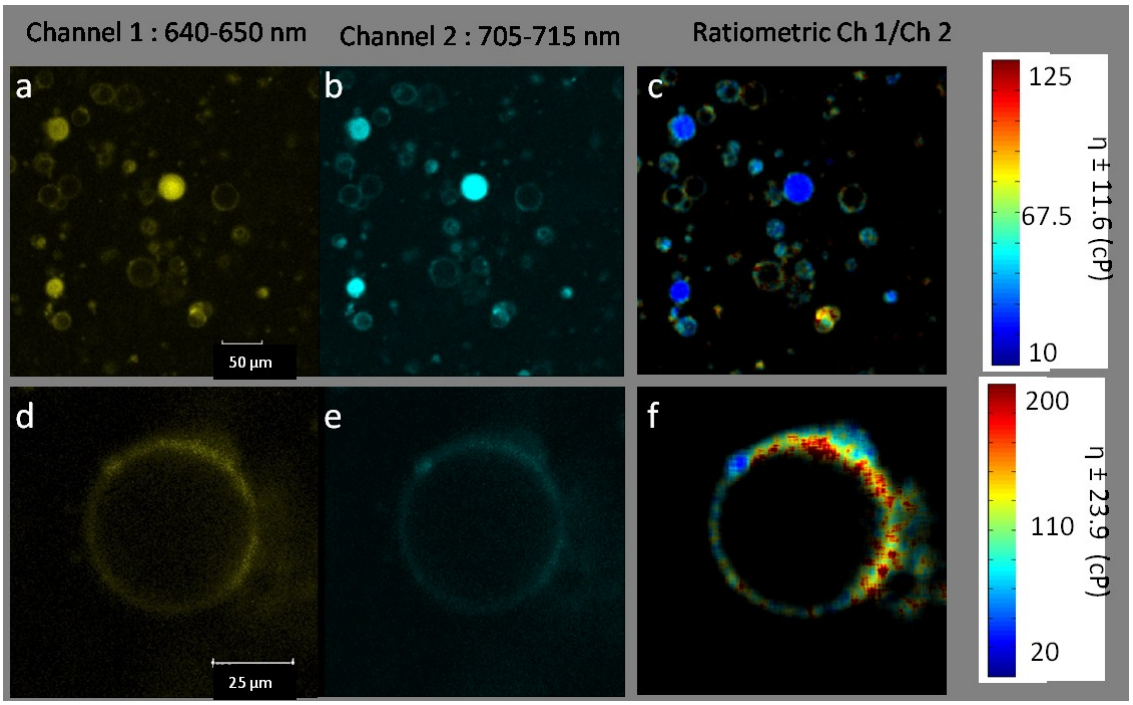

Figure 6.8: Ratiometric imaging of GUVs electroformed from a dehydrated mixture of DOPC and P_2NMe_3 (DOPC: P_2NMe_3 1000: 1; λ_{ex} = 454 nm; 512 x 512 pixels). Twisted (640-650nm; 79766 counts) and planar (705-715 nm; 65025 counts) emission are collected by two spectral channels at x40 magnification Viscosities estimated from approx 10 to 80 cP in different GUVs ± 11.6.Figure d, e, (x63; 512 x 512 pixels, with 32106 and 36608 counts in channel 1 and 2, respectively). Detection ranges are different from those in calibration curves due to solvatochromic shift of the twisted peak in the presence of lipid. Ratiometric figures (c, f) are produced from image processing of the two spectral channels (binning, thresholding, ratiometric images as described in Methodology) showing a large range of detected viscosities from approx 15 cP to 200 cP ± 23.9 in the same GUV.

Two series of images from this system are shown in Figure 6.8, representing the same sample at two different magnifications. 'Twisted' emission, from 640-650 nm, is recorded in 'Channel 1' (Figure 6.8 a,d), 'planar', from 705-715 nm, is recorded in 'Channel 2' (Figure 6.8 b,e). Ratiometric images of the two channels are shown in the last panels, Figure 6.8c and f. The intensities of the emission in each channel are not in true scale; brightness of the image is arbitrary for the purpose of demonstrating the presence of fluorescence light. We see in Figure 6.8a, application of the viscosity calibration as fitted by equation 6.1, yields viscosity values similar to those observed on the fluorometer in Chapter V (DOPC vesicles from dehydrated mixtures of lipid and dimer at 293 K) at approximately 30 cP, indeed the majority of dimer emission, even from aggregates is seen to have ratios corresponding to 30-40 cP, this confirms

our hypothesis from previous data (Figure 5.8) that the charged porphyrin dimer is associated to the surface of phospholipid bilayers and possibly partially embedded within them. Upon closer inspection of a single vesicle, as in Figure 6.8d-f, we sought higher resolution of this interaction between the dimer and membrane. However, we see that the ratiometric viscosity reported shows a higher viscosity in some regions and a high distribution of observed ratios. It appears that a diffuse lipid aggregate attached to the upper right region of the GUV reports higher viscosity than the remainder of the vesicle at approx 150 cP. The disagreement between these two measurements is, however, plagued by high proportion of error inherent to the ratiometric measurement. For instance, the number of counts collected in each channel determines the accuracy of the ratio, with higher counts giving low errors, assuming a Poisson distribution. We estimated the error of the whole image, rather than per pixel. In Figure 6.8c the error is given as ± 11.6 cP, while Figure 6.8f has an error of 23.9 cP: both proportionally significant to the measurement of viscosity. We used equation 6.2 to quantify errors in ratiometric measurement:

$$\frac{Error\ (Emission\ Ratio)}{Emission\ Ratio} = \sqrt{\frac{1}{Counts_{Channel\ 1}} + \frac{1}{Counts_{Channel\ 2}}} \times Emission\ Ratio \qquad (6.2)$$

Which we then converted to viscosity values using equation 6.1. As can be seen in comparisons between Figure 6.8c and 6.8f, the number of counts per pixel are significantly low, at 0.06 – 0.66, prior to binning. Binning the images increases the average number of counts/pixel but we find that this does not significantly lower the error without considerable loss in spatial resolution. This is discussed further in later sections.

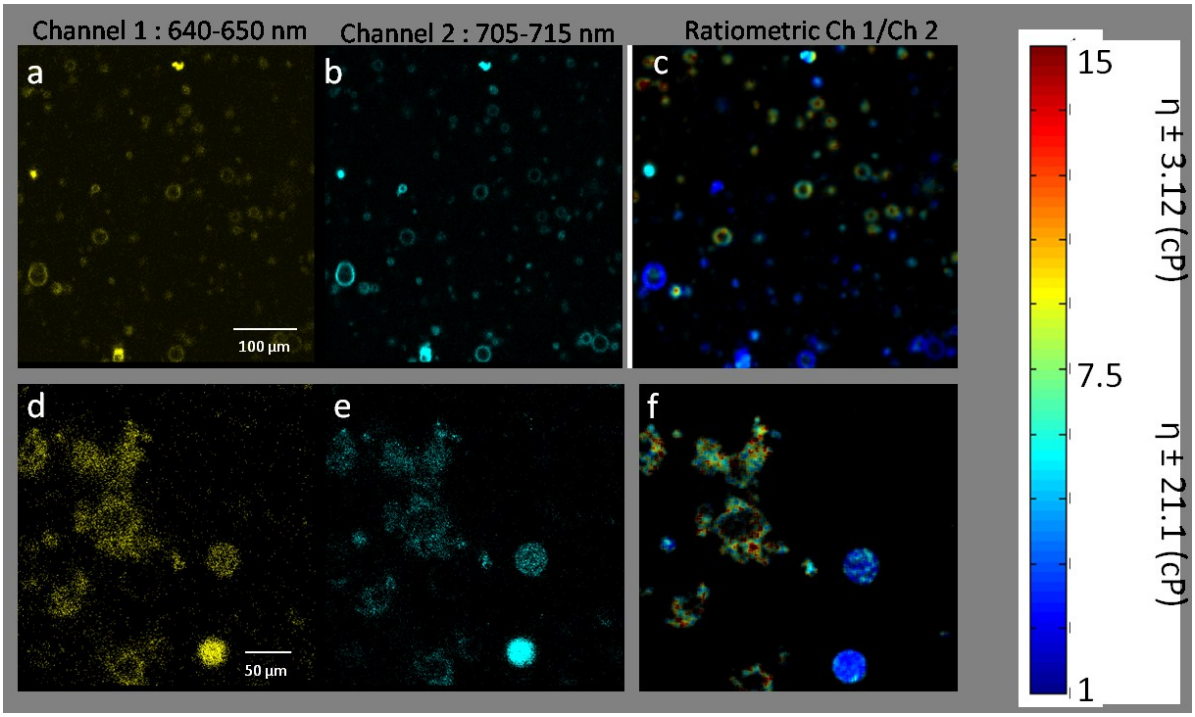

Figure 6.9: Ratiometric imaging of DOPC GUVs of incubated with P_2NMe_3 (10 µM, in 200 mM glucose) . Image is 512 x 512 pixels, with two channels: twisted (640-650nm; 179460 counts) and planar (705-715 nm; 952679 counts) at x20 magnification. Figure d, e, x40, 512 x 512 pixels with 50508 and 95397 counts for channel 1 and 2, respectively. Detection ranges are different from those in calibration curves due to solvatochromic shift of the twisted peak in the presence of lipid. Ratiometric figures (c, f) are produced from image processing of the two spectral channels (binning, thresholding, ratiometric images as described in Methodology) showing a large range of detected viscosities from approx 1-15 cP due to aggregation in the sample. (λ_{ex} = 454 nm).

Figure 6.9 shows pure DOPC GUVs to which the P_2NMe_3 dimer has attached from solution. Figures 6.9a and d show emission in the 'twisted' spectral region, 6.9b and e show the 'planar' region and Figure 6.9c and f show ratiometric images after image processing. The two images differ in magnification of the sample. We observe the confirmation of our measurements in Chapter V, where interaction between the dimer and the vesicle in solution yields extremely low viscosity values, in this case between 1 and approximately 8 cP with significant error at up to 21.1 cP in Figure 6.9f. If we interpret these values, this is a reflection of the planar conformation attached to the membrane surface, likely in aggregates, as we observed in Figure V (Figure 5.8). In comparison with GUVs made from the lipid and dimer mix, these are excluded further from the interior of the membrane. Though experiments in Chapter V had shown that incubation time need not be longer than 10 minutes for P_2NMe_3 to reach a position around the membrane that did not change, we incubated samples for up to 3 hours prior to imaging. There was minimal

change in dimer localisation after 10 minutes around vesicular structures and signal to noise remains low, however we observe that background fluorescence in this protocol is higher than that observed for GUVs made from the lipid and dimer mix. This accounts for the increased counts/pixel from 0.36-3.6 relative to that observed in Figure 6.8. Nonetheless, the increased number of counts are from background fluorescence. This leads us to believe that due to mixing of the sample with lipid, when P_2NMe_3 is present during electroformation, it is forced into micelles prior to any exposure to aqueous solution.

We found that in the case of the P_2NMe_3 dimer in DOPC membranes, ratiometric images confirm what we have seen using the fluorometer in suspensions of LUVs without spatial resolution. However, further investigation of GUVs is limited due to the weakness of emission spectra in both channels. Ratiometric images of GUVs with porphyrin dimers suffered from two major drawbacks: firstly, ratios from low emission intensity are not as accurate as those from high intensity imaging, exemplified by considerable errors in viscosity values, and secondly, that spatial resolution is compromised by necessary methods of image processing. This loss of spatial resolution is an artefact of low emission viscosity in both channels prior to ratio calculation. Low intensity in each pixel makes ratio calculations less accurate, but also decreases the distribution of emission ratios over the image, i.e. pixels associated with 'signal' are closer in absolute ratio to pixels associated with 'noise'. Signal-to-noise ratios of the initial channels can be improved by techniques applied after acquisition of the image such as 'binning' of pixels as has been applied to the images shown in Figures 6.8 and 6.9. This image processing protocol was developed by Aurimas Vysniauskas for the express purpose of improving the quality of ratiometric images of porphyrin dimer emission[29]. Without the use of binning, viscosity measurements from these images are highly erratic. This is a quantization method applied to image processing where signal to noise ratio in an image is increased by the grouping of multiple neighbouring pixels with varying intensities into a single 'super pixel'. Signal to noise is improved by the increase of contrast between the single-intensity super pixel representing fluorescence emission and surrounding regions with false, 'noise' signal that is reduced to

darkness. Reducing the number of pixels creates contrast but decreases spatial resolution of the image.

The application of this binning in image analysis of GUVs is particularly misleading due to the presence of multilamellar vesicles in the electroformed product, which are impossible to separate from GUVs. Multilamellar vesicles are often seen to be brighter than GUVs during imaging due to the increased concentration of the dimer due to multiple bilayers. As a result, many of the images collected are of multilamellar vesicles which are impossible to distinguish by eye from GUVs. There are two structures in Figure 6.8c that display much lower viscosity than the surrounding lipid material. These structures are not considered to be authentically unilamellar vesicles, as bright field shows them to be highly dense aggregates within vesicles or lipid droplets where the corresponding viscosity value probably does not reflect a reliable lipid macrostructure. The weakness of the dimer's emission intensity enhances problems with correctly identifying the condition of imaged vesicles due to the lack of spatial resolution after image processing. This is a major drawback of using the charged porphyrin dimer in GUVs.

6.4.2 Ratiometric imaging with uncharged porphyrin dimer, P_2

We sought to reproduce successful experiments from Chapter V involving mixtures of the uncharged dimer P_2 with DOPC. These experiments are performed after electroformation lipid and dimer mixtures at a ratio of 1000 to 1 from dried films.

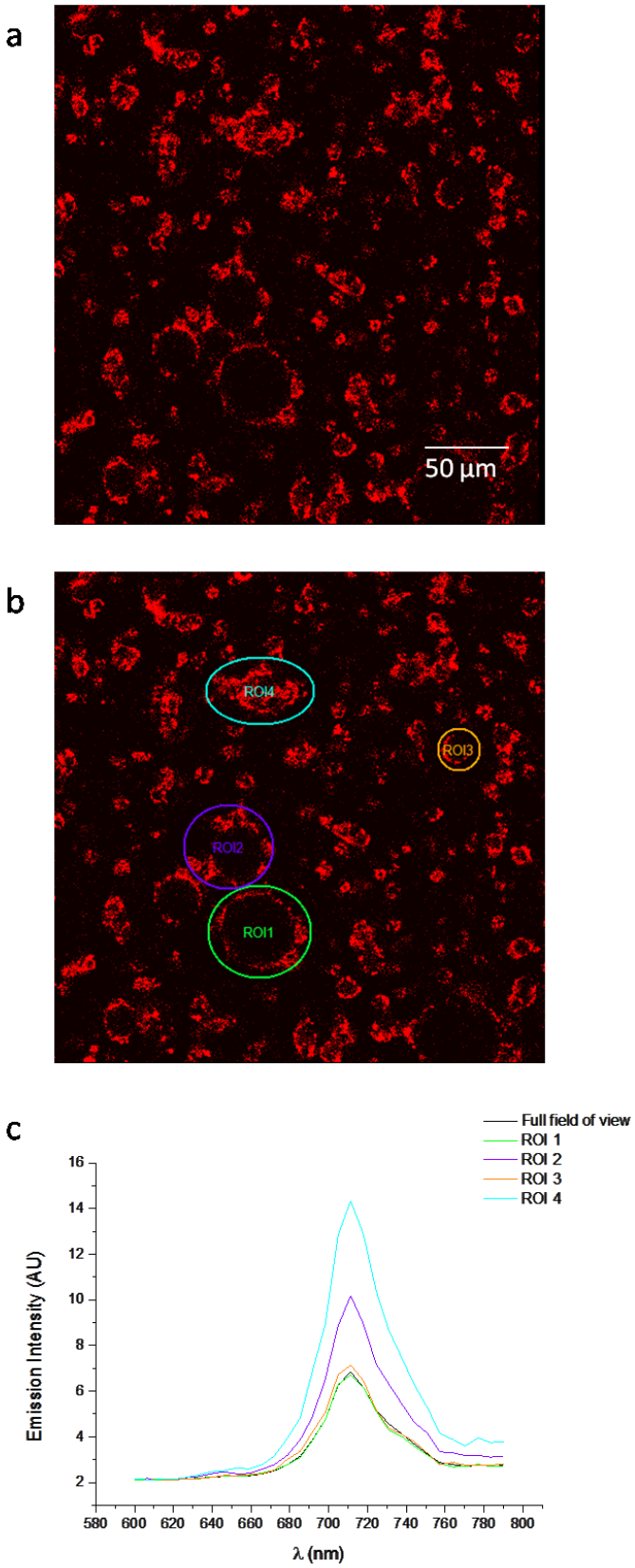

Figure 6.10: a) GUVs made from dehydrated mixture of P_2 and DOPC (lipid:dimer ratio of 1000:1), fluorescence from λ_{ex} = 448 nm, detection range of 600-800 nm; 512 x 512 pixels at 6646 counts; b) selected GUVs and aggregates display unimodal emission spectra; c) indicating aggregation in all ROIs.

Figure 6.10 shows images from a wide fluorescence channel (600-700 nm) of the uncharged dimer fluorescence in DOPC vesicles. Where emission is intense, it appears to originate from lipid aggregates or aggregates around circular structures which are thought to be GUVs. Signal is too low for us to yield ratiometric measurements from the P_2 DOPC sample, though we have been able to collect spectra directly, on the microsope, as shown in Figure 6.10c. We examine the spectra of the dimer in varying structures shown in the image. Figure 6.10c shows that the spectra of vesicular structures, by separating ROIs (region of interest). ROIs 1, 2 and 3 are GUVs of varying size, but are shown to have a unimodal peak at 710 nm, corresponding to the planar maximum of the dimer's emission spectrum. This confirms that the fluorescence visible in images is origninating from a completely planar, and most likely, aggregated dimer. ROI 4 selects a large aggregate, with no larger macrostucture and exhibits the same shape of emission spectra. Counts per pixel observed for this data are extremely low, at 0.02. Weak fluorescence, taken together with the unimodal peak leads us toconclude that P_2 is entirely aggregated in the sample.

This confirms our hypothesis that electroformation of dimer and lipid samples are not suitable for the production of dimer-embedded GUVs. From experiments with the P_2NMe_3 dimer, we had assumed that the charges at the *meso* positions were responsible for aggregation of the dimer and subsequent lipid aggregation. We believe that the charges on both ends of the porphyrin dimer caused disturbances to vesicle structure whilst bilayers were being formed. These disturbances could cause small aggregates which would engender larger ones. This could be due to the charged Zn^{2+} centre of the porphyrin macrocycle, which may have the interaction with the electrode surface from which lipids swell. Experiments with the uncharged dimer suggest that the dimer acts as a contaminant in the possibly creating micellar structures during electroformation.

From this data, we conclude that the presence of the porphyrin dimer during electroformation is either an impediment to formation of viable GUVs with embedded dimer, or the charged

centre of the macrocycle precludes inclusion of the dimer into lipid bilayers, as it interacts too strongly with electrodes rather than the hydrophobic lipid tail region.

6.5 Photobleaching and photosensitization

One barrier to satisfactory ratiometric images using the porphyrin dimer is that already low emission signal quickly reduces over the course of long exposure to excitation. We had prolonged image acquisition time in order to collect more photons for each pixel scanned. However, we found that at laser powers greater than 1 mW, this caused a bleaching of the dimer signal. Figure 6.11 shows the decrease in emission signal over one round of imaging, i.e. 50 frame averages per image. Figure 6.11a shows both emission channels before and Figure 6.11b, after, exposure to λ_{ex} =453 nm over four minutes of excitation where counts/pixel decrease from 0.04 to 0.01 during the course of imaging.

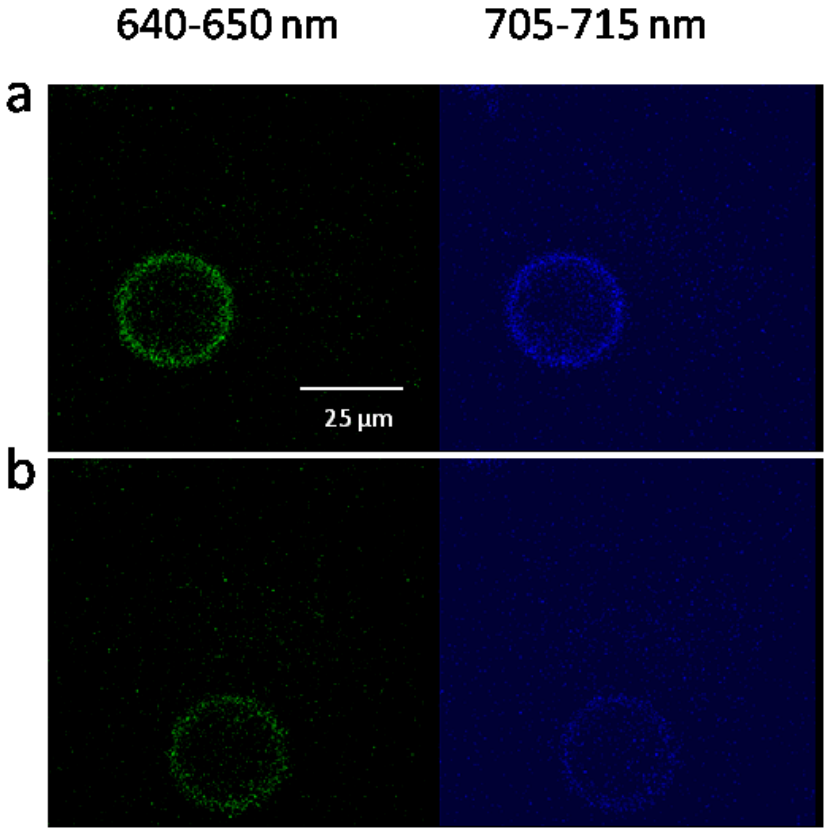

Figure 6.11: GUVs made from dehydrated mixture of P_2NMe_3 and DOPC (lipid:dimer ratio of 1000:1), fluorescence from λ_{ex} = 448 nm at 512 x 512 pixels, in two detection channels for twisted (640 -650 nm; 8686 counts) and planar (705-715 nm; 12426 counts) confomers; at a) Time 0; and b) 3830, 2796 counts in channel 1 and 2, respectivrely at time = 4 minutes of laser excitation (50 frame averages per image) showing loss of fluorescence signal during imaging.

High rates of photodegradation became apparent again when we increased laser power to achieve higher signal in shorter acquisition times. We hypothesize that this might be due to the high singlet oxygen quantum yield of the porphyrin dimer, where enough singlet oxygen is produced that it oxidises sites on the dimer itself, observed by a decrease in fluorescence signal. While observing this phenomenon, we took ratiometric images at regular time points as shown in Figure 6.12

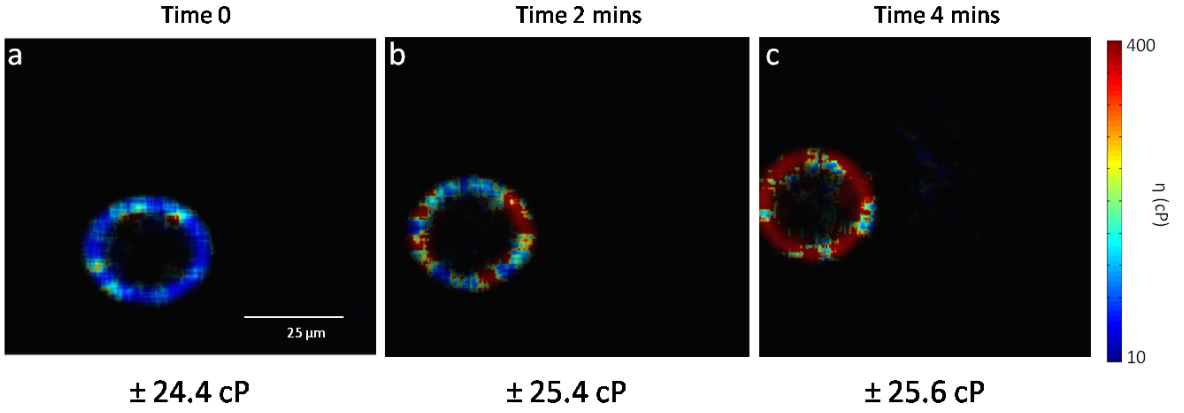

Figure 6.12: Ratiometric images of GUVs made from dehydrated mixture of P_2NMe_3 and DOPC (lipid: dimer ratio of 1000:1), fluorescence from λ_{ex} = 448 nm at 512 x 512 pixels, in two detection channels for twisted (640 -650 nm) and planar (705-715 nm) confomers; at a) Time 0 (8686, 12426 counts, respectively); and b) Time 2 minutes (5033, 4584 counts, respectively) of laser excitation and; c) Time 4 minutes (3850, 2796 counts, respectively). Image processing parameters are kept the same for each image, even though loss of signal is observed between the three images. Ratios associated with the imaged GUV appear to increase in proportion with imaging time (50 frame averages per image).

Figure 6.12 summarises our finding: the apparent viscosity of GUVs during imaging increases as a function of exposure time to excitation light, though we acknowledge the significant error of our measurements, and the increase in error at longer imaging times. We hypothesize that this is the effect of lipid bilayers exposed to singlet oxygen but sufficiently reliable an accurate measurements of viscosity are not possible with the use of the porphyrin dimer as a viscosity probe. The next chapter is devoted to an investigation of the effect of singlet oxygen on lipid membranes, while using the porphyrin dimer as a viscosity probe.

6.6 Conclusions

The use of molecular rotors to measure membrane viscosity is fundamentally different from previously established imaging techniques. Fluorescence methods measure translational diffusion, when compared with mechanical methods that measure membrane deformation, they yield largely different viscosity measurements. This is due to assumptions regarding the nature of friction in the bilayer. The use of molecular rotors was suggested as an optimal way to resolve these differences due to the specific relationship between rotational diffusion and viscosity. Porphyrin dimers were seen to be good candidates for the ratiometric measurement of viscosity in lipid bilayers due to their pseudo-amphiphilic structure, temperature independence and sensitivity to small changes in viscosity.

However, ratiometric imaging of GUVs with porphyrin dimers proved to be feasible but limited in resolution and reliability. We have identified sample preparation and the nature of the lipid-dimer interaction as causes of lack of signal and lack of localisation to relevant parts of the lipid bilayer. Future experiments will need to involve either a novel method of GUV production that is not affected by the presence of the charged dimer or an entirely hydrophobic molecular rotor that is able to embed within the membrane during electroformation. The porphyrin dimer has shown to be highly sensitive to photodegradation, most likely as a result of singlet oxygen production. We aim to continue using the porphyrin dimer as a photosensitizer in order to investigate the effects of singlet oxygen on membranes. In this vein, the next chapter shows the use of a second previously published molecular rotor to measure changing membrane viscosity upon exposure to singlet oxygen.

6.7 References

1. Saffman, P. G. & Delbruck, M. Brownian motion in biological membranes. Proc. Natl. Acad. Sci. 72, 3111–3113 (1975).

2. Saffman, P. G. Brownian motion in thin sheets of viscous fluid. J. Fluid Mech. 73, 593 (2006).

3. Veatch, W. & Stryer, L. Effect of cholesterol on the rotational mobility of diphenylhexatriene in liposomes: A nanosecond fluorescence anisotropy study. J. Mol. Biol. 117, 1109–1113 (1977).

4. Gielen, E. et al. Measuring diffusion of lipid-like probes in artificial and natural membranes by raster image correlation spectroscopy (RICS): use of a commercial laser-scanning microscope with analog detection. Langmuir 25, 5209–18 (2009).

5. Nipper, M. E. et al. Characterization of changes in the viscosity of lipid membranes with the molecular rotor FCVJ. Biochim. Biophys. Acta 1778, 1148–53 (2008).

6. Guo, L. et al. Molecular diffusion measurement in lipid bilayers over wide concentration ranges: a comparative study. Chemphyschem 9, 721–8 (2008).

7. Schmidt, T., Schuetz, G. J., Baumgartner, W., Gruber, H. J. & Schindler, H. Characterization of Photophysics and Mobility of Single Molecules in a Fluid Lipid Membrane. J. Phys. Chem. 99, 17662–17668 (1995).

8. Bacia, K., Scherfeld, D., Kahya, N. & Schwille, P. Fluorescence correlation spectroscopy relates rafts in model and native membranes. Biophys. J. 87, 1034–43 (2004).

9. Petrov, E. P. & Schwille, P. Translational diffusion in lipid membranes beyond the Saffman-Delbruck approximation. Biophys. J. 94, L41–3 (2008).

10. Kahya, N. & Schwille, P. Fluorescence correlation studies of lipid domains in model membranes. Mol. Membr. Biol. 23, 29–39 (2009).

11. Przybylo, M. et al. Lipid diffusion in giant unilamellar vesicles is more than 2 times faster than in supported phospholipid bilayers under identical conditions. Langmuir 22, 9096–9 (2006).

12. Ariola, F. S., Li, Z., Cornejo, C., Bittman, R. & Heikal, A. A. Membrane fluidity and lipid order in ternary giant unilamellar vesicles using a new bodipy-cholesterol derivative. Biophys. J. 96, 2696–708 (2009).

13. Cicuta, P., Keller, S. L. & Veatch, S. L. Diffusion of liquid domains in lipid bilayer membranes. J Phys. Chem. B 111, 3328–3331 (2007).

14. Dietrich, C. et al. Lipid rafts reconstituted in model membranes. Biophys. J. 80, 1417–28 (2001).

15. Schütz, G. J., Schindler, H. & Schmidt, T. Single-molecule microscopy on model membranes reveals anomalous diffusion. Biophys. J. 73, 1073–80 (1997).

16. Harms, G. S., Sonnleitner, M., Schütz, G. J., Gruber, H. J. & Schmidt, T. Single-Molecule Anisotropy Imaging. Biophys. J. 77, 2864–2870 (1999).

17. Einstein, A. Über die von der molekularkinetischen Theorie der Wärme geforderte Bewegung von in ruhenden Flüssigkeiten suspendierten Teilchen. Ann. Phys. 322, 549–560 (1905).

18. Hughes, B. D., Pailthorpe, B. A., White, L. R. & Sawyer, W. H. Extraction of membrane microviscosity from translational and rotational diffusion coefficients. Biophys. J. 37, 673–6 (1982).

19. Fushimi, K., Dix, J. a & Verkman, a S. Cell membrane fluidity in the intact kidney proximal tubule measured by orientation-independent fluorescence anisotropy imaging. Biophys. J. 57, 241–54 (1990).

20. Levitt, J. A. et al. Lifetime Imaging †. Structure 11634–11642 (2009).

21. Dent, M. R. et al. Imaging Phase Separation in Model Lipid Membranes Through the use of BODIPY Based Molecular Rotors. Phys. Chem. Chem. Phys. 17, 18393–18402 (2015).

22. Kuimova, M. K., Yahioglu, G., Levitt, J. A. & Suhling, K. Molecular rotor measures viscosity of live cells via fluorescence lifetime imaging. J. Am. Chem. Soc. 130, 6672–3 (2008).

23. Levitt, J. A. et al. Membrane-Bound Molecular Rotors Measure Viscosity in Live Cells via Fluorescence Lifetime Imaging †. J. Phys. Chem. C 113, 11634–11642 (2009).

24. Angelova, M. I. & Dimitrov, D. S. Liposome electroformation. Faraday Discuss. Chem. Soc. 81, 303 (1986).

25. Rodriguez, N., Pincet, F. & Cribier, S. Giant vesicles formed by gentle hydration and electroformation: a comparison by fluorescence microscopy. Colloids Surf. B. Biointerfaces 42, 125–30 (2005).

26. Politano, T. J., Froude, V. E., Jing, B. & Zhu, Y. AC-electric field dependent electroformation of giant lipid vesicles. Colloids Surf. B. Biointerfaces 79, 75–82 (2010).

27. Taylor, P., Xu, C., Fletcher, P. D. I. & Paunov, V. N. Fabrication of 2D arrays of giant liposomes on solid substrates by microcontact printing. Phys. Chem. Chem. Phys. 5, 4918 (2003).

28. Angelova, M. & Dimitrov, D. A mechanism of liposome electroformation. Trends Colloid Interface Sci. II 67, 59–67 (1988).

29. Vyšniauskas, A., Balaz, M., Anderson, H. L. & Kuimova, M. K. Dual mode quantitative imaging of microscopic viscosity using a conjugated porphyrin dimer. Phys. Chem. Chem. Phys. 17, 7548–54 (2015).

VII. The photosensitizing effect of the porphyrin dimer upon lipid bilayer viscosity

In Chapter VI we show how the viscosity-sensitivity of the porphyrin dimer can be adapted for microscopy, giving ratiometric images of the dimer associating with DOPC membranes. The quality of ratiometric images was severely limited by the solubility of the dimers, on the one hand prohibiting the charged dimer from entering the hydrocarbon region of the membrane and on the other, causing the uncharged dimer to aggregate during vesicle production by electroformation. We tested a number of ways of increasing emission signal, for example testing longer exposure to laser excitation and/or increasing excitation power. However both these conditions resulted in significant photobleaching. We hypothesized that the photobleaching can be in fact caused by the production of singlet oxygen by the dimers in high yield, as previously demonstrated[1,2]. Thus, it is possible that the singlet oxygen produced by the dimer is (i) affecting the dimer by photobleaching and (ii) is affecting the unsaturated lipids in a bilayer, analogously to what has been previously observed in mammalian cells[1]. This Chapter explores the effect of the dimer's singlet oxygen production on lipid bilayers, and attempts to detect a viscosity change associated with the production of singlet oxygen. To enable the independent verification of viscosity measurements during singlet oxygen production we decided to complement the dimer ratiometric measurements with the measurements of another molecular rotor,that was previously shown by our group to be a superior probe for hydrocarbon bilayer region: a boron dipyrromethene (BODIPY).

7.1 Singlet oxygen

Valued for its therapeutic capacity, the targeted and controlled generation of singlet oxygen is the subject of considerable study. Molecules that produce singlet oxygen are termed *photosensitizers*, and are manipulated to become compatible with uptake by cells. This section

describes some of the basic features of singlet oxygen and the role of the photosensitizer in its production.

7.1.1 Generation of singlet oxygen

Ground state molecular oxygen has an unusual electronic configuration that leaves two unpaired electrons in the HOMO. The bonding of two oxygen atoms, each with six electrons, results in an electron configuration of: $(2\sigma_g{}^2)$ $(2\sigma_u{}^2)$ $(3\sigma_g{}^2)$ $(1\pi_g{}^4)$ $(1\pi_u{}^2)$ as shown in Figure 7.1a. Here, the two degenerate antibonding orbitals, $\pi_{g,x}$ and $\pi_{g,y}$ are occupied by one electron each, while all others are occupied by two. As such, the ground state of molecular oxygen is triplet ($X^3\,\Sigma_g^-$) and there are two excited states: both singlet (electron configuration of one of which is shown in Figure 7.1b) $1\Delta_g$ and $b\,{}^1\Sigma_g^+$, all close in energy[3].

Transitions between all three states are spin-forbidden by electric-dipole coupling, the usual means by which excited states are reached, as outlined in Chapter I. This is due to the Laporte rule, applied to centrosymmetric molecules such as O_2, which states that the total spin quantum number of a transition must remain the same during a transition, that is, must remain either + or – ½, such that electric energy transfer cannot occur between singlet and triplet states or vice versa. Experimental evidence of molecular oxygen in isolation, i.e. in gas, shows extremely weak absorption lines corresponding to these forbidden transitions, as observed by Childs and Mecke et al., 1931[4]. However, in solution, subject to molecular collisions and perturbations of the electronic structure by interaction with solvent or other solutes, the symmetry of the molecule is interrupted. As such, the transitions between the triplet and singlet excited states become more likely, that is, they take on 'partially allowed character'. This is observed by an increase in absorption intensity corresponding to the transition from the $X^3\,\Sigma_g^-$ ground state and the $1\Delta_g$ and $b\,{}^1\Sigma_g^+$ excited sates[5]. Singlet to triplet transitions occur by spin-orbit coupling, that is, electromagnetic interaction between an electron's spin and the electromagnetic field generated by its orbit about the nucleus of the atom resulting in the 'flipping' of the electron's spin. This coupling lowers the energies of the energy levels of coupled electrons such that transitions are

more likely. That is, spin orbit coupling is associated with a value for total angular momentum *j*, which is the sum of the *l* and *s* quantum numbers. Indeed the band gap between $X^3\Sigma_g^-$ and $1\Delta_g$ is the well-known quantity 94.3 kJ/mol (0.98 eV)[3]. In solution, triplet excited state solutes (such as photosensitizers) in close proximity to molecular oxygen ($X^3\Sigma_g^-$) can excite it to the $1\Delta_g$ state, by electronic energy transfer. Indeed, for the application of PDT, this energy transfer is desirable and conditions to increase its frequency are sought.

Generally, the term 'singlet oxygen' and its effects are associated with only one of the singlet excited states, the $1\Delta_g$ state, rather than the $b\ ^1\Sigma_g^+$ state. The latter describes a singlet excited state whereby both electrons occupy the same orbital, in contravention of Hund's rule. $b\ ^1\Sigma_g^+$ is characterised by an extremely short lifetime (e.g. 0.65 s in carbon tetrachloride (CCl_4) at room temperature)[6] until it reverts to the $1\Delta_g$ state which we have shown in Figure 7.1b.

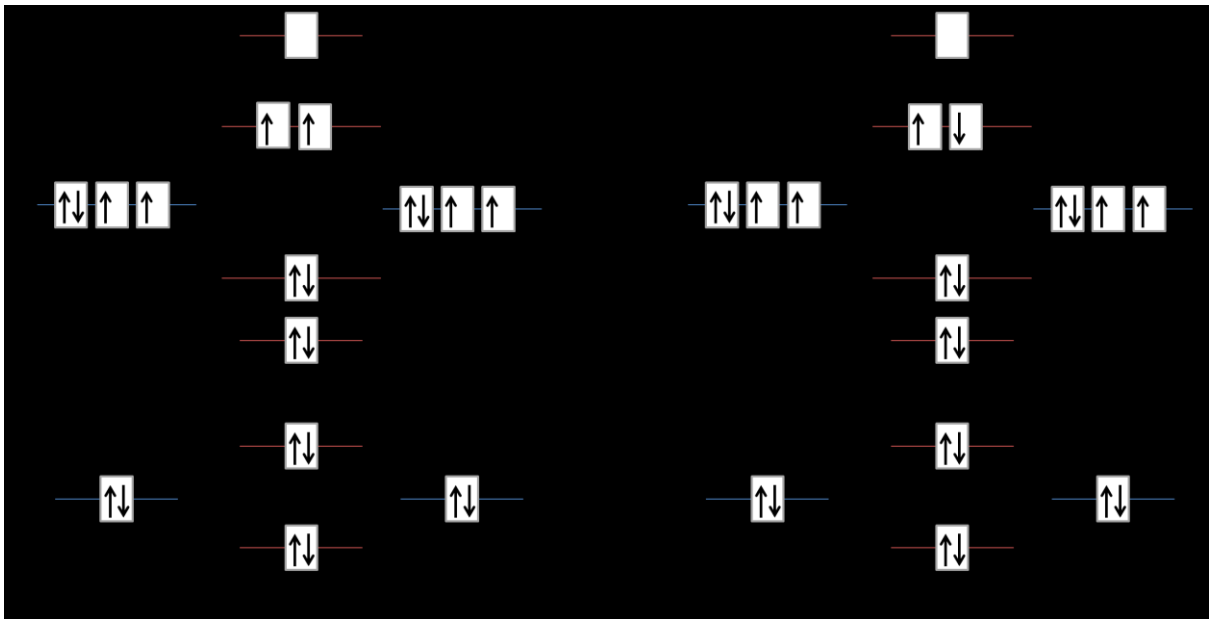

Figure 7.1: a) Electronic configuration of ground state triplet molecular oxygen ($X^3\Sigma_g^-$) and b) electronic configuration of one of the two singlet excited states: $1\Delta_g$.

7.2.1 Deactivation of singlet oxygen

Most significant studies on $1\Delta_g$ and its behaviour within biological environments focus around its deactivation which can take place by multiple mechanisms:

Radiative Decay

In Chapter 1, we briefly discussed the deactivation of the triplet state of a molecule by radiative decay, termed phosphorescence due to the long lifetimes at which it is observed. Phosphorescence at 1270 nm is observed when the excited state singlet oxygen, $1\Delta_g$, decays to the triplet ground state $X\,^3\Sigma_g^-$. In gas, the lifetime of $1\Delta_g$ is remarkably long, at 72 minutes.[7,8] However, biologically relevant media are not isolated, and the interactions between $1\Delta_g$ and the surrounding media play an extremely important role in deactivation of the excited state. Radiative transitions are enhanced by molecular collisions, due to the mixing between the molecular orbitals of colliding molecules and those of the $\pi_{g,x}$ and $\pi_{g,y}$ antibonding orbitals of molecular oxygen. The polarizability of the colliding molecule determines the extent to which radiative rate constants are enhanced relative to those of molecular oxygen in isolation.[3]

Interactions between $1\Delta_g$ and solvent or solute molecules in solution are crucially important for understanding the therapeutic consequences of singlet oxygen. Generally, the non radiative deactivation of singlet oxygen is the major component of PDT. Three different modes of non radiative decay take place for the transition from $1\Delta_g$ to $X\,^3\Sigma_g^-$ we summarise them below.

Non radiative decay

1. *Electronic to vibrational energy transfer:*

Hurst and Schuster et al., 1982 developed a theory of $1\Delta_g$ in solution where vibrational modes of $1\Delta_g$ and a given solvent bond X-Y, overlap in energy. The greater the vibrational energy of the bond X-Y, the more likely its overlap with a vibronic energy transition of O_2 $1\Delta_g$, resulting in the deactivation of $1\Delta_g$ by vibrational energy transfer to the solvent bond X-Y.[3,9]

2. *Charge transfer induced quenching*

Far more common than electronic to vibrational energy transfer is charge transfer to another solute. Physical proximity of O_2 $1\Delta_g$ to a molecule with low oxidation potentials ($E_{ox} \leq 1.9$ V vs. saturated calomel electrode (SCE)) results in the formation of an transient complex, termed an 'exciplex'[3]. The energy of this exiplex is lowered by the transfer of electric charge from the

molecule to oxygen, that is, oxidation. The exciplex subsequently decays by intersystem crossing to a triplet ground state complex, which then separates, leaving O_2 $X\ ^3\Sigma_g^-$. and the oxidized molecule.[3] Rate constants for charge transfer-induced quenching are approximately seven times higher than those for electronic to vibrational energy transfer, and as such, is considered the most common form of non radiative deactivation of singlet oxygen. This is the mechanism that governs the 'Type II' reactions (discussed in section 7.2.1) that are observed in PDT, valued for their therapeutic effect.

3. *Electronic energy transfer*

The singlet excited state, O_2 $1\Delta_g$ can transfer its electronic energy to a molecule with singlet ground state of sufficiently low energy (≤ 0.94 kJ/mol or 0.98 eV). Molecules most commonly associated with efficient quenching of O_2 $1\Delta_g$ include carotenoids, phthalocyanines, and iodine amongst others.[3]. These molecules are extremely useful in their capacity to deactivate O_2 $1\Delta_g$ without chemical change to the system, as they often decay from their excited states by fluorescence.

7.2 Porphyrin dimers as photosensitizers

Singlet oxygen ($^1O_2$) is produced very efficiently by macrocyclic structures such as tetrapyrroles and porphyrinoids, meaning that excitation of the porphyrin dimers in aerobic environments could give significant doses of singlet oxygen. Indeed, we know that the porphyrin dimers have high $^1O_2$ quantum yields (φ_Δ). Kuimova et al., 2009 first published φ_Δ for all variants of the dimer in an aqueous environment (D_2O) and in organic solvent (MeOH) as shown in Table 7.1, where the relevant dimers used in this chapter have been highlighted in yellow[10]. The difference between φ_Δ in hydrophobic solvent and in D_2O is significant for both the charged and uncharged dimers, which was previously attributed to aggregation effects. As we have discussed previously, Chapters V and VI suggest that the charged dimer is associated with the surface of lipid bilayers, not truly embedded within the hydrocarbon region and at least partly exposed to water, suggesting that the φ_Δ might reflect to a certain extent exposure to aqueous conditions.

However, in our system, the dimers are associated with the lipid bilayer, at least partially, which may suggest that the ϕ_Δ of the dimers relevant to the work reported here is somewhere in-between the organic solvent and the aqueous environment.

Table 7.1: Summary of spectroscopic parameters for a series of porphyrin dimers*

	P_2	P_2-NMeI	P_2C_2-NMeI	P_2-NMeOAc	P_2-SO_3NH_4	P_2C_2-CO_2NH_4	P_2-Suc
λ_{max}(em) DMSO	700	730	795	715	715	760	720
λ_{max}(em) H_2O	712	760	800	733	725	780	729
ϕ_f, MeOH[a]	0.11	0.11	0.01	0.10	0.13	< 0.001	0.06
ϕ_f, D_2O[b] 0.5% DMSO	< 0.001	0.002	< 0.001	0.005	0.03	< 0.001	0.008
ϕ_f, D_2O/ BSA + heat	< 0.001	0.08	0.02	0.05	0.05	0.01	0.01
ϕ_Δ, MeOH[c]	0.89	0.54	0.60	0.70	0.69	0.20	0.87
ϕ_Δ, D_2O[d]	0.14	0.50	0.25	0.36	0.59	0.24	0.43

** Table from Kuimova et al., 2009 (Ref [10])*
λ_{max}(em) describes the emission maximum of the planar confomer, as reported in DMSO and H_2O; φ_f, fluorescence quantum yield in the specified solvent, φ_Δ, $^1O_2$ quantum yield. Reported values are measured [a] vs Chla in ether (0.32), [b] verteporfin in D_2O (0.05), [c] Chla (0.77) and $[Ru(bpy)_3]^{2+}$ (0.8); [d] TMPyP (0.74).

At the time of the publication of the data shown in Table 7.1 it was not yet discovered that the porphyrin dimer can exist in two separate conformations: twisted and planar. Thus the singlet oxygen quantum yields determined above did not take into account the conformational flexibility of the dimer. However, the relationship between the dimers' viscosity-dependent conformational dynamics and singlet oxygen production efficiency was later examined in detail[11]The effects of porphyrin dimer torsional rotation on φ_Δ were examined and it was found that the planar confomer of the porphyrin dimer has higher efficiency of $^1O_2$ production than the twisted[10,12]. Figure 7.2c shows that φ_Δ is maximised by absorption of the planar confomer at λ_{ex} = 480 nm, rather than at 450 nm, the maximum absorption of the high energy twisted confomer. In Figure7.2b, we see that λ_{ex} = 450 nm can give relatively high production of $^1O_2$, but this is prohibited by high viscosity media, meaning that 450 nm excitation is only efficient for production of $^1O_2$ due to intermolecular rotation from the twisted excited state to the planar excited state, which goes on to form the triplet state[11].

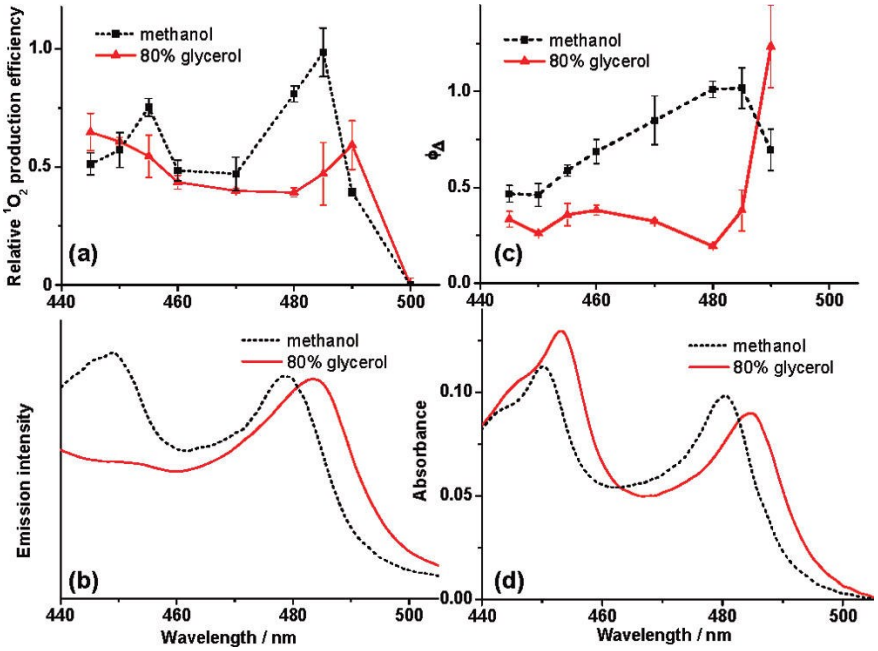

Figure 7.2: a) $^1O_2$ production efficiency; b) emission intensity; c) φ_Δ and d) absorbance spectra recorded in methanol (dashed line, black) and 80% glycerol/ 20% methanol (red). (Reproduced from ref [11])

This study suggests a useful strategy for efficient $^1O_2$ production in our experiments. Excitation of the porphyrin dimer at the peak of the planar confomer produces $^1O_2$, yet excitation at the peak of the twisted confomer allows for viscosity measurement, effectively separating the two functions. With this separation we should be able to minimise $^1O_2$ production during viscosity measurement. We will test this strategy here by performing bulk viscosity measurements in LUVs accompanied with singlet oxygen production, however, as shown in Chapter VI, this separation was not sufficient for ratiometric imaging, as excessive bleaching decreased the emission signal beyond useful values.

7.2.1 Photosensitization of membranes

In biological systems a large 'dose' of $^1O_2$ ($^1\Delta_g$) is cytotoxic and when used for therapeutic purposes in the damage of malignant cells is termed photodynamic therapy (PDT). Energy transfer to ground state molecular oxygen from the triplet state of the photosensitizer produces $^1O_2$, however electron transfer is also possible resulting in radical formation – these two pathways are termed Type II and Type I, respectively (as described above) as shown in Figure 7.3. Photosensitization in membranes is particular due to the long lifetime of $^1O_2$ (36 μs)[13] and

the high concentration of ground state oxygen in the hydrocarbon region of bilayers. The likelihood of either of the two pathways dominating depends primarily on efficiency of the photosensitizer in its environment. For example most studies involving porphyrin photosensitizers, which generally exhibit high triplet energy transfer to O_2, have found that solvent effects other than aggregation can greatly influence $^1O_2$ production, this topic is reviewed in detail by Valenzano et al., 1987 [14,15]. Given this effect, the nature of the association between porphyrins and membranes is a determining factor in the efficacy of $^1O_2$ production, the diffusion of $^1O_2$ within the membrane, and the observed effects of PDT on membranes[16–20]. Lavi et al., have studied in detail the localisation of porphyrins within biomimetic membranes and observed effects of oxidation, finding that increased depth of the porphyrin in the membrane is proportional to φ_Δ but $^1O_2$ associated effects are reduced[19]. Fluidity of the membrane is inversely related to φ_Δ[19–21] suggesting that membrane structure is strongly affected by exposure to $^1O_2$.

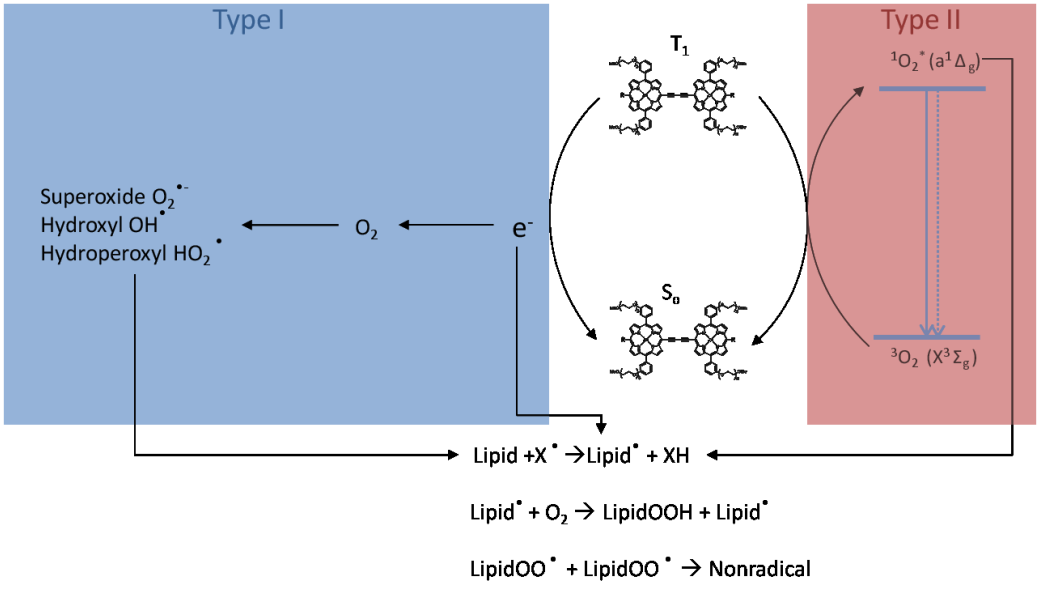

Figure 7.3: Scheme of Type I (electron transfer) and II (energy transfer) reactions with the porphyrin dimer photosensitizer and O_2 and possible effect of these processes on membrane lipids

7.2.2 Lipid peroxidation and membrane structure

Once $^1O_2$ is present its effects are dependent upon the local concentration and the availability of reactants; in some cases, $^1O_2$ is physically deactivated by energy transfer, resulting in dioxygen

and heat, in other cases, the $^1O_2$ reacts with nearby molecules causing reorganisation of chemical bonds on lipids. Figure 7.3 lists the interactions observed in oxygenated lipid systems, whereby $^1O_2$ interacts with lipids by the 'ene' mechanism, ultimately producing a lipid peroxide which can participate in the radical chain mechanism (lipid peroxides abstract H from nearby lipids, creating further peroxides) under specific conditions [22–24]. The ultimate result of both Type I and Type II pathways appears to be lipid peroxidation, though it has been shown that position of the peroxide group is likely to change depending on the oxidative pathway[23]. Peroxide groups will alter the fundamental shape and electrostatic interactions between lipid chains, there is existing evidence that PDT-related lipid peroxidation is associated with alteration of macroscopic membrane structure. Wratten et al., 1992 have suggested that the hydrophilic character of peroxides cause reorientation of the lipid chain, bending it towards the membrane interface (e.g. the glycerol moiety of a phosphocholine molecule)[25] as shown in Figure 7.4. This hypothesis has been reiterated by measurements of oxidised bilayer spontaneous curvature[26], changes in membrane depolarisation and permeability[27], and most recently, a reduction in membrane elastic stretching as measured by micropipette aspiration[28]. These changes are consistent with a reduction in membrane order, and of phospholipid packing within the bilayer[29].

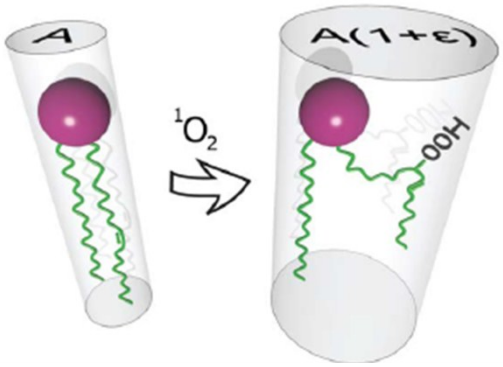

Figure 7.4: Hypothesized change in unsaturated lipid volume after lipid hydroperoxides formation from Type I or Type II reaction. Hydroperoxide is hypothesized to localise to aqueous solution. Figure from Weber et al., 2014 . (Ref [28])

We have shown that molecular rotors are sensitive to lipid packing and the 'free volume' in the hydrocarbon region, which we term 'membrane viscosity'. Any alteration to the structure and

volume of individual phospholipids is expected to be observable by measurement of the dynamics of molecular rotors. This change has strong bearing on our hypothesis regarding membrane viscosity and $^1O_2$ exposure as measured by molecular rotors. We have observed an increase in membrane viscosity that is proportional to porphyrin dimer irradiation; this Chapter will attempt to explain the mechanism by which $^1O_2$ production is affected by porphyrin dimer localisation and suggest a relationship between lipid peroxidation and membrane viscosity.

7.3 Irradiation of LUV suspensions in the presence of the dimer

Chapter V summarised the production and measurement of bilayer viscosity in small unilamellar vesicles (LUVs) where we found that the uncharged dimer was soluble in the hydrocarbon region of the membrane and reported viscosities consistent with those from literature. We used the LUV system to examine the photosensitizing effect of the dimer upon lipid bilayer viscosity in the hydrocarbon region. Figure 7.5 shows preliminary data of change in dimer emission ratio upon irradiation of a DOPC and P_2 LUV suspension (at 1000:1 lipid: dimer ratio) that are consistent with increased viscosity within the bilayer. This data gives strong evidence in support of our hypothesis regarding the effect of photosensitization on lipid bilayer viscosity. We take advantage of the dual functionality of the dimer, as both photosensitizer and viscosity-probe to further investigate this relationship. Our preliminary data shows evidence of viscosity increase after irradiation: Figure 7.5a and b show the change in emission spectra of the P_2 dimer in DOPC vesicles (Figure 7.5a, absolute; 7.5b, normalised) before, in black, and after, in red, irradiation at 479 nm for 60 minutes at 150 mW. Though there is considerable photobleaching of the dimer, resulting in a much weaker emission signal after irradiation, we see the rise of the twisted emission peak at 640 nm relative to the planar peak at 690 nm, which is consistent with viscosity increase.

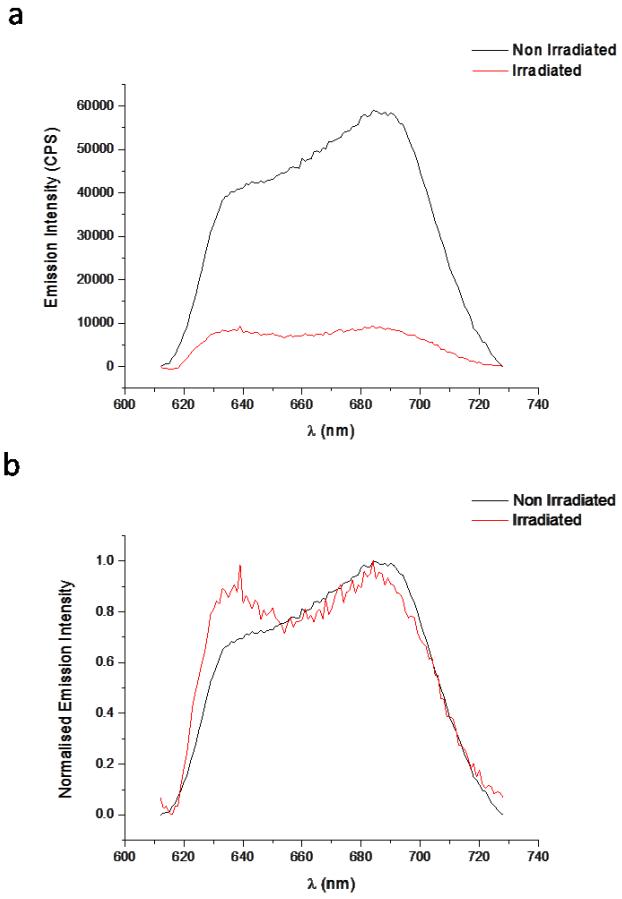

Figure 7.5: a) Absolute; b) Normalised fluorescence spectra of LUVs made from dehydrated mixture of DOPC and P_2 (0.66 μM) before and after irradiation at 480nm at 50 mw for 60 minutes; (lipid: dimer ratio of 1000:1, λ_{ex} = 448 nm)

The spectra shown in Figure 7.5a and b are measured at the excitation peak of the P_2 'twisted' confomer, 458 nm. However, the LUV suspension was irradiated at the P_2 low-energy 'planar' peak, 480 nm, according to the principles reported in Kuimova et al., 2009[11]. We chose to selectively irradiate the planar confomer due to evidence from Kuimova et al., 2009[11] that the φ_Δ of the lower energy planar confomer is higher than that of the twisted across the entire width of the Soret peaks. In the event of low viscosity, we could expect that the intermolecular rotation from the twisted confomer to the planar could yield high concentrations of singlet oxygen, however our results from Chapter V show that the twisted-to-planar emission ratio at 333 K for DOPC LUVs is relatively high, limiting the presence of the planar S_1, and therefore T_1 state. Additionally, maximising singlet oxygen yield by exciting the planar confomer should

reduce the irradiation time and power, which would moderate rates of photobleaching. All further experiments on LUVs are carried out under these conditions.

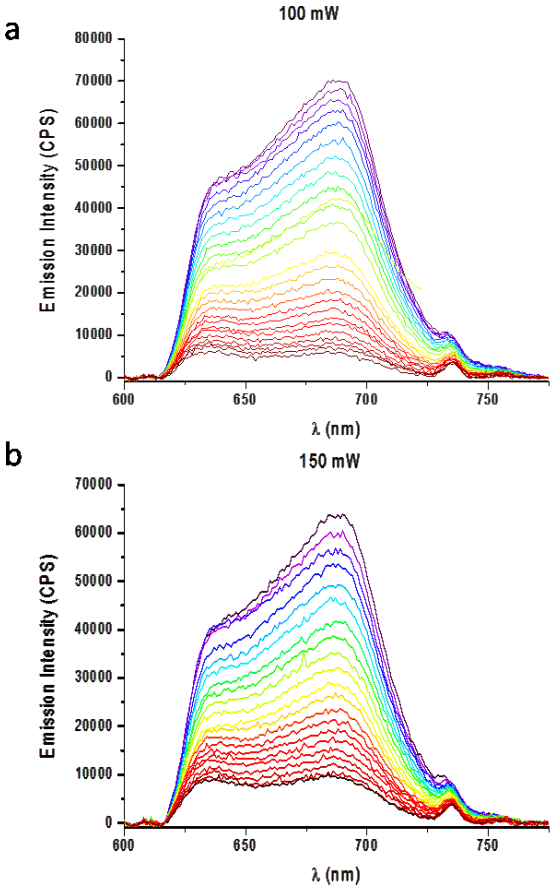

Figure 7.6 Decrease in fluorescence intensity and change in emission peak ratio in emission spectra of LUVs made from dehydrated mixture of DOPC and P_2 (0.66 μM) after irradiation at 480nm at a) 100 mW b)150 mw for 60 minutes. Time 0 shown in violet to Time 60 shown in red (lipid: dimer ratio of 1000:1, λ_{ex} = 448 nm).

Figure 7.6 shows raw data from the irradiation of DOPC LUVs with embedded P_2 with regular sampling of the emission ratio over irradiation time. Figure 7.6 demonstrates the decrease in spectral quality over a time course of irradiation over 2 hours as a result of photobleaching of the dimer. However, we also observe apparent change in emission ratio, over the course of the irradiation. Figure 7.7 describes the relationship between ratiometric viscosity measurement and irradiation time.

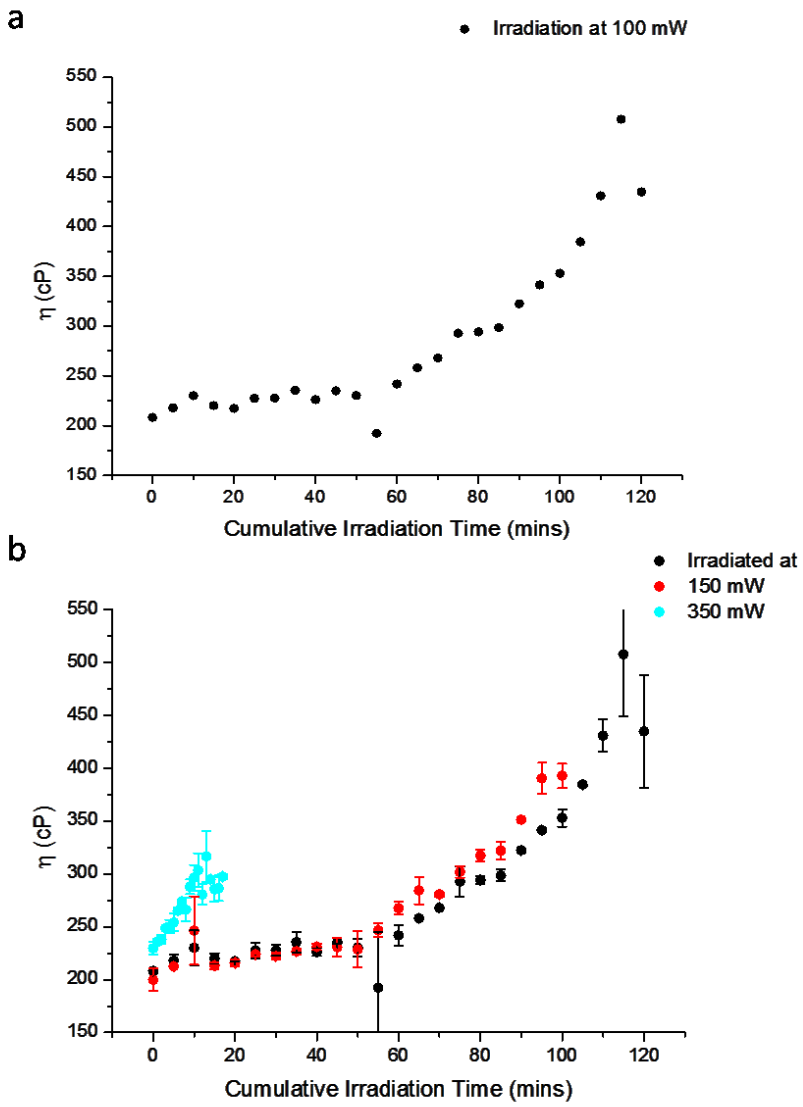

Figure 7.7: Ratiometric viscosity measurements of LUVs made from dehydrated mixture of DOPC and P_2 during irradiation; b) varying with laser power at 100 (black), 150 (red) and 350 (cyan) mW. Viscosity values calculated using P_2 in Castor oil calibration, Chapter III (lipid: dimer ratio of 1000:1, λ_{ex} = 448 nm)

Figure 7.7a shows the increase in viscosity upon irradiation at 100 mW at increasing exposure time up to 120 minutes, and this data supports our hypothesis that the observed viscosity increase is correlated with exposure time of irradiation. Moreover, Figure 7.7b shows that the rate of viscosity increase changes with irradiation power, suggesting that the total energy of exposure is proportional to the viscosity increase. In Figure 7.7b, irradiation at 350 mW induces a higher rate of viscosity increase than irradiation at 100 and 150 mW, however the reduction in fluorescence signal greatly increases the error as seen either upon prolonged irradiation at

lower powers or at early times at high powers. Comparison between data sets of lower power irradiation series show that irradiation at 150 mW appears to give marginally faster rates of viscosity increase after 60 minutes.

As we have seen in Chapter V, temperature is a crucial factor in determining the viscosity of LUVs, which we have demonstrated has a liquid-like sensitivity to temperature in the hydrocarbon region. The irradiating source used was a dye laser with 3 mm laser spot, to which the cuvette was intermittently exposed before being placed back within the fluorometer for emission measurements. This set up poses a number of difficulties for accurate interpretation of the data; firstly, the highly localised power of the laser spot can cause local heating which would change the bilayer viscosity within a given area surrounding the spot, making the LUV suspension heterogeneous for ratiometric measurements. Secondly, due to the density of the LUV suspension, diffusion of LUVs into and out of the laser spot is relatively limited; meaning that exposure to irradiation would be confined to a small fraction of total cuvette volume and any change would not be measureable by fluorometry or again, make the LUV suspension heterogeneous for dimer emission ratio. Furthermore, we showed in Chapter V that significant temperature change induces phase change within the hydrocarbon region of bilayers which can cause reorientation or expulsion of the dimer from the bilayer. Our hypothesis predicts lipid viscosity changes that could amount to unpredictable phase behaviour and could result in the same ejection or repositioning of the dimer, rendering pre and post irradiation measurements incompatible. Interpreting this kind of response from fluorometry data requires that the sample be largely homogenous. Moreover, it became clear due to the extent of photobleaching our ratiometric viscosity measurements are subject to increased error as irradiation times and laser powers are increased.

Given these drawbacks, we determined that adequate investigation of the phenomenon that we have observed in preliminary data would require that the experiment be carried out under different conditions. Ideally, we would like to image the effects of photosensitization using

microscopy, however, we showed in Chapter VI that ratiometric measurements are unreliable for quantification and particularly unsuitable for irradiation experiments where photobleaching reduces emission signal even further than initially low levels. We determined that the photosensitising effect of the porphyrin dimer would have to be studied independently from its viscosity sensitivity in order to gather trustworthy data. Once we have established the physical consequences of $^1O_2$ production in the presence of lipid bilayers, then we would reassess whether the porphyrin dimer is a good candidate for PDT in these systems. In order to measure the effect of viscosity change on lipid membranes, we used a hydrophobic molecular rotor, with good viscosity sensitivity in lipid bilayers, a C_{10} meso substituated m-phenyl boron dipyrrin (BODIPY C_{10}).[30]

7.4 PDT in lipid bilayers as measured by BODIPY C_{10}

These experiments are carried out in collaboration with Aurimas Vysniauskas.

BODIPY C_{10} is a molecular rotor that has high solubility within the hydrocarbon region of membranes[30,31]. Figures 7.8a, b reproduce published data obtained in our group[32], verifying the BODIPY-C_{10} is a molecular rotor with a good sensitivity of its lifetime to viscosity of methanol-glycerol mixtures. Figures 7.8b show the structure of BODIPY C_{10}, and the arrow indicates the mode of twisting which comprises the mode of non-radiative deactivation from the excited state. In the case of BODIPY C_{10}, restriction to intermolecular twisting is measured by an increase in fluorescence lifetime rather than fluorescence quantum yield. Figure 7.8a shows the increase in fluorescence lifetime in solutions of increasing viscosity as measured by time-correlated single photon counting (TCSPC). The Förster-Hoffmann law predicts that there is a linear relationship between viscosity and τ_f when both are plotted on a logarithmic scale; this is true of BODIPY C_{10} as shown in Figure 7.8b.

Figure 7.8c shows emission intensity of BODIPY C_{10} as added from solution to a sample of GUVs. In fact, Wu et al., 2013[30] and Dent et al., 2015[31] have already shown its capacity for detection of lipid phase change as a function of temperature, as well as accurate measurement of lipid

bilayer viscosity in ternary mixtures exhibiting both the L_o (liquid ordered) and L_d (liquid disordered) phases. Given this data, BODIPY-C_{10} molecular rotor appeared to be an ideal candidate for measuring viscosity of hydrocarbon region of GUVs during singlet oxygen production, by porphyrin dimers.

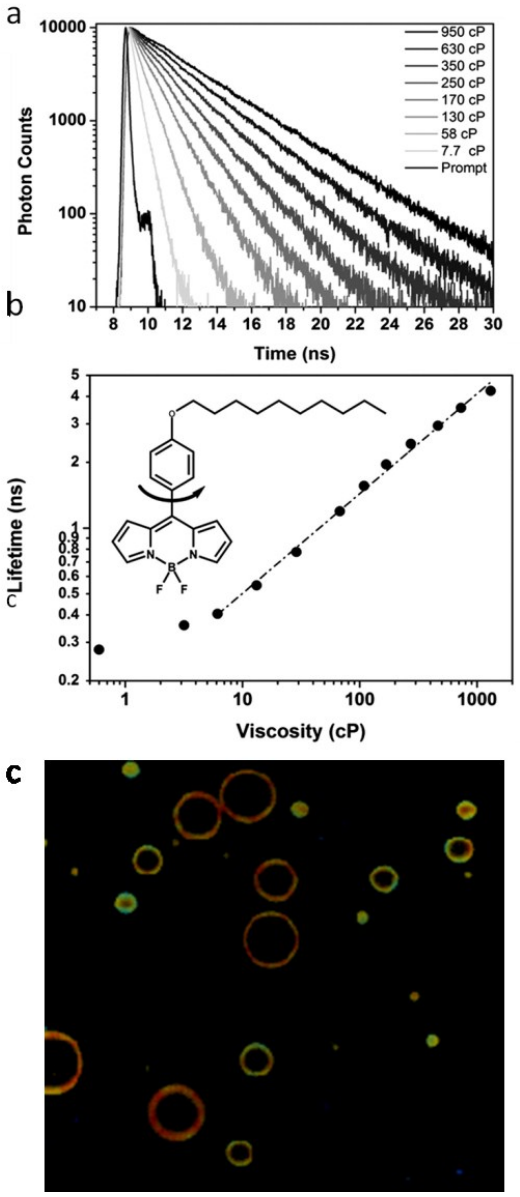

Figure 7.8: a) TCSPC fluorescence decays of BODIPY C_{10} in solutions of varying viscosity (w/v % methanol/glycerol solutions); b) linear calibration of BODIPY C_{10} τ_f against solution η as measured by mechanical rheometry, inset: structure of BODIPY C_{10} and mechanism of viscosity sensitivity due to phenol rotation; c) BODIPY C_{10} fluorescence in DOPC GUVs after addition from aqueous solution (10 μM BODIPY C_{10}) λ_{ex} = 488 nm (detection range 600-800 nm). Figure 7.7a,b are adapted from Hosny et al., 2013 (Ref [32])

Chapter VI showed that electroformation with P_2NMe_3 yields structurally viable GUVs. We optimised this protocol for the incorporation of BODIPY C_{10} into GUVs made from a mixture of DOPC and P_2NMe_3, at ratios of 600:1 DOPC: BODIPY C_{10} and 1000:1 DOPC: P_2NMe_3. A concentrated solution of BODIPY C_{10} added to the GUV suspension was found to localise to GUVs within 10 minutes. We compared the distribution of fluorescence lifetimes of this sample to those of GUVs made from a mixture of DOPC and BODIPY C_{10} and found them to be the same, indicating that the positioning of the probe in the membrane is the same in both preparations. To test the compatibility of the two compounds in close proximity we also compared fluorescence lifetimes and ratiometric measurements of a mixture of BODIPY C_{10} and P_2NMe_3 in a mixture of methanol and glycerol (w/w; 20/80 %, respectively) that gives the same lifetime-calculated viscosity measurement as seen in GUVs at 20 °C. We found that the two fluorophores behave independently of one another even when dissolved in the same solution during irradiation. Figure 7.9 shows absorption spectra of BODIPY C_{10} and P_2NMe_3 and indicates where each was excited; BODIPY C_{10} is excited at 488 nm at 5 mW for imaging, P_2NMe_3 is excited at 453 nm, both at 5 mW.

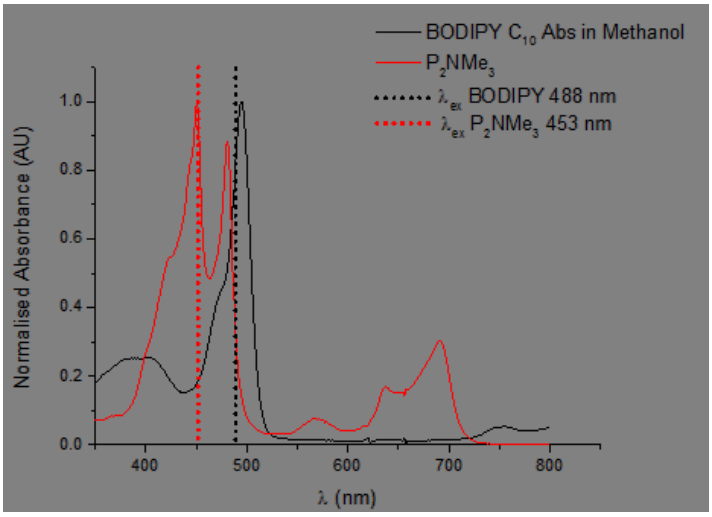

Figure 7.9: Normalised absorption spectra of P_2NMe_3 (red) and BODIPY C_{10} (black) in methanol. Excitation wavelengths for fluorescence experiments are selected according to absorption maxima for either compound (dashed lines: 453 nm for P_2NMe_3, 488 nm for BODIPY C_{10}).

With these controls in place, we used the fluorescence lifetime of BODIPY C_{10} to measure the change in GUV bilayer viscosity upon excitation of the charged porphyrin dimer at higher

intensities with the intention of producing singlet oxygen, conditions which we term 'PDT irradiation'. GUVs were electroformed from mixtures of DOPC and P_2NMe_3 at 333 K and BODIPY C_{10} was added as a concentrated solution and allowed to penetrate the vesicle membrane.

The experiment was carried out with the intention of imaging BODIPY fluorescence lifetime in GUVs, a technique known as Fluorescence Lifetime Imaging Microscopy (FLIM). Here, an image reflects the variation in exponential decay from the excited state (lifetime, and by our calibration, viscosity) as measured in each pixel of an image. Lifetimes are assigned a colour according to their value in a psuedocolour scale.

In our experiment, we compare GUVs in close physical proximity, one in which the porphyrin dimer has been excited at λ_{ex} = 453 nm, and another that has not been exposed. A FLIM image (Figure 7.10a) is generated by imaging the τ_f of BODIPY C_{10} at the peak emission 550 nm. Next, (Figure 7.10b) using the 'zoom' function of the microscope software, a small square region of the original field of view is selected such that it frames a solitary GUV. Under 'zoomed' conditions, images are collected by normal imaging but is limited to the selected 'zoomed' region of the field of view, whereby the laser spot 'scans' lines of the image from left to right from top to bottom (Figure 7.10c). Due to a decrease in the area of exposure, laser excitation intensity per GUV is increased during 'irradiation' relative to imaging. By exciting at the peak excitation band of the porphyrin dimer (453 nm) at high laser power and at sufficiently long exposure times, we were able to use these conditions to selectively irradiate a solitary GUV within a group Then, the full 'zoomed out' field of view is imaged by BODIPY C_{10} fluorescence lifetime for the second time, producing the 'post PDT irradiation' image. . We chose to excite the porphyrin dimer at 453 nm rather than 480 nm, even though the latter gives a higher yield of $^1O_2$, in order to prevent absorption by BODIPY C_{10}, which has significant absorption at 480 nm.

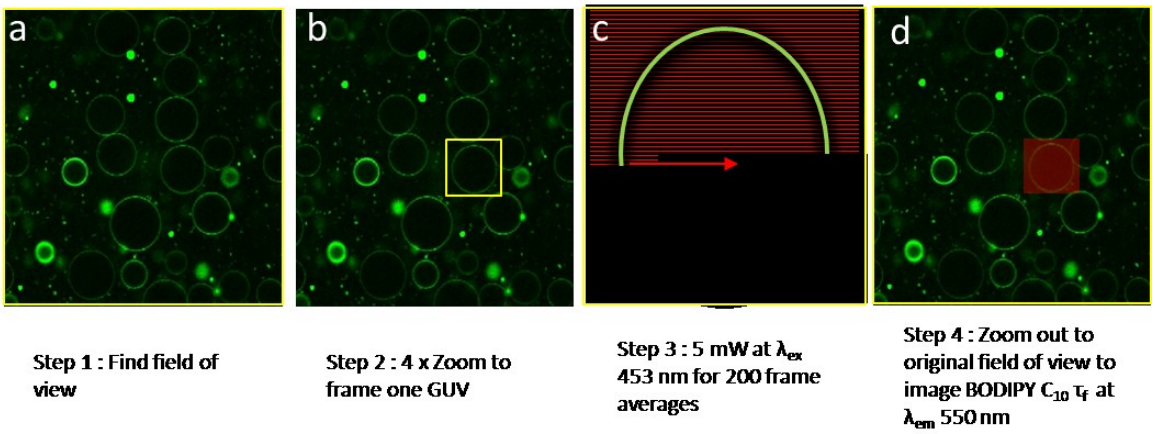

Figure 7.10: Steps for selective irradiation of a single GUV: a) locate field of view with multiple GUVs; b) selection of zoomed image at the borders of solitary GUV; c) 'zoomed' imaging of solitary GUV, often with compensation for movement at 200 frame averages for maximum exposure to laser excitation; d) collection of 'zoomed out' image of original field of view with neighbouring non-irradiated GUVs for reference.

We used this imaging protocol to measure the gradual change in DOPC bilayer membrane viscosity after small exposure times to PDT. Figure 7.11a shows FLIM images taken at regular intervals of irradiation. The distributions of lifetimes of the GUV selected in Figure 7.11a are shown in Figure 7.11b. Mean BODIPY C_{10} τ_f increases from 1535 ± 107 psec to 2437 ± 196 psec, which we have calculated to be equivalent to 105 ± 1.45 cP to 323 ± 6.03 cP over 520 seconds of irradiation of P_2NMe_3. Thus we conclude that excitation of the porphyrin dimer, as a PDT photosensitizer, is correlated with increased lipid bilayer viscosity.

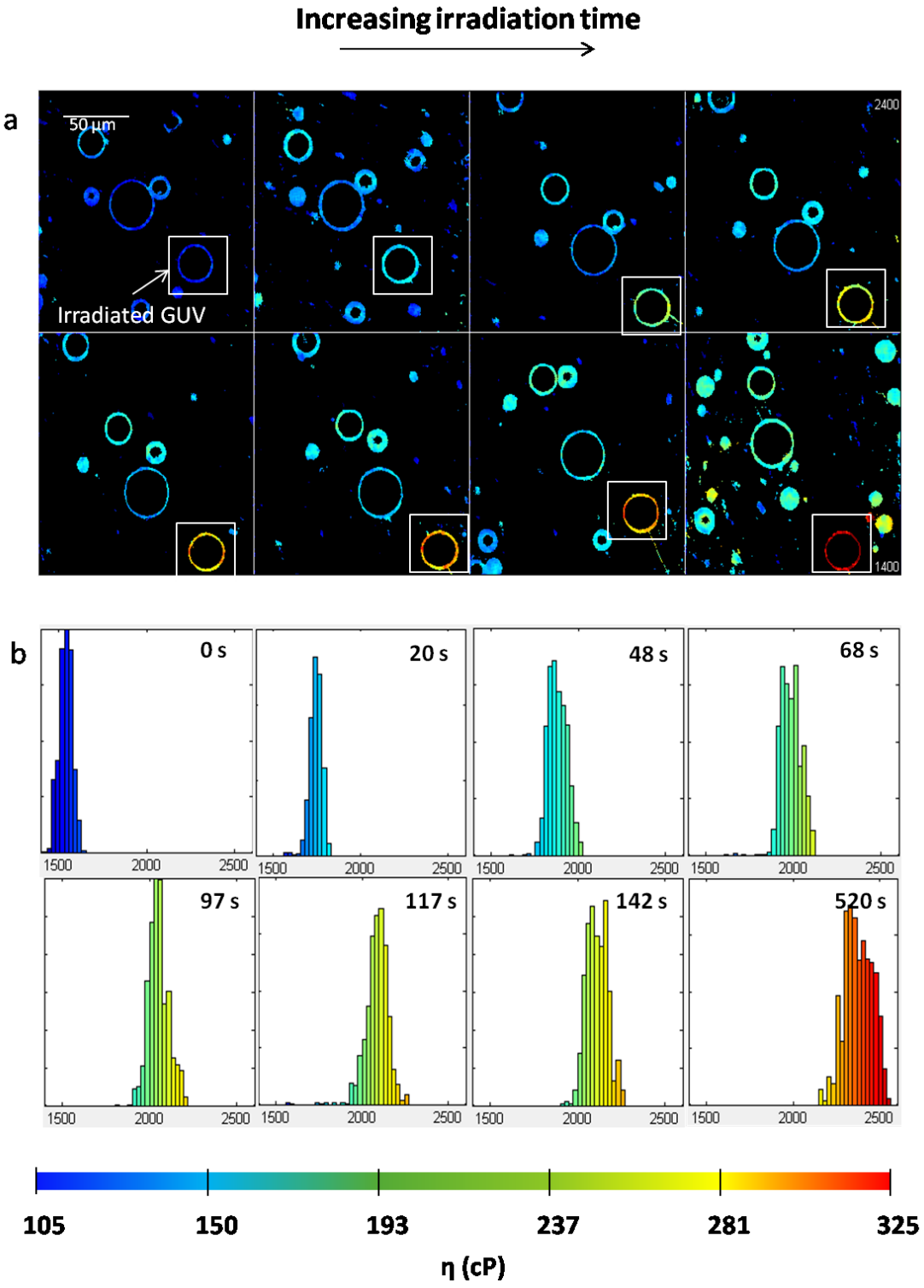

Figure 7.11: FLIM data of BODIPY C_{10} in GUVs electroformed from dehydrated mixtures of DOPC, P_2NMe_3 (lipid; dimer ratio 1000:1) during irradiation. a) Series of images collected at regular intervals over 520 s after irradiation of a single GUV, marked in the Figure; b) BODIPY C_{10} (lipid:BODIPY C_{10} 600:1) τ_f for each image are displayed, a shift to longer BODIPY C_{10} τ_f is observed during irradiation. Irradiation is carried out at 453 nm (5 mW, zoomed), imaging 448 nm (5 mW).

The quality of BODIPY C_{10} FLIM images in comparison with ratiometric images of P_2NMe_3 demonstrates a number of advantages to the use of the BODIPY C_{10}: spatial resolution of viscosity is much higher due to strong emission intensity from the hydrocarbon region. We know that the BODIPY C_{10} is hydrophobic and so will have far more solubility in the lipid chain region of the membrane than the charged P_2NMe_3.

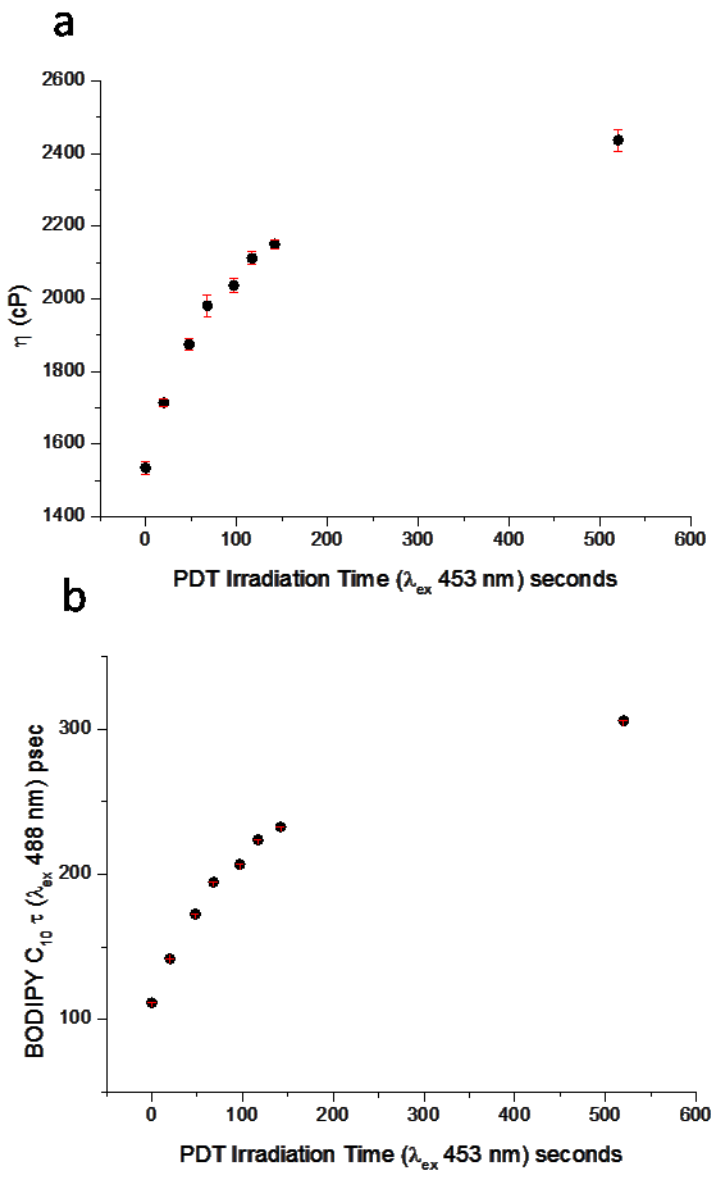

Figure 7.12: The change in (a) lifetime and (b) viscosity of the single GUV shown in Figure 7.11 containing P_2NMe_3 as measured by BODIPY C_{10}. τ_f were extracted from Figure 7.11 and converted to viscosity according to the calibration curve from Ref [32] *and represented graphically. Error bars represent the standard error of the mean BODIPY C_{10} τ shown in Figure 7.11. Viscosity change upon irradiation is observed to reach saturation at approx 100 seconds.*

Figure 7.12 summarises the relationship between irradiation time and viscosity increase, suggesting that PDT irradiation of DOPC GUVs can increase from 106 ± 5.7 cP to approx 309 ± 12.5 cP before saturation of the observed trend. Chapter V showed that P_2NMe_3 binds largely to the surface of the vesicle and that any penetration of the bilayer is partial, nevertheless, we have observed that excitation of the dimer has effects within the hydrocarbon region of the bilayer as measured by BODIPY C_{10}. This must reflect the fact that the dimer is partially embedded in a bilayer and that the concentration of molecular oxygen in the hydrocarbon region of the bilayer is high. Also, the increase in viscosity upon application of PDT in GUVs is approximately equivalent to that observed in LUV systems, as shown in Figure 7.7 (c.a. 350 cP after irradiation at 150 mW). Thus both molecular rotors, P_2 and BODIPY-C_{10}, which are both thought to reside in the hydrocarbon region of the bilayer, show the same trend of viscosity increase upon irradiation as well as the same final value.

We further sought to investigate the component causes of this viscosity change in lipid bilayers upon exposure to irradiation, namely: confirm that the change is caused by $^1O_2$ which interact with lipids. In order to do so, we performed a series of control experiments that are crucial to confirm that any change in lipid viscosity is dependent on PDT effects.

7.4.1 PDT in the presence of NaN_3

Sodium azide (NaN_3) is a routinely used quencher of $^1O_2$, with diffusion-controlled quenching rates[33]. We performed the P_2NMe_3 irradiation experiment in the presence of BODIPY-C_{10}, similar to that described above, in the presence of 1 M NaN_3 in order to determine what, if any, of the observed irradiation-dependent viscosity change is caused by the presence of $^1O_2$. Azide cannot penetrate the lipid bilayer so quenching is limited to $^1O_2$ produced external to the hydrocarbon region, but in our case, should affect the P_2NMe_3 dimer which we believe is attached by its planar porphyrin macrocycles to the external surfaces of the vesicles.

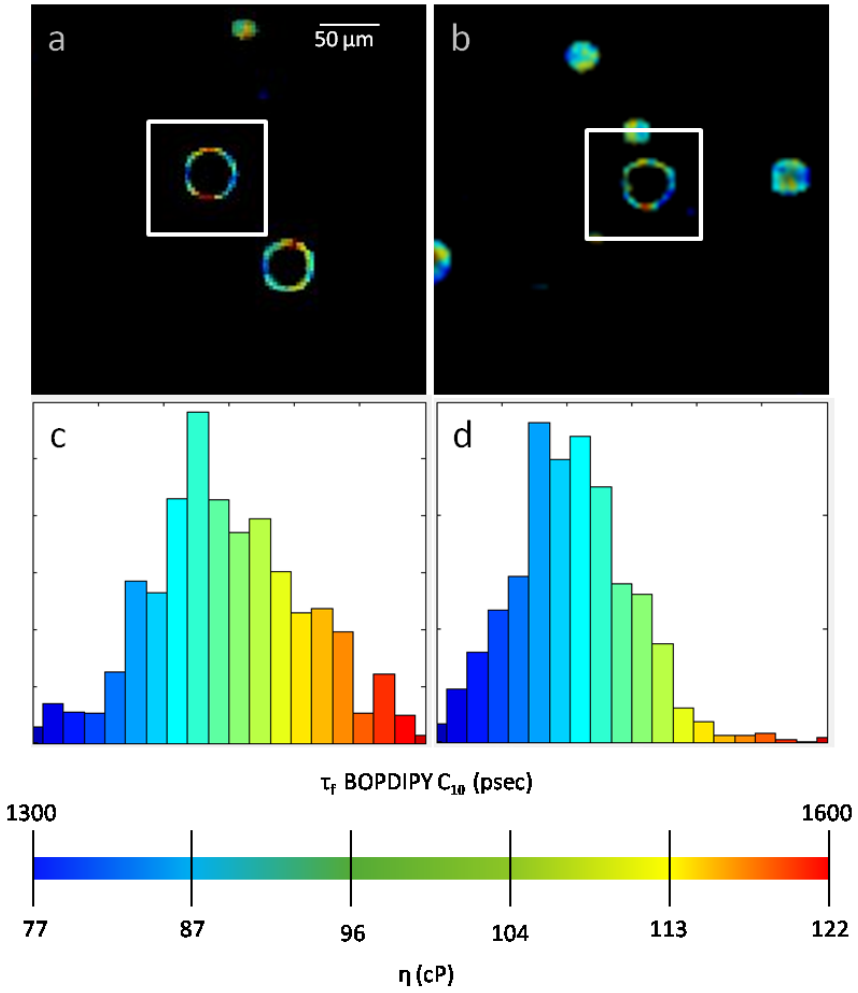

Figure 7.13: FLIM imaging of BODIPY C_{10} GUVs electroformed from dehydrated mixtures of DOPC and P_2NMe_3 in the presence of NaN_3 (lipid: dimer 1000:1, BODIPY C_{10} added from solution at 10 uM); a,c) before and; b,d) after irradiation at 453 nm at 5 mW.

Figure 7.13 shows GUVs of DOPC, BODIPY C_{10} and P_2NMe_3 prior to and after exposure to PDT irradiation. Figures 7.13c,d are histograms of the lifetime distributions of images from 7.13a, b, which are far narrower than those from the experiment shown in Figure 7.11, scaled at 1300 to 1600 psec rather than 1000 to 2000 psec as in Figure 7.11. The mean lifetime of the selected GUV before irradiation is approximately 1435 ± 135 psec, (96 ± 0.55 cP) remaining the same after irradiation at 1420 ± 90 psec (94 ± 0.3 cP). This experiment was repeated three times, with consistent results showing little to no change in BODIPY C_{10} τ in the presence of an external quencher of $^1O_2$. From this, we confirm that $^1O_2$ is the source of PDT-related viscosity change, rather than lipid auto oxidation, or ROS generated by Type I sensitizer deactivation pathways.

Next, we determine the effects of PDT irradiation without the PDT photosensitizer. Irradiation conditions applied to DOPC vesicles which are electroformed only with the viscosity-probe BODIPY C_{10}. This could be a convenient way to establish whether or not BODIPY C_{10} itself produces $^1O_2$. It is worth noting however that at the irradiation wavelength λ_{ex} 453 nm BODIPY C_{10} absorbance is relatively low, and excitation of the BODIPY C_{10} peak for FLIM imaging is relatively short in exposure time and performed at lower laser powers. Figure 7.14 summarises the results of the irradiation experiment without the inclusion of the porphyrin dimer. The change in mean lifetime in this GUV was 1680 ± 45 to 1710 ± 60 ps, reflecting a viscosity increase from 135 ± 0.33 to 139 ± 0.43 cP. We attribute this viscosity change to a small contribution of $^1O_2$ produced by BODIPY C_{10} when irradiated at 453 nm. This is roughly 10% of the change we observed in the original experiment involving the porphyrin dimer, giving a change of approx. 200 cP under identical conditions of irradiation.

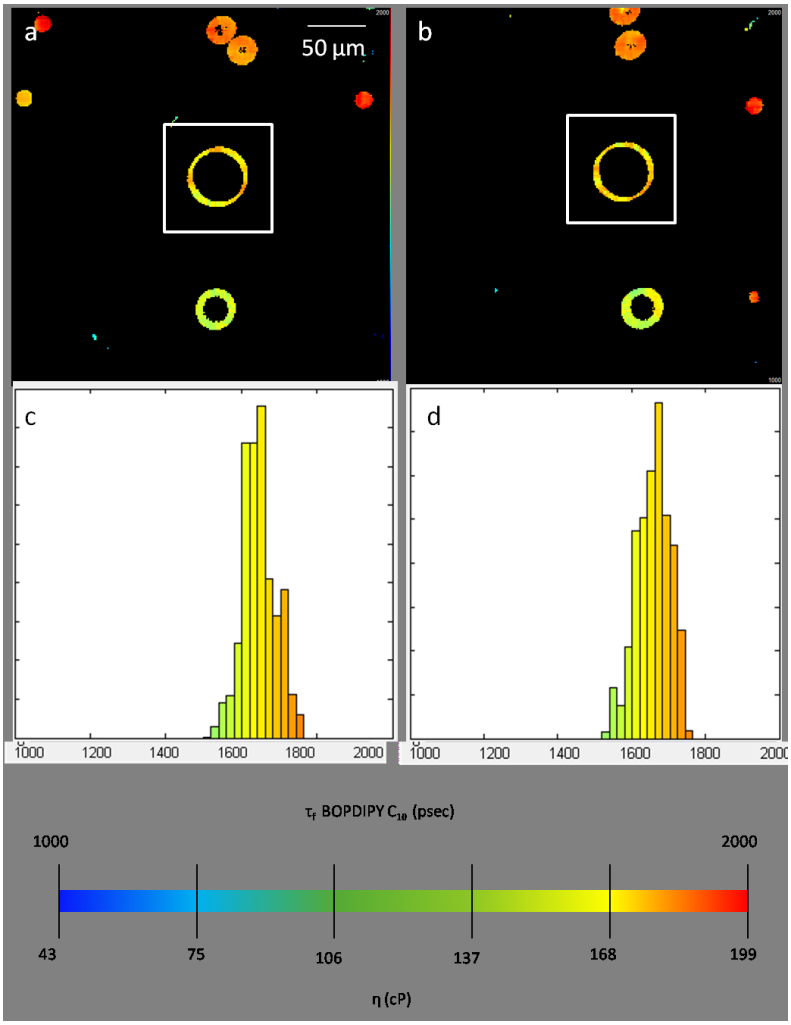

Figure 7.14: FLIM imaging of BODIPY C_{10} GUVs electroformed from dehydrated mixtures of DOPC, and BODIPY C_{10} (lipid: BODIPY 600:1) a) before and b) after irradiation at 453 nm at 5 mW. Histograms of the lifetime vs. photon count are shown c) before and d) after irradiation.

These control experiments have supported our theory that the presence of $^1O_2$, produced by selective and strong excitation of the P_2NMe_3 dimer, causes viscosity increase in DOPC bilayers. The mechanism for viscosity change is as yet unknown, but we carried out preliminary investigations that test a hypothesis centering around the interaction between $^1O_2$ and C=C double bonds that may result in the formation of lipid hydroperoxides and results in lipid cross-linking. The details of this process are discussed in further detail at the end of this chapter. Thus, we devise a control experiment to establish that viscosity change occurs only in the presence of the carbon double bond. We perform the PDT irradiation in GUVs of a saturated lipid, which will not form lipid hydroperoxides.

We chose the saturated lipid diphytanoyl phosphatidylcholine (DPhPC), which has a similar gel transition temperature (T_g) to that of DOPC. The compatibility of lipids in terms of T_g is to ensure that the temperature-dependent viscous behaviour of the two bilayers, from saturated (DPhPC) and unsaturated (DOPC) matches as closely as possible, so that the experiment solely compares PDT-related viscosity change. The intrinsic viscous behaviour of the lipid will affect diffusion of $^1O_2$, and the interaction with the fluorophores which are important variables for comparison of PDT-related viscosity change. Figure 7.15 shows two sets of FLIM images of DPhPC GUVs containing P_2NMe_3 and BODIPY C_{10} collected before and after irradiation.

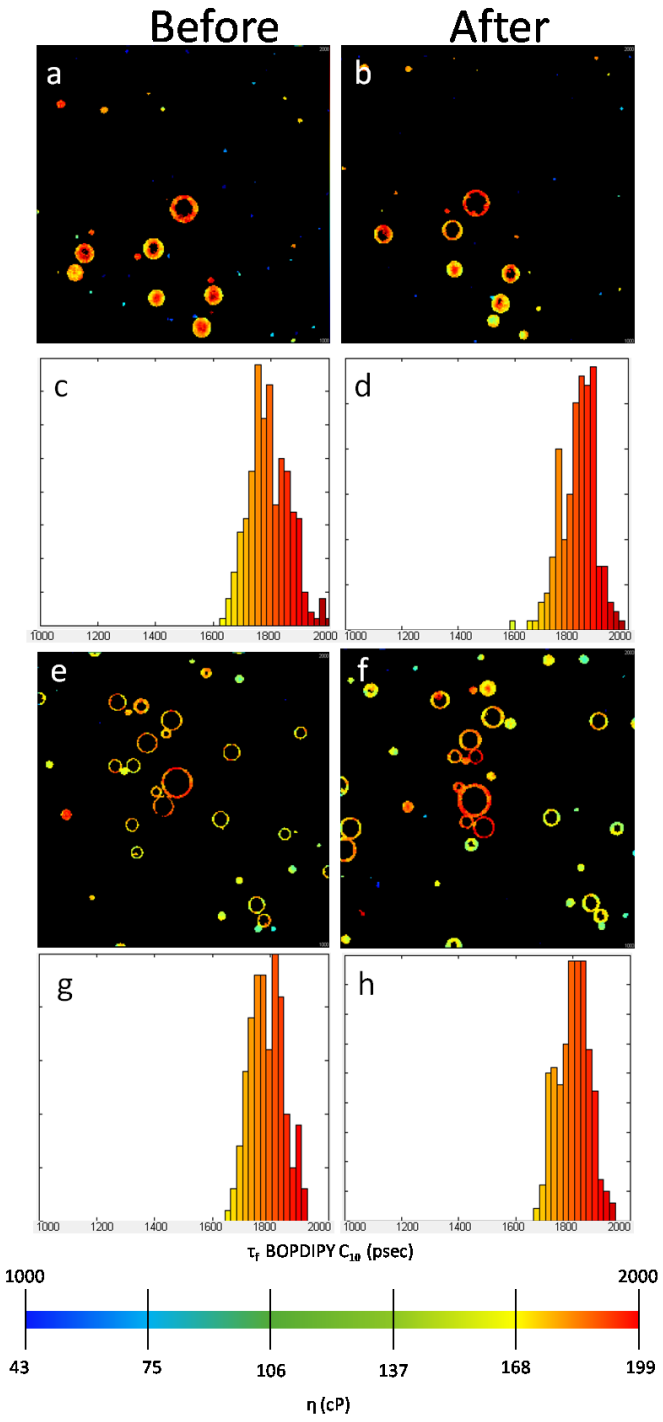

Figure 7.15: FLIM imaging of BODIPY C_{10} GUVs electroformed from dehydrated mixtures of DPhPC, BODIPY C_{10} and P_2NMe_3 (lipid: P_2NMe_3: BODIPY 1000:1:600). Showing no significant change in lifetime of BODIPY C_{10}

Figures 7.15a and 7.15c, showing FLIM images prior to and after irradiation indicate that DPhPC vesicles exhibit BODIPY C_{10} τ_f-measured viscosity of approximately 170 ± 2.7 cP. Figures 7.15b and 7.15d, collected after irradiation show little change in the average τ_f. Five repeated experiments gave similar results, with the change in mean lifetime estimated to be roughly 8 ±

0.40 cP, much less than observed in the case of DOPC GUVs. Thus we show that PDT irradiation performed under identical conditions on bilayers made from saturated lipids as those of unsaturated lipids does not yield a change in lipid bilayer viscosity. Instead, GUVs made from saturated lipids are resistant to PDT-related viscosity change which we attribute to the lack of carbon-carbon double bonds, preventing the formation of lipid hydroperoxides.

7.5 Hypothetical mechanisms for change of bilayer viscosity mediated by $^1O_2$

Chapters IV and V showed that molecular rotors are sensitive to a change in free volume; we showed that the volume occupied by lipid hydrocarbons in the isotropic environment of a lipid bilayer hydrocarbon region is related to the restriction of molecular rotation in viscosity-sensitive rotors. We suggest that the $^1O_2$-mediated (Type II) viscosity change in DOPC bilayers can be attributed to three sources:

Firstly, we have associated change in lipid bilayer viscosity to the first product of an interaction between $^1O_2$ with unsaturated lipids that does not occur with saturated lipids, namely the formation of hydroperoxides. Existing literature relates bilayer fluidity change to the movement of the peroxide towards the membrane interface, altering the basic shape of the lipid. We hypothesize that the change in molecular volume from an unsaturated lipid chain to lipid peroxide can cause expansion of the lipid chain volume. The extent of peroxidation will determine the overall change in free volume, which could be observed by BOPDIPY τ_f. However, we propose that excessive formation of the phospholipid peroxide would fundamentally alter bilayer integrity; due to the inverse conical shape of the peroxide lipid. Generally, this shape of phospholipids forms inverse micelles rather than bilayers; however this effect is expected to be observed only at high yields of lipid peroxide relative to the overall phospholipid concentration. Measurement of the overall free volume change as caused by the presence of peroxide chains depends on the localisation of BODIPY C_{10} relative to the peroxide. This is as yet, unknown. Secondly, we suggest that breakdown of hydroperoxide lipids into smaller alkane fragments may contribute to the changing viscosity. Small alkane fragments could dissolve in the existing

lipid network, decreasing free volume around the BODIPY C_{10}. This would be observed as an increase in local viscosity. However, this effect is likely to be observed as disintegration of membrane integrity or an alteration of the vesicle shape.

Lastly, the most likely source of viscosity increase caused by Type II reactions is the formation of lipid cross linking as a result of reactive hydroperoxide radicals. Type II reactions are not generally associated with the formation of peroxide radicals, instead $^1O_2$ reacts with the double bond at the C_9 position of a DOPC hydrocarbon chain, forming a stable lipid-hydroperoxide that does not partake in hydrogen abstraction from other nearby lipids. This process, strongly associated with Type I reactions, is termed the radical chain mechanism and is attributed with spreading lipid peroxides far from the site of photosensitization, and so the mechanisms of viscosity change. If hydroperoxides were localised just around the photosensitizer, observed viscosity increase would be very quickly saturated, which we have found not to be true. However, Stratton et al., 1997 have shown that Type II reactions can produce hydroperoxide radicals, by either interaction with the excited photosensitizer, with radical species, or by depletion of local hydrogen concentrations. Generation of peroxide radicals is of crucial importance to our proposed mechanism of viscosity increase. We suggest that peroxide radicals generated on the C_9 position of the DOPC chain can bond with nearby C_9 double bonds on neighbouring lipid chains. Cross linking would create a single or multiple phospholipids that are bonded together further down in the lipid chains, which would greatly restrict their fluid motion, and would be reflected by restriction of BODIPY C_{10}.This is a possible explanation for observed viscosity increase upon irradiation of P_2NMe_3. For this to occur, it is necessary that the reaction takes place prior to peroxidation of all or a large majority of DOPC C_9 positions. We believe that the kinetics of the reaction must be observed in high time resolution in order to rule it the major component of oxidative viscosity increase during PDT in membranes.

To further investigate the possibility of cross linking; we applied our hypothesis in an isotropic fluid medium, 1-Heptene, which has a double bond at the C_1 position, where interaction with $^1O_2$

is expected to form the hydroperoxide and cross link with another molecule as in phospholipid hydrocarbon chains. Figure 7.16 shows emission spectra of the hydrophobic P_2 dimers taken at regular intervals during irradiation (λ_{ex} = 480 nm; at 200 mW). Figure 7.16a shows spectra of 1-Heptene irradiated in the presence of the P_2 dimer, which is compared with Figure 7.16b in which 1-Heptene is irradiated for a period of time and P_2 is added after irradiation for the purpose of measuring the post-irradiation viscosity. Figure 7.16c summarises viscosity change of 1-Heptene under irradiation conditions with respect to time for both samples, showing that, as we had expected, the emission peak ratio of P_2 increases with cumulative irradiation time when the dimer is present in the sample and irradiated as a PDT agent but solution viscosity remains unchanged when 1-Heptene is irradiated in the absence of the porphyrin dimer.

This finding is significant to our assertion that $^1O_2$-related alkene cross linking is a purely chemical reaction presumably resulting from the formation of a hydroperoxide radical. This experiment shows that PDT-related viscosity increase is observed regardless of factors circumstantial to the experiment in GUVs, such as, porphyrin dimer localisation, BODIPY C_{10} localisation, local oxygen concentration, and the isotropic environment of a lipid bilayer.

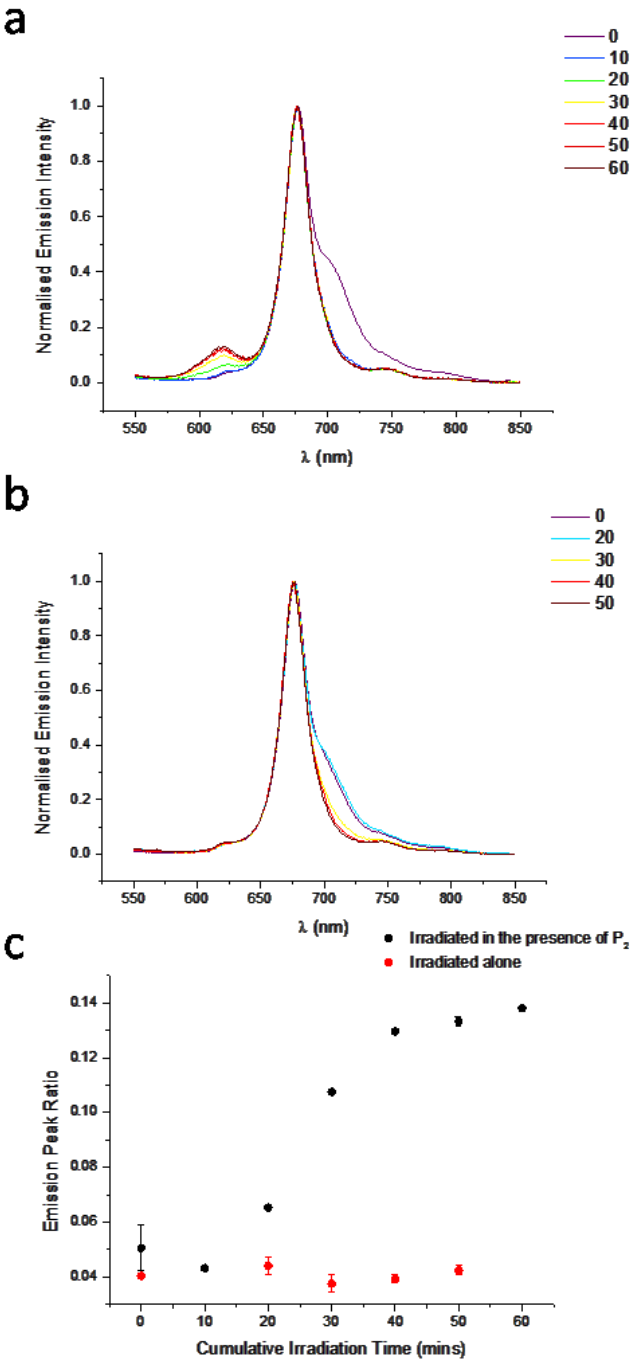

Figure 7.16: a) Normalised emission spectra of P_2 in solutions of 1-Heptene (0.66 μM) during irradiation at 480 nm at 200 mW; b) normalised spectra of P_2 added to solutions of 1-Heptene (0.66 uM) after irradiation; c) P_2 emission peak ratios against cumulative irradiation time of 1-Heptene solutions irradiated in the presence (black) and absence (red) of P_2

7.6 Conclusions

In summary, we have used two types of molecular rotors: a neutral porphyrin dimer P_2 and a hydrophobic dye BODIPY-C_{10}, to measure dynamically changing viscosity in lipid bilayers during

singlet oxygen production, replicating the Photodynamic Therapy (PDT) irradiation conditions. Both dyes are shown to embed deeply in the hydrocarbon region of the bilayer and thus we hypothesized that they would measure the same microscopic viscosity.

We have first established that prolonged, high intensity excitation of the planar confomer of the porphyrin dimer P_2 in lipid bilayers is correlated to viscosity increase as measured by ratiometric fluorescence measurements of the porphyrin dimer. However, high degrees of photobleaching were also observed, which were prohibitive to sustained and accurate measurement of viscosity change over longer periods of PDT irradiation and this made dynamic imaging highly challenging. In addition, based on the results of the previous Chapter and given poor incorporation of the P_2 dimer into GUV, the imaging of bilayer oxidation using P_2 was not attempted. However, we were able to extract reliable dynamic information on viscosity change from the oxidation of DOPC LUVs, which, however, could not take into account any inhomogeneities in the bulk sample of LUVs.

In addition, we used a different molecular rotor, a BODIPY C_{10} as the viscosity probe to measure the effects of the porphyrin dimer as a PDT sensitizer. The fluorescence lifetime of the BODIPY C_{10} can be calibrated to viscosity in a large viscosity range as previously shown and, importantly, we were able to develop a protocol for simultaneous incorporation of the dimer P_2NMe_3 and BODIPY-C_{10} into the same GUVs. Thus we were able to use separate excitation wavelengths to induce PDT (by irradiation of the dimer) and to excited fluorescence of a BODIPY rotor, that was used to construct Fluorescence Lifetime Images (FLIM images) of GUVs. We showed that GUVs made from the unsaturated lipid DOPC exhibited irradiation dose-dependent viscosity increase that was prohibited by the presence of a $^1O_2$ quencher, sodium azide, and that the increase was not observed in the saturated lipid DPhPC. We hypothesize that the mechanism of viscosity increase is caused by reaction of $^1O_2$ with C-C double bonds to form a lipid hydroperoxide. The hydroperoxide (which can form the radical) reacts with proximal double bonds and forms

lateral linkages between lipids. This dramatically alters fluid phase behaviour, resulting in a highly restricted fluid environment, which inhibits intermolecular rotation of BODIPY C_{10}.

Importantly, we compared the dynamics of viscosity increase during PDT, as monitored by both P_2 and BODIPY-C_{10} and we consequently find excellent agreement. This observation confirms our hypothesis that both dyes are likely to localize in the same hydrocarbon region of the bilayer and thus measure the viscosity of the same microenvironment.

Finally, the work reported in this chapter emphasizes two important advantages of using molecular rotors for measuring viscosity: (i) the possibility to perform the measurements dynamically, by monitoring the *changing* viscosity accompanying some process of interest (in this case PDT) and (ii) the possibility to *image* viscosity, rather than perform single point measurements. The latter advantage was only fully realized for the BODIPY C_{10} molecular rotor that incorporated well in the system of interest (GUV) and showed bright fluorescence signal, but we believe that the porphyrin dimers can also be used for imaging, as long as good incorporation in the system of interest could be achieved. Previously, a similar porphyrin dimer to the ones studied here was used for imaging dynamically changing viscosity in cells and we believe that the dimers investigated in this work will also prove useful for that purpose. However, testing the dimers for imaging the cellular viscosity was outside the scope of this work and will be attempted in the future studies.

7.7 References

1. Kuimova, M. K. et al. Imaging intracellular viscosity of a single cell during photoinduced cell death. Nat. Chem. 1, 69–73 (2009).

2. Breitenbach, T. et al. Photosensitized production of singlet oxygen: spatially-resolved optical studies in single cells. Photochem. Photobiol. Sci. 8, 442–52 (2009).

3. Schweitzer, C. & Schmidt, R. Physical mechanisms of generation and deactivation of singlet oxygen. Chem. Rev. 103, 1685–757 (2003).

4. Childs, W. H. J. & Mecke, R. Intensitatsmessungen in der atmospharischen Sauerstoffbande ? 7600. Zeitschrift fur Phys. 68, 344–361 (1931).

5. Ellis, J. W. & Kneser, H. O. Kombinationsbeziehungen im Absorptionsspektrum des flussigen Sauerstoffs. Zeitschrift fur Phys. 86, 583–591 (1933).

6. Chou, P.-T. et al. Photophysical Properties of (O 2 (1 Δ g)) 2 and O 2 (1) in Solution Phase. J. Phys. Chem. A 101, 8581–8586 (1997).

7. Spalek, O., Kodymová, J., Stopka, P. & Micek, I. Experimental verification of the Einstein A - coefficient used for evaluation of O 2 (^1Delta g) concentration in the chemical oxygen-iodine laser. J. Phys. B At. Mol. Opt. Phys. 32, 1885–1892 (1999).

8. Miller, H. C., McCord, J. E., Choy, J. & Hager, G. D. Measurement of the radiative lifetime of O2(a1Δg) using cavity ring down spectroscopy. J. Quant. Spectrosc. Radiat. Transf. 69, 305–325 (2001).

9. Hurst, J. R., McDonald, J. D. & Schuster, G. B. Lifetime of singlet oxygen in solution directly determined by laser spectroscopy. J. Am. Chem. Soc. 104, 2065–2067 (1982).

10. Kuimova, M. K. et al. Photophysical properties and intracellular imaging of water-soluble porphyrin dimers for two-photon excited photodynamic therapy. Org. Biomol. Chem. 7, 889–96 (2009).

11. Kuimova, M. K., Balaz, M., Anderson, H. L. & Ogilby, P. R. Intramolecular rotation in a porphyrin dimer controls singlet oxygen production. J. Am. Chem. Soc. 131, 7948–9 (2009).

12. Kuimova, M. K. et al. Determination of the triplet state energies of a series of conjugated porphyrin oligomers. Photochem. Photobiol. Sci. 6, 675–82 (2007).

13. Ehrenberg, B., Anderson, J. L. & Foote, C. S. Kinetics and Yield of Singlet Oxygen Photosensitized by Hypericin in Organic and Biological Media. Photochem. Photobiol. 68, 135–140 (1998).

14. Valenzeno, D. P. Photomodification of biological membranes with emphasis on singlet oxygen mechanisms. Photochem. Photobiol. 46, 147–160 (1987).

15. Spiller, W. et al. Singlet Oxygen Quantum Yields of Different Photosensitizers in Polar Solvents and Micellar Solutions. J. Porphyrins Phthalocyanines 02, 145–158 (1998).

16. Kessel, D. Determinants of Hematoporphyrin-catalyzed photosensitization. Photochem. Photobiol. 36, 99–101 (1982).

17. Kohn, K. & Kessel, D. On the mode of cytotoxic action of photo-activated porphyrins. Biochem. Pharmacol. 28, 2465–70 (1979).

18. Kessel, D. Effects of photoactivated porphyrins at the cell surface of leukemia L1210 cells. Biochemistry 16, 3443–3449 (1977).

19. Lavi, A., Weitman, H., Holmes, R. T., Smith, K. M. & Ehrenberg, B. The depth of porphyrin in a membrane and the membrane's physical properties affect the photosensitizing efficiency. Biophys. J. 82, 2101–10 (2002).

20. Gross, E. & Ehrenberg, B. The partition and distribution of porphyrins in liposomal membranes. A spectroscopic study. Biochim. Biophys. Acta - Biomembr. 983, 118–122 (1989).

21. Bronshteint, I. et al. In vitro and in vivo photosensitization by protoporphyrins possessing different lipophilicities and vertical localization in the membrane. Photochem. Photobiol. 82, 1319–25

22. Dix, T. A. & Aikens, J. Mechanisms and biological relevance of lipid peroxidation initiation. Chem. Res. Toxicol. 6, 2–18 (1993).

23. Stratton, S. P. & Liebler, D. C. Determination of singlet oxygen-specific versus radical-mediated lipid peroxidation in photosensitized oxidation of lipid bilayers: effect of beta-carotene and alpha-tocopherol. Biochemistry 36, 12911–20 (1997).

24. Harding, L. B. & Goddard, W. A. The mechanism of the ene reaction of singlet oxygen with olefins. J. Am. Chem. Soc. 102, 439–449 (1980).

25. Wratten, M. Lou et al. Structural and dynamic effects of oxidatively modified phospholipids in unsaturated lipid membranes. Biochemistry 31, 10901–10907 (1992).

26. Heuvingh, J. & Bonneau, S. Asymmetric oxidation of giant vesicles triggers curvature-associated shape transition and permeabilization. Biophys. J. 97, 2904–12 (2009).

27. Kochevar, I. E., Lambert, C. R., Lynch, M. C. & Tedesco, A. C. Comparison of photosensitized plasma membrane damage caused by singlet oxygen and free radicals. Biochim. Biophys. Acta - Biomembr. 1280, 223–230 (1996).

28. Weber, G. et al. Lipid oxidation induces structural changes in biomimetic membranes. Soft Matter 10, 4241–7 (2014).

29. Van Ginkel, G. & Sevanian, A. Lipid peroxidation-induced membrane structural alterations. Methods Enzymol. 233, 273–88 (1994).

30. Wu, Y. et al. Molecular rheometry: direct determination of viscosity in Lo and Ld lipid phases via fluorescence lifetime imaging. Phys. Chem. Chem. Phys. 15, 14986–93 (2013).

31. Dent, M. R. et al. Imaging Phase Separation in Model Lipid Membranes Through the use of BODIPY Based Molecular Rotors. Phys. Chem. Chem. Phys. 17, 18393–18402 (2015).

32. Hosny, N. A. et al. Mapping microbubble viscosity using fluorescence lifetime imaging of molecular rotors. Proc. Natl. Acad. Sci. U. S. A. 110, 9225–30 (2013).

33. Kuimova, M. K., Yahioglu, G. & Ogilby, P. R. Singlet Oxygen in a Cell : Spatially Dependent Lifetimes and Quenching Rate Constants. Cell 332–340 (2009). doi:10.1039/b809049a.

VIII. Conclusions and Future Work

8.1 Summary and Conclusions

Many macromolecular interactions within the cell are governed by the likelihood of diffusion-controlled collisions between the interacting partners. Viscosity-sensitive fluorophores called molecular rotors have recently been proposed for use in imaging viscosity in cells. Cell membranes, in particular are a topic of growing interest for viscosity quantification in order to better understand the relationship between membrane viscosity and disease states. We presented a detailed investigation into the mechanism and photophysical behaviour of a range of molecular rotors, based on the structure of porphyrin dimers, which differ in size, degree of conjugation and charge. Here we attempted to measure the viscosity of model lipid bilayers in order to establish porphyrin dimers as a means of imaging and quantifying membrane viscosity, which can be ultimately applicable for cells.

We show that the conformational flexibility of the porphyrin dimer in solution can be used to indicate solution viscosity by measurement of the ratios between its two confomers. Intermolecular rotation about a butadiyne bond between the two porphyrin macrocycles produces the 'twisted' and 'planar' confomers which, due to a difference in excited state energy are spectroscopically distinct species. Unidirectional conversion from the twisted to the planar confomer in the excited state allows measurement of their relative ratios ('ratiometric') from emission spectra, making the measurement independent of concentration, a considerable advantage in live imaging. The ratiometric methodology of imaging enables fast and accurate measurement of solution viscosity even in instances of environmental heterogeneity.

We have investigated the effects of physical parameters such as temperature, solvent polarity and probe solubility to describe variation in viscosity-sensitivity and viscosity dynamic range of the *meso* substituated porphyrin dimers. This shows the necessity of judiciously choosing the appropriate dimer by the influence of these factors. For instance;

i. The cationic dimers studied in this Thesis have been shown to be compatible with methanol and glycerol solutions of relatively high polarity for calibration purposes. Solvatochromic effects in polar solutions are shown to be minimal, and all cationic dimers were classified in order of their viscosity-sensitivity.

ii. On the other hand, the uncharged dimer, P_2, is more compatible with hydrophobic environments and was observed to be poorly soluble in methanol and glycerol solutions. However, the dimer was successfully calibrated in Castor oil, a viscous hydrophobic solution, with comparable viscosity-sensitivity to the most sensitive cationic dimer, P_2NMe_3.

As a result, P_2 and P_2NMe_3 are recommended as the most applicable and sensitive molecular rotors for use in polar (P_2NMe_3) and non-polar (P_2) environments in cells and model biological systems. Furthermore, calibration of porphyrin dimer emission ratios to solution viscosity is independent of solution temperature; which allows us to use the dimers in variable-temperature environments such as cells and tissues. This represents a significant advantage in comparison with other molecular rotors, as demonstrated by our group [1].

Having established the success of ratiometric measurements in predicting Netwonian solution viscosity, we sought to establish the utility of the porphyrin dimer in the presence of macromolecules. We performed ratiometric viscosity measurements in

polymer systems, both dilute and concentrated. In dilute systems, where the dimer is preferentially solvated near the polymer chain, we were able to use the dimer's emission ratio as an indicator of the polymer's conformation, and ultimately, its molecular weight. Our qualitative preliminary studies indicate that in dilute polymer solutions, the porphyrin dimer can accurately measure the *intrinsic viscosity* of polymers, a parameter that relates the molecular weight of a polymer in solution to its bulk viscosity. However, precise quantitative parameters needed to make this measurement are not reproducible in a variety of solvents. Additionally, biological media are highly complex and variable. Thus application of the dimer in a biologically relevant medium is unlikely to provide credible and reliable measures of macromolecular weight and size.

Next, we investigated the applicability of the dimer ratiometric fluorescence to highly crowded macromolecular environments, modeled by pure polymer solutions. We judge these solutions to be akin to tightly packed cellular domains, such as lipid membranes, or certain cellular compartments such as the synaptic cleft or nucleus. We found that we were able to measure the temperature-dependent viscosity of pure polymer 'melts', where the viscosity predicted by the dimer's emission ratio matches that measured by mechanical methods. Based on this data, we propose that in highly crowded environments, such as polymer melts, the ratiometric viscosity measurement is determined by the temperature-dependent 'free volume' of the solution rather than the polymer's molecular weight.

The lipid membrane is a clear target for measurement of viscosity: the mechanical properties of the bilayer are intrinsically related to the structural integrity of the cell[2–8] and its role as a host for biochemical reactions[9–12]. Thus we examined the mode of

interaction of four *meso* substituated porphyrin dimers of varying size and charge, with planar lipid bilayers as modeled by large unilamellar vesicles (LUVs). We were able to establish protocols for inclusion of the dimer into the bilayer for maximum signal/noise ratio for use of ratiometric viscosity measurement. We determined that anionic dimers do not incorporate into the phospholipid membrane, presumably due to repulsion by the phosphate 'head' groups. As such, cationic dimers are shown to incorporate into the membrane with high efficiency, even from aqueous solution. The neutrally charged dimer, P_2, with significant hydrophobic character, was shown to aggregate in aqueous suspensions of phospholipid vesicles, but was highly compatible with the hydrocarbon region of the bilayer when vesicles were made from dry films of lipid premixed with P_2.

We determined a number of experimental variables that affect viscosity measurements of lipid bilayers and optimized our protocol to account for them: for instance, the lipid: dimer ratio and lipid composition. We showed that the positively charged porphyrin dimer, P_2NMe_3 is best suited to measure viscosity in the liquid-disordered phase of the bilayer, however, resulting viscosity values are low in comparison with existing literature. This is due to the localisation of the porphyrin dimer relative to the membrane, the positively charged dimer is predominantly associated with the phosphate 'head' groups of the bilayer and not, as we aimed, to the hydrocarbon interior. We observed that P_2NMe_3 is ejected from the bilayer upon the liquid to gel phase transition, that was tested by varying the temperature of the bilayer. As such, P_2NMe_3 is deemed unsuitable for measuring phospholipid phase transitions and indeed, the viscosity of the hydrocarbon region. However, P_2, the neutral porphyrin dimer was well solvated in the hydrocarbon region of the membrane in both the liquid and gel phases. We were able to observe a change in the temperature-dependent viscosity of

the bilayer in these two phases, at the published transition temperature, showing that we could observe the transition as it affected the porphyrin dimer's emission ratio.

Lastly, we compared our viscosity measurements with those from existing literature reporting viscosity from rotational diffusion, finding good compatibility between the two. Thus, we conclude that the porphyrin dimer P_2 is a successful molecular rotor for application to lipid bilayers, measuring the three-dimensional viscosity of the lipid hydrocarbon region. However, we also caution using an inappropriate dimer for measurement of the lipid bilayer, as these experiments are highly sensitive to the localisation of the dimer into the interior of the bilayer, dependent upon its charge and size.

Amongst the advantages of molecular rotors are their capacity as agents for real-time imaging of viscosity. We used the porphyrin dimer to image viscosity in giant unilamellar vesicles (GUVs) that are visible under confocal microscopy. However, we found that the best method for production of GUVs, electroformation, is not compatible for use with the porphyrin dimers. Electroformed GUVs that are made from films of lipid and dimer (the combination that we used to produce LUVs) were found to include almost no dimer in the hydrocarbon region, as they showed almost no signal under microscopy. Even in the case of partial incorporation (tested with P_2 and P_2NMe_3) ratiometric images were plagued by low signal/noise ratios, giving unreliable values of bilayer viscosity. Image processing to increase the signal reduced spatial resolution of the images, negating the original advantage of using molecular rotors. Nevertheless, our experiments showed that apparent ratiometric viscosity of the GUVs changes during imaging. With the knowledge that the dimer is an efficient photosensitizer, we set out to investigate the role of singlet oxygen in this light-induced viscosity change.

We first returned to the LUV model to explore the change in model membrane viscosity after prolonged excitation of the P_2 dimer in 1,2-Dioleoyl-*sn*-glycero-3-phosphocholine (DOPC) membranes, which we termed 'Photodynamic Therapy (PDT) irradiation'. We found that the increase in viscosity was positively correlated with irradiation time. However, our measurements were strongly affected by bleaching of the dimer fluorescence signal during these experiments, reducing the reliability of the spectra for ratiometric analysis.

To investigate the phenomenon by alternative means, we used a second molecular rotor, a BODIPY substituted with a 10-carbon tail, which we imaged by Fluorescence lifetime Imaging (FLIM). BODIPY C_{10} has already been characterized by our group as a molecular rotor whose excited state lifetime is a good predictor of solution viscosity, and whose hydrophobic nature makes is well compatible with the hydrocarbon region of lipid membranes. We showed that singlet oxygen, produced by the porphyrin dimer, is indeed the cause of an apparent increase in membrane viscosity as measured by BODIPY C_{10}. Control experiments showed that the increase is only observed in bilayers composed of unsaturated lipids and can be prevented by the presence of a singlet oxygen quencher. Thus we attribute the photosensitized viscosity increase to a chemical reaction taking place with the hydrocarbon tails of component phospholipids, which restricts free volume in the bilayer interior.

In summary, we have demonstrated the wide applicability of the *meso*-subsituted conjugated porphyrin dimer as probes of microviscosity in bulk solutions, polymer solutions and melts, and in lipid membranes. We also showed that different dimers are suitable for different applications, noting that dimer size and charge determine their localisation and specific interactions, which ultimately affect the ratiometric viscosity

measurement. We have established 'ideal' conditions for the use of two dimers: one charged and one uncharged.

It is worth noting that the series of substituated porphyrin dimers described above offers great advantages for the purposes of cell and tissue imaging, namely in that the ratiometric method of viscosity sensing that is possible with these dimers is concentration independent. Therefore, upon application of the dimer in living cells and ultimately in living tissues, the heterogeneous and highly variable uptake of dimers in cells will not influence the validity of a viscosity measurement. We have been able to show that the dynamic range of the most sensitive dimer is between 1 and 7000 cP, and also spans a large temperature range (273 – 373 K) in such a way that temperature itself does not affect the measurement, only the viscosity of the system under study. This enables us to measure viscosity in many environments. Moreover, it enables dynamic measurements, as demonstrated by monitoring viscosity increases caused by lipid oxidation.

8.2 Future Work

This section outlines several directions for possible future work that were highlighted by experiments performed in this Thesis.

8.2.1 Temperature imaging with existing porphyrin dimers

We have already shown that, in porphyrin dimer P_2NMe_3, the ratiometric method of viscosity sensitivity was independent of temperature. However, recent work from our group reported the temperature sensitivity of the dimers' excited state lifetime[1]. This is an extremely interesting phenomenon and deserves further detailed investigation. We hypothesize that differences in the *meso*-substitution of the dimer that affect conjugation and, ultimately the energy of rotation, will result in a different response of

the photophysical properties of the dimers to temperature. Thus the detailed investigation of the ratio and lifetime dependence on temperature is proposed for an extended range of existing conjugated dimers.

8.2.2 Characterisation of novel porphyrin dimers

The ratiometric viscosity-sensitivity and red-shifted fluorescence of the porphyrin dimers shown in this Thesis are conferred by the basic structure of the molecule. As such, the incompatibility of existing dimers with certain media, for instance, the lipid bilayer and polymer systems, can be addressed by modulating the meso-substituents to optimize for charge and size. As such, our collaborators in this effort, the group of Prof. Harry Anderson at Oxford University, are planning to design and synthesise a series of novel porphyrin dimers for photophysical characterisation as second generation viscosity and/or temperature probes.

For instance, the dimer can be made more likely to incorporate into lipid bilayers by introducing asymmetry: namely, inclusion of a lipid/hydrophobic tail on one end and the presence of hydrophilic PEG-chains on the other, anchoring it into one leaflet of the phospholipid membrane by electrostatic forces (Figure 8.1a). Alternatively, both ends could be modified by inclusion of PEG chains, making the dimer more soluble in aqueous environments and increasing the likelihood of solubility in the cell cytoplasm (Figure 8.1b). The synthesis of such probes is currently underway and when available they will be tested in our group for viscosity sensitivity.

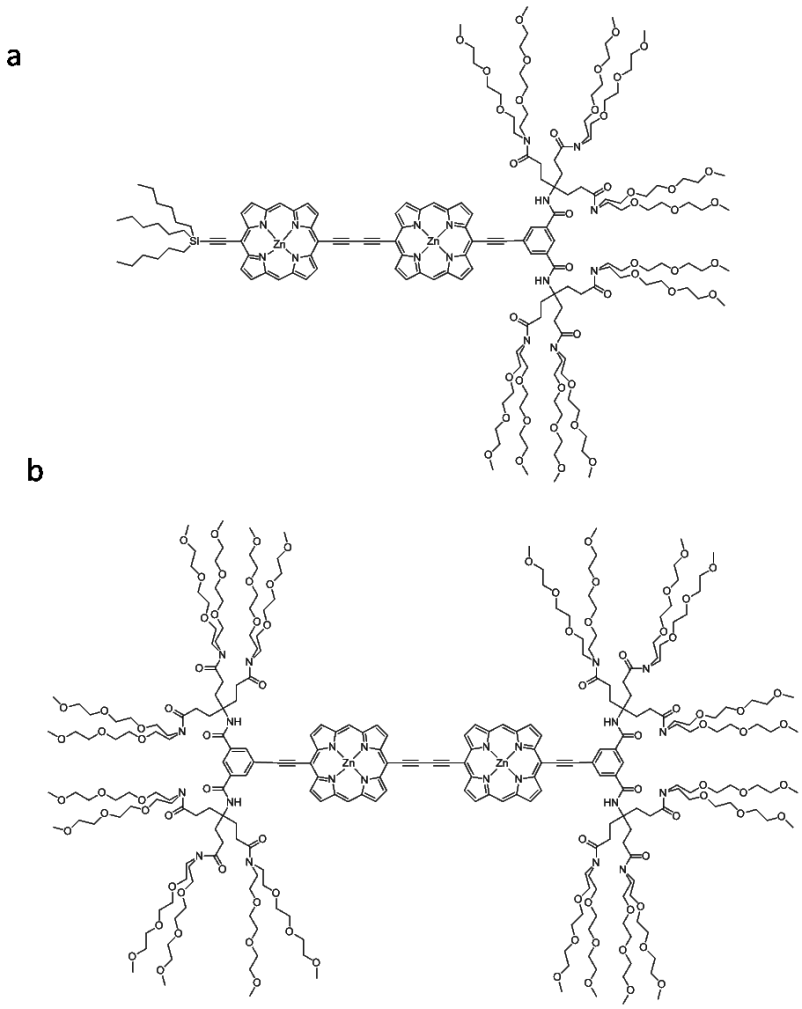

Figure 8.1: a) proposed structure for a novel Zn^{2+} porphyrin dimer, with a three-carbon tailed hydrophobic end and four triethylene glycol (TEG) groups on the other end. b) proposed structure for a second Zn^{2+} porphyrin dimer with four TEG groups on either meso position of the molecule. Structures courtesy of Harry Anderson, University of Oxford.

8.2.3 Cellular experiments

In this Thesis all viscosity measurements using conjugated dimers were performed in model systems. However, it is intended that this approach would be applicable to live cells and tissues, for dynamic imaging of these relevant environments. Thus what we have learned regarding the size and charge of the dimer, and its compatibility with model systems may be applied to cells. Furthermore, the red shifted absorption spectra of the porphyrin dimer compared to monomeric porphyrins confers the advantage of being able to be used for deep tissue penetration of light. Thus we believe that the work

performed in this Thesis will lay the foundation for the future development of conjugated dimers as viscosity imaging tools in living tissues. The design of the second generation dimers outlined above will be able to further aid the issues of biocompatibility and localization, and can be tailored to a biological application at hand.

8.2.4. *Investigation of the effects of oxidation upon viscosity of the lipid membrane*

Lastly, it is envisaged that the research into the singlet-oxygen mediated viscosity increase observed in Chapter VII of this Thesis will be further continued in our group. We discovered that the porphyrin dimer is an effective photosensitizer, and its localisation at the interface of the bilayer is advantageous for producing singlet oxygen that affects the hydrocarbon interior at distances far from origin. We imaged the viscosity change upon exposure to singlet oxygen by use of an another molecular rotor, BODPIY-C_{10}. This dual-probe experiment was highly successful and we intend to find more photosensitizer and molecular rotor pairs that are able to provide dynamic viscosity imaging of this effect. Permutations of the experiment in terms of the relative localization of the sensitizer and the rotor may further elucidate the effects of the photosensitizer's localisation in the bilayer and/or the effects on other parts of the phospholipid bilayer than the hydrocarbon region.

8.3 References

1. Vyšniauskas, A. et al. Unravelling the effect of temperature on viscosity-sensitive fluorescent molecular rotors. Chem. Sci. (2015). doi:10.1039/C5SC02248G

2. Verkman, a S. & Masur, S. K. Very low osmotic water permeability and membrane fluidity in isolated toad bladder granules. J. Membr. Biol. 104, 241–51 (1988).

3. Engelhardt, H. & Sackmann, E. On the measurement of shear elastic moduli and viscosities of erythrocyte plasma membranes by transient deformation in high frequency electric fields. Biophys. J. 54, 495–508 (1988).

4. Evans, E. A. & Hochmuth, R. M. Membrane viscoelasticity. Biophys. J. 16, 1–11 (1976).

5. Yeung, A. & Evans, E. Unexpected Dynamics in Shape Fluctuations of Bilayer Vesicles. J. Phys. II 5, 1501–1523 (1995).

6. Bloom, M., Evans, E. & Mouritsen, O. G. Physical properties of the fluid lipid-bilayer component of cell membranes: a perspective. Q. Rev. Biophys. 24, 293–397 (1991).

7. Evans, E. A. New membrane concept applied to the analysis of fluid shear- and micropipette-deformed red blood cells. Biophys. J. 13, 941–54 (1973).

8. Ladha, S., James, P. S., Clark, D. C., Howes, E. a & Jones, R. Lateral mobility of plasma membrane lipids in bull spermatozoa: heterogeneity between surface domains and rigidification following cell death. J. Cell Sci. 110 (Pt 9, 1041–50 (1997).

9. Kusumi, A., Ike, H., Nakada, C., Murase, K. & Fujiwara, T. Single-molecule tracking of membrane molecules: plasma membrane compartmentalization and dynamic assembly of raft-philic signaling molecules. Semin. Immunol. 17, 3–21 (2005).

10. Feder, T. J., Brust-Mascher, I., Slattery, J. P., Baird, B. & Webb, W. W. Constrained diffusion or immobile fraction on cell surfaces: a new interpretation. Biophys. J. 70, 2767–73 (1996).

11. Maczek, C. et al. Environmental influence on age-related changes of human lymphocyte membrane viscosity using severe combined immunodeficiency mice as an in vivo model. Exp. Gerontol. 33, 485–498 (1998).

12. Benga, G. & Holmes, R. P. Interactions between components in biological membranes and their implications for membrane function. Prog. Biophys. Mol. Biol. 43, 195–257 (1984).

Appendix A:

Absorbance spectra of all molecular rotors in DMF + 0.05% pyridine from Kuimova et al., 2009 (Ref 59)

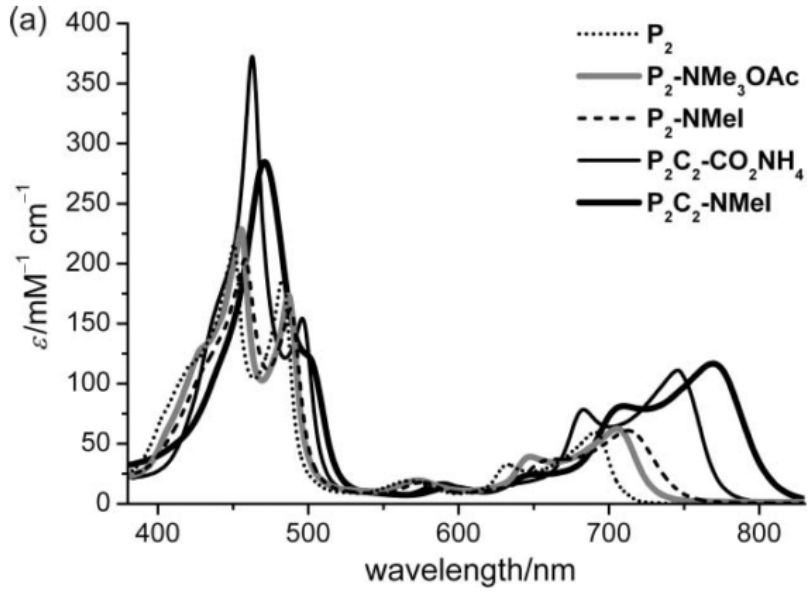

Appendix B:

Calculation of porphyrin dimer scattering length density and volume

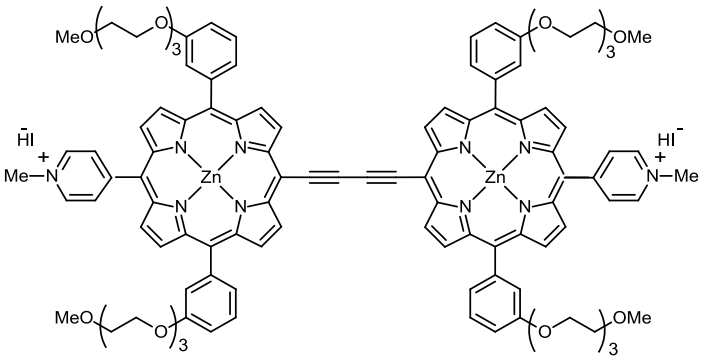

Element	Scattering Length (m)	N in 1 Porphyrin macrocycle	N in β substituent	N in 2x C triple bond linker	N in *meso* substituent		
Carbon	6.65E-05	20	13	4	7	110	7.31E-03
Oxygen	5.84E-05	0	4	0	0	16	9.35E-04
Hydrogen	-3.74E-05	8	19	0	7	106	-3.96E-03
Nitrogen	9.36E-05	4	0	0	2	12	1.12E-03
Zinc	5.68E-05	1	0	0	0	2	1.14E-04
Iodine	5.28E-05	0	0	0	1	2	1.06E-04
multiples		2	4	1	2		
Total							5.62E-03

Volume (cylindrical approximation):

Phenyl β-substituent length	Zn-Porphyrin base radius[133]	2 x C triple bond linker length	Methylpyridinium *meso*-substituent[134]
4.02 Å*	3.547 Å	7.5 Å	4.2 Å
4.02E-10 m	3.547E-10 m	7.5E-10 m	4.2E-10 m
length	30.088 Å		
base area	179.88599 $Å^2$		
	5412.409667 $Å^3$		
	5.41241E-27 m^3		